

A PHENOMENOLOGICAL CONSTITUTIVE MODEL FOR MAGNETIC SHAPE
MEMORY ALLOYS

A Dissertation

by

BJOERN KIEFER

Submitted to the Office of Graduate Studies of
Texas A&M University
in partial fulfillment of the requirements for the degree of

DOCTOR OF PHILOSOPHY

December 2006

Major Subject: Aerospace Engineering

A PHENOMENOLOGICAL CONSTITUTIVE MODEL FOR MAGNETIC SHAPE
MEMORY ALLOYS

A Dissertation

by

BJOERN KIEFER

Submitted to the Office of Graduate Studies of
Texas A&M University
in partial fulfillment of the requirements for the degree of

DOCTOR OF PHILOSOPHY

Approved by:

Chair of Committee,	Dimitris C. Lagoudas
Committee members,	Ibrahim Karaman
	Junuthula N. Reddy
	Jay R. Walton
Head of Department,	Helen L. Reed

December 2006

Major Subject: Aerospace Engineering

ABSTRACT

A Phenomenological Constitutive Model for Magnetic Shape Memory Alloys.

(December 2006)

Bjoern Kiefer, Diplom, Ruhr-Universität Bochum

Chair of Advisory Committee: Dr. Dimitris C. Lagoudas

A thermodynamics-based constitutive model is derived which predicts the nonlinear strain and magnetization response that magnetic shape memory alloys (MSMAs) exhibit when subjected to mechanical and magnetic loads. The model development is conducted on the basis of an extended thermo-magneto-mechanical framework. A novel free energy function for MSMAs is proposed, from which the constitutive equations are derived in a thermodynamically-consistent manner. The nonlinear and hysteretic nature of the macroscopic material behavior is captured through the evolution of internal state variables which are motivated by the crystallographic and magnetic microstructures of MSMAs. Model predictions are presented for different relevant loading cases and analyzed in detail. Finally, magnetostatic boundary value problems for MSMAs are considered and numerically solved using the finite element method. For these computations the developed constitutive model provides the nonlinear magnetic properties of the MSMA. The knowledge of the magnetic field distribution in the computational domain as a function of the applied field, which results from this magnetostatic analysis, is useful for the proper interpretation of experimental results as well as the design of experiments and applications.

To my family, who has always been my foundation

ACKNOWLEDGMENTS

I wish to express my sincere gratitude to Dr. Dimitris Lagoudas, my advisor and chair of the Ph.D. advisory committee, for his guidance and support. I have benefitted tremendously from his knowledge and experience, his determination and his strive for excellence. He has both encouraged and challenged me. I am especially grateful for the opportunity to participate in many national and international conferences as well as other professional meetings. I am certain these experiences will prove to be immensely important for my future professional career.

Special thanks are also due to the members of my graduate advisory committee: Dr. Ibrahim Karaman, Dr. Junuthula N. Reddy, and Dr. Jay Walton. All of them, as my advisor, have been and will continue to be role models for me, as researchers, teachers and on a personal level. Their support throughout my studies has greatly contributed to the final form of this dissertation. Dr. Karaman, and his students Haluk Karaca and Burak Basaran, have greatly aided my research with their experimental work on magnetic shape memory alloys, which is frequently referenced throughout this dissertation. Thanks also to Dr. Amine Benzerga for serving as a committee member substitute during my final defense.

I wish to thank Alicia Broederdorf for her technical assistance, especially with the finite element analysis of magnetostatic boundary value problems. I am also grateful for the administrative support provided by Ms. Pam McConal, who many times made my life much easier. Finally, I gratefully acknowledge the support of the National Science Foundation (NSF) and the Army Research Office (ARO) for this research.

On a personal level I want to thank first and foremost my wife Anette, the love of my life, for her support. It has been the hard work she invested in establishing herself

as a freelance journalist in a foreign country, while also raising our lovely daughters, that has afforded me the opportunity to pursue this professional goal. She has also always made sure that I participate in a healthy share of non-work related activities.

I wish to acknowledge the important role my parents have played in my life. They taught me to work hard, pursue my goals and dreams while respecting others and being grateful for every opportunity given in life. They also taught me the value of education and knowledge. My Dad always had a saying that I remember from my early childhood: *Was macht man mit Problemen? Lösen!* (*What is the proper way of handling problems? You solve them!*) This approach of solving difficult tasks not by finding a way around them but to face them head on, has been a key to my successful education as an engineer.

I want to thank Gary-Don Seidel for his friendship and the numerous scientific, philosophical and personal discussions that have been very valuable to me. His contagious excitement about everything "Aggie" has been an important factor in my decision to come to Texas A&M to pursue a Ph.D. degree. I am also very grateful for the various professional and personal interactions with my colleagues and friends Olivier Godard, Todd Griffith, Darren Hartl, Parikshith Kumar, Luciano Machado, Peter Popov, Chad Searcy, Lesley Weitz, and Matt Wilkins, which have, to a great extent, defined the quality of my experience at Texas A&M.

TABLE OF CONTENTS

CHAPTER		Page
I	INTRODUCTION	1
	A. General Aspects of Magnetic Shape Memory Alloys	1
	B. Literature Review of MSMA Models	4
	C. Outline of the Present Research	8
II	INFLUENCE OF THE CRYSTALLOGRAPHIC AND MAGNETIC MICROSTRUCTURE ON THE MACROSCOPIC RESPONSE OF MSMAS	11
	A. The Magnetic Field-Induced Strain Response of MSMAs	11
	B. The Magnetization Response of MSMAs	20
	1. Magnetization by Magnetic Domain Wall Motion	22
	2. Magnetization by Rotation of Magnetization Vectors	23
	3. Magnetization by Variant Reorientation	25
	4. The Coupling of the Magnetization Mechanisms for MSMAs.	26
III	A CONTINUUM DESCRIPTION OF MAGNETIZABLE SOLIDS	30
	A. Maxwell's Equations	33
	B. Conservation of Mass, Momentum and Energy	37
	C. Extended Thermodynamic Framework	41
IV	PHENOMENOLOGICAL MODELING OF MSMA	47
	A. The Choice of Internal State Variables	47
	B. Formulation of the Specific Gibbs Free Energy	50
	C. Evolution Equations and Activation Conditions	58
V	MSMA RESPONSE UNDER SPECIFIC MAGNETOMECHANICAL LOADING	64
	A. Loading Case 1: Variable Magnetic Field at Different Levels of a Perpendicular Compressive Uniaxial Stress	65
	1. Fixed Magnetic Domain Structure	67

CHAPTER	Page
a. Reduced Model Equations	67
b. Calibration of the Model Parameters	70
c. The Reorientation Diagram	74
d. Model Predictions	77
2. Variable Magnetic Domain Structure	87
a. Reduced Model Equations	87
b. Calibration of the Model Parameters	90
c. The Reorientation Diagram	91
d. Model Predictions	92
B. Loading Case 2: Variable Compressive Uniaxial Stress at Different Levels of a Perpendicular Magnetic Field . . .	96
C. Loading Case 3: Variable Magnetic Field Collinear to a Constant Compressive Uniaxial Stress at Different Lev- els of a Perpendicular Magnetic Field	105
VI MAGNETOMECHANICAL BOUNDARY VALUE PROB- LEMS FOR MSMAS	115
A. Review of the Magnetostatic Problem	116
B. The Demagnetization Effect	117
C. Finite Element Analysis of the Magnetostatic Problem . .	122
D. Interpretation of Experimental Data through Magneto- static Analysis	131
VII SUMMARY AND CONCLUSIONS	138
REFERENCES	141
APPENDIX A CONCEPTS OF CONTINUUM MECHANICS: DEFINITIONS AND DERIVATIONS	162
A1. Mathematical Preliminaries	162
A2. Kinematics	162
A3. Derivation of the Local Forms of the Balance Laws	164
A4. Stress Power for a Small Strain Approximation	168
A5. Derivation of Thermodynamic Restrictions on Consti- tutive Equations	170
APPENDIX B DERIVATIONS RELATED TO ELECTROMAGNETISM . .	172
B1. Magnetostatic Poisson Equations	172

CHAPTER	Page
B2. Field Transformations	173
APPENDIX C DISCUSSION OF THE GIBBS FREE ENERGY	176
C1. Interpretation of the Gibbs Free Energy for a Hyper- elastic Material	176
C2. Discussion of an Alternative Gibbs Free Energy Ex- pression for MSMA	177
C3. Accounting for Temperature Changes During Variant Reorientation	184
APPENDIX D SELECTED MAPLE FILES	187
D1. Determination of Model Parameters	187
D2. Numerical Evaluation of the Constitutive Response	188
VITA	193

LIST OF TABLES

TABLE		Page
I	Relations between material constants and model parameters.	72
II	Material parameters for the considered $\text{Ni}_{50.7}\text{Mn}_{28.4}\text{Ga}_{20.9}$ composition, and the resulting hardening and hysteresis parameters calibrated at -1.0 MPa.	73
III	Configuration schematics and data for the strain hysteresis curve at -1.0 MPa.	81
IV	Material parameters for the $\text{Ni}_{50.7}\text{Mn}_{28.4}\text{Ga}_{20.9}$ composition, and the resulting hardening and hysteresis parameters when calibrated at -0.2 MPa.	91
V	Configuration schematics and data for the strain hysteresis curve at -0.2 MPa with partial magnetic domain wall motion.	95
VI	Configuration schematics and data for the strain hysteresis curve under variable σ_{xx} and $\mu_0 H_y = 0.4$ T.	102
VII	Configuration schematics and data for the strain hysteresis curve under variable H_x at $\mu_0 H_y = 0.4$ T and $\sigma_{xx} = -0.2$ MPa.	112
VIII	Material parameters for the $\text{Ni}_{51.1}\text{Mn}_{24.0}\text{Ga}_{24.9}$ composition, and the resulting hardening and hysteresis parameters when calibrated at -2 MPa.	125

LIST OF FIGURES

FIGURE	Page	
1	Crystal structure of the austenitic and the tetragonal martensite phases in Ni ₂ MnGa. Arrows indicate possible magnetization vector orientations along the magnetic easy axis of each variant.	12
2	Schematic of a typical loading sequence for magnetic field-induced strain measurements in MSMA. Inserts (a)–(c) depict the arrangement of martensitic variants and magnetic domains at different loading stages.	13
3	Typical total strain-magnetic field response curves for MSMAs at different stress levels.	15
4	Magneto-thermo-mechanical setup used for MFIS measurements. . .	17
5	Evolution of the MFIS in a Ni ₂ MnGa single crystal at different stress levels during the first magnetic cycle.	18
6	Evolution of the MFIS in a Ni ₂ MnGa single crystal at different stress levels during the second magnetic cycle.	19
7	A schematic of the initial single variant 1 martensite state. The variant reorientation is suppressed by an axial compressive stress higher than the blocking stress. Also shown, schematics of the corresponding microscopic scale and the crystallographic scale.	21
8	Magnetization of the single variant specimen along the easy axis. . .	22
9	Magnetization of the single variant specimen along the hard axis. . .	23
10	Qualitative magnetization curves of the single variant MSMA specimen magnetized along the compression and perpendicular axes. For quantitative experimental results.	24
11	Relative magnetization response in Ni-Mn-Ga as reported by Heczko.	26

FIGURE	Page
12	Experimentally observed magnetic domain structures in two-variant Ni-Mn-Ga samples. 28
13	Schematic representation of the microstructure showing the coexistence of martensitic variants and magnetic domains. 48
14	Schematic illustration of the three modeled loading cases. Small arrows indicate the direction of the average magnetization in each variant at an exemplary load level during the reorientation process. 64
15	The variant reorientation process with fixed domain structure $\alpha=1$ 67
16	Calibration of the model parameters using the experimental MFIS curve at -1.0 MPa. Solid line—model simulation, dashed line—experimental data. 71
17	Numerical $\mu_0 H_y - \sigma_{xx} $ variant reorientation diagram. The dashed line represents the magnetic loading path at the constant stress levels of -1.0 MPa. 74
18	Predicted MFIS hysteresis curves at different stress levels (solid lines) and comparison to experimental data (dashed line). 78
19	Prediction of MSMA magnetic field-induced strain response in Kiefer et al. Experimental data (cf. Fig. 6)—dashed lines; numerical results—solid lines. 79
20	Detail: MFIS hysteresis loop under -1.0 MPa. 80
21	Predicted magnetization hysteresis curves at different stress levels (solid lines) and comparison to experimental data at -1.0 MPa (dashed line). 85
22	Variant reorientation diagram for the parameters listed in Table IV. Loading path for model calibration A \rightarrow E. 92
23	Simulation of the magnetic field-induced strain response at -0.2MPa. Solid line—model, dashed line—experiment. 93

FIGURE	Page
24	Prediction of the magnetization response at -0.2 MPa when accounting for partial magnetic domain wall motion. Solid line—model, dashed line—experiment. 94
25	Loading paths in the $\mu_0 H_y$ - $ \sigma_{xx} $ variant reorientation diagram. Exemplary loading path E \rightarrow H. 97
26	Stress-induced reorientation strain vs. stress and magnetic field. Initial constant stress loop at -0.2 MPa. 99
27	Stress-induced reorientation strain vs. stress at different levels of $\mu_0 H_y$ 100
28	Detail: Stress-induced reorientation strain hysteresis loop at 0.4 T. . . 101
29	Normalized magnetization vs. stress and magnetic field. Initial constant stress loop at -0.2 MPa. 103
30	Normalized magnetization vs. stress at different levels of $\mu_0 H_y$ 104
31	Loading paths in the $\mu_0 H_x$ - $\mu_0 H_y$ variant reorientation diagram at -0.2 MPa. 108
32	Magnetic field-induced reorientation strain vs. two components of the magnetic field at a constant stress of -0.2 MPa. 109
33	Magnetic field-induced reorientation strain vs. the x-component of the magnetic field at different levels of $\mu_0 H_y$ and $\sigma_{xx} = -0.2$ MPa. . 110
34	Detail: H_x -induced reorientation strain hysteresis loop under 0.4 T. . 111
35	Normalized magnetization vs. the magnetic field components at -0.2 MPa. 113
36	Normalized magnetization vs. the x-component of the magnetic field at different levels of $\mu_0 H_y$ and $\sigma_{xx} = -0.2$ MPa. 114
37	Magnetic field of a rectangular permanent magnet. The white arrow indicates the direction of the magnetization. Contour plot: $ H_y $; arrows and streamlines: direction of \mathbf{H} 118

FIGURE	Page
38	Magnetic field of an ellipsoidal permanent magnet. The white arrow indicates the direction of the magnetization. Contour plot: $ H_y $; arrows and streamlines: direction of \mathbf{H} 119
39	Domain geometry, mesh and boundary conditions for the magnetostatic problem. Dashed lines indicate the location of the non-magnetic grips of the load frame. 123
40	Model Calibration. Experimental data (diamonds) and model simulation (solid line). Data for a $\text{Ni}_{51.1}\text{Mn}_{24.0}\text{Ga}_{24.9}$ alloy tested at -95°C under the compressive stress of 2 MPa. 126
41	Predicted y -component of the magnetization at the compressive stress of 2 MPa. Only the solid portion of the curve is used in the magnetostatic analysis. 127
42	Distribution of H_y in the computational domain at the applied magnetic field of $\mu_0 H_y^a = 2.0$ T. 129
43	Distribution of the magnetic field and magnetization within the specimen at the applied magnetic field of $\mu_0 H_y^a = 1.3$ T. 130
44	Distribution of the y -components of the magnetic field and the magnetization across the specimen and its immediate vicinity at different levels of x , as indicated in Fig. 43, for the exemplary applied flux level of 1.3 T. 131
45	Magnetization data corrected for demagnetization. Specimen aspect ratio 2:1. 133
46	Influence of specimen aspect ratios on the correction of the magnetization data. 134
47	Influence of specimen aspect ratios on the correction of the magnetic field-induced strain data. 135
48	Comparison of the corrections through demagnetization factors and FEM analysis. Specimen aspect ratio 2:1. 136
49	Position dependence of the magnetization response within the rectangular specimen. 137

CHAPTER I

INTRODUCTION

A. General Aspects of Magnetic Shape Memory Alloys

Shape memory alloys (SMAs) have been an important member of the class of active materials for at least two decades now. They have successfully been used in actuator and sensor design as well as biomedical and numerous other technological applications [1–3]. The large strains of 6–10% these materials exhibit when being subjected to thermal or mechanical loads, are caused by the change in crystallography associated with a reversible austenite to martensite phase transformation. *Magnetic shape memory alloys* (MSMAs), often also referred to as ferromagnetic shape memory alloys (FSMAs) [4–6], have more recently emerged as an interesting extension of this class of materials. In addition to the strains originating from temperature- or stress-activated conventional shape memory behavior [7–10], large strains can be produced in these alloys under the application of magnetic fields. The macroscopically observable *field-induced strains* in MSMA are caused by the microstructural *reorientation of martensitic variants*. Since the variants have different preferred directions of magnetization, applied magnetic fields can be used to select certain variants over others, which results in the macroscopic shape change.

Magnetic shape memory alloys exhibit one or even two orders of magnitude higher recoverable *magnetic field-induced strains* (MFIS) [11] than ordinary magnetostrictive materials, such as Terfenol-D [12] and Galfenol [13], and these strains are also much larger than the electric field-induced strains in piezoelectrics [3]. At comparable recoverable strains they also have an advantage over conventional shape

The journal model is International Journal of Engineering Science.

memory alloys due to the much higher, up to 1kHz, frequency range at which they can be operated for some applications [14]. This is because their actuation is driven by the magnetic-field induced reorientation of martensitic variants and is, thus, not limited by heat transfer [15]. The main limitation of MSMA is the relatively low blocking stress of typically 6-10 MPa, above which magnetic field-induced strains are completely suppressed. The field-induced strain response of MSMA is nonlinear, hysteretic, stress-dependent and intrinsically coupled to the magnetization response of the material. The coupled macroscopic response is driven by three mechanisms, the motion of magnetic domain walls, the local rotation of magnetization vectors (both of which also occur in regular ferromagnetic materials [16–18]), and field-induced variant reorientation.

This unique coupling of mechanical and magnetic properties (and thermal if one considers the conventional shape memory behavior) makes MSMA interesting materials for smart structures, actuator and sensor applications [14, 19]. A different class of applications aims to take advantage of the unique and adjustable magnetic properties of MSMA in solenoid transducers [5] or voltage generators [20].

The most widely investigated magnetic shape memory materials have been Ni-Mn-Ga alloys [21]. Martensitic transformations in Ni₂MnGa alloys were first conclusively reported by Webster et al. [22]. Zasimchuk et al. [23] and Martynov and Kokorin [9] performed detailed studies on the crystal structure of martensite in the Ni₂MnGa alloy. Ullakko et al. [12] are credited with first suggesting the possibility of a magnetic field-controlled shape memory effect in these materials. They observed magnetic field-induced strains of nearly 0.2% in stress-free experiments on martensitic Ni₂MnGa single crystals. Further work on off-stoichiometric intermetallic compounds near the composition Ni₂MnGa, in combination with thermo-mechanical treatments and the utilization of a better understanding of the crystallographic structure of the-

ses alloys, have yielded larger field-induced strains of 6% [4] and up to 10% [11, 24] in single crystals. Other magnetic shape memory alloys have been studied including Fe-Pd [25–28], Fe-Ni-Co-Ti, Fe-Pt, Co-Ni-Ga, Ni-Mn-Al [24, 29–33] and Co-Ni-Al [10, 34]. These alloys exhibit lower field-induced strains, but can have other advantages. The largest field-induced strains that have been observed in Fe-Pd, for example are 3.1% [28, 35], but this material is much more ductile than Ni-Mn-Ga [25].

The magnetic field-induced strains that can be generated in polycrystalline magnetic shape memory alloys are smaller than those observed for single crystals [36–40]. One effort aimed towards increasing the strain output of polycrystals is based on creating favorable texture in these materials. Marioni et al. [41] calculated the upper bound for the achievable field-induced strain in untextured NiMnGa polycrystals to be 21% of the single-crystal value and at most 50% for textured crystals.

The phenomenon of magnetic field-induced austenite-martensite phase transformations has also been investigated. Such transformations have been observed in Fe-Pt [42], Ni-Mn-Ga [43] and Ni-Mn-Fe-Ga [36] alloys. Magnetic fields have also been shown to influence the temperature- or stress-induced austenite-martensite phase transformation in MSMAAs [36]. Furthermore, it has been observed that Ni-Mn-Ga alloys exhibit several different martensite morphologies and thus intermartensitic phase transformations [8, 44, 45]. The work presented here, however, is focused on the well-established MSMA behavior as caused by the magnetic field-induced martensitic variant reorientation.

A more detailed description of macroscopic constitutive response of MSMAAs, and of the micro-scale mechanisms causing it, will be provided in Chapter II.

B. Literature Review of MSMA Models

Several models have been proposed in the literature to describe the constitutive response related to the magnetic field-induced variant reorientation. The approach most commonly taken is the minimization of a free energy function characterizing the system to find equilibrium configurations for given temperature, stress and magnetic field.

The model presented by James and Wuttig [26] is based on a *constrained theory of micromagnetics* (see also [46–48]). The terms contributing to the free energy in their model are the Zeeman energy, the magnetostatic energy and the elastic energy. The magnetization is assumed to be fixed to the magnetic easy axis of each martensitic variant because of high magnetic anisotropy. The microstructural deformations and the resulting macroscopic strain and magnetization response are predicted by detecting low-energy paths between initial and final configurations. They conclude that the typical strains observed in martensite, together with the typical easy axes observed in ferromagnetic materials lead to layered domain structures that are simultaneously mechanically and magnetically compatible.

O’Handley [49, 50] proposed a 2-D model in which two variants are separated by a single twin boundary and each variant itself consists of a single magnetic domain. The local magnetization is not necessarily constrained to the crystallographic easy axis. Depending on the magnitude of the magnetic anisotropy, either the magnetic anisotropy difference (low magnetic anisotropy case) or the Zeeman energy (high magnetic anisotropy case) are identified as the driving forces for twin boundary motion. For the intermediate anisotropy case a parametric study is conducted showing the influence of varying elastic and magnetic anisotropy energies. All cases assume an initial variant distribution that implies a remnant magnetization.

Likhachev and Ullakko [51] presented a model which identifies the magnetic anisotropy energy difference in the two variant twinned-martensite microstructure as the main driving force for the reorientation process. The free energies associated with magnetizing a single variant martensite along the magnetic easy and hard axes are computed from integration over the experimental magnetization curves. The driving force for twin boundary motion is proposed to be the derivative of the difference between the two free energy terms with respect to the martensitic variant volume fraction. They argue that, regardless of the physical nature of the driving force, twin boundary motion should be initiated at equivalent load levels. With this assumption experimentally obtained detwinning-under-stress data in addition to the magnetization data are used to predict the MSMA constitutive behavior associated with field-induced variant reorientation.

Hirsinger and Lexcellent [52, 53] introduced the outline of a non-equilibrium thermodynamics based model. The free energy contains chemical, mechanical, magnetic and thermal contributions. The magnetic term is given by the Zeeman energy. Two internal state variables, the martensitic variant volume fraction and the magnetic domain volume fraction, are introduced to represent the influence of the microstructure. The rate independent dissipative nature of their approach motivates the definition of driving forces for the twin boundary motion and the domain wall motion.

Kiefer and Lagoudas formulated a thermodynamics-based phenomenological constitutive model for MSMA with internal state variables describing the evolution of the crystallographic and magnetic microstructures. Their approach is aimed at capturing the hysteretic effects associated with the magnetic field-induced reorientation of martensitic twins and the resulting loading history dependence of the material response. Emphasis is also placed on modeling the nonlinear and stress-level-dependent nature of the magnetic field-induced strain and magnetization response. The Kiefer

and Lagoudas model mainly distinguishes itself from the Hirsinger and LExcellent approach by allowing the magnetization vectors to rotate away from the magnetic easy axes, which leads to much more accurate predictions of the magnetization response. The model development was discussed in [54–57]. Experimental work, with Karaman et al., was presented in [58] and compared with model predictions. The numerical analysis of magnetostatic boundary value problems for MSMA was described in [59, 60]. All of the listed aspects of this research work are also presented in detail in this dissertation. Faidley et al. [5] proposed an extension of an earlier version of the Kiefer and Lagoudas model [54] to predict the reversible strain effect in Ni-Mn-Ga with collinear field and stress. In their approach internal restoring forces orthogonal to the applied field are attributed to pinning sites which elastically deform twin boundaries. Tan and Elahinia [61] utilized the Kiefer and Lagoudas model [55, 56] to study the dynamic response of MSMA actuators.

Glavatska et al. [62] proposed a constitutive model for the martensitic twin rearrangement based on a statistical approach. The rearrangement of twins and resulting macroscopic strain is assumed to be triggered by magnetic field-induced micro-stresses originating from magnetoelastic interactions. The probability for the rearrangement of the twins in which the stresses are near the critical stress is described through a statistical distribution. This model was utilized by Chernenko et al. [63, 64], who also followed a microscopic approach to the magnetic field-induced deformation of martensite in MSMA.

Another model that uses the principles of statistical physics has been proposed by Buchelnikov and Bosko [65] who extended a model derived by Govindjee and Hall [66] for conventional shape memory alloys. Their model derivation follows what is referred to as a *multi-well approach*. They identify four phases, the cubic austenite and the three tetragonal variants. These phases can, in principle, transform into any

of the other phases under the influence of temperature, stress and magnetic field. The rate of transformation between the different phases is assumed to be proportional to the net probability that one phase will overcome the energetic barrier required to transform to a second phase. The free energy expression that is utilized to compute the energetic barrier consists of elastic, thermal and magnetic energy terms. The magnetic energy consists of the magnetic anisotropy energy, the magnetostatic energy of the demagnetization field and the Zeeman energy.

Smith et al. recently proposed a unified framework for modeling hysteresis in ferroic materials [67], which briefly discusses the subject of magnetic shape memory alloys. A detailed comparison of many of the described models can be also found in the recent paper by Kiang and Tong [68].

A general approach to phenomenological modeling of the loading history dependent constitutive response of materials undergoing phase transformation, detwinning, or variant reorientation has widely been utilized in the literature on conventional shape memory alloys [66, 69–77]. A detailed review of the modeling of shape memory alloys has recently been published by Patoor et al. [78] and Lagoudas et al. [79]. Since the austenite to martensite phase transformation in SMAs is induced by cooling or the application of mechanical forces, the independent state variables in this case are usually chosen to be temperature and stress. In phenomenological constitutive modeling the system can be characterized by a macroscopic free energy expression which is a function of these independent state variables. A common approach of incorporating path dependence and dissipation is through the introduction of internal state variables [80], whose evolution then accounts for the loading history dependence of the material behavior. Motivated by the crystallographic microstructure of martensite, a common choice for an internal state variable is the martensitic volume fraction. Constitutive equations, which relate the dependent state variables to the independent

ones, follow directly from applying the well-known *Coleman and Noll procedure* [81] commonly used in phenomenological modeling. The dependent state variables, such as the strain or entropy, are themselves also functions of the internal state variables through the constitutive relations and depend therefore on the loading history. The lack of apparent intrinsic time scales (diffusionless, thermoelastic phase transformation) makes the shape memory effect subject to rate independent modeling. This approach lends itself to the introduction of transformation functions, similar to yield functions of rate-independent plasticity models, which govern the onset and termination of the phase transformation [82]. Transformation hardening functions account for the interactions of different phases during the transformation process, which influence the activation of the phase transformation. The evolution of transformation strain is related to the evolution of the martensitic volume fraction and its direction is given by a postulated transformation tensor [71].

The variant reorientation process in magnetic shape memory alloys is, from a modeling standpoint, also similar to the detwinning (i. e. self-accommodated to detwinned martensite) and reorientation (i. e. change in the selection of martensitic variants under changes in the stress state) phenomena that are observed in conventional shape memory alloys [75, 83–86].

C. Outline of the Present Research

The research presented in this dissertation is focused on three main objectives.

1. Formulation of a general thermo-magneto-mechanical framework for the modeling of continuous, deformable and magnetizable materials with evolving microstructure.
2. Development of a phenomenological constitutive model with internal state vari-

ables for the martensitic variant reorientation in MSMA.

3. Analysis of magnetomechanical boundary value problems for MSMA.

Objective 1 is addressed in Chapter III, which includes the discussion of Maxwell's equations for continua, the presentation of the balance laws of continuum mechanics with magnetic source terms and the derivation of an extended thermodynamic framework.

The second objective is addressed in Chapters IV and V. Since this is the main aspect of the research work, it shall be outlined briefly. In order to apply the discussed approach of rate-independent phenomenological modeling to MSMA the independent variable state space of the free energy, which typically consists of the temperature and stress tensor, is expanded to include the magnetic field strength vector. The Zeeman energy and the magnetocrystalline anisotropy energy are introduced as additional terms in the free energy expression. Due to the magnitude of the magnetic field-induced strain in MSMA the magnetomechanical coupling through ordinary magnetostriction is neglected. The evolution of the crystallographic and magnetic microstructure, which causes the macroscopically observed response of MSMA is taken into account through internal state variables such as the martensitic variant volume fraction. Constitutive equations for the dependent state variables is conducted in a thermodynamically-consistent manner by taking derivatives of the free energy function. A reorientation function takes the role of the aforementioned transformation function, and governs the start and finish of the magnetic field-induced strain evolution. The stress level dependence of the critical magnetic fields for this activation are visualized in a reorientation diagram in magnetic field-stress space. This diagram is analogous to the stress-temperature phase diagrams frequently plotted for conventional SMA. Evolution equations for the internal state variables are

derived. A procedure to calibrate the model parameters from a limited number of clearly defined experiments is described.

In Chapter V the model is applied to special loading cases for which the general constitutive equations can be reduced. The predicted strain and magnetization response is analyzed for each loading case and the macroscopic behavior is physically interpreted by connecting it to the predicted evolution of the microstructure.

The work presented in Chapter VI is concerned with objective 3. Maxwell's equations are solved using the finite element method for magnetostatic conditions. The nonlinear magnetic properties and the coupling to the mechanical problem are provided by the developed constitutive model. This analysis provides the necessary tool for the design of applications involving MSMA components. It also enables a more accurate interpretation of experimental data and thus leads to more accurate model calibrations.

CHAPTER II

INFLUENCE OF THE CRYSTALLOGRAPHIC AND MAGNETIC
MICROSTRUCTURE ON THE MACROSCOPIC RESPONSE OF MSMAS

A general introduction to the constitutive behavior of MSMAs was given in Chapter I. In this chapter a more detailed description of the connection between the evolving crystallographic and magnetic microstructure of MSMAs and the observed macroscopic response is provided. This knowledge will then be used to motivate the formulation of the constitutive model.

A. The Magnetic Field-Induced Strain Response of MSMAs

Since the ternary intermetallic compound Ni-Mn-Ga is the most widely investigated magnetic shape memory alloy, it shall be the focus of the following discussion, which does not imply that the basic concepts or the modeling approach presented in this work are restricted in any way to this particular alloy.

The high temperature austenite phase of Ni-Mn-Ga alloys near the composition Ni_2MnGa exhibits a $L2_1$ Heusler type structure, in which all of the atoms are located on the sites of a body centered cubic lattice [22]. The austenite phase is paramagnetic above the Curie temperature, which for the stoichiometric composition of Ni_2MnGa is 376 K [87], and ferromagnetic below it. The Curie temperature only shows a slight variation with changes in the composition [87, 88]. A strong compositional dependence, however, is observed for the austenite-martensite phase transformation start temperature [88–90], which is 202 K in stoichiometric Ni_2MnGa [87]. The martensite in these alloys can be of five-layered tetragonal (5M), seven-layered orthorhombic (7M), and non-modulated tetragonal martensite (NM) morphology [8, 44, 45]. Here only the most commonly observed tetragonal martensite of Ni_2MnGa is considered.

A simplified representation of the crystal structure, which is usually adopted for convenience [91, 92], is shown in Fig. 1. The undeformed austenite has cube edges of length a_0 , whereas the undeformed tetragonal martensite unit cell has short and long edges of lengths a and c , respectively. Typical lattice parameters for Ni_2MnGa have been reported in the literature [22, 23, 93–95].

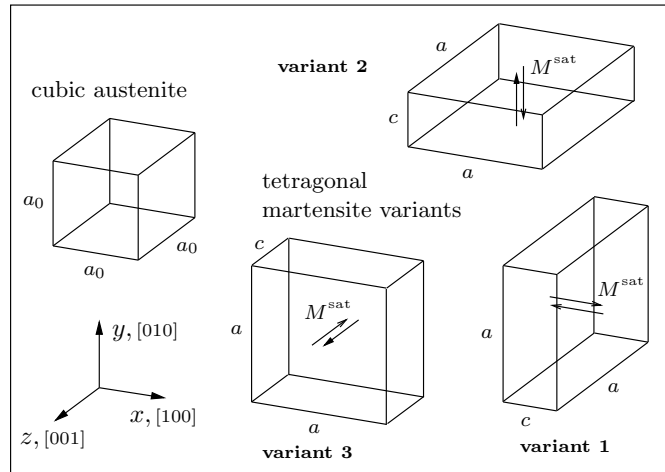


Fig. 1. Crystal structure of the austenitic and the tetragonal martensite phases in Ni_2MnGa . Arrows indicate possible magnetization vector orientations along the magnetic easy axis of each variant.

Since this transition temperature is well below Curie temperature the martensitic phase is ferromagnetic such that, even in the absence of an external magnetic field, the martensitic variants are *spontaneously magnetized* [16, 18]. The local magnetization vector in each ferromagnetic variant is oriented along one preferred crystallographic direction named the *magnetic easy axis*, which in this case is aligned with the short edge c of the tetragonal unit cell. The magnetization vectors can be oriented in either the positive or negative easy axis direction.

If an external field is applied, it is energetically favorable for the magnetization

vectors to align with the applied field. In MSMA three competing mechanisms are available to achieve this alignment. The first two, the *magnetic domain wall motion* and the *magnetization vector rotation* are common to all ferromagnetic materials and shall be discussed shortly. The third mechanism, which is unique for magnetic shape memory alloys, is the magnetic field-driven *reorientation of martensitic variants*. This is possible since the preferred axes of the tetragonal variants are mutually perpendicular, such that an external magnetic field can be used to favor certain variants over others. The induced redistribution of variants leads to the observed macroscopic shape change.

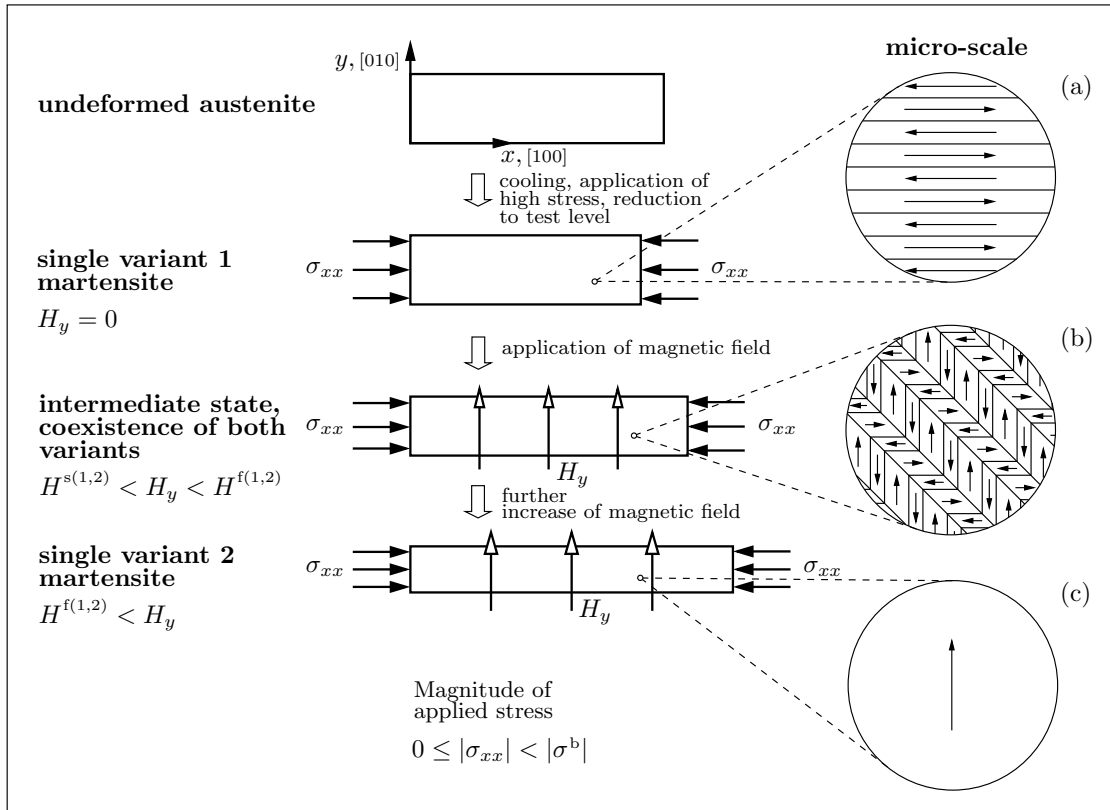


Fig. 2. Schematic of a typical loading sequence for magnetic field-induced strain measurements in MSMA [58, 96–98]. Inserts (a)–(c) depict the arrangement of martensitic variants and magnetic domains at different loading stages.

Fig. 2 on the preceding page schematically illustrates a typical thermo-magneto-mechanical loading sequence of an experiment in which the magnetic field-induced strain response of MSMA is measured. Initially, the single crystalline MSMA specimen is cooled to induce the austenite to martensite phase transformation. Then a sufficiently high compressive stress is applied to produce a single variant configuration. In the depicted case the sample has been cut such that the $[100]$ -direction of the austenitic crystal aligns with the compression axis, which is also denoted the x -axis. The compression along this axis in the martensitic state favors variant 1 (for nomenclature see Fig. 1), since its short axis is along the x -direction, and the two other tetragonal variants are eliminated. The stress is then lowered to the desired test level, during which the single variant state is preserved, and kept constant for the remainder of the experiment. The upper stress bound above which the variant reorientation is completely suppressed is called the *blocking stress* σ^b [96].

The micro-scale Schematic (a) of Fig. 2 shows the described stress-induced single martensitic variant configuration, before a magnetic field is applied. Also depicted are magnetic domains, i. e. regions of uniform magnetization, which are separated by 180° magnetic domain walls, indicated by horizontal lines. These magnetic domains form to minimize the magnetostatic energy of the configuration [16, 17, 99, 100]. In each domain the magnetization vectors are aligned with the magnetic easy axis of variant 1, which according to Fig. 1 coincides with the c -edge of the tetragonal variant and the $[100]$ -direction. These magnetization vectors point in either the positive or negative coordinate direction. Since no external magnetic field is applied the two domains are of equal volume fraction, such that the macroscopic magnetization vanishes.

The application of a magnetic field perpendicular to the direction of mechanical loading induces the nucleation of variant 2 once a critical threshold value is reached. This variant is favored by the magnetic field because its easy axis is aligned with the y -

direction. With increasing H_y variant 2 grows at the expense of stress-favored variant 1. This results in an elongation of the sample along the x -axis, because the long edge a of variant 2 replaces the short edge c of variant 1 along this direction. The magnetic field-induced strain is usually measured with respect to the initial single variant state. Typical magnetic field-induced strain response curves are schematically plotted in Fig. 3. Note that vertical axis marks the total strain, not just the reorientation strain. The initial strains for the hysteresis loops at each stress level are non-zero, since the undeformed austenite was assumed as the reference configuration [97], and are comprised of elastic strain as well as austenite to partially-twinned martensite transformation strain [71, 85].

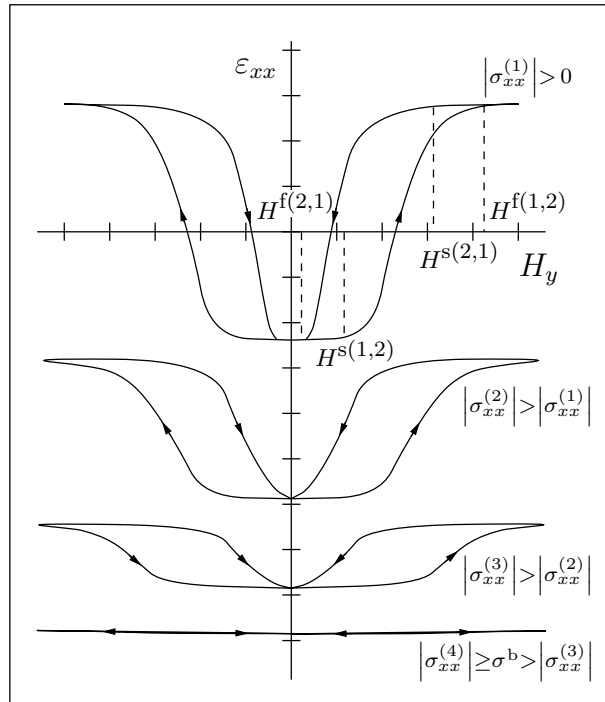


Fig. 3. Typical total strain-magnetic field response curves for MSMA at different stress levels.

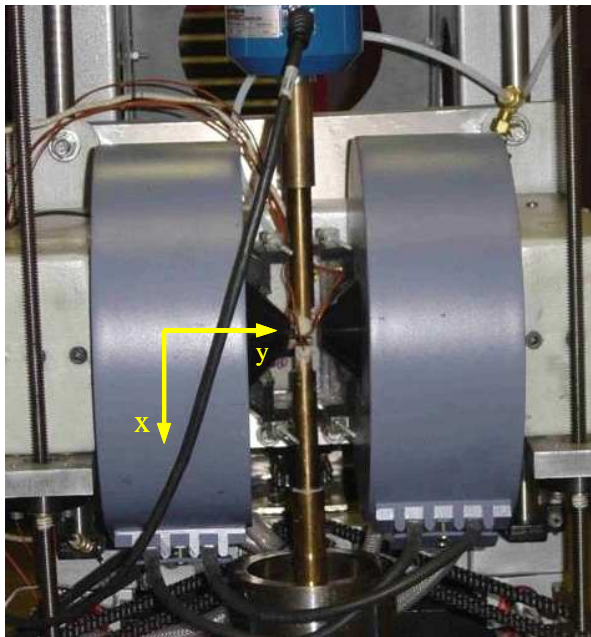
The reorientation from the stress-favored into the magnetic field-favored variant shows a strong stress level dependence. Fig. 3 also explains the notation for the critical magnetic fields for the start of the forward reorientation process (variant 1 \rightarrow variant 2), which is denoted $H^{s(1,2)}$ and its finish $H^{f(1,2)}$. Equivalently, $H^{s(2,1)}$ and $H^{f(2,1)}$ are defined as the critical magnetic fields to start and finish the reverse (variant 2 \rightarrow variant 1) reorientation process.

The arrangement of twinned martensitic variants and magnetic domains after the activation of the reorientation process is sketched in Schematic (b) of Fig. 2 for a generic intermediate applied magnetic field level $H^{s(1,2)} < H_y < H^{f(1,2)}$. Again, horizontal and vertical lines indicate 180° magnetic domain walls. Slanted lines indicate twin boundaries [2], which coincide with 90° domain walls. The variant reorientation process can also be visualized as occurring through the motion of these twin boundaries. Two types of magnetic domains are present in each twin band.

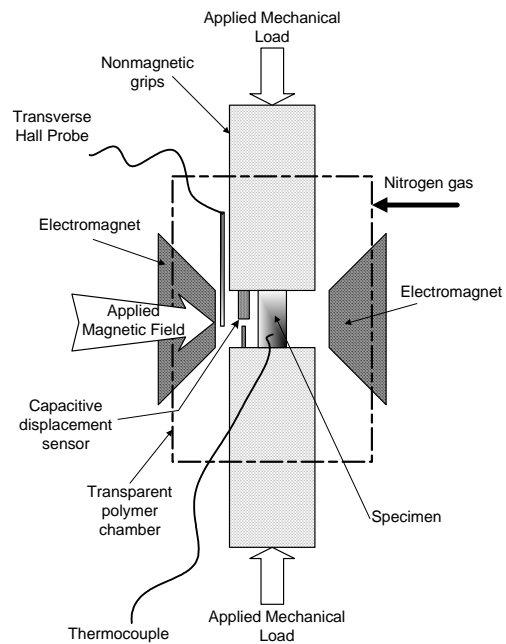
The volume fraction of the domain in which the magnetization vector opposes the applied field is less than that of the favorable domain, which yields a non-zero macroscopic magnetization. At large fields, the unfavorable domains are eliminated [11]. The magnetization of the material also changes due to the simultaneously occurring rotation of the magnetization vectors in variant 1 away from the magnetic easy axis. These rotations are not explicitly shown in the schematic, but will be addressed in detail in Section B of this chapter.

At low stress levels, further increase of the magnetic field completely eliminates variant 1 at the threshold value of $H^{f(1,2)}$ such that the maximum reorientation strain is achieved. If the field is increased above $H^{f(1,2)}$ the strain remains constant. The resulting single variant, single domain configuration is depicted in Schematic (c). At

most stress levels, however, variant 1 is not completely eliminated, such that the achievable magnetic field-induced strain is reduced. At the blocking stress in the field-induced strain is completely suppressed. The mechanism that causes the stress level dependence of the achievable reorientation strain will be discussed in Chapter V in more detail.



(a) Detail of the test setup showing the electromagnets, the grips and the load cell on the MTS frame, with the polymer chamber removed.



(b) Schematic showing the components of test setup as well as the applicable mechanical and magnetic load directions.

Fig. 4. Magneto-thermo-mechanical setup used for MFIS measurements [58, 98].

An experimental setup designed to measure magnetic field-induced strains in MSMA following the basic principle qualitatively described in the preceding paragraphs is shown in Fig. 4 [58, 98]. The setup consists of a 2 T electromagnet, which is adjustably mounted on a mechanical load frame such that the directions of applied

force and magnetic field are perpendicular. The specimen is held in place by non-magnetic grips. A polymer chamber, which encloses the grips and specimen, is filled with nitrogen gas for cooling. As depicted in Fig. 4(b), temperature, deformation, and magnetic field measurements are taken by a thermocouple, a capacitive displacement sensor and a Hall probe. Similar experiments have been reported by Tickle [96, 97], Heczko [44], Shield [27] and others.

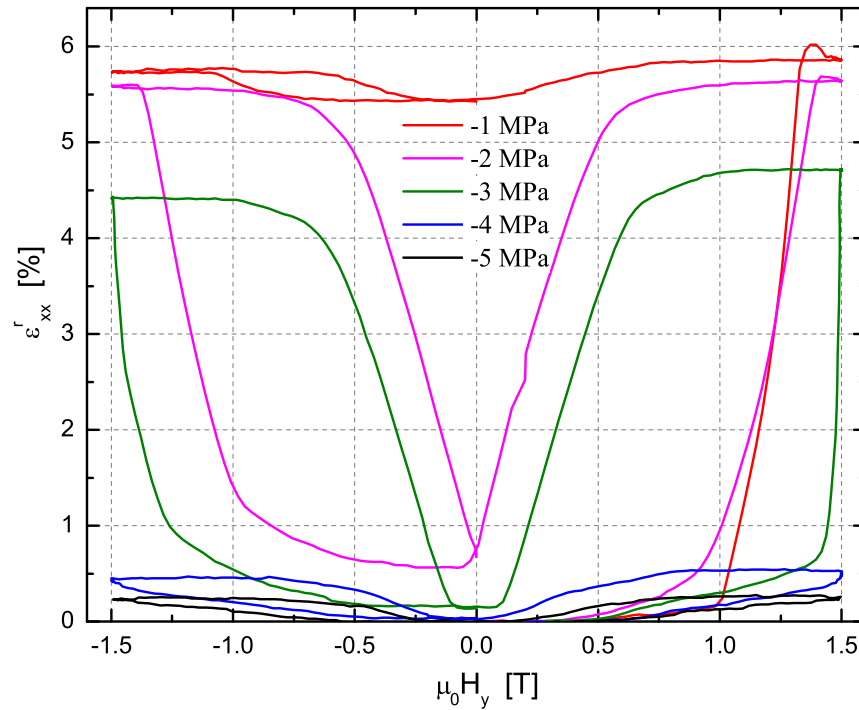


Fig. 5. Evolution of the MFIS in a Ni_2MnGa single crystal at different stress levels during the first magnetic cycle. Data taken from [58].

Magnetic field-induced strain data obtained from measurements on this test frame are plotted in Figs. 5 and 6 for first and second magnetic field cycles. For reasons of comparison all of the second cycle magnetic field-induced strain curves plotted in Fig. 2 have been shifted to start at the origin. Unlike the qualitative strain

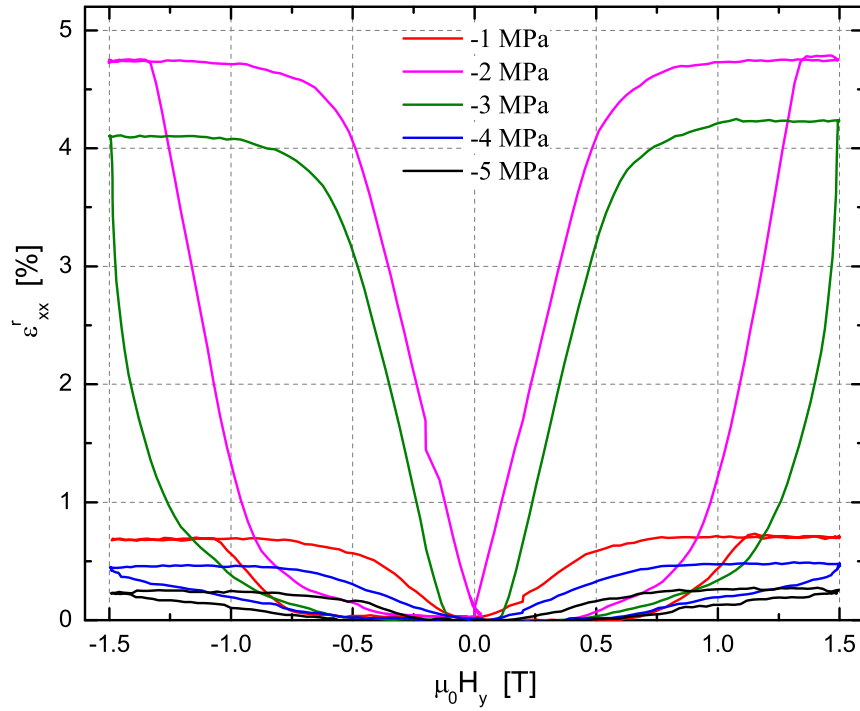


Fig. 6. Evolution of the MFIS in a Ni_2MnGa single crystal at different stress levels during the second magnetic cycle. Data taken from [58].

curves of Fig. 3 these figures show the magnetic field-induced strain as a function of the magnetic field, not the total strain, such that all curves start at the origin. These data exhibit all the characteristic features of MSMA behavior discussed in Chapter I. The observed response is nonlinear and hysteretic, which indicates that there is considerable dissipation associated with the variant reorientation. The achievable field-induced reorientation strain and the shape of the hysteresis loops show the strong stress level dependence.

It is observed that after the first magnetic cycle at low stress levels the initial single variant configuration is not restored and residual strains are observed. Since the stress level is not raised in between cycles, the second cycle tests at low stress levels start from mixed variant configurations corresponding to the only partially

recovered magnetic field-induced strain of the first cycle. At low stress levels, the reorientation strain that is produced in the second cycle is then significantly reduced as compared to the corresponding test at the same stress level during the first cycle. This phenomenon has been termed the *first cycle effect* [58, 98] and will further be explained in Chapter V. Hysteresis loops of subsequent cycles are experimentally observed to be nearly identical to those of the second cycle.

B. The Magnetization Response of MSMA

In the previous section it was explained that the process of magnetizing a MSMA specimen involves three mechanisms which help to achieve alignment of its magnetization with the external magnetic field. These are the redistribution of martensitic variants, the magnetic domain wall motion and the rotation of the magnetization vectors away from their preferred magnetic axes. In order to better understand the individual mechanisms, it is helpful to consider a thought experiment in which these effects can be separated. If the reorientation of martensitic variants in a MSMA single crystal is completely suppressed by the application of a stress above the blocking stress, then the magnetization of the crystal can only change by means of the domain wall motion or magnetization rotation, or combinations thereof. The magnetization process of the MSMA in this case is the same as that of a regular ferromagnetic material.

Fig. 7 shows a sketch of the initial single variant 1 configuration, which corresponds to that of Fig. 2, except here a stress level above the blocking stress is considered to analyze the magnetization process without variant reorientation. Next to the macroscopic view of the specimen, Fig. 7 also depicts schematics of magnetic domains on the micro-scale. The crystallographic scale is shown simply to indicate

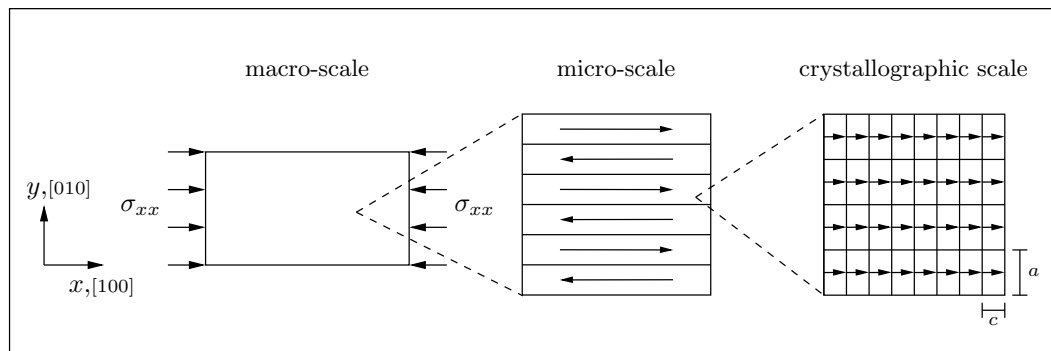


Fig. 7. A schematic of the initial single variant 1 martensite state. The variant reorientation is suppressed by an axial compressive stress higher than the blocking stress. Also shown, schematics of the corresponding microscopic scale and the crystallographic scale.

the fact that magnetic domains generally span many unit cells. As discussed in the previous section, magnetic domains form to reduce the macroscopic magnetization of the material and thereby the magnetostatic energy [16–18, 101]. They are separated by magnetic domain walls. In these walls the magnetization vectors (magnetic dipole moments) are rotated over short distances to accommodate the magnetization directions of neighboring domains. The formation of many small domains leads to an increase in the amount of domain walls, whose formation also costs energy. This competition of energy terms determines the size of the domains and also the thickness of the domain walls. Depending on the material the domain wall thickness can range from 10 nm to $1\mu\text{m}$ [17].

If the constrained single crystal of is magnetized along different crystallographic directions, one observes an anisotropy of the magnetization response. The direction along which the least amount of energy is required to magnetize the crystal is termed the magnetic *easy axis*, and, correspondingly, the *hard axis* is the direction for which the most energy needs to be expended. This anisotropic behavior can be explained

by the mechanism of magnetic domain wall motion and magnetization rotation as shown in the following sections.

1. Magnetization by Magnetic Domain Wall Motion

Fig. 8 schematically shows the evolution of the magnetic domain distribution at different applied field levels for the magnetization of the MSMA specimen along the [100]-direction. The starting configuration (left box) is the same microstructural view of the compressed single variant specimen that was presented in Fig. 7 (middle box).

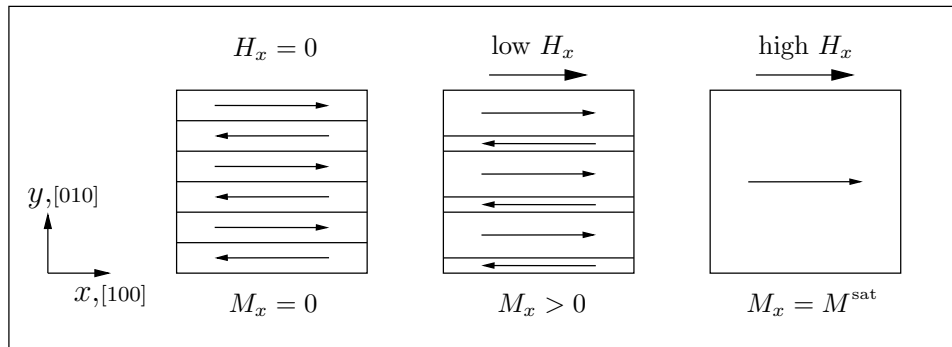


Fig. 8. Magnetization of the single variant specimen along the easy axis.

The applied field promotes the growth of these domains with favorably oriented magnetization vectors at the expense of the other domains. Since the external field is applied in the [100]-direction, which coincides with the magnetic easy axis of the compressive stress-favored variant 1, the magnetization to saturation can completely be achieved by 180° domain wall motion.

2. Magnetization by Rotation of Magnetization Vectors

Fig. 9 schematically illustrates the magnetization of the same single variant 1 sample perpendicular to the compression axis.

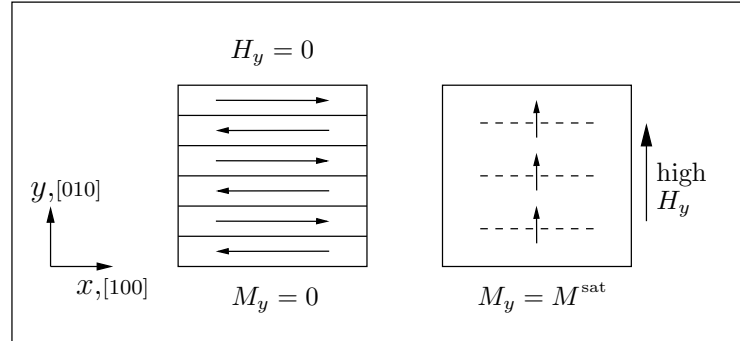


Fig. 9. Magnetization of the single variant specimen along the hard axis.

Since the magnetization vectors in both domains are equally unfavorable with respect to the applied field, no domain wall motion mechanism is available to accommodate the magnetization along the $[010]$ -direction. The magnetization in both domains must be rotated away from the common easy axis. The rotation of the magnetization within a martensitic variant requires work against the magnetocrystalline anisotropy energy. The amount of energy expended in activating this mechanism is higher than that associated with domain wall motion. The $[010]$ -direction is therefore the hard axis for this material. The magnetization of the MSMA specimen along directions in between $[100]$ and $[010]$, requires an intermediate amount of energy and involves the activation of both mechanisms. Unlike the motion of 180° domain walls, the rotation of the magnetization is associated with ordinary magnetostriction, i. e. the crystal elongates in the direction of the rotating magnetization vector [16, 18].

Fig. 10 qualitative shows the resulting magnetization curves for the easy $[100]$

and the hard $[010]$ -directions. The coordinate axes are normalized by the saturation magnetization M^{sat} and an arbitrary maximum applied field value H^{max} , respectively. Data for the magnetization of constrained MSMA single crystals have been reported by Tickle and James [96], Cui et al. [25], Shield [27], Likhachev and Ullakko [51] and Hezcko [102].

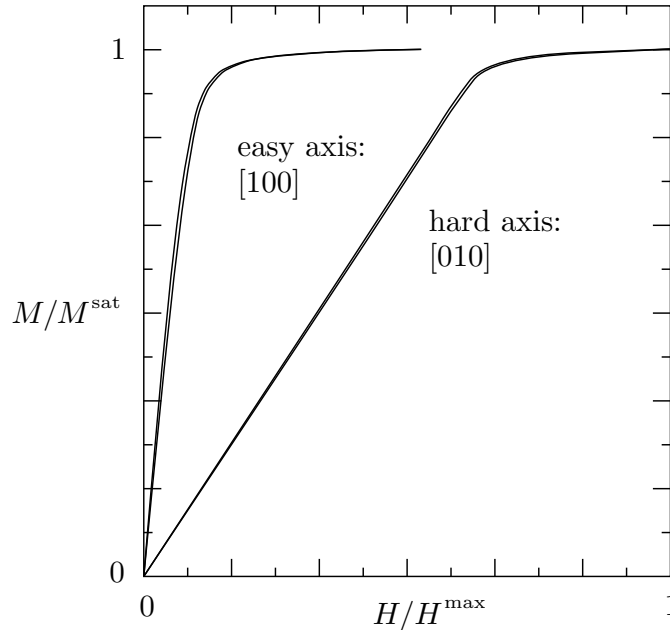


Fig. 10. Qualitative magnetization curves of the single variant MSMA specimen magnetized along the compression and perpendicular axes. For quantitative experimental results [96].

The magnetization curves in Fig. 10 are explained by the mechanisms discussed in the context of Figs. 8 and 9. Recall that the mechanism for alignment with the applied field is the domain wall motion, in the easy axis case, and rotation of the magnetization vectors, in the hard axis case. According to O’Handley [17], the energy

per unit volume u_a needed to saturate a material in a particular direction is given by

$$u_a = \mu_0 \int_0^{M^{\text{sat}}} H(M) dM . \quad (2.1)$$

It is clearly seen that by this measure the energy required to magnetize the material to saturation along the hard axis does in fact require much more energy.

Furthermore, it is observed that the hystereses for both magnetization curves are almost negligible. This is expected for the hard axis magnetization curve, since the magnetization rotation in is a reversible process. Magnetic domain wall motion on the other hand can be associated with dissipation. Permanent magnets, for example, are made from materials that exhibit a strong internal resistance to magnetic domain wall motion, due to micro-scale pinning sites and other phenomena [5, 16, 17], which leads to large hysteresis effects. In MSMA, however, the magnetic domain wall motion appears to be associated with only a very small amount of dissipation.

3. Magnetization by Variant Reorientation

In MSMA the variant reorientation process provides an additional mechanism to change the magnetization of the material. This is due to the fact that the magnetic easy axes in the martensitic variants have different directions with respect to a global coordinate system. In the presence of an external field the structural rearrangement is therefore always coupled to a magnetization change. If the reorientation process is initiated by mechanical loading instead of applying a magnetic field, and the applied field is constant, the variant reorientation is in fact the only mechanism that changes the magnetization. This aspect will be explained in more detail in connection with the model predictions presented in Chapter V.

4. The Coupling of the Magnetization Mechanisms for MSMA.

For stress levels below the blocking stress, the magnetic field-induced change of the magnetization observed in MSMA is driven by all three mechanisms, the magnetic domain wall motion, the magnetization rotation and the variant reorientation. Typical magnetization response curves, measured under the loading conditions depicted in Fig. 2, have been reported by Heczko et al. [44] and are shown in Fig. 11. Similar data have been obtained by Likhachev and Ullakko [51].

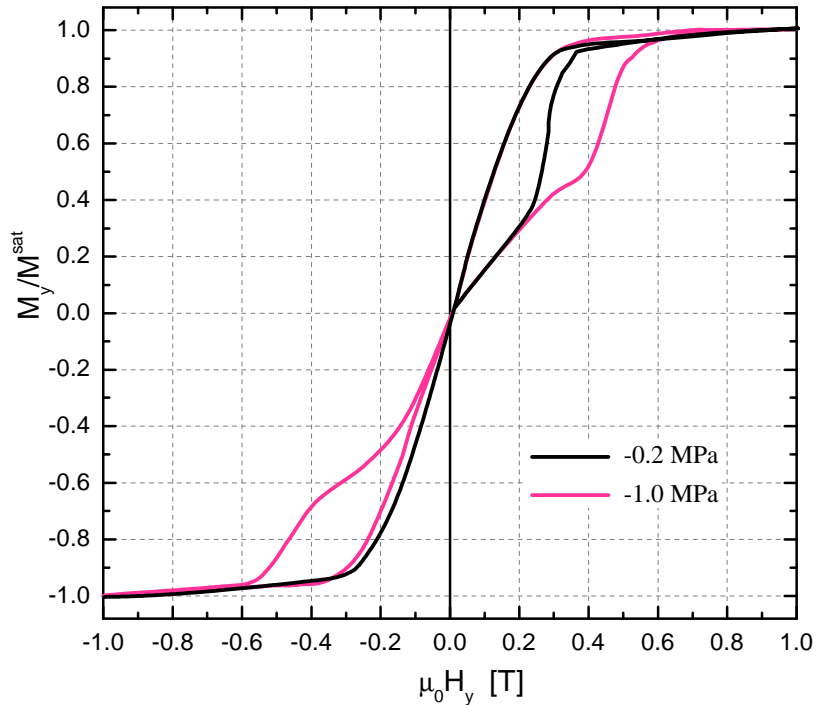


Fig. 11. Relative magnetization response in Ni-Mn-Ga as reported by Heczko [103].

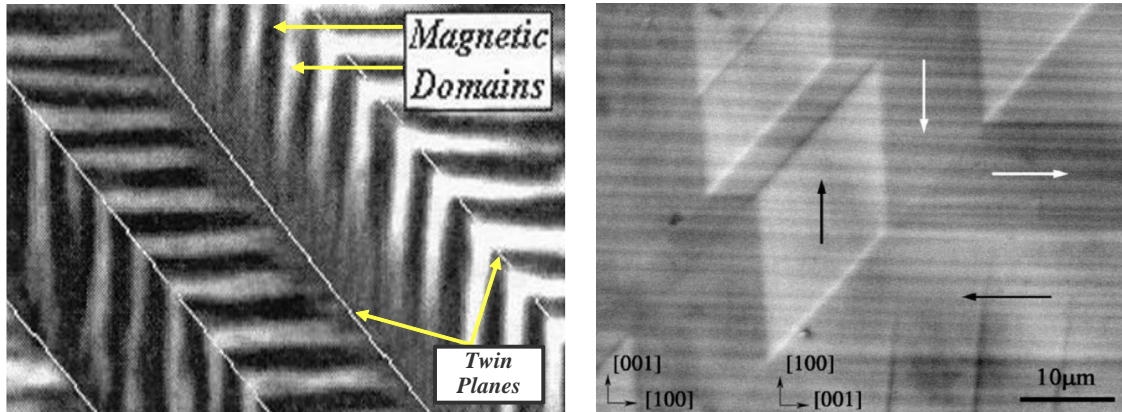
The sequence of activation of the different mechanisms is the following: The initial linear slope of the magnetization curves in Fig. 11 corresponds to the magnetization of the constrained crystal along the magnetic hard axis, as shown in Fig. 10. The mechanism that drives the magnetization change is thus the rotation of the

magnetization vectors, as was schematically illustrated Fig. 9. Since both magnetic domains in the stress-favored variant are equally unfavorable with respect to the applied field, see Fig. 8, domain wall motion does not occur. Here it is assumed, of course, that the direction of the applied field is perfectly perpendicular to the easy axis of variant 1. In reality this may not be the case and some domain wall motion may occur. More experimental evidence is needed to clarify this point.

Once the critical field for variant reorientation has been reached, the magnetic field-favored variant 2 nucleates and a sharp change in the slope of the magnetization curves occurs. Fig. 11 clearly shows evidence of the stress dependence of the critical field to initiate the variant reorientation. In the reorientation region the magnetization change is nonlinear and similar to the evolution of the magnetic field-induced strain observed in the same field regime. During the reorientation process magnetic domains and martensitic variants coexist in the arrangement qualitatively depicted in Schematic (b) of Fig. 2. Such configurations have been observed experimentally in Ni-Mn-Ga [104–107]. Corresponding micrographs are shown in Fig. 12 on the next page. Sullivan and Chopra also reported that more complex magnetic domain structures can exist in twinned Ni-Mn-Ga martensite under certain conditions [106, 107].

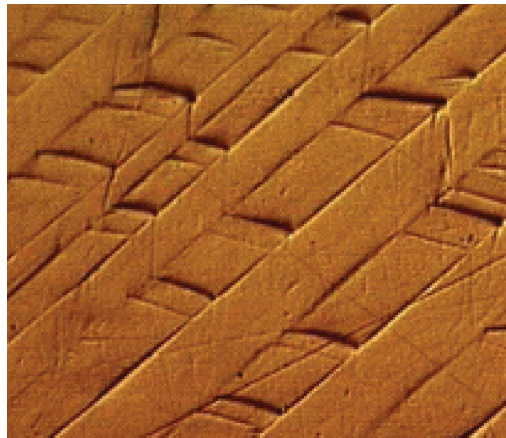
In this configuration the third mechanism, the magnetic domain wall motion, is activated, since the magnetization vectors in some of the magnetic domains in variant 2 oppose the applied field. It is generally believed that these unfavorable magnetic domains are eliminated almost simultaneously with activation of the reorientation process [11, 97], such that the magnetization change in the reorientation region is mainly governed by the rearrangement of variants and the magnetization rotation.

At high fields the stress-favored variant is completely eliminated and the material is magnetically saturated in the field direction. The resulting single variant, single domain configuration at magnetic saturation is illustrated in Schematic (c) of Fig. 2.



(a) Magneto-optical images using the magnetic garnet film technique as observed by Likhachev et al. [104].

(b) Scanning electron microscopy (SEM) images taken by Ge et al. [105].



(c) Interference-contrast-colloid (ICC) technique images reported by Sullivan and Chopra [106].

Fig. 12. Experimentally observed magnetic domain structures in two-variant Ni-Mn-Ga samples.

At higher stress levels, however, magnetic saturation can be reached through magnetization rotation before variant 1 is eliminated, and the variant reorientation process is not completed. This explains why at these stress levels only a fraction of the theoretically possible reorientation strain can be induced by the magnetic field.

At stress levels above the blocking stress the critical field for the activation of the reorientation process is larger than the field needed to fully rotate the magnetization vector toward the direction of the applied field. The magnetization process then corresponds to the magnetization of the constrained crystal along the magnetic hard axis described earlier in this section. The value of the blocking stress depends on the magnetocrystalline anisotropy energy [58]. This explanation of the stress-level dependence of the achievable magnetic field-induced strain will further be discussed in the context of analyzing model predictions in Chapter V.

It is observed that magnetization curves of Fig. 11 exhibit large hysteresis, whereas the magnetization curves of the constrained single crystal of Figs. 9 and 10 exhibited negligible hysteresis. It can thus be concluded that the only source of internal dissipation is the variant reorientation process, which then leads to the hysteretic nature of the magnetic field-induced strain curves in Figs. 5 and 6, and the magnetization curves in Fig. 11.

The analysis of the experimental field-induced strain and magnetization response data, such as those presented in this chapter, is of great importance for the development of a constitutive model. In order to properly capture the complex magneto-mechanical behavior of MSMA, the model has to take all three of the described mechanisms into account. In the particular approach taken here this is done through the evolution of internal state variables as will be described in Chapter IV. A general continuum level thermo-magneto-mechanical framework is introduced in the next chapter on the basis of which the constitutive model will be built.

CHAPTER III

A CONTINUUM DESCRIPTION OF MAGNETIZABLE SOLIDS

Magnetic shape memory alloys can be considered as continua that deform under mechanical and magnetic forces. In this chapter a general framework for the modeling of continuous, deformable and magnetizable materials with evolving microstructure is established. This framework consists of Maxwell's equations, the extended conservation laws of continuum mechanics and a generalized version of continuum thermodynamics. The electromagnetic, mechanical and caloric (energy) equations are generally coupled, for example through magnetic force and energy source terms that appear in the mechanical balance laws or, as it turns out, for MSMA through constitutive relations.

The pioneering work on the complex subject of the *mechanics of electromagnetic continua* [108] has been conducted by Guggenheim [109, 110], Landau and Lifshitz [111], Tiersten [112], Brown Jr. [113], Penfield Jr. and Haus [114], Coleman [115, 116], Noll, Truesdell and Toupin [117, 118], Eringen and Maugin [119, 120], Pao, Hutter and van de Ven [121–123], Woodson and Melcher [124, 125], among others. It is a research field in which there does not yet exist a unified theory that is generally agreed upon for reasons that will be discussed shortly. Pao, Hutter and van de Ven as well as Penfield and Haus discussed the thermodynamic equivalency of the various theories [114, 121, 122]. With the focus of this work on the constitutive modeling of MSMA, it is not possible to fully explore the depths of this subject. However, even though the modeling process is limited to magneto-static or magneto-quasi-static cases, at least a basic understanding of the underlying more general framework is important. One especially has to be aware of the assumptions that are associated with a particular theory, because these may have profound implications even for the static case. Thus,

instead of simply providing the reduced equations of magnetostatics, a brief discussion of the underlying more general framework is presented here.

The main challenge of any theory in this field is related to the fact that electromagnetic fields measured by a stationary observer differ from those experienced by an observer in a moving frame and transformation relations between those fields need to be established. The second difficulty is to formulate expressions for body force, body couple and energy source terms that are caused by electromagnetic phenomena. Before specific equations are presented, a few comments are due on why there exists such a host of different theories, such as the Minkowski, the Ampère, the Chu and the Boffi formulations, to name the most prominent ones [121]. These comments are meant to convey some appreciation for the fundamental questions that arise in this subject:

1. One inherent problem of any electro-magneto-mechanical theory is related to the fact that one desires to combine the laws of classical non-relativistic mechanics with the special relativity formulation of Maxwell's equations. The former are invariant under Galilean transformations (cf. Eqs. (B.5)), while the later are invariant under Lorentz transformations [114]. In the context of constitutive modeling, for example, this becomes an issue if one is concerned with material frame indifference [117, 126, 127], since it is not clear which invariance properties one ought to require. The process of deriving semi-relativistic or non-relativistic approximations is not at all straightforward or unique and has led to many different formulations. Depending on the invariance properties, the different theories distinguish themselves by the form of the field transformations that relate the electromagnetic fields observed by a stationary observer to those observed in a moving frame.

2. Although the formulations of Maxwell's equations in the different theories coincide for stationary matter, the expressions for the electromagnetic body forces, body couples and energy sources generally do not. A major complication is due to the fact that measurements can only be performed in free space, where all theories are identical. It is inside electromagnetic matter, however, that the definitions and physical meaning of the electromagnetic fields differ. One can not analyze those quantities without relying on a particular theory, which essentially makes it impossible to favor one theory over another. The advantages and disadvantages of several theories have been discussed in [114].
3. Another complication in deriving expressions for the body forces and stress tensors is the fact that the decomposition into long range and short range effects is not as straightforward as in the mechanical case, where, nonlocal theories excluded, all short range interactions are described by the surface traction vector and all long range effects, such as gravity, are captured by the body force term.

The continuum description of magnetizable solids presented here mainly follows the most widely used theory known as the *Maxwell-Minkowski* formulation, in the description presented in the work of Pao, Hutter and van de Ven [121, 122]. The different parts of the framework are presented in the following sections, A: Maxwell's equations, B: Conservation of Mass, Momentum and Energy, C: Extended Thermodynamic Framework.

A. Maxwell's Equations

The global form of *Maxwell's equations* in the *stationary (laboratory) frame* is given by [124]:

$$\text{Gauss' law:} \quad \oint_{\partial\mathcal{R}} \mathbf{D} \cdot \mathbf{n} \, dA = \int_{\mathcal{R}} \rho_f \, dV ; \quad (3.1a)$$

$$\text{Gauss-Faraday law:} \quad \oint_{\partial\mathcal{R}} \mathbf{B} \cdot \mathbf{n} \, dA = 0 ; \quad (3.1b)$$

$$\text{Ampère's law:} \quad \oint_{\partial\mathcal{S}} \mathbf{H} \cdot d\mathbf{x} = \int_{\mathcal{S}} \left[\mathbf{J}_f + \frac{\partial \mathbf{D}}{\partial t} \right] \cdot \mathbf{n} \, dA ; \quad (3.1c)$$

$$\text{Faraday's law:} \quad \oint_{\partial\mathcal{S}} \mathbf{E} \cdot d\mathbf{x} = - \int_{\mathcal{S}} \frac{\partial \mathbf{B}}{\partial t} \cdot \mathbf{n} \, dA . \quad (3.1d)$$

\mathbf{D} is the electric displacement vector, ρ_f the free charge density, \mathbf{B} the magnetic flux density (or magnetic induction), \mathbf{H} the magnetic field strength and \mathbf{J}_f the free current and \mathbf{E} the electric field strength. The integrations are carried out either over the fixed (control) volume \mathcal{R} with boundary $\partial\mathcal{R}$ and outward unit normal \mathbf{n} , or the fixed surface \mathcal{S} , with the simple closed boundary curve $\partial\mathcal{S}$ whose directionality is determined by the orientation of the normal \mathbf{n} . Maxwell's equations are supplemented by the following constitutive equations

$$\mathbf{D} = \varepsilon_0 \mathbf{E} + \mathbf{P} ; \quad (3.2a)$$

$$\mathbf{B} = \mu_0 (\mathbf{H} + \mathbf{M}) . \quad (3.2b)$$

ε_0 is the permittivity of free space that is connected to the permeability of free space μ_0 through the relation $\varepsilon_0 \mu_0 = 1/c^2$, which reflects the constancy of the speed of light c *in vacuo*. \mathbf{P} and \mathbf{M} are the polarization and magnetization vectors of a material

body.

By applying Ampère's law Eq. (3.1c) to a closed surface, using the divergence theorem (A.1) and Gauss' law Eq. (3.1a), one can also derive the commonly used *conservation of charge* balance equation

$$\oint_{\partial\mathcal{R}} \mathbf{J}_f \cdot \mathbf{n} \, dA = - \int_{\mathcal{R}} \frac{\partial \rho_f}{\partial t} \, dV . \quad (3.3)$$

Clearly Eq. (3.3) is not an independent equation. It has been argued [122] that Maxwell's equations are derivable from two basic principles, namely Faraday's law Eq. (3.1d), which is sometimes called the *conservation of magnetic flux*, and the conservation of charge Eq. (3.3). The Gauss-Faraday law Eq. (3.1b) is then considered a special case of Eq. (3.1d) for closed surfaces and Gauss' law Eq. (3.1a) as the definition of the electric displacement. Finally, it is argued that the conservation of charge is satisfied if a magnetic field \mathbf{H} exists such that Ampère's law Eq. (3.1c) is satisfied. However, this logic does not lead to a unique definition of \mathbf{D} or \mathbf{H} and it is the general consensus that all four of Maxwell's equations are fundamental and independent statements from which the conservation of charge can be derived.

By applying the divergence theorem, Eq. (A.1), or Stokes' theorem, Eq. (A.2), to the global expressions of Eqs. (3.1), the local form of Maxwell's equations in the stationary (laboratory) frame can be derived as

$$\text{Gauss' law:} \quad \text{div} \mathbf{D} = \rho_f ; \quad (3.4a)$$

$$\text{Gauss-Faraday law:} \quad \text{div} \mathbf{B} = 0 ; \quad (3.4b)$$

$$\text{Ampère's law:} \quad \text{curl} \mathbf{H} = \mathbf{J}_f + \frac{\partial \mathbf{D}}{\partial t} ; \quad (3.4c)$$

$$\text{Faraday's law:} \quad \text{curl} \mathbf{E} = - \frac{\partial \mathbf{B}}{\partial t} . \quad (3.4d)$$

The local form of the conservation of charge can either be derived from its global form of Eq. (3.3), or by taking the divergence of Eq. (3.4c) and using Eq. (3.4a), which yields

$$\operatorname{div} \mathbf{J}_f = -\frac{\partial \rho_f}{\partial t} . \quad (3.5)$$

According to Woodson and Melcher [124], nearly all electromagnetic problems of technical interest, in which the propagation of electromagnetic waves is not important, can be described by one of two limiting cases, the electro-quasi-static or the magneto-quasi-static approximation. In the former the magnetic flux is of negligible importance, in the latter the displacement current. In the *quasi-static magnetic field system* the local form of Maxwell equations reduces Eq. (3.4) to

$$\text{Gauss-Faraday law:} \quad \operatorname{div} \mathbf{B} = 0 ; \quad (3.6a)$$

$$\text{Ampère's law:} \quad \operatorname{curl} \mathbf{H} = \mathbf{J}_f ; \quad (3.6b)$$

$$\text{Faraday's law:} \quad \operatorname{curl} \mathbf{E} = -\frac{\partial \mathbf{B}}{\partial t} . \quad (3.6c)$$

Note that in this case Ampère's law and Faraday's law are not fully coupled. Thus, even with time-varying sources, the magnetic field \mathbf{H} and magnetic flux \mathbf{B} are determined as if the system were magnetostatic. Then the electric field is found from Eq. (3.6c). *Magnetic diffusion* problems, for example, are solved with this set of equations [125, 128].

In the *magnetostatic* approximation the equations further reduce to

$$\text{Gauss-Faraday law:} \quad \operatorname{div} \mathbf{B} = 0 ; \quad (3.7a)$$

$$\text{Ampère's law:} \quad \operatorname{curl} \mathbf{H} = \mathbf{J}_f . \quad (3.7b)$$

Keeping the discussion from the beginning of this chapter in mind, the global form of Maxwell's equations in the *co-moving (rest) frame* is now considered. The rest frame is defined to move with the velocity of the material body. For a deformable body in general motion each particle possesses its own local and instantaneous rest frame [121]. The integrals in the following expressions are defined over the material volume \mathcal{P}_t with boundary $\partial\mathcal{P}_t$ and outward unit normal \mathbf{n} or the material surface \mathcal{S}_t with boundary $\partial\mathcal{S}_t$, all of which, through the motion of the material points [127], change with time (cf. Appendix A, Section A2). The electromagnetic variables in the integrand are *spatial fields* defined in the *deformed configuration* [127] as observed from a *moving frame of reference*. According to Pao and Hutter [121, 122], Maxwell's equations for a moving and deforming continuum can than be written as by

$$\text{Gauss's law: } \oint_{\partial\mathcal{P}_t} \mathbf{D} \cdot \mathbf{n} \, dA = \int_{\mathcal{P}_t} \rho_f \, dV ; \quad (3.8a)$$

$$\text{Gauss-Faraday law: } \oint_{\partial\mathcal{P}_t} \mathbf{B} \cdot \mathbf{n} \, dA = 0 ; \quad (3.8b)$$

$$\text{Ampère's law: } \oint_{\partial\mathcal{S}_t} \mathbf{H}' \cdot d\mathbf{x} = \frac{d}{dt} \int_{\mathcal{S}_t} \mathbf{D} \cdot \mathbf{n} \, dA + \int_{\mathcal{S}_t} \mathbf{J}'_f \cdot \mathbf{n} \, dA ; \quad (3.8c)$$

$$\text{Faraday's law: } \oint_{\partial\mathcal{S}_t} \mathbf{E}' \cdot d\mathbf{x} = - \frac{d}{dt} \int_{\mathcal{S}_t} \mathbf{B} \cdot \mathbf{n} \, dA . \quad (3.8d)$$

Primed field variables are those measured by an observer moving with the material body. In a non-relativistic approximation \mathbf{D} and \mathbf{B} are identical to their counterparts in the moving frame [122], and have thus been left unprimed (cf. Appendix B, Section B2). The local form of Maxwell's equations in the co-moving (rest) frame can either be derived by applying the transport theorems (A.6) and (A.7) to the corresponding global form, Eqs. (3.8), and localizing the expressions, or by using the field

transformations (3.10) in the laboratory frame version (3.4) of these equations.

$$\text{Gauss's law:} \quad \operatorname{div} \mathbf{D} = \rho_f ; \quad (3.9a)$$

$$\text{Gauss-Faraday law:} \quad \operatorname{div} \mathbf{B} = 0 ; \quad (3.9b)$$

$$\text{Ampère's law:} \quad \operatorname{curl} \mathbf{H}' = \mathbf{J}'_f + \rho_f \mathbf{v} + \frac{\partial \mathbf{D}}{\partial t} - \operatorname{curl}(\mathbf{v} \times \mathbf{D}) ; \quad (3.9c)$$

$$\text{Faraday's law:} \quad \operatorname{curl} \mathbf{E}' = -\frac{\partial \mathbf{B}}{\partial t} - \operatorname{curl}(\mathbf{v} \times \mathbf{B}) . \quad (3.9d)$$

Eqs. (3.8) and Eqs. (3.9) have to be considered general in the sense that many different formulations can be cast in this form. The difference between formulations is reflected in the particular transformation relations that map fields observed in the stationary frame to those observed in the co-moving frame. For the Minkowski formulation the field transformations, which are derived in Appendix B, Section B2, are given by

$$\begin{aligned} \rho'_f &= \rho_f ; & \mathbf{D}' &= \mathbf{D} ; & \mathbf{B}' &= \mathbf{B} ; \\ \mathbf{H}' &= \mathbf{H} - \mathbf{v} \times \mathbf{D} ; & \mathbf{J}'_f &= \mathbf{J}_f - \rho_f \mathbf{v} ; & \mathbf{E}' &= \mathbf{E} + \mathbf{v} \times \mathbf{B} , \end{aligned} \quad (3.10)$$

where \mathbf{v} is the velocity of the moving frame. By definition, substituting these transformation relations into the moving frame version of Maxwell's equations in global form Eqs. (3.8) and local form Eqs. (3.9), again leads to the Minkowski version of Maxwell's equation in the stationary frame Eqs. (3.1) or Eqs. (3.4), respectively.

B. Conservation of Mass, Momentum and Energy

Although eventually the modeling will be restricted to a small deformation theory, the derivation of the balance laws in this section is general and they hold for finite deformations. As mentioned, the balance laws presented are generalized in the sense that they include source terms due to electromagnetic interactions. The derivation

again mainly follows the work of Pao, Hutter and van de Ven [121, 122]. A similar formulation has also been proposed by Eringen and Maugin [108, 119, 129].

The global balance equations are formulated as integrations over the material volume \mathcal{P}_t (closed system), rather than a fixed volume in space (open system). Previously the same was done for Maxwell's equations in the moving frame (cf. Eq. (3.8)). The usual description of the kinematics of a continuum implied here is discussed in Appendix A, Section A2.

The principle of the **conservation of mass** states: *The total mass of a part of a body can not change with time or its deformation* [127], which yields

$$\frac{d}{dt} \int_{\mathcal{P}_t} \rho \, dV = 0 , \quad (3.11)$$

where ρ is the mass density and the material time derivative is defined by Eq. (A.5a). As a consequence of Eq. (3.11) the following useful relation for any smooth spatial field Φ

$$\frac{d}{dt} \int_{\mathcal{P}_t} \rho \Phi \, dV = \int_{\mathcal{P}_t} \rho \dot{\Phi} \, dV , \quad (3.12)$$

can be derived [127]. Using Reynold's transport theorem Eq. (A.6) and acknowledging that Eq. (3.12) has to hold for any volume \mathcal{P}_t , the local form of the conservation of mass is given by

$$\frac{d\rho}{dt} + \rho \operatorname{div} \mathbf{v} = \frac{\partial \rho}{\partial t} + \operatorname{div}(\rho \mathbf{v}) = 0 , \quad (3.13)$$

where \mathbf{v} is the spatial velocity field. Alternatively the conservation of mass can be expressed by the relation $\rho = J\rho_0$, where ρ_0 is the density in the reference configuration and J is the determinant of the deformation gradient defined in Eq. (A.4). In the small strain approximation changes in the density are negligible so that $J \approx 1$ and the conservation of mass takes the simple form $\rho = \rho_0$ (see Appendix A, Section A4).

The **conservation of linear momentum** states: *The rate of change of linear momentum of any part of the body is equal to the total sum of body and surface forces applied to it.* In global form this balance equation is given by [121, 122]

$$\frac{d}{dt} \int_{\mathcal{P}_t} \rho \mathbf{v} dV = \oint_{\partial \mathcal{P}_t} \mathbf{t} dA + \int_{\mathcal{P}_t} \rho (\mathbf{f} + \mathbf{f}^m) dV , \quad (3.14)$$

where $\mathbf{t}(\mathbf{n})$ is the traction vector, \mathbf{f} is the usual body force which captures long-range interactions that are not electromagnetic in nature, and \mathbf{f}^m is the body force due to electromagnetic effects. Using Cauchy's formula $\mathbf{t}(\mathbf{n}) = \boldsymbol{\sigma} \mathbf{n}$, with $\boldsymbol{\sigma}$ denoting the Cauchy stress tensor, the conservation of mass in the form of Eq. (3.13), the divergence theorem Eq. (A.1) and localizing the local form of the conservation of linear momentum takes the form

$$\operatorname{div} \boldsymbol{\sigma} + \rho \mathbf{f} + \rho \mathbf{f}^m = \rho \frac{d\mathbf{v}}{dt} . \quad (3.15)$$

The **conservation of angular momentum** states: *The rate of change of angular momentum of any part of the body is equal to the total sum of the moments applied by the body and surface forces and the moments exerted by distributed body couples.* In global form it is expressed as [121, 122]

$$\frac{d}{dt} \int_{\mathcal{P}_t} \mathbf{x} \times \rho \mathbf{v} dV = \oint_{\partial \mathcal{P}_t} \mathbf{x} \times \mathbf{t} dA + \int_{\mathcal{P}_t} [\mathbf{x} \times \rho (\mathbf{f} + \mathbf{f}^m) + \rho \mathbf{l}^m] dV . \quad (3.16)$$

The local form is derived in detail in Appendix A, Section A3 and is given by

$$\operatorname{skw} \boldsymbol{\sigma} = \rho \mathbf{L}^m , \quad (3.17)$$

where \mathbf{L}^m is the dual of the vector \mathbf{l}^m (cf. Eq. (A.13)). Thus, in the presence of magnetic body couples, the stress tensor is generally not symmetric.

For reasons of convenience one often defines the Maxwell stress tensor $\boldsymbol{\sigma}^M$ [122, 125], such that $\operatorname{div} \boldsymbol{\sigma}^M = \rho \mathbf{f}^m$ and $\operatorname{skw} \boldsymbol{\sigma}^M = -\rho \mathbf{L}^m$. The momentum conservation equations Eq. (3.15) and Eq. (3.17), can then be rewritten as

$$\operatorname{div}(\boldsymbol{\sigma} + \boldsymbol{\sigma}^M) + \rho \mathbf{f} = \mathbf{0} ; \quad (3.18a)$$

$$\operatorname{skw}(\boldsymbol{\sigma} + \boldsymbol{\sigma}^M) = \mathbf{0} . \quad (3.18b)$$

The **conservation of energy** states: *The rate of change of the total energy (i. e. the sum of kinetic and internal energy) of any part is equal to the power and heat input into the system.* In the generalized context considered here, the power input can be mechanical or electromagnetic in nature. Mathematically this statement in global form is expressed as

$$\begin{aligned} \frac{d}{dt} \int_{\mathcal{P}_t} \left[\frac{1}{2} \rho \mathbf{v} \cdot \mathbf{v} + \rho u \right] dV &= \oint_{\partial \mathcal{P}_t} \mathbf{t}(\mathbf{n}) \cdot \mathbf{v} dA + \int_{\mathcal{P}_t} \left[\rho(\mathbf{f} + \mathbf{f}^m) \cdot \mathbf{v} + \rho \mathbf{l}^m \cdot \mathbf{w} + \rho \tilde{r}^m \right] dV \\ &+ \int_{\mathcal{P}_t} \rho r^h dV - \oint_{\partial \mathcal{P}_t} \mathbf{q} \cdot \mathbf{n} dA , \end{aligned} \quad (3.19)$$

where u is the internal energy per unit mass and \mathbf{w} is the angular velocity vector defined by $2\mathbf{w} := \operatorname{curl} \mathbf{v}$. The energy source term $\rho \tilde{r}^m$ accounts for the energy supply generated by electromagnetic fields [121], whereas ρr^h is a non-electromagnetic heat source. The heat flux over the boundary of the material body is denoted \mathbf{q} .

The local form of the conservation of energy is derived in Appendix A, Section A3 and only the result is stated here as

$$\rho \dot{u} = \boldsymbol{\sigma} : (\operatorname{grad} \mathbf{v}) + \rho r^m + \rho r^h - \operatorname{div} \mathbf{q} . \quad (3.20)$$

The electromagnetic energy supply term $r^m := \tilde{r}^m + \mathbf{l}^m \cdot \mathbf{w}$ contains the work done by

the electromagnetic body couple.

The particular form of the electromagnetic body force $\rho \mathbf{f}^m$, body couple $\rho \mathbf{L}^m$ and energy source term ρr^m varies between different formulations. In the magnetostatic approximation that will be of interest here, the Minkowski formulation specifies the following terms [114, 122]

$$\rho \mathbf{f}^m = \mathbf{J}_f \times \mathbf{B} + \mu_0 (\text{grad } \mathbf{H})^T \mathbf{M} ; \quad (3.21a)$$

$$\rho \mathbf{L}^m = \text{skw} (\mu_0 \mathbf{M} \otimes \mathbf{H}) ; \quad (3.21b)$$

$$\rho r^m = \mu_0 \mathbf{H} \cdot \dot{\mathbf{M}} . \quad (3.21c)$$

C. Extended Thermodynamic Framework

A constitutive theory is said to be *thermodynamically-consistent* if the constitutive equations are derived in such a manner that they satisfy the restrictions posed by the conservation of energy, also known as the *first law of thermodynamics*, and the *second law of thermodynamics* [126, 130]. A thermodynamic framework of this kind shall be established here for a general continuum which possesses thermal, mechanical and magnetic energy. This formulation is an extension of the thermomechanical framework used for the modeling of conventional SMAs [71, 72, 76].

In continuum thermodynamics a *thermodynamic potential* is defined to characterize all thermodynamic properties of a material body [126]. The constitutive model presented in this work is formulated in terms of the *Gibbs potential* because its independent state variable space consists of the scalar temperature T and the Cauchy stress tensor $\boldsymbol{\sigma}$, which are easily controllable in experiments. For the MSMA modeling the state space is extended to include the vector-valued magnetic field strength \mathbf{H} . Physically the Gibbs free energy is less intuitive than the internal energy or

the Helmholtz potential. For a *hyperelastic* material under isothermal conditions the Gibbs free energy can be interpreted as the complementary elastic strain energy or complementary hyperelastic potential [117, 130–132], which is shown in Appendix C, Section C1.

To account for dissipative effects in thermodynamics-based constitutive modeling Coleman and Noll [81] and Coleman and Gurtin [80] introduced the method of including internal state variables. This approach is followed here, and therefore the free energy function is assumed to also be a function of a generic set of internal state variables $\boldsymbol{\zeta}$. These variables allow the constitutive model to capture the dissipation associated with the evolution of the microstructure in MSMAs. Such dissipative effects also lead to a loading history dependence of the constitutive response which can be accounted for with this approach. Evolution equations for the internal state variables have to be derived in accordance with the laws of thermodynamics. For MSMAs a specific set $\boldsymbol{\zeta}$ of internal state variables will be chosen in Chapter IV, motivated by the crystallographic and magnetic microstructures observed in these materials, and described earlier in Chapter II.

Based on the above discussion, the following constitutive assumption is made regarding the specific Gibbs free energy per unit mass for the thermodynamic description of a general continuous, deformable and magnetizable material

$$g = \hat{g}(T, \boldsymbol{\sigma}, \mathbf{H}, \boldsymbol{\zeta}) . \quad (3.22)$$

The Gibbs free energy is related to the internal energy $u = \hat{u}(s, \boldsymbol{\varepsilon}, \mathbf{M}, \boldsymbol{\zeta})$ through the Legendre transformation [122]

$$g = u - sT - \frac{1}{\rho} \boldsymbol{\sigma} : \boldsymbol{\varepsilon} - \frac{\mu_0}{\rho} \mathbf{H} \cdot \mathbf{M} , \quad (3.23)$$

where s is the specific entropy.

The total strain tensor has been chosen here as the independent state variable for the internal energy. For materials in which a separation between the recoverable elastic strain and an irrecoverable inelastic strain is convenient and clearly definable, for example in elasto-plastic materials or shape memory alloys, one needs to decide whether to use the total strain tensor as the appropriate state variable, as done here, or only the elastic part. Lubliner discusses different approaches proposed in the literature on plasticity theory (cf. [133], pp. 457). He refers to the *Mandel approach* in which $\psi = \bar{\psi}(T, \boldsymbol{\varepsilon}^e, \tilde{\boldsymbol{\zeta}})$ and the *Green and Naghdi approach* in which $\psi = \tilde{\psi}(T, \boldsymbol{\varepsilon}, \boldsymbol{\varepsilon}^p, \tilde{\boldsymbol{\zeta}})$. Therein ψ is the Helmholtz potential, which is related to the free energy through the Legendre transformation $\psi = u - sT$. The tensors $\boldsymbol{\varepsilon}^e$ and $\boldsymbol{\varepsilon}^p$ denote the elastic and plastic strains, respectively, where the latter is treated as an internal state variable.¹ $\tilde{\boldsymbol{\zeta}}$ again denotes a generic set of additional internal state variables. In the modeling of conventional SMAs, both approaches have been followed, where the elastic strain was identified as the appropriate independent state variable in [71, 83, 131, 134], and the total strain was used in [66, 76, 86, 135]. In the modeling of MSMA one faces an additional difficulty due to fact that the magnetization response of the material, as described in Chapter II, also is hysteretic and thus associated with dissipation. However, an analogous separation between the recoverable and irrecoverable part of the magnetization is not apparent. This aspect will be discussed in more detail in Chapter IV and Appendix C, Section C2. For reasons of consistency, the internal energy and consequentially the Gibbs free energy in this work have been chosen to depend on the total strain and the total magnetization. It must be noted, however, that this approach ultimately results to the same set of constitutive equations as proposed in previous publications [55–57], in which the elastic strain was taken to be

¹The discussion in [133] actually uses finite strain theory, but the same arguments hold for small strains.

the independent state variable for the internal energy.

Furthermore, it shall be remarked that the thermo-magneto-mechanical framework presented so far is not limited to small strains. Finite strain constitutive models for conventional SMAs have been developed [131, 136, 137] based on similar frameworks. However, in the present work a small strain and negligible rotation approximation has been considered sufficient to model the constitutive response of MSMAs, since the maximum strains are less than 10%. In this case the energy term $\boldsymbol{\sigma} : (\text{grad } \mathbf{v})$ in Eq. (3.20) reduces to $\boldsymbol{\sigma} : \dot{\boldsymbol{\varepsilon}}$, as demonstrated in Appendix A, Section A4. The infinitesimal strain tensor $\boldsymbol{\varepsilon}$ is symmetric and connected to the displacement field by the definition [138]

$$\boldsymbol{\varepsilon} = \frac{1}{2} \left(\nabla \mathbf{u} + (\nabla \mathbf{u})^T \right). \quad (3.24)$$

There is no longer a distinction made between the reference and deformed configurations, such that one assumes $\text{Grad}(\cdot) = \text{grad}(\cdot) = \nabla(\cdot)$ [132].

By substituting the magnetic energy source term (3.21c) into Eq. (3.20), the conservation of energy then takes the form

$$\rho \dot{u} = \boldsymbol{\sigma} : \dot{\boldsymbol{\varepsilon}} + \mu_0 \mathbf{H} \cdot \dot{\mathbf{M}} + \rho r^h - \text{div } \mathbf{q}. \quad (3.25)$$

Using the Legendre transformation, Eq. (3.23), the conservation of energy Eq. (3.25) can also be rewritten as

$$\rho \dot{g} + \rho (\dot{s}T + s\dot{T}) + \dot{\boldsymbol{\sigma}} : \boldsymbol{\varepsilon} + \mu_0 \dot{\mathbf{H}} \cdot \mathbf{M} - \rho r^h + \text{div } \mathbf{q} = 0. \quad (3.26)$$

A limitation on the direction in which a thermodynamic process can be carried out in a physical system is given by the *second law of thermodynamics*, which can be formulated in terms of the internal entropy production rate γ as [130]

$$\gamma := \dot{s} - \frac{r^h}{T} + \frac{1}{\rho T} \text{div } \mathbf{q} - \frac{1}{\rho T^2} \mathbf{q} \cdot (\nabla T) \geq 0. \quad (3.27)$$

The thermodynamically-consistent derivation of constitutive relations from the free energy function, as applied next, is known as the *Coleman and Noll procedure* [81]. The combination of the first and the second laws in the form of Eqs. (3.25) and (3.27), respectively, is often referred to as the *Clausius-Duhem inequality* [126]². If thermal gradients are negligible, or the heat conduction problem is considered separately, this inequality reduces to the *Clausius-Planck inequality* [126], which in this case, using Eqs. (3.23), (3.25) and (3.27), can be written as

$$-\rho \left(\frac{\partial \hat{g}}{\partial T} + s \right) \dot{T} - \left(\rho \frac{\partial \hat{g}}{\partial \boldsymbol{\sigma}} + \boldsymbol{\varepsilon} \right) : \dot{\boldsymbol{\sigma}} - \left(\rho \frac{\partial \hat{g}}{\partial \mathbf{H}} + \mu_0 \mathbf{M} \right) \cdot \dot{\mathbf{H}} - \rho \frac{\partial \hat{g}}{\partial \boldsymbol{\zeta}} : \dot{\boldsymbol{\zeta}} \geq 0. \quad (3.28)$$

A detailed derivation of this relation is given in Appendix A, Section A5. Note that the rates \dot{T} , $\dot{\boldsymbol{\sigma}}$ and $\dot{\mathbf{H}}$ appear linearly in equation (3.28), and through the constitutive assumptions of Eq. (3.22) their parenthesized coefficients are independent of those rates. Therefore, in order for the inequality to hold for arbitrary processes, these coefficients must vanish, which leads to the constitutive relations

$$s = -\frac{\partial \hat{g}}{\partial T}; \quad (3.29a)$$

$$\boldsymbol{\varepsilon} = -\rho \frac{\partial \hat{g}}{\partial \boldsymbol{\sigma}}; \quad (3.29b)$$

$$\mu_0 \mathbf{M} = -\rho \frac{\partial \hat{g}}{\partial \mathbf{H}}. \quad (3.29c)$$

Through the relations (3.29) the Clausius-Planck inequality (3.28) reduces to

$$-\rho \frac{\partial \hat{g}}{\partial \boldsymbol{\zeta}} : \dot{\boldsymbol{\zeta}} \geq 0. \quad (3.30)$$

With the presentation of Maxwell's equations in Section A, the derivation of the

²The terminology is not always consistent in the literature. Some authors refer to the second law as the Clausius-Duhem inequality [130], some to the form in which the heat input terms have been replaced by using the first law.

generalized conservation laws in Section B and the formulation of the extended thermodynamic framework in Section C of this Chapter, the underlying thermo-magneto-mechanical framework for the MSMA constitutive model has been established.

There are 9 unknown components of the magnetic field variables \mathbf{B} , \mathbf{H} and \mathbf{M} . The mechanical field variables $\boldsymbol{\sigma}$, $\boldsymbol{\varepsilon}$ and \mathbf{u} represent 18 unknowns. The temperature T is an additional unknown, which appears in the energy balance if, for example, *Fourier's law of heat conduction* ($\mathbf{q} = -k\nabla T$) is considered [139]. Consequently, there are a total of 28 unknowns. Maxwell's equations (3.7) and Eq. (3.2b) provide 7 relations. The conservation laws for linear momentum, Eq. (3.15), angular momentum, Eq. (3.17), and energy, Eq. (3.26), represent an additional 7 equations to relate the field variables. One also has to consider the 6 strain-displacement relations, Eq. (3.24), or, alternatively, strain compatibility conditions [132, 138]. A total of 9 additional relations are given by the constitutive equations for the strain tensor and the magnetization vector, Eqs. (3.29b) and (3.29c), respectively, which have been derived under consideration of the second law of thermodynamics. In summary, there are a total of 29 equations to relate 28 unknowns and 1 thermodynamic potential, the Gibbs free energy in this case, which will be specified for MSMA in the following chapter. Additionally, for each of the internal state variables in the set $\boldsymbol{\zeta}$ an evolution equation will be derived.

CHAPTER IV

PHENOMENOLOGICAL MODELING OF MSMA

The thermo-magneto-mechanical framework for the phenomenological MSMA model was established in the previous chapter. In this chapter the specific constitutive equations are derived. The approach is to propose a specific form of the Gibbs free energy function that incorporates elastic, magnetic and magnetoelastic coupling terms that are relevant for the MSMA constitutive response as it was discussed in Chapter II. The influence of the changing crystallographic and magnetic microstructure is incorporated through suitable internal state variables, which also account for the dissipative effects associated with the reorientation of martensitic variants. Additional internal state variables are introduced to describe changes in the free energy caused by the motion of magnetic domain walls and the rotation of local magnetization vectors away from magnetic easy axes. According to the generic constitutive relations (3.29), which were derived from thermodynamic restrictions, the expressions for the dependent state variables entropy s , strain $\boldsymbol{\varepsilon}$ and magnetization \mathbf{M} , then follow directly from taking partial derivatives of the specific Gibbs free energy function with respect to the independent state variables temperature T , mechanical stress $\boldsymbol{\sigma}$ and magnetic field strength \mathbf{H} . Through the constitutive relations the dependent state variables also depend on the internal state variables, whose evolution accounts for the loading history dependence of the material behavior.

A. The Choice of Internal State Variables

Motivated by the experimentally observed arrangement of martensitic twins and magnetic domains in MSMA, as previously discussed in Chapter II, specifically in the context of Fig. 12, an idealized microstructure is assumed. Fig. 13 shows its schematic

representation. Other experiments have indicated that the actual microstructure of MSMA can be much more complex [106, 107], but this chosen representation has proven sufficient to explain all of the main characteristics of the MSMA response. Many researchers have proposed a similar representations [5, 49, 51, 52].

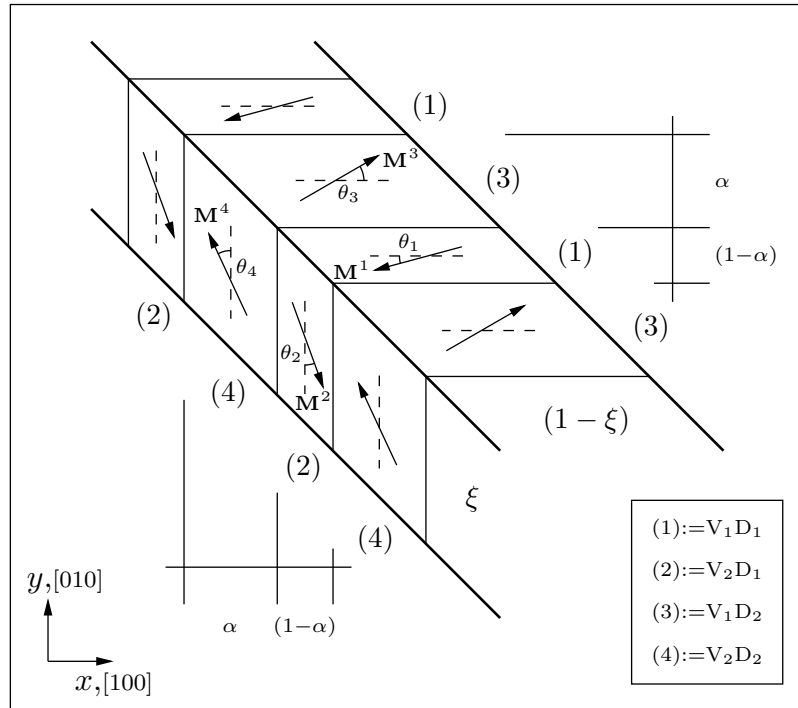


Fig. 13. Schematic representation of the microstructure showing the coexistence of martensitic variants and magnetic domains. The abbreviation V_1D_2 , for example, stands for "variant 1, domain 2". The four distinct subdomains are numbered 1–4 to simplify the notation.

Fig. 13 depicts the coexistence of two martensitic variants, and two magnetic domain types. The third martensitic variant, and thus the third magnetic domain type, are thought to have been eliminated by proper load application. This idealized microstructure was also indicated in Fig. 2, for a generic intermediate applied magnetic field level. In this sketch, however, the possibility of the rotation of the

local magnetization away from the magnetic easy axes is included and defined by the rotation angles θ_i , with $i = 1, \dots, 4$ and $0 \leq \theta_i \leq \frac{\pi}{2}$. Variant 1, as previously defined in Fig. 1, is magnetized along the x , $[100]$ -direction, whereas variant 2 has its magnetic easy axis along the y , $[010]$ -direction. The magnetic domains are defined by the preferred orientation of their magnetization vectors. In magnetic domain 1 the magnetization is oriented in the negative direction of the respective coordinate axis, and in domain 2 it points in the opposite direction. The two variants are separated by a twin boundary shown here at a 45° angle. The twin boundary coincides with the 90° domain walls between adjacent magnetic domains. Both are assumed to have zero thickness on the considered scale. Within each variant 180° domain walls separate the domains. The local magnetization vectors and their associated rotation angles are, by definition, considered constant within each domain. Note that the rotations shown in the sketch do not necessarily correspond to realistic arrangement of magnetization vectors, but serve the purpose of illustrating the nomenclature. Compatibility of domains along twin planes, which separates different variants, has also been assumed, such that the domain walls of neighboring twins meet on the twin boundary in a compatible manner.

Based on this discussion, the scalar volume fractions ξ and α for the martensitic variant 2 and the magnetic domain 2 (cf. Fig. 13), respectively, are introduced as internal state variables. The volume fraction of variant 1 is equal to $(1 - \xi)$, and that of domain 1 is similarly given by $(1 - \alpha)$, such that no additional variables need to be introduced. Additionally the inelastic reorientation strain tensor $\boldsymbol{\varepsilon}^r$ is formally identified as an internal state variable, although its evolution is later connected to the rate of ξ . It is implied that for a small strain approximation the additive decomposition

$$\boldsymbol{\varepsilon} = \boldsymbol{\varepsilon}^e + \boldsymbol{\varepsilon}^r, \quad (4.1)$$

is assumed to be sufficiently accurate. The set of internal state variables is completed by the rotation angles of the magnetization vectors θ_i depicted in Fig. 13.

B. Formulation of the Specific Gibbs Free Energy

Before presenting a specific form, the approach to constructing the Gibbs free energy expression for the proposed MSMA model shall be discussed in general terms. A generic form of the Gibbs free energy was specified by Eq. (3.22) in Chapter III, Section C. The basic properties of the Gibbs potential were also discussed there. To construct the specific form of the Gibbs free energy for the MSMA model different approaches are conceivable. Certainly the free energy expression must contain an elastic, a magnetic and a magnetoelastic part to capture the characteristic features of the constitutive response of MSMA. The approach that first comes to mind is a Taylor series expansion of the Gibbs free energy. This approach is typically followed for modeling materials that exhibit multi-field coupling, such as piezoelectrics, piezomagnetism or electro- and magnetostrictive materials because the interaction terms can then easily be constructed [119, 140, 141]. All of the coupling properties are then captured by coefficients whose components can, at least in principle, be determined from experiments. The individual Gibbs free energy contributions of the thermoelastic austenite and martensite phases in conventional SMAs have usually been constructed by such Taylor series expansions [71, 72]. It is demonstrated in Appendix C, Section C2, that in order to predict the reversible anisotropic magnetization response of MSMA a free energy based model can be constructed following the series expansion approach. This model leads to identical constitutive predictions of the reversible magnetization as the approach that will be taken here.

A number of reasons discourage utilizing the series expansion approach for mod-

eling MSMA. An in-depth discussion of this matter can also be found in Appendix C, but the key points will be summarized here: 1) The inelastic reorientation strain was accounted for by assuming an additive decomposition of the total strain in Eq. (4.1) and then postulating Eq. (4.15) to describe its evolution. A similar decomposition of the magnetization in this case is difficult to justify because due to magnetic domain wall motion, which is typically reversible in MSMA (cf. Fig. 8), the macroscopic magnetization always vanishes as the applied field is reduced to zero. Thus, remnant magnetization is not observed in MSMA and the irreversible magnetization can therefore not simply be connected to the evolution of variant volume fraction. 2) The Gibbs free energy expression proposed in this work directly incorporates the Zeeman energy and the magnetocrystalline anisotropy energy that have briefly been discussed in Section B of Chapter II. These terms have the advantage that they are directly connected to the internal state variables α and θ_i , which allow the tracking of the magnetic domain volume fraction and the magnetization vector rotation angles. This promotes a better understanding of the micro-scale phenomena which cause the macroscopic constitutive response. This physical intuition is lost if the effect of magnetic domain wall motion and magnetization rotation are simply captured by different coefficients of a magnetic susceptibility tensor. 3) The discussed energy terms are commonly used in the modeling of magnetic materials [17, 18, 100] and have also been used in other MSMA models [26, 49, 52]. Based on these arguments it was decided to not follow the series expansion approach.

Motivated by the discussed micro-scale arrangement of martensitic twins in MSMA, the Gibbs free energy is constructed as a weighted average between the contributions of each variant. This assumes an appropriate *separation of scales*, which means that the characteristic internal features of the material, such as the martensitic variants and magnetic domains in MSMA, are thought to be small enough to allow

the definition of such average quantities at each material point. The deviation of the free energy from the weighted average of the individual contributions, as caused by the interaction of martensitic variants, is captured by a mixing term $g^{\xi\text{-mix}}$. In accordance with the general constitutive assumption of Eq. (3.22), the choice of internal state variables made in the previous section and the above discussion about the general approach to formulating the Gibbs free energy, the following expression is proposed

$$\begin{aligned} g &:= \hat{g}(T, \boldsymbol{\sigma}, \mathbf{H}, \boldsymbol{\varepsilon}^r, \xi, \alpha, \theta_j) \\ &= \xi \hat{g}^{\text{V}_2}(T, \boldsymbol{\sigma}, \mathbf{H}, \boldsymbol{\varepsilon}^r, \alpha, \theta_2, \theta_4) + (1 - \xi) \hat{g}^{\text{V}_1}(T, \boldsymbol{\sigma}, \mathbf{H}, \boldsymbol{\varepsilon}^r, \alpha, \theta_1, \theta_3) + \hat{g}^{\xi\text{-mix}}(\xi). \end{aligned} \quad (4.2)$$

Since MSMA are typically used at constant temperatures, isothermal conditions are assumed and thermal as well as thermoelastic and thermomagnetic coupling terms are not explicitly included. If one is interested in temperature changes occurring in the martensitic phase, it is fairly straightforward to include the relevant thermal energy terms in the total Gibbs free energy expression of Eq. (4.8). This is demonstrated in Appendix C, Section C3, where the temperature change per magnetic cycle due to the dissipation associated with the variant reorientation is computed.

The contribution of each martensitic variant g^{V_i} , with $i = \{1, 2\}$, to the total Gibbs free energy, Eq. (4.2), is then proposed to be given by

$$\begin{aligned} g^{\text{V}_i} &= -\frac{1}{2\rho} \boldsymbol{\sigma} : \mathcal{S}^{\text{V}_i} \boldsymbol{\sigma} - \frac{1}{\rho} \boldsymbol{\sigma} : \boldsymbol{\varepsilon}^r + (1 - \alpha) \left[-\frac{\mu_0}{\rho} \mathbf{M}^{\text{V}_i \text{D}_1} \cdot \mathbf{H} + g^{\text{an, V}_i \text{D}_1} \right] \\ &+ \alpha \left[-\frac{\mu_0}{\rho} \mathbf{M}^{\text{V}_i \text{D}_2} \cdot \mathbf{H} + g^{\text{an, V}_i \text{D}_2} \right] + g^{\alpha\text{-mix}}(\alpha) + g_0(T). \end{aligned} \quad (4.3)$$

Here, \mathcal{S}^{V_i} denotes the elastic compliance tensor of variant i . The magnetization vectors $\mathbf{M}^{\text{V}_i \text{D}_j}$ have been defined in Eqs. 4.4. The scalar constant g_0 is the reference state value of the Gibbs free energy.

The first term in Eq. (4.3) describes the energy stored in the material due to elastic deformation. The second term is due to the interaction of the stress and inelastic strain. For the magnetic terms the contributions of each magnetic domain are again taken into account in a weighted average sense, with the correcting mixing term $g^{\alpha\text{-mix}}$. It has been assumed that the density, the elastic compliance tensor, the reorientation strain tensor and the reference value of the free energy are the same in both magnetic domain types.

The first magnetic energy term in Eq. 4.2 is the Zeeman energy for which the individual contributions are of the form $-\mathbf{M}^{\text{V}_i\text{D}_j} \cdot \mathbf{H}$, where the magnetization vectors of the different variant-domain combinations, cf. Fig. 13, are defined as

$$\mathbf{M}^1 := \mathbf{M}^{\text{V}_1\text{D}_1} = -M^{\text{sat}} (\cos(\theta_1) \mathbf{e}_x + \sin(\theta_1) \mathbf{e}_y) ; \quad (4.4a)$$

$$\mathbf{M}^2 := \mathbf{M}^{\text{V}_2\text{D}_1} = M^{\text{sat}} (\sin(\theta_2) \mathbf{e}_x - \cos(\theta_2) \mathbf{e}_y) ; \quad (4.4b)$$

$$\mathbf{M}^3 := \mathbf{M}^{\text{V}_1\text{D}_2} = M^{\text{sat}} (\cos(\theta_3) \mathbf{e}_x + \sin(\theta_3) \mathbf{e}_y) ; \quad (4.4c)$$

$$\mathbf{M}^4 := \mathbf{M}^{\text{V}_2\text{D}_2} = M^{\text{sat}} (-\sin(\theta_4) \mathbf{e}_x + \cos(\theta_4) \mathbf{e}_y) . \quad (4.4d)$$

In the above relations, M^{sat} is the saturation magnetization and $\mathbf{e}_x, \mathbf{e}_y$ are unit vectors in the respective coordinate directions. If the magnetization vectors are assumed to be fixed to the respective magnetic easy axes (i. e. $\theta_i = 0$) these expressions reduce to the formulation proposed by Hirsinger and Lexcellent [52]. As discussed in Chapter II, the Zeeman energy accounts for the interaction of the local magnetization with the magnetic field [100]. The Zeeman energy difference across the twin boundary is the main magnetic driving force for variant reorientation. It must be emphasized that \mathbf{H} is the internal field at a generic material point, not the applied field.

Other approaches, such as the formulation by proposed by Buchelnikov and

Bosko [65], include the Zeeman energy in the form of $-\mathbf{M} \cdot \mathbf{H}^a$, where \mathbf{H}^a is the applied field¹. They introduce an additional term, namely the magnetostatic energy of the demagnetization field \mathbf{DM}^2 , where \mathbf{D} is the demagnetization tensor. This method of calculating the magnetostatic fields of magnetized bodies will extensively be discussed in Chapter VI. According to Eq. (6.6) the internal magnetic field is the sum of the applied field and the demagnetization field. The latter can be calculated from Eq. (6.7) as $\mathbf{H}^d = -\mathbf{DM}$. It is shown in the following derivation that these approaches are equivalent.

$$\begin{aligned}
 & \text{Energy of demagnetization} + \text{Zeeman energy of external field} \\
 &= (\mathbf{DM}) \cdot \mathbf{M} - \mathbf{M} \cdot \mathbf{H}^a = -(-\mathbf{DM}) \cdot \mathbf{M} - \mathbf{M} \cdot \mathbf{H}^a = -(\mathbf{H}^d + \mathbf{H}^a) \mathbf{M} = -\mathbf{H} \cdot \mathbf{M} \quad (4.5) \\
 &= \text{Zeeman energy of internal field.}
 \end{aligned}$$

The second magnetic term in the free energy expression 4.3 is the magnetocrystalline anisotropy energy, whose contributions are denoted $g^{\text{an}, V_i D_j}$. It is the energy stored in the material due to the work done by the magnetic field in rotating the magnetization vectors away from the magnetic easy axes. Magnetoelastic interactions in the form of ordinary magnetostriction has also been neglected since the associated strains are at least two orders of magnitude smaller in MSMA than the strains caused by the variant rearrangement [96, 102].

An explicit form of the magnetocrystalline anisotropy energy for *uniaxial symmetry*, i. e. for crystals which exhibit only one preferred direction of magnetization,

¹The Buchelnikov and Bosko formulation is one-dimensional, but for reasons of comparison an equivalent three-dimensional formulation is discussed here

is usually given in the form of a trigonometric power series [17, 100, 142]

$$g^{\text{an}} = \sum_{n=0}^N K_n \sin^{2n}(\theta) , \quad (4.6)$$

where K_n are coefficients to be determined from magnetization measurements [25, 97] and θ is again the rotation angle between the magnetization and the easy axis.²

The influence of the interaction of evolving martensitic variants or magnetic domains on the free energy, introduced in (4.2) by the mixing terms $g^{\xi\text{-mix}}$ and $g^{\alpha\text{-mix}}$, respectively, is assumed to be captured by hardening functions of the generic form

$$g^{\xi\text{-mix}} = \frac{1}{\rho} f^{\xi}(\xi) ; \quad (4.7a)$$

$$g^{\alpha\text{-mix}} = \frac{1}{\rho} f^{\alpha}(\alpha) . \quad (4.7b)$$

Specific hardening function will be specified at the end of this chapter.

The combination of Eqs. (4.2), (4.3) and (4.7) yields the following explicit form of the total Gibbs free energy

$$\begin{aligned} g &= \hat{g}(T, \boldsymbol{\sigma}, \mathbf{H}, \boldsymbol{\varepsilon}^r, \xi, \alpha, \theta_j) \\ &= -\frac{1}{2\rho} \boldsymbol{\sigma} : \mathcal{S} \boldsymbol{\sigma} - \frac{1}{\rho} \boldsymbol{\sigma} : \boldsymbol{\varepsilon}^r \\ &\quad + \xi \left[(1 - \alpha) \left[-\frac{\mu_0}{\rho} \mathbf{M}^2 \cdot \mathbf{H} + g^{\text{an},2}(\theta_2) \right] + \alpha \left[-\frac{\mu_0}{\rho} \mathbf{M}^4 \cdot \mathbf{H} + g^{\text{an},4}(\theta_4) \right] \right] \\ &\quad + (1 - \xi) \left[(1 - \alpha) \left[-\frac{\mu_0}{\rho} \mathbf{M}^1 \cdot \mathbf{H} + g^{\text{an},1}(\theta_1) \right] + \alpha \left[-\frac{\mu_0}{\rho} \mathbf{M}^3 \cdot \mathbf{H} + g^{\text{an},3}(\theta_3) \right] \right] \\ &\quad + \frac{1}{\rho} f^{\xi}(\xi) + \frac{1}{\rho} f^{\alpha}(\alpha) + g_0(T) . \end{aligned} \quad (4.8)$$

²A tetragonal symmetry expression for the anisotropy energy has been considered by Cui et al. [25], based on the work of Bozorth [143]. If only up to quadratic terms are taken into account (N=2), as done in this work, the expressions for the uniaxial and tetragonal symmetries coincide.

The density has been assumed to be identical in both martensitic variants. The effective compliance tensor is defined by $\mathcal{S} := \mathcal{S}^{V_1} + \xi \Delta \mathcal{S} = \mathcal{S}^{V_1} + \xi(\mathcal{S}^{V_2} - \mathcal{S}^{V_1})$. For isotropic polycrystalline materials, it has been shown by the use of micromechanical techniques, that this linear average for effective material properties is a good approximation [71, 76, 144]. The compliance tensor of the two variants only differ by a rotation. The elastic properties of tetragonal martensite have been discussed in [8, 145, 146].

According to Eqs. (3.29), constitutive equations for the entropy, the strain and the magnetization follow from taking partial derivatives of the free energy, Eq. (4.8)

$$s = - \frac{\partial \hat{g}}{\partial T} = - \frac{\partial g_0}{\partial T} ; \quad (4.9a)$$

$$\boldsymbol{\varepsilon} = - \rho \frac{\partial \hat{g}}{\partial \boldsymbol{\sigma}} = \mathcal{S} \boldsymbol{\sigma} + \boldsymbol{\varepsilon}^r ; \quad (4.9b)$$

$$\mathbf{M} = - \frac{\rho}{\mu_0} \frac{\partial \hat{g}}{\partial \mathbf{H}} = \xi [(1 - \alpha) \mathbf{M}^2 + \alpha \mathbf{M}^4] + (1 - \xi) [(1 - \alpha) \mathbf{M}^1 + \alpha \mathbf{M}^3] , \quad (4.9c)$$

where the local magnetization vectors \mathbf{M}^i have been defined in Eqs. (4.4). Note that according to (4.9a) the entropy is only a function of temperature, and therefore must be constant throughout the reorientation process, if isothermal conditions are assumed. This means that the entropy changes due to dissipative effects must be balanced by suitable heat transfer to maintain a constant temperature. For adiabatic conditions the entropy increases due to the dissipation associated with the reorientation of variants. It is shown in Appendix C, Section C3 how the model must be slightly extended to capture adiabatic loading paths.

By taking derivatives of the total free energy, Eq. (4.8), with respect to the internal state variables, the following thermodynamic driving forces are derived

$$\boldsymbol{\pi}^r := - \rho \frac{\partial \hat{g}}{\partial \boldsymbol{\varepsilon}^r} = \boldsymbol{\sigma} ; \quad (4.10a)$$

$$\begin{aligned}\tilde{\pi}^\xi &:= -\rho \frac{\partial \hat{g}}{\partial \xi} \\ &= \frac{1}{2} \boldsymbol{\sigma} : \Delta \mathcal{S} \boldsymbol{\sigma} - \rho(1-\alpha) \left[-\frac{\mu_0}{\rho} (\mathbf{M}^2 - \mathbf{M}^1) \cdot \mathbf{H} + g^{\text{an},2}(\theta_2) - g^{\text{an},1}(\theta_1) \right] \quad (4.10\text{b})\end{aligned}$$

$$- \rho \alpha \left[-\frac{\mu_0}{\rho} (\mathbf{M}^4 - \mathbf{M}^3) \cdot \mathbf{H} + g^{\text{an},4}(\theta_4) - g^{\text{an},3}(\theta_3) \right] - \frac{\partial f^\xi}{\partial \xi};$$

$$\begin{aligned}\pi^\alpha &:= -\rho \frac{\partial \hat{g}}{\partial \alpha} \\ &= -\rho(1-\xi) \left[-\frac{\mu_0}{\rho} (\mathbf{M}^3 - \mathbf{M}^1) \cdot \mathbf{H} + g^{\text{an},3}(\theta_3) - g^{\text{an},1}(\theta_1) \right] \quad (4.10\text{c})\end{aligned}$$

$$- \rho \xi \left[-\frac{\mu_0}{\rho} (\mathbf{M}^4 - \mathbf{M}^2) \cdot \mathbf{H} + g^{\text{an},4}(\theta_4) - g^{\text{an},2}(\theta_2) \right] - \frac{\partial f^\alpha}{\partial \alpha}.$$

Similarly, the driving forces for rotation the rotation of the magnetization vectors are given by

$$\begin{aligned}\pi^{\theta_1} &:= -\rho \frac{\partial \hat{g}}{\partial \theta_1} \\ &= -\rho(1-\xi)(1-\alpha) \left[\frac{\mu_0 M^{\text{sat}}}{\rho} \left[-\sin(\theta_1) H_x + \cos(\theta_1) H_y \right] + \frac{\partial \hat{g}^{\text{an},1}}{\partial \theta_1} \right]; \quad (4.11\text{a})\end{aligned}$$

$$\pi^{\theta_2} := -\rho \frac{\partial \hat{g}}{\partial \theta_2} = -\rho \xi(1-\alpha) \left[-\frac{\mu_0 M^{\text{sat}}}{\rho} \left[\cos(\theta_2) H_x + \sin(\theta_2) H_y \right] + \frac{\partial \hat{g}^{\text{an},2}}{\partial \theta_2} \right]; \quad (4.11\text{b})$$

$$\pi^{\theta_3} := -\rho \frac{\partial \hat{g}}{\partial \theta_3} = -\rho(1-\xi)\alpha \left[-\frac{\mu_0 M^{\text{sat}}}{\rho} \left[-\sin(\theta_3) H_x + \cos(\theta_3) H_y \right] + \frac{\partial \hat{g}^{\text{an},3}}{\partial \theta_3} \right]; \quad (4.11\text{c})$$

$$\pi^{\theta_4} := -\rho \frac{\partial \hat{g}}{\partial \theta_4} = -\rho \xi \alpha \left[-\frac{\mu_0 M^{\text{sat}}}{\rho} \left[-\cos(\theta_4) H_x - \sin(\theta_4) H_y \right] + \frac{\partial \hat{g}^{\text{an},4}}{\partial \theta_4} \right], \quad (4.11\text{d})$$

where the definitions of the magnetization vectors, Eqs. (4.4), have been utilized. The

defined quantities $\boldsymbol{\pi}^r$, $\tilde{\pi}^\xi$, π^α and π^{θ_i} are driving forces that are thermodynamically conjugate to the internal state variables such that, using the above definitions, the Clausius-Planck inequality (3.30) can be rewritten as

$$\boldsymbol{\pi}^r : \dot{\boldsymbol{\varepsilon}}^r + \tilde{\pi}^\xi \dot{\xi} + \pi^\alpha \dot{\alpha} + \sum_{i=1}^4 \pi^{\theta_i} \dot{\theta}_i \geq 0 . \quad (4.12)$$

C. Evolution Equations and Activation Conditions

The effective number of internal state variables can be reduced by enforcing additional thermodynamic constraints, based on the following considerations. From physical observations it is reasonable to assume that the motion of magnetic domain walls and the rotation of the magnetization vectors are thermodynamically reversible processes [16, 100], and thus do not contribute to the entropy production. The single variant sample magnetization curves of Fig. 10, for example, in which only the mechanisms of domain wall motion (easy axis) and magnetization rotation (hard axis) are active, exhibit almost no hysteresis. The magnetization curves in Fig. 11, however, exhibit significant hysteresis due to the dissipation associated with the variant rearrangement. If the internal dissipation production is entirely attributed to the reorientation process, Eq. (4.12) implies

$$\pi^\alpha := -\rho \frac{\partial \hat{g}}{\partial \alpha} = 0 ; \quad (4.13a)$$

$$\pi^{\theta_i} := -\rho \frac{\partial \hat{g}}{\partial \theta_i} = 0 . \quad (4.13b)$$

This does not mean that the domain walls do not move, nor that the magnetization vectors do not rotate, but rather that no dissipation is associated with these processes. Eqs. (4.13) represent a set of five relations, which can be solved to determine evolution equations, or more precisely direct functional dependencies, of the domain volume

fraction α and the four rotation angles θ_i on the independent state variables as well as the loading history through the remaining internal state variables. With Eqs. (4.13) the inequality (4.12) takes the reduced form

$$\boldsymbol{\pi}^r : \dot{\boldsymbol{\epsilon}}^r + \tilde{\pi}^\xi \dot{\xi} \geq 0 . \quad (4.14)$$

In the modeling of conventional shape memory behavior the transformation strain is usually related to the martensitic volume fraction [71, 72, 76]. Following this approach, the evolution of the reorientation strain associated with the magnetic shape memory effect is proposed to be proportional to the rate of the martensitic variant volume fraction

$$\dot{\boldsymbol{\epsilon}}^r = \boldsymbol{\Lambda}^r \dot{\xi} . \quad (4.15)$$

The reorientation strain is then no longer an independent internal state variable. In the equation above $\boldsymbol{\Lambda}^r$ is the reorientation tensor defining the direction in which the reorientation strain develops. An explicit form of the tensor will be given in Chapter V for a specific example. For the special case of constant $\boldsymbol{\Lambda}^r$ expression (4.15) can be integrated to yield the reorientation strain, so that the total strain, using Eq. (4.9b), is then given by

$$\boldsymbol{\epsilon} = \mathcal{S}\boldsymbol{\sigma} + \boldsymbol{\Lambda}^r \xi . \quad (4.16)$$

If $\boldsymbol{\Lambda}^r$ is not constant, for example for non-proportional loading, equation (4.15) has to be evaluated incrementally [82].

One can further define the total thermodynamic driving force for the twin boundary motion associated with the variant reorientation process as

$$\pi^\xi := \boldsymbol{\pi}^r : \boldsymbol{\Lambda}^r + \tilde{\pi}^\xi = \boldsymbol{\sigma} : \boldsymbol{\Lambda}^r - \rho \frac{\partial \hat{g}}{\partial \xi} , \quad (4.17)$$

where the definitions (4.10a) and (4.10b) have been utilized. Then, using Eqs. (4.15)

and Eq. (4.17), the Clausius-Planck inequality (4.14) can finally be written as

$$\pi^\xi \dot{\xi} \geq 0. \quad (4.18)$$

The rate-independent nature of the formulation motivates the introduction of the following *reorientation function*

$$\Phi^\xi(\boldsymbol{\sigma}, \mathbf{H}, \xi) := \begin{cases} \pi^\xi - Y^\xi, & \dot{\xi} > 0 \\ -\pi^\xi - Y^\xi, & \dot{\xi} < 0 \end{cases}, \quad \Phi^\xi \leq 0, \quad (4.19)$$

which defines the activation threshold for variant reorientation or conversely the elastic regime. The proposed reorientation function is similar to transformation functions used in the rate-independent phenomenological modeling of conventional shape memory behavior [72, 82]. The positive scalar quantity Y^ξ is physically related to internal dissipation associated with twin boundary motion. It is assumed that the reorientation process is subject to constraints derived from a principle of maximum dissipation, which can be expressed in terms of the Kuhn-Tucker type reorientation conditions [147]

$$\Phi^\xi(\boldsymbol{\sigma}, \mathbf{H}, \xi) \leq 0, \quad \Phi^\xi \dot{\xi} = 0. \quad (4.20)$$

Note that in the elastic regime where $\Phi^\xi < 0$ the conditions (4.20) require $\dot{\xi} = 0$. The forward reorientation process is characterized by $\Phi^\xi = 0$ and $\dot{\xi} > 0$, whereas for the reverse process the conditions $\Phi^\xi = 0$ and $\dot{\xi} < 0$ hold. Since the thermodynamic driving force π^ξ , and therefore the reorientation function Φ^ξ , contain the hardening function f^ξ , the reorientation conditions (4.20) depend on the martensitic variant volume fraction and thereby on the loading history, not just the current values of stress and magnetic field.

In order to complete the formulation of the constitutive model, the generically

introduced hardening functions (4.7) need to be specified. These functions account for all micro-scale interactions which result in macroscopically observed hardening. Such hardening behavior is clearly observed in MSMA, for example in the strain response curves of Fig. 29 on page 103, where a much higher magnetic field is needed to finish the reorientation process, than is required to start it. Thus, even though the martensitic twins are compatible across a twin boundary, the presence of one variant clearly influences the growth of the others. Effects such as the trapping of the progressing twin boundary at *pinning sites* as proposed by Faidley et al. [5], which influence the macroscopic evolution of the reorientation strain can also be accounted for in this manner.

Several types of hardening functions have been presented in the literature in the context of martensitic phase transformation of conventional shape memory alloys, such as the exponential hardening model [69, 148], the polynomial hardening model [71, 72], and the trigonometric hardening model [70, 72]. The exponential hardening function is related to the nucleation process of martensite and was actually the first model introduced in the literature. The polynomial function is motivated by a series expansion of the free energy. The trigonometric hardening model has been introduced to better match results with experimental observations and has been shown to yield good agreement between experimental results and model predictions in conventional SMAs.

The polynomial and the trigonometric hardening functions are adapted here in the context of the variant reorientation process. The quadratic polynomial hardening function is given by

$$f^{\xi,p}(\xi) = \begin{cases} \frac{1}{2}A^p\xi^2 + (B_1^p + B_2^p)\xi, & \xi > 0 \\ \frac{1}{2}C^p\xi^2 + (B_1^p - B_2^p)\xi, & \xi < 0 \end{cases}, \quad (4.21)$$

which yields

$$\frac{\partial f^{\xi,p}}{\partial \xi} = \begin{cases} A^p \xi + B_1^p + B_2^p, & \dot{\xi} > 0 \\ C^p \xi + B_1^p - B_2^p, & \dot{\xi} < 0 \end{cases}, \quad (4.22)$$

where A^p, B_1^p, B_2^p and C^p are adjustable parameters of the quadratic polynomial hardening function [55].

The trigonometric hardening function is of the form

$$f^{\xi,c}(\xi) = \begin{cases} \int_0^\xi -A^c [\pi - \cos^{-1}(2\tilde{\xi} - 1)] d\tilde{\xi} + (B_1^c + B_2^c)\xi, & \dot{\xi} > 0 \\ \int_0^\xi -C^c [\pi - \cos^{-1}(2\tilde{\xi} - 1)] d\tilde{\xi} + (B_1^c - B_2^c)\xi, & \dot{\xi} < 0 \end{cases}, \quad (4.23)$$

and thus

$$\frac{\partial f^{\xi,c}}{\partial \xi} = \begin{cases} -A^c [\pi - \cos^{-1}(2\xi - 1)] + (B_1^c + B_2^c), & \dot{\xi} > 0 \\ -C^c [\pi - \cos^{-1}(2\xi - 1)] + (B_1^c - B_2^c), & \dot{\xi} < 0 \end{cases}. \quad (4.24)$$

It will be shown in Section b of Chapter V, how the parameters A^c, B_1^c, B_2^c and C^c can be connected to physically more meaningful and measurable quantities.

To better capture the reorientation strain evolution in observed in Ni-Mn-Ga, a power law type hardening function was recently proposed by Kiefer et al. [58]

$$f^{\xi,pl}(\xi) = \begin{cases} \frac{1}{n} A^{pl} \xi^n + (B_1^{pl} + B_2^{pl})\xi & , \dot{\xi} > 0 \\ C^{pl} \left[\xi + \frac{1}{n} (1 - \xi)^n \right] + (B_1^{pl} - B_2^{pl})\xi, & \dot{\xi} < 0 \end{cases}, \quad (4.25)$$

which has the derivative

$$\frac{\partial f^{\xi,pl}}{\partial \xi} = \begin{cases} A^{pl} \xi^{n-1} + B_1^{pl} + B_2^{pl} & , \dot{\xi} > 0 \\ C^{pl} [1 - (1 - \xi)^{n-1}] + B_1^{pl} - B_2^{pl}, & \dot{\xi} < 0 \end{cases}. \quad (4.26)$$

Similar hardening functions for the evolution of the magnetic domains can in principle be obtained by simply replacing ξ with α in the above expression. However, the limited experimental data that is available at this point suggests that it is sufficient to assume a quadratic hardening behavior of the type specified in Eq. (4.22), which leads to a linear variation of the magnetization if magnetic domain wall motion is the only active mechanism. This was demonstrated in the constrained MSMA single crystal example in Appendix C).

The next chapter is concerned with the reduction of the general constitutive equations developed in this chapter for specific loading conditions.

CHAPTER V

MSMA RESPONSE UNDER SPECIFIC MAGNETOMECHANICAL LOADING

In the previous section the constitutive model was introduced in its most general form. In this section a number of simplifying assumptions are made and specific loading conditions are considered, such that reduced versions of the constitutive equations are obtained. The MSMA response is modeled for the following loading cases which are schematically depicted in Fig. 14: 1) Variable magnetic field at different levels of a perpendicular compressive uniaxial stress; 2) Variable compressive uniaxial stress at different levels of a perpendicular magnetic field; 3) Variable magnetic field collinear to a constant compressive uniaxial stress at different levels of a perpendicular magnetic field.

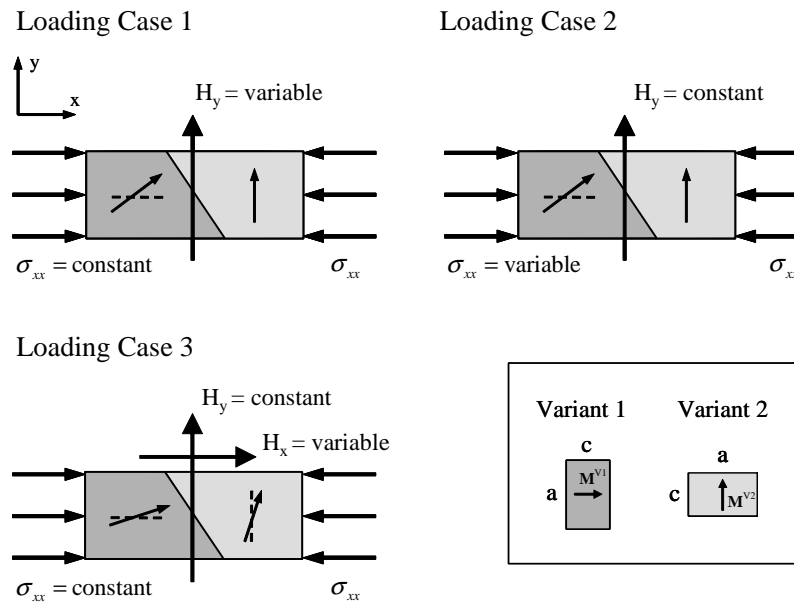


Fig. 14. Schematic illustration of the three modeled loading cases. Small arrows indicate the direction of the average magnetization in each variant at an exemplary load level during the reorientation process.

It is assumed that it is possible to only apply certain components of the stress and magnetic field at each material point. The assumption of a homogeneous uniaxial stress state in a prismatic specimen is justified by Saint-Venants's principle [132]. A uniaxial magnetic field applied at the boundary of the same prismatic (non-ellipsoidal) specimen, however, leads to a non-uniform distribution of the magnetic field inside the sample whose magnitude is significantly reduced by the demagnetization effect [16, 17]. The influence of the inhomogeneity of the magnetic field and the specimen shape dependent demagnetization effect are investigated in Chapter VI by using magnetostatic analysis in combination with the constitutive model. In this chapter, however, the focus is on the constitutive response and thus \mathbf{H} is the magnetic field acting at a generic material point. For the comparison of model predictions with experimental results, \mathbf{H} can be interpreted as the average magnetic field in the specimen. Of course, in general, cases can be modeled involving structures in which neither the stress nor the magnetic field are uniform, since the constitutive model is formulated to hold at each point in the continuum.

Based on these assumptions, the three loading cases specified in Fig. 14 are considered in the following sections.

A. Loading Case 1: Variable Magnetic Field at Different Levels of a Perpendicular Compressive Uniaxial Stress

In this first loading case $\sigma_{xx} = \text{const.} \leq 0$ is the only non-zero component of the stress and H_y is the non-zero component of the magnetic field. For the chosen coordinate

system the non-zero components of the proposed reorientation tensor are given by¹

$$\Lambda_{xx}^r = -\Lambda_{yy}^r = \varepsilon^{r,\max} ; \quad \Lambda_{zz}^r = \Lambda_{xy}^r = \Lambda_{xz}^r = \Lambda_{yz}^r = 0 . \quad (5.1)$$

The maximum strain value can be measured experimentally or is often approximated as $\varepsilon^{r,\max} = (a - c)/a$, where a and c are the lattice parameters of the tetragonal martensite. Reorientation strain tensors for arbitrary single crystal orientations have been discussed in the literature [26, 28, 93].

Typically, the motion of magnetic domain walls is neglected in the modeling of MSMAAs [5, 49, 52, 53], since it is assumed that unfavorable domains are eliminated at relatively low fields [11, 97] such that they do not significantly influence the magnetic field-induced variant reorientation process and therefore do not justify the formulation of even more complex constitutive models. However, from comparison with experimental data [57] it has become evident, that under some circumstances neglecting the motion of magnetic domain walls leads to very inaccurate predictions of the magnetization behavior at low stresses and low fields. For example, the model will predict significant remnant magnetization values, up to saturation, at zero applied field, whereas experiments show that the macroscopic magnetization vanishes. Since the evolution of magnetic domain walls is incorporated in the general form of the constitutive model, this problem can be addressed. In Section 1 model predictions under the common assumption of a fixed magnetic domain structure are presented. This version of the model is valid for a wide range of loads and is much easier to calibrate, implement and evaluate. In Section 2 a special case is considered in which accounting for the motion of magnetic domains significantly improves the model predictions of the magnetization response at low stress levels.

¹Typically specimen are cut such that the $\langle 100 \rangle_m$ -directions of the tetragonal martensite align with the direction of the applied loads.

1. Fixed Magnetic Domain Structure

a. Reduced Model Equations

If the motion of magnetic domain walls at low fields is neglected, the domain volume fraction takes the value of $\alpha = 1$, for $H_y > 0$, and $\alpha = 0$ for $H_y < 0$. Fig. 15 represents a modification of Fig 2 for the assumption $\alpha = 1$.

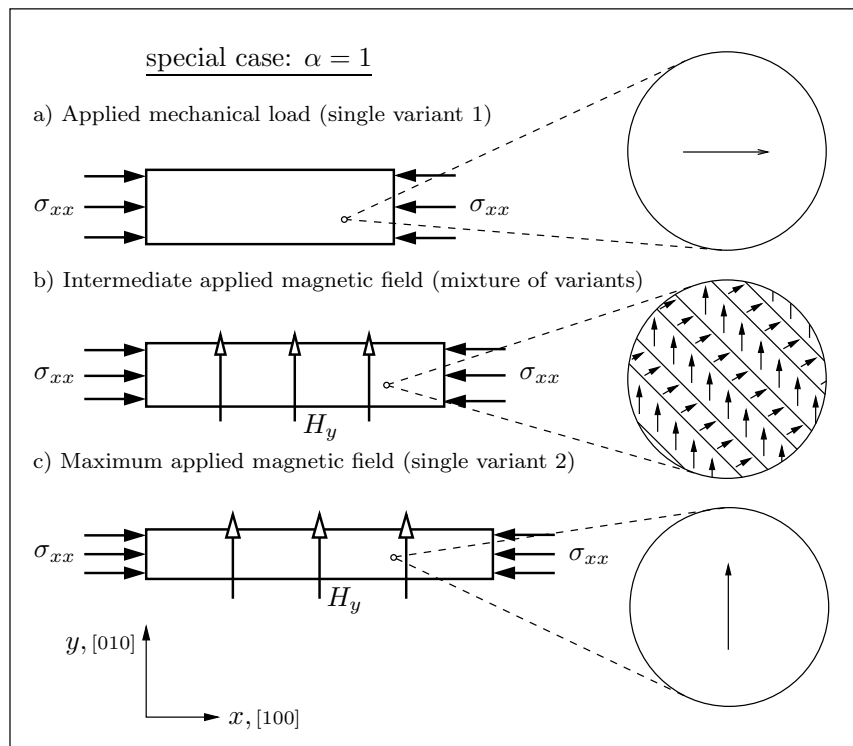


Fig. 15. The variant reorientation process with fixed domain structure $\alpha = 1$.

For the described magnetomechanical loading and the assumed fixed domain configuration a reduced set of constitutive equations is now derived². The constraint

²All of the reduced equations presented in this section are derived for the case of $\alpha = 1$. It is straightforward to derive their counterparts for $\alpha = 0$ by using the general expressions provided in Chapter IV.

(4.13b) on θ_3 , utilizing Eq. (4.11c), takes the form

$$\pi^{\theta_3} = (1 - \xi) [\mu_0 M^{\text{sat}} H_y - 2\rho K_1 \sin(\theta_3)] \cos(\theta_3) = 0. \quad (5.2)$$

From this it is concluded that

$$\sin(\theta_3) = \frac{\mu_0 M^{\text{sat}}}{2\rho K_1} H_y, \quad (5.3)$$

for $0 \leq \theta_3 < \frac{\pi}{2}$ and $0 \leq \xi < 1$. Since the easy axis of variant 2 is aligned with the direction of the applied field, its magnetization vector does not rotate, such that the corresponding constraint $\pi^{\theta_4} = 0$ is identically satisfied.

For the considered loading case, using Eqs. (4.10a), (4.10b) and (4.17), the driving force for variant rearrangement reduces to

$$\pi^\xi = \sigma_{xx} \varepsilon^{\text{r,max}} + \mu_0 M^{\text{sat}} [1 - \sin(\theta_3)] H_y + \rho K_1 \sin^2(\theta_3) - \frac{\partial f^\xi}{\partial \xi}, \quad (5.4)$$

where the difference in the elastic compliance of the variants ΔS has been considered small and thus neglected. If one further utilizes the relation (5.3) to eliminate θ_3 , Eq. (5.4) can be rewritten as

$$\pi^\xi = \sigma_{xx} \varepsilon^{\text{r,max}} + \mu_0 M^{\text{sat}} H_y - \frac{(\mu_0 M^{\text{sat}})^2}{4\rho K_1} H_y^2 - \frac{\partial f^\xi}{\partial \xi}, \quad (5.5)$$

The derivative $\frac{\partial f^\xi}{\partial \xi}$ has been specified in Chapter IV, Section C for different hardening models. The trigonometric hardening function (4.24) is employed here. For the assumed fixed magnetic domain structure, the driving force π^α need not be considered.

Combining the reorientation function (4.19) with the driving force expression (5.5) and enforcing the Kuhn-Tucker loading conditions (4.20), the evolution equations for the martensitic variant volume fraction are derived as follows:

For the *forward reorientation process* (Variant 1 \rightarrow Variant 2, $\dot{\xi} > 0$):

$$\Phi^\xi \dot{\xi} = 0 \quad \Rightarrow \quad \Phi^\xi = 0 \quad \Rightarrow \quad \pi^\xi = Y^{\xi,c}. \quad (5.6)$$

$$\begin{aligned} \pi^\xi &= \sigma_{xx} \varepsilon^{r,\max} + \mu_0 M^{\text{sat}} H_y - \frac{(\mu_0 M^{\text{sat}})^2}{4\rho K_1} H_y^2 + A^c [\pi - \cos^{-1}(2\xi - 1)] - B_1^c - B_2^c \\ &= Y^{\xi,c}. \end{aligned} \quad (5.7)$$

Since Eq. (5.7) contains only one scalar internal variable, the usual procedure of enforcing consistency conditions [71, 147, 149] is not necessary, and one can solve for ξ , which can be viewed as the equivalent of a plastic multiplier, directly in closed-form to find

$$\begin{aligned} \xi^{(1,2)} &= \frac{1}{2} \cos \left(-\frac{1}{A^c} \left[-\sigma_{xx} \varepsilon^{r,\max} - \mu_0 M^{\text{sat}} H_y + \frac{(\mu_0 M^{\text{sat}})^2}{4\rho K_1} H_y^2 + B_1^c + B_2^c \right. \right. \\ &\quad \left. \left. + Y^{\xi,c} \right] + \pi \right) + \frac{1}{2}. \end{aligned} \quad (5.8)$$

Similarly, it follows for the *reverse reorientation process* (Variant 2 \rightarrow Variant 1, $\dot{\xi} < 0$):

$$\Phi^\xi \dot{\xi} = 0 \quad \Rightarrow \quad \Phi^\xi = 0 \quad \Rightarrow \quad \pi^\xi = -Y^{\xi,c}. \quad (5.9)$$

$$\begin{aligned} \pi^\xi &= \sigma_{xx} \varepsilon^{r,\max} + \mu_0 M^{\text{sat}} H_y - \frac{(\mu_0 M^{\text{sat}})^2}{4\rho K_1} H_y^2 + C^c [\pi - \cos^{-1}(2\xi - 1)] - B_1^c + B_2^c \\ &= -Y^{\xi,c}, \end{aligned} \quad (5.10)$$

so that

$$\begin{aligned} \xi^{(2,1)} &= \frac{1}{2} \cos \left(-\frac{1}{C^c} \left[-\sigma_{xx} \varepsilon^{r,\max} - \mu_0 M^{\text{sat}} H_y + \frac{(\mu_0 M^{\text{sat}})^2}{4\rho K_1} H_y^2 + B_1^c - B_2^c \right. \right. \\ &\quad \left. \left. - Y^{\xi,\text{pl}} \right] + \pi \right) + \frac{1}{2}. \end{aligned} \quad (5.11)$$

From the integration of Eq. (4.15) and the kinematic assumptions of Eq. (5.1) the components of the reorientation strain follow as

$$\varepsilon_{xx}^r = \varepsilon^{r,\max}\xi ; \quad \varepsilon_{yy}^r = -\varepsilon_{xx}^r ; \quad \varepsilon_{zz}^r = \varepsilon_{xy}^r = \varepsilon_{xz}^r = \varepsilon_{yz}^r = 0 \quad (5.12)$$

The components of the magnetization vector, using Eqs. (4.4) and (5.3) in Eq. (4.9c), are found to be

$$\begin{aligned} M_x &= (1 - \xi)M^{\text{sat}} \cos(\theta_3) = (1 - \xi)M^{\text{sat}} \sqrt{1 - \left(\frac{\mu_0 M^{\text{sat}}}{2\rho K_1} H_y\right)^2} ; \\ M_y &= \xi M^{\text{sat}} + (1 - \xi)M^{\text{sat}} \sin(\theta_3) = \xi M^{\text{sat}} + (1 - \xi) \frac{\mu_0 (M^{\text{sat}})^2}{2\rho K_1} H_y ; \end{aligned} \quad (5.13)$$

$$M_z = 0 .$$

Again, the activation of the reorientation process and the evolution of ξ in Eqs. 5.12 and Eqs. 5.13 are governed by the reorientation function (4.19), subject to the reorientation conditions (4.20), and the evolution equations (5.8) and (5.11).

b. Calibration of the Model Parameters

The material parameters consist of the magnetocrystalline anisotropy constant ρK_1 , the saturation magnetization M^{sat} and the maximum reorientation strain $\varepsilon^{r,\max}$, which follow from standard experiments described in the literature [90, 98]. Additionally, the critical magnetic field values $H_y^{s(1,2)}$, $H_y^{f(1,2)}$, $H_y^{s(2,1)}$ and $H_y^{f(2,1)}$ must be specified, which denote the start and finish of the forward and reverse magnetic field-induced reorientation process, respectively. Fig. 16 shows how the critical magnetic fields and the maximum reorientation strain $\varepsilon^{\max}\xi^{\text{crit}}$ are estimated from one positive magnetic field-induced strain cycle at the calibration stress level, denoted σ_{xx}^* , which can be arbitrarily chosen in the range between zero and the blocking stress. The plotted

experimental data was published by Heczko et al. [44] for the $\text{Ni}_{50.7}\text{Mn}_{28.4}\text{Ga}_{20.9}$ composition. In general, first estimates of the critical fields can be obtained by drawing tangent lines to the hysteresis curves, as indicated in Fig. 16. The calibration can then be refined by adjusting these parameters such that the best simulation of the magnetic field-induced strain response is obtained at the calibration stress level. The value of $H_y^{f(2,1)}$ was determined such that the correct residual reorientation strain was obtained in the simulation.

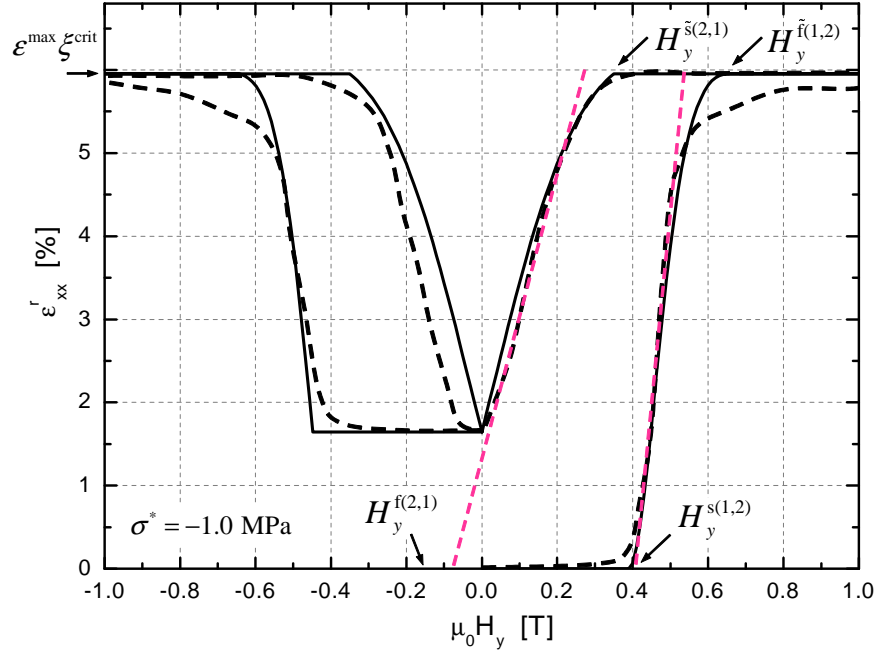


Fig. 16. Calibration of the model parameters using the experimental MFIS curve at -1.0 MPa. Solid line—model simulation, dashed line—experimental data [44].

The general relations between the material and the model parameters are listed in Table I. They have been derived by evaluating the evolution equations for the martensitic variant volume fraction in case of the forward Eq. (5.8) and reverse Eq. (5.11) reorientation process at $\xi = 0$ and $\xi = \xi^{\text{crit}}$, respectively, and enforcing continuity of

the hardening function at $\xi = 1$. ξ^{crit} is the maximum volume fraction of variant 2 obtained at the stress level σ^* , which can be estimated by relating the maximum reorientation strain for this stress level to the maximum achievable reorientation strain $\varepsilon^{\text{r,max}}$. The magnetic field $H_y(\xi^{\text{crit}})$ at which the forward reorientation strain is terminated prior to its completion is denoted $H_y^{\tilde{f}(1,2)}$ (see Eq. (5.16) for the computation of its magnitude). The magnetic field at which the reverse reorientation process is then activated for $\xi = \xi^{\text{crit}} < 1$ is denoted $H_y^{\tilde{s}(2,1)}$. For the case of complete reorientation ξ^{crit} is equal to 1, $H_y^{\tilde{f}(1,2)} = H_y^{f(1,2)}$ and $H_y^{\tilde{s}(2,1)} = H_y^{s(2,1)}$, such that the listed relations simplify.

Table I. Relations between material constants and model parameters.

$$\begin{aligned}
 A^c &= \frac{\mu_0 M^{\text{sat}}}{(\pi - \cos^{-1}(2\xi^{\text{crit}} - 1))} \left(H_y^{s(1,2)} - H_y^{\tilde{f}(1,2)} \right) - \frac{(\mu_0 M^{\text{sat}})^2}{4\pi\rho K_1} \left[\left(H_y^{s(1,2)} \right)^2 - \left(H_y^{\tilde{f}(1,2)} \right)^2 \right] \\
 B_1^c &= \frac{1}{2}\mu_0 M^{\text{sat}} \left(H_y^{s(1,2)} + H_y^{f(2,1)} \right) - \frac{(\mu_0 M^{\text{sat}})^2}{8\rho K_1} \left[\left(H_y^{s(1,2)} \right)^2 + \left(H_y^{f(2,1)} \right)^2 \right] + \sigma^* \varepsilon^{\text{r,max}} \\
 B_2^c &= \frac{\pi}{4} \left(A^c - C^c \right) \\
 C^c &= \frac{\mu_0 M^{\text{sat}}}{(\pi - \cos^{-1}(2\xi^{\text{crit}} - 1))} \left(H_y^{f(2,1)} - H_y^{\tilde{s}(2,1)} \right) - \frac{(\mu_0 M^{\text{sat}})^2}{4\pi\rho K_1} \left[\left(H_y^{f(2,1)} \right)^2 - \left(H_y^{\tilde{s}(2,1)} \right)^2 \right] \\
 Y^{\xi,c} &= \frac{1}{2}\mu_0 M^{\text{sat}} \left(H_y^{s(1,2)} - H_y^{f(2,1)} \right) - \frac{(\mu_0 M^{\text{sat}})^2}{8\rho K_1} \left[\left(H_y^{s(1,2)} \right)^2 - \left(H_y^{f(2,1)} \right)^2 \right] - B_2^c
 \end{aligned}$$

The parameter set listed Table II on the next page was calibrated by employing the described methodology and utilizing the relations of Table I.

It was observed in Fig. 16 that for this choice of parameters the model simulation at the calibration stress level agrees well with the experimental data. For model predictions at other stress levels the parameters are, of course, not adjusted, as this would then result in a pure curve-fitting exercise. The details of the model predictions

Table II. Material parameters for the considered $\text{Ni}_{50.7}\text{Mn}_{28.4}\text{Ga}_{20.9}$ composition [44], and the resulting hardening and hysteresis parameters calibrated at -1.0 MPa.

Material Parameters						Model Parameters		
Quantity	Value	Unit	Quantity	Value	Unit	Quantity	Value	Unit
ρK_1	167.0	kJm^{-3}	$\mu_0 H_y^{s(1,2)}$	0.39	T	A^c	-9.747	kPa
M^{sat}	514.0	kAm^{-1}	$\mu_0 H_y^{\tilde{r}(1,2)}$	0.65	T	B_1^c	-34.847	kPa
$\varepsilon^{\text{r,max}}$	6.2	%	$\mu_0 H_y^{\tilde{s}(2,1)}$	0.35	T	B_2^c	54.700	kPa
σ^*	-1.0	MPa	$\mu_0 H_y^{f(2,1)}$	-0.15	T	C^c	-79.394	kPa
ξ^{crit}	0.96					$Y^{\xi,c}$	58.451	kPa

will be discussed in the following sections.

Although the outlined procedure itself is straightforward, calibrating material parameters can be a tedious effort due to the complexity of the magnetomechanical response of MSMA and the fact that real materials never behave as ideally as the model assumes. The model calibration is especially cumbersome for MSMA because the demagnetization effect makes experimental measurements difficult to interpret [59]. Measured data has to be corrected to account for the specimen shape dependence. The accurate interpretation of experimental results based magnetostatic analysis for MSMA is discussed in Chapter VI. Advanced parameter optimization techniques, such as *constrained optimization methods* [5, 131], may be also employed to find more accurate sets of parameters.

c. The Reorientation Diagram

With a complete model at hand, a novel variant reorientation diagram is proposed as shown in Fig. 17. It is the graphical representation of the activation surfaces for variant reorientation. This diagram has been constructed based on the reduced constitutive equations presented in Section A.1.a of this chapter and the set of model parameters listed in Table II, specifically by evaluating the reorientation conditions Eq. (5.7) and Eq. (5.10) at $\xi=0$ and $\xi=1$, respectively.

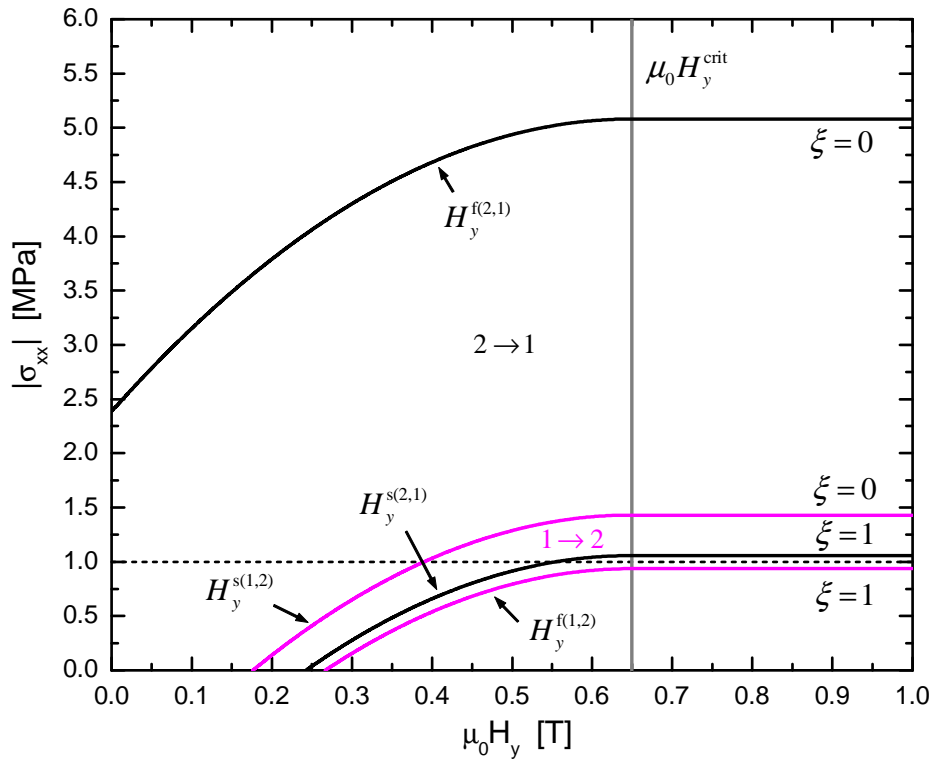


Fig. 17. Numerical $\mu_0 H_y - |\sigma_{xx}|$ variant reorientation diagram. The dashed line represents the magnetic loading path at the constant stress levels of -1.0 MPa.

Analogous visualizations of phase transformation surfaces in phase diagrams are common for conventional shape memory alloys [72, 150]. A reorientation diagram for

MSMA was previously proposed by Kiefer and Lagoudas [55] for an earlier version of the constitutive model, in which the magnetization was assumed to be fixed to the respective magnetic easy axes of the martensitic variants and a normalized martensitic volume fraction was used. Other activation diagrams have been proposed by [151] for variant reorientation and by [28] for martensitic phase transformation in MSMA.

In accordance with the reorientation function (4.19) and the Kuhn-Tucker loading conditions (4.20) the forward reorientation process ($\dot{\xi} > 0$) in the variant reorientation diagram is activated at the line $\xi^{(1,2)} = 0$ and completed at the line $\xi^{(1,2)} = 1$. The reverse process ($\dot{\xi} < 0$) is activated at the line $\xi^{(2,1)} = 1$ and terminates at the line $\xi^{(2,1)} = 0$. The activation of each process takes place only if the activation lines are crossed in the proper loading direction, as determined by the Kuhn-Tucker loading conditions, and the value of the variant volume fraction is such that reorientation can occur.

The slopes of the activation lines in the reorientation diagram can be calculated from Eqs. (5.7) or (5.10), respectively, and are given by the following *Clausius-Clapeyron* type relation

$$\frac{d\sigma_{xx}}{dH_y} = -\frac{1}{\varepsilon_{r,\max}} \left[\mu_0 M^{\text{sat}} - \frac{(\mu_0 M^{\text{sat}})^2}{2\rho K_1} H_y \right]. \quad (5.14)$$

A similar expression was derived by Kiefer and Lagoudas in [55] for the earlier model, which does not account for the rotation of the magnetization vectors. Tickle et al. [151], who also assumed that the magnetization vectors do not rotate, proposed the relation

$$\frac{d\sigma_{xx}}{dH_y} = -\frac{\mu_0 M^{\text{sat}}}{\varepsilon_{r,\max}}, \quad (5.15)$$

which has been translated into the notation used here. The two expressions (5.14) and (5.15) for the slope of the reorientation activation lines coincide at $H_y = 0$, i. e. the

intersection with the stress axis, since the magnetization vectors at this field level are aligned with the easy axes in both models.

As depicted in the reorientation diagram of Fig. 17, the loading path at the calibration stress level of $\sigma^* = -1.0$ MPa only intersects the reorientation activation lines $H_y^{s(1,2)}(\sigma_{xx})$ and $H_y^{s(2,1)}(\sigma_{xx})$. The corresponding critical values were specified in Table II on page 73. The line $H_y^{s(1,2)}(\sigma_{xx})$ is not crossed, such that only partial variant reorientation occurs at this stress level. In other words, the stress-independent critical value $\mu_0 H^{\text{crit}} = 0.65$ T, at which the magnetization in both variant has fully aligned with the applied field, is reached before the reorientation process is completed. This issue will be discussed in detail in the following section in the context of the interpretation of the model predictions. On the basis of the experimental data [44] it was assumed for the parameter calibration that only 96% of the second variant are produced during the forward reorientation process (cf. Table II). Likewise, variant 1 is not completely recovered at this stress level as the magnetic field is removed, since the line $H_y^{f(2,1)}(\sigma_{xx})$ is not intersected. It is important to note that for cases of incomplete reorientation ($0 < \xi < 1$), the appropriate activation lines lie within the regions bounded by the lines for $\xi = 0$ and $\xi = 1$ depicted in the reorientation diagram.

Several characteristic features can be concluded from the variant reorientation diagram for this particular set of parameters: i) the blocking stress is predicted to be -1.43 MPa. For higher stresses the forward reorientation activation line at $\xi = 0$ is not intersected; ii) only in the range of 0 to -0.94 MPa is the maximum strain obtained by complete variant reorientation. For higher stress levels the reorientation is only partial, since the forward reorientation termination line is not intersected; iii) For this set of parameters the model predicts that at least some of variant 1 is recovered at low stress levels, because the activation line for the reverse process is intersected as the field reduces to zero; iv) variant 1 can, in this case, not be fully recovered under any

constant stress level, since the appropriate stress level is above the blocking stress.

d. Model Predictions

The Magnetic Field-Induced Strain Response

Based on the activation lines specified in the variant reorientation diagram of Fig. 17, and the evolution of the variant volume fraction and the reorientation strain given by Eqs. (5.8), (5.11) and (5.12), respectively, magnetic field-induced reorientation strain curves have been computed for three different stress levels. Fig. 18 displays the results. To be able to easily compare the curves at different bias stresses the reorientation strain and not the total strain has been plotted in this figure.

The curve at -1.0 MPa is the simulation of the response used for the model calibration previously shown in Fig. 16 and it agrees well with the experimental data. The model is thus capable of capturing the nonlinear and hysteretic nature of the material response. The two other curves at -1.1 MPa and -1.2 MPa are model predictions, for which the same set of parameters listed in Table II was used.³

It is observed that the model also predicts the expected delay in the onset of the reorientation process from the stress-favored to the magnetic field-favored variant with an increase in the stress level. Furthermore, the model predicts the reduction of the obtainable reorientation strain for higher stress levels.

In an earlier version of the model [54, 55, 58], in which the rotation of the magnetization within each variant was ignored, this stress dependence of the maximum reorientation strain had to be provided as input. The magnetic field-induced strain

³Unfortunately experimental data was not available for comparison at these stress levels. Nonetheless, the Heczko et al. data was chosen for the validation of the model predictions because they also provide data for the corresponding magnetization response.

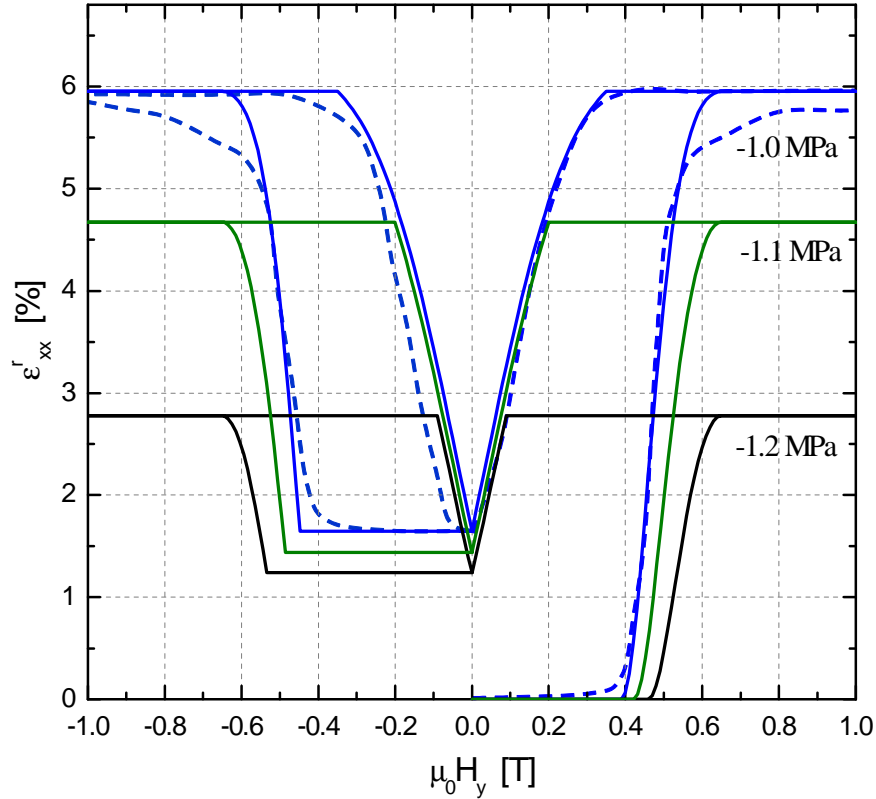


Fig. 18. Predicted MFIS hysteresis curves at different stress levels (solid lines) and comparison to experimental data (dashed line) [44].

curves for the earlier model are shown in Fig. 19, where the hysteresis loop under -5 MPa has been omitted to avoid overloading the figure. It can be seen that there is a good agreement between experimental data, which was previously shown in Fig. 6 and the model predictions. However, since the variant reorientation is the only mechanism for magnetization change that is accounted for, this more constrained model leads to magnetization curves that have the same shape as the reorientations strain curves, and thus poor representations of the magnetization response observed in experiments (cf. Fig. 11 on page 26). It will be demonstrated shortly that the current model, which accounts for the local rotation of magnetization vectors, leads to a much better representation of the magnetization behavior of MSMA. Nonetheless,

if mainly the field-induced strain response is of interest and a simpler easily implementable model is sought, the constrained model as presented in [54] works well.

Another characteristic feature of the MSMA response that is captured in the model predictions shown in Fig. 18 the *first cycle effect* discussed in Chapter II. Subsequent cycles are predicted to be symmetric, which is in agreement with experimental observations as seen in Fig. 19.

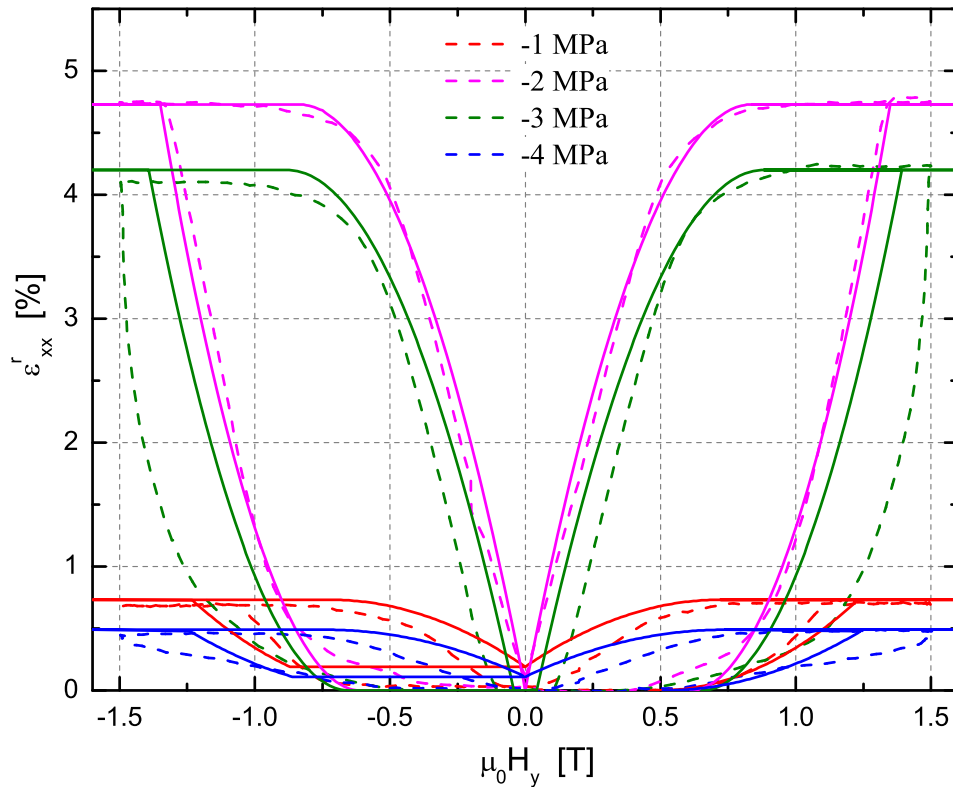


Fig. 19. Prediction of MSMA magnetic field-induced strain response in Kiefer et al. [58]. Experimental data (cf. Fig. 6)—dashed lines; numerical results—solid lines.

To explain the predicted evolution of the magnetic field-induced reorientation strain in more detail, Fig. 20 takes a closer look at the hysteresis loop under -1.0 MPa.

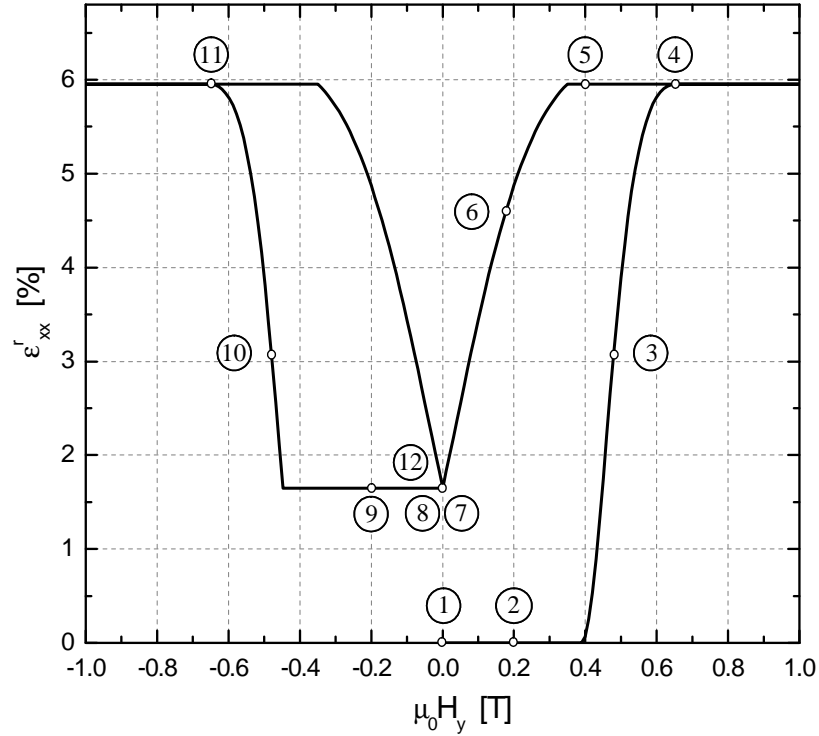









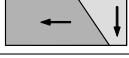




Fig. 20. Detail: MFIS hysteresis loop under -1.0 MPa.

Different characteristic configurations along the loading path have been numbered. For each of them Table III shows a schematic representation of the variant volume fraction and the magnetization rotation along with listing the corresponding values of the applied magnetic field, and the internal state variables, namely the reorientation strain, the variant volume fraction and the magnetization rotation angle. It should be emphasized that the schematics shown in Table III are only designed to illustrate the connection of the macroscopic behavior to the evolution of the internal state variables. They do not represent the actual distribution of the variants throughout a single crystal specimen.

Since it has been assumed that the error made by neglecting the magnetic domain wall motion at low magnetic fields is small, the single variant configuration 1 only

consists of a single magnetic domain. The magnetic field of 0.2 T in configuration 2 is not sufficient to initiate the rearrangement of variants against the mechanical stress and the internal resistance to twin boundary motion. This field causes the magnetization vector in variant 1 to rotate, by 17.9° , and thus changes the magnetization of the specimen, but does not produce any reorientation strain.

Table III. Configuration schematics and data for the strain hysteresis curve at -1.0 MPa.

#	Schematic	$\mu_0 H_y$	ε_{xx}^r	ξ	$\theta_3(\theta_1)$
1		0.0 T	0.0 %	0.0	0.0°
2		0.2 T	0.0 %	0.0	17.9°
3		0.48 T	3.1 %	0.5	47.6°
4		0.65 T	5.95 %	0.96	90.0°
5		0.4 T	5.95 %	0.96	38.0°
6		0.18 T	4.65 %	0.75	16.1°
7		0.0^+ T	1.65 %	0.27	0.0°
8		0.0^- T	1.65 %	0.27	0.0°
9		-0.2 T	1.65 %	0.27	17.9°
10		-0.5 T	3.1 %	0.5	47.6°
11		-0.65 T	5.95 %	0.96	90.0°
12		0.0^- T	1.65 %	0.27	0.0°

By increasing the magnetic field to the critical value, which is 0.39 T in this case (cf. Fig. 17 and Table II), the reorientation process is initiated and variant 2 nucleates. In configuration 3, at 0.48 T, the variant rearrangement has produced 50 % of variant 2, or 3.1% MFIS, while the magnetization has rotated by 47.6°. The stress of -1.0 MPa, which favors variant 1 and therefore counteracts the reorientation process, is higher than the resistance against 90° rotation of the magnetization in variant 1, as dictated by the magnetocrystalline anisotropy energy. The magnetization in variant 1 therefore aligns with the external field before the reorientation process is completed, as indicated in schematic 4. Only 96 % of variant 2 and therefore 5.95 % reorientation strain can be magnetically induced at this stress level. The physical justification for this effect is given by the consideration that when the magnetization in variant 1 has completely aligned with the magnetic field the Zeeman energy difference across the twin boundary vanishes and the driving force Eq. (5.5) does no longer depend on the magnetic field. Thus the reorientation process is terminated prematurely. This mechanism explains the reduction of the maximum magnetic field-induced with increasing stress levels in the presented modeling approach.

According to Eq. (5.3) the critical magnetic field at which the magnetization in variant 1 has fully rotated is in the limit of $\theta_3 \rightarrow \frac{\pi}{2}$ given by

$$\mu_0 H_y^{\text{crit}} = \frac{2\rho K_1}{M^{\text{sat}}} = 0.65 \text{ T} . \quad (5.16)$$

Note that the critical field is independent of the applied stress. The relative position of the critical field and the activation and termination fields for the forward reorientation process determine the amount of strain produced at each stress level. As previously observed from the variant reorientation diagram in Fig. 17, the magnetic field-induced strain ranges from 0 % at the blocking stress to its theoretical maximum of 6.2 % for stresses below $|\sigma_{xx}|=0.94 \text{ MPa}$.

When the magnetic field is subsequently decreased below H_y^{crit} , to 0.4 T in configuration 5, for example, the magnetization in variant 1 rotates back towards the magnetic easy axis but the MFIS stays constant. It must be emphasized that the activation field for the reverse reorientation process is not 0.55 T, as the variant reorientation diagram in Fig. 17 suggests for $\xi = 1$, but rather at 0.35 T, which is the appropriate activation field for $\xi = 0.96$. By further lowering the field variant 2 is reduced to 75 % at 0.18 T in configuration 6, while the magnetization rotation angle in variant 1 has decreased to 16.1° . However, for this stress level, not all of variant 1 is recovered, even at complete removal of the magnetic field, and a residual MFIS of 1.65 % remains in configuration 7. As evident from Fig. 18 as well as the variant reorientation diagram, higher compressive stresses help to recover a greater amount of variant 1. At zero field in configuration 7 the magnetization vectors in both variants are aligned with their respective easy axes. Since the effect of domain wall motion at low magnetic fields has been neglected, a remnant macroscopic magnetization is predicted by the model.

With the application of a negative magnetic field, the magnetization in both variants is assumed to instantaneously switch directions as indicated in schematics 7 and 8. In configuration 9 the ratio of variants remains unchanged, but the magnetization has rotated by 17.9° . Due to the mixture of variants, the activation of the reorientation process under a negative magnetic field is slightly delayed compared to the positive field hysteresis loop, and occurs at -0.45 T, which is the appropriate activation value for $\xi = 0.27$. After the activation of the reorientation process through the magnetic field in the negative y -direction, the evolution of the magnetic field-induced strain is symmetric to its positive counterpart described above in detail, and is consistent with the microstructure schematically shown in configurations 10 and 11. In terms of the residual strain, configuration 12 at the end of the negative loop

is identical to configurations 7 and 8 at the end of the positive and beginning of the negative loop, respectively. Unless a single variant configuration is purposely restored by temporarily raising the stress level, the reorientation strain that is obtainable in subsequent cycles is limited to 4.3 %, which is the difference in strain between the configurations 7 (or 8, 9, 12) and 4 (or 5, 11). The reduction of the obtainable MFIS is thus limited to the first cycle and hence the term first cycle effect. It should also be clear that if the negative magnetic field had been applied first, the resulting hysteresis loop had been the mirror image of the presented one.

The Magnetization Response

The strong coupling between the deformation and changes in the magnetization that are characteristic of MSMA constitutive response is made evident by considering the corresponding nonlinear magnetization hysteresis curves. The magnetic field-induced magnetization curves plotted in Fig. 21 have been computed using Eq. (5.13) in addition to the evolution equations for the variant volume fraction Eqs. (5.8) and (5.11). All of the depicted curves represent model predictions, since the model parameters were entirely calibrated using information from experimental strain curves.

The schematics of Table III again prove helpful to understand the connection between the evolution of the internal variables and the macroscopic material response, especially for the magnetization curve at -1.0 MPa.

At low magnetic fields, when the material is in its initial single variant state, the M_y -curve represents the magnetization of variant 1 along its magnetic hard axis, which occurs via magnetization rotation. The magnetization M_y , according to Eq. (5.13), is predicted to have a linear dependence on H_y in this region, since only the first term in the expansion of the anisotropy energy Eq. (3.1c) has been considered, which agrees

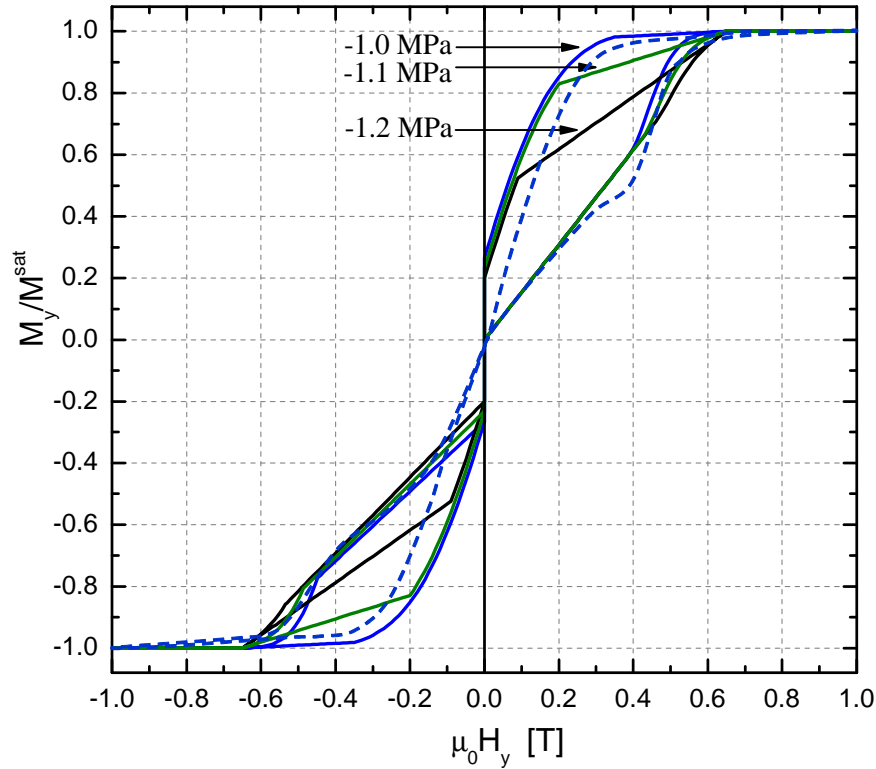


Fig. 21. Predicted magnetization hysteresis curves at different stress levels (solid lines) and comparison to experimental data [44] at -1.0 MPa (dashed line).

well with the experimental observations. From Eq. (5.13), a slope of 1.53 T^{-1} has been calculated, a result which is in excellent agreement with the experimental data (dashed line) measured by Heczko et al. [44]. According to Eq. (5.3), the magnetization rotation is independent of the applied stress and all curves coincide in this initial region. The abrupt deviation from linearity of the magnetization curves occurs when the stress-dependent critical magnetic field is reached and the variant rearrangement is initiated. The magnetization in this region changes via the mechanism of variant rearrangement as well as magnetization rotation. The influence of the variant 2 magnetization becomes more prominent as the reorientation process progresses. When the critical magnetic field for full magnetization rotation in variant 1 has been reached,

the reorientation process is terminated and the material is magnetized to saturation in the direction of the applied magnetic field.

Since the forward reorientation process is not completed for this stress level, the magnetization rotation in the residual variant 1 volume fraction is reduced when the magnetic field is subsequently decreased below H^{crit} , resulting again in a linear variation of the magnetization. The slope, however, is different from the one initially observed for variant 1 at low magnetic fields, since 96 % of the material still consist of variant 2, whose magnetization remains unaffected by the decrease of the magnetic field. Another abrupt nonlinear change in the magnetization occurs when the reverse reorientation process is activated. Due to the residual variant 2 volume fraction of 27 %, a remnant magnetization is predicted at zero applied field, even though the magnetization in variant 1 has rotated back to its reference configuration. The model also predicts a jump of the magnetization curve as the applied field switches sign. As discussed, this discontinuity is a direct consequence of neglecting the mechanism of domain wall motion. The prediction of magnetization curves in this region thus deviates from the experimental measurements. However, the importance of this difference has not been deemed sufficient to justify raising the level of complexity of the model by accounting for the complicated evolution of the magnetic domains. This is only necessary if the main goal is to predict the MSMA magnetization response at low magnetic fields. It is thus concluded that for actuator applications the assumption of a fixed magnetic domain structure yields sufficiently accurate predictions of the magnetic field-induced strain and magnetization response of MSMA. Model predictions which account for the magnetization change due to magnetic domain wall motion at very low stress levels and low magnetic fields are presented next.

2. Variable Magnetic Domain Structure

It was demonstrated in the previous section that the assumption of a fixed magnetic domain structure leads to reasonable predictions of the magnetization behavior for stress levels at which most of the initial variant is recovered. It is observed in experiments [4, 44, 51], however, that low compressive stresses can be insufficient to even partially restore the stress-favored variant 1. If no reverse reorientation occurs a residual strain of magnitude ε^{\max} remains at zero applied field and this mechanism can not contribute to changing the magnetization of the material. The remaining variant 2 has its easy axis aligned with the applied field such that also no local rotation of its magnetization occurs. The vanishing of the macroscopic magnetization as the applied field is removed, cf. Fig. 11, can at low stresses thus only be explained by magnetic domain wall motion. With the assumption of a fixed magnetic domain structure as used in the previous section the model would, however, predict a remnant magnetization of M^{sat} . At such low stress levels, the evolution of magnetic domains can therefore not be neglected. This mechanism is already incorporated in the general form of the constitutive model introduced in Chapter IV. Reduced model equations for the considered loading case with the possibility of magnetic domain wall motion shall now be derived.

a. Reduced Model Equations

Enforcing the constraint (4.13b) on θ_1 and utilizing Eq. (4.11a) leads to

$$\pi^{\theta_1} := -(1 - \xi)(1 - \alpha) [\mu_0 M^{\text{sat}} H_y + 2\rho K_1 \sin(\theta_1)] \cos(\theta_1) = 0 . \quad (5.17)$$

It follows that

$$\sin(\theta_1) = -\frac{\mu_0 M^{\text{sat}}}{2\rho K_1} H_y , \quad (5.18)$$

for $0 \leq \theta_1 < \frac{\pi}{2}$, $0 \leq \xi < 1$ and $0 \leq \alpha < 1$. The equivalent relation for θ_3 was derived as Eq. (5.3) in the previous section. Note that

$$\sin(\theta_1) = -\sin(\theta_3) . \quad (5.19)$$

The corresponding constraints on the remaining rotation angles, with Eqs. (4.11b) and (4.11d), are identically satisfied for $\theta_2 = \theta_4 = 0$.

The derivation of the expression for the driving force π^α and the associated evolution of magnetic domains is similar to that conducted in Appendix C in the context of predicting the magnetization of the constrained MSMA single crystal. For the considered loading conditions, the constraint (4.13a) on the driving force for magnetic domain wall motion, Eq. (4.10c), takes the form

$$\begin{aligned} \pi^\alpha = & (1 - \xi) \left[\mu_0 M^{\text{sat}} [\sin(\theta_1) + \sin(\theta_3)] H_y - \rho K_1 [\sin^2(\theta_1) - \sin^2(\theta_3)] \right] \\ & + 2\xi \mu_0 M^{\text{sat}} H_y - \frac{\partial f^\alpha}{\partial \alpha} = 0 . \end{aligned} \quad (5.20)$$

Again assuming a hardening behavior of the type $\frac{\partial f^\alpha}{\partial \alpha} = a\alpha + b$, and utilizing the relation (5.19), Eq. (5.20) can be written as

$$a\alpha + b = 2\xi \mu_0 M^{\text{sat}} H_y . \quad (5.21)$$

With the conditions $\alpha(H_y = 0) = 1/2$ and $\alpha(H_y = H^{\text{crit},\alpha}) = 1$ the evolution equation for the magnetic domain volume fraction is derived from Eq. (5.21) as

$$\alpha = \frac{\xi H_y + H^{\text{crit},\alpha}}{2H^{\text{crit},\alpha}} . \quad (5.22)$$

Recall that $H^{\text{crit},\alpha}$ has been defined to be the critical field at which magnetic saturation is achieved through domain wall motion.

The driving force for variant rearrangement, using Eqs. (4.10a), (4.10b) and

(4.17), takes the form

$$\pi^\xi = \sigma_{xx}\varepsilon^{r,\max} - \mu_0 M^{\text{sat}}(1 - 2\alpha)H_y - \frac{(\mu_0 M^{\text{sat}})^2}{4\rho K_1}H_y^2 - \frac{\partial f^\xi}{\partial \xi}. \quad (5.23)$$

Note that for $\alpha = 1$ Eq. (5.23) appropriately reduces to Eq. (5.5). For the forward reorientation process, with trigonometric hardening (cf. Eq. (4.24)) and substituting Eq. (5.22), it then follows

$$\begin{aligned} \pi^\xi &= \sigma_{xx}\varepsilon^{r,\max} + \frac{\mu_0 M^{\text{sat}}}{H^{\text{crit},\alpha}}\xi H_y - \frac{(\mu_0 M^{\text{sat}})^2}{4\rho K_1}H_y^2 + A^c[\pi - \cos^{-1}(2\xi - 1)] \\ &- B_1^c - B_2^c = Y^{\xi,c}. \end{aligned} \quad (5.24)$$

This equation describes the evolution of the variant volume fraction under the simultaneous rotation of the magnetization vectors and the motion of magnetic domain walls in both variants. Due to its transcendental nature it can not be solved for ξ in closed-form. If one assumes a quadratic polynomial hardening behavior of the form (4.21), rather than the trigonometric hardening assumed here, a closed-form solution for ξ can be found. However, the implementation of the model in which all three mechanism for magnetization change are simultaneously active has proven to be very difficult. Preliminary analysis with a quadratic polynomial suggests that a simple linear variation of the term $\frac{\partial f^\alpha}{\partial \alpha}$ leads to an unsatisfactory evolution of the magnetic-field induced strain in the reorientation region. The use of other hardening functions, which lead to an exponential evolution of the magnetic domain volume fraction may yield the desired result.

Here, the motion of magnetic domain walls will be considered only in magnetic field regimes in which no variant reorientation occurs. This assumption is very reasonable for those low stress levels at which no reverse reorientation is induced. Initially the magnetic domain volume fraction takes the value of $\alpha = 0.5$, which is consistent

with Eq. (5.24) when evaluated at $\xi=0$, and leads to a macroscopic magnetization of zero. For the forward reorientation process, which occurs at relatively high magnetic fields it is assumed as in the previous section that $\alpha=1$. Since the reverse reorientation process does not occur at the considered stress levels, no further assumptions on the evolution of the magnetic domain wall motion have to be made. The evolution of α is then properly described by Eq. (5.22).

The reorientation strain equations (5.12) are unaffected by the evolution of α , since only cases are considered for which it is reasonable to assume that the variant reorientation and magnetic domain wall motion do not occur simultaneously. The y -component of the magnetization, using Eqs. (4.4), (5.3) and (5.18) in Eq. (4.9c), is derived to be

$$M_y = \xi M^{\text{sat}}(2\alpha - 1) + (1 - \xi) \frac{\mu_0 (M^{\text{sat}})^2}{2\rho K_1} H_y . \quad (5.25)$$

The evolution of α for fixed ξ is given by Eq. (5.22). The evolution of ξ is coupled to the condition $\alpha = 1$ and is then described by Eq. (5.8). Alternatively, the same expression follows from solving Eq. (5.24) for ξ at $\alpha=1$.

b. Calibration of the Model Parameters

In principle the same set of parameters as that listed in Table II on page 73 could be used here. However, as can be deduced from the variant reorientation diagram of Fig. 17 on page 74, these parameters lead to the prediction of a partial recovery of variant 1 at the stress level of -0.2 MPa, which is inconsistent with the experimental strain data at this stress level [44]. In order to obtain a more accurate account of the magnetic field-induced strain response at low stress levels the alternative parameter set specified in Table IV is used, which was obtained from a calibration at -0.2 MPa.

Table IV. Material parameters for the $\text{Ni}_{50.7}\text{Mn}_{28.4}\text{Ga}_{20.9}$ composition [44], and the resulting hardening and hysteresis parameters when calibrated at -0.2MPa .

Material Parameters						Model Parameters		
Quantity	Value	Unit	Quantity	Value	Unit	Quantity	Value	Unit
ρK_1	167.0	kJm^{-3}	$\mu_0 H_y^{s(1,2)}$	0.22	T	A^c	-12.683	kPa
M^{sat}	514.0	kAm^{-1}	$\mu_0 H_y^{f(1,2)}$	0.36	T	B_1^c	-3.730	kPa
$\varepsilon^{\text{r,max}}$	6.2	%	$\mu_0 H_y^{s(2,1)}$	0.0	T	B_2^c	9.188	kPa
σ^*	-0.2	MPa	$\mu_0 H_y^{f(2,1)}$	-0.135	T	C^c	-24.382	kPa
ξ^{crit}	1.0		$\mu_0 H^{\text{crit},\alpha}$	0.22	T	$Y^{\xi,c}$	76.080	kPa

c. The Reorientation Diagram

The reorientation diagram in Fig. 22 was computed based on the set of parameters listed in Table IV that were determined from a calibration at -0.2MPa . This diagram is the equivalent of that shown in Fig. 17 for which the model parameters were found from the calibration at -1.0MPa . In principle one could of course have chosen to use just one calibration for all loading cases. However, the model calibration at -1.0MPa has proven to be fairly accurate in a relatively wide range of stresses, while the calibration at -0.2MPa leads to a more accurate prediction of the residual strain at very small stresses, which are considered in this section.

In the considered loading case the magnetic field is applied at a constant stress of -0.2MPa , as indicated by a dashed line in the reorientation diagram. Several characteristic points in this loading sequence have been labeled $A \rightarrow E$. Following the discussion from the beginning of this section, the magnetic domain wall motion is only considered at low stress levels and low magnetic fields, for which the reorientation

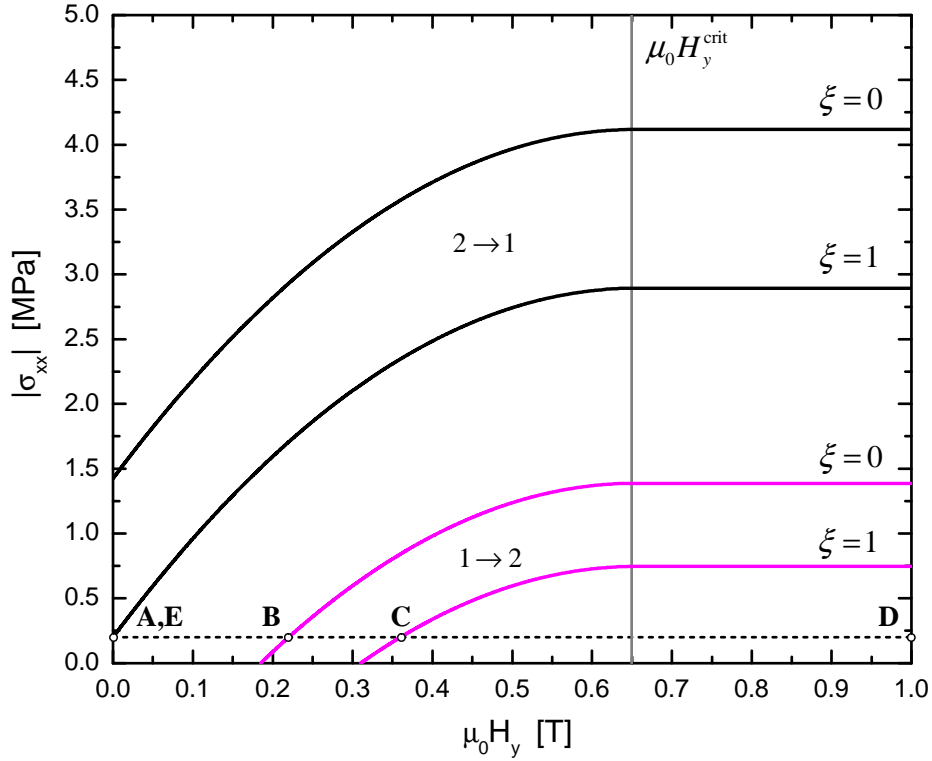


Fig. 22. Variant reorientation diagram for the parameters listed in Table IV. Loading path for model calibration A \rightarrow E.

process does not occur simultaneously.

d. Model Predictions

The magnetic field-induced reorientation strain response is computed by evaluating Eqs. (5.8) and (5.12) with the reorientation conditions given by Eq. (4.20) and utilizing the parameters set listed in Table V. The magnetization in the direction of the applied field follows from additionally evaluating the relations (5.8), (5.22) and (5.25). The results have been plotted in Figs. 23 and 24, respectively.

It is observed that the simulation of the magnetic field-induced strain evolution as well as the prediction of the magnetization response agree rather well with the ex-

perimental data. The connection between the macroscopic response and the evolution of the internal variables, which capture the main characteristic features of the crystallographic and magnetic microstructure, shall again be discussed in detail. Table V shows schematics for the sequence of numbered configurations defined in Fig. 24. These are analogous to the schematics presented in Table III, with the difference that in this case the motion of magnetic domain walls has not be neglected.

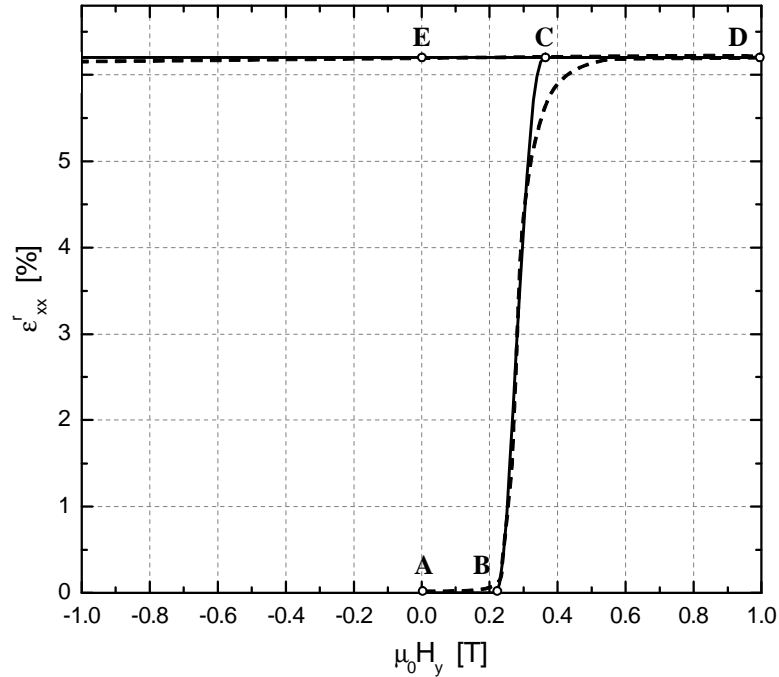


Fig. 23. Simulation of the magnetic field-induced strain response at -0.2 MPa. Solid line—model, dashed line—experiment [44].

In configuration 1 the magnetization vectors are arranged along the easy axis of variant 1 and both domain types are of equal volume fraction, such that the macroscopic magnetization is zero. As the magnetic field is applied perpendicularly to this easy axis in configuration 2, the equally unfavorably oriented magnetization vectors of both domains rotate towards the direction of the applied field. Upon

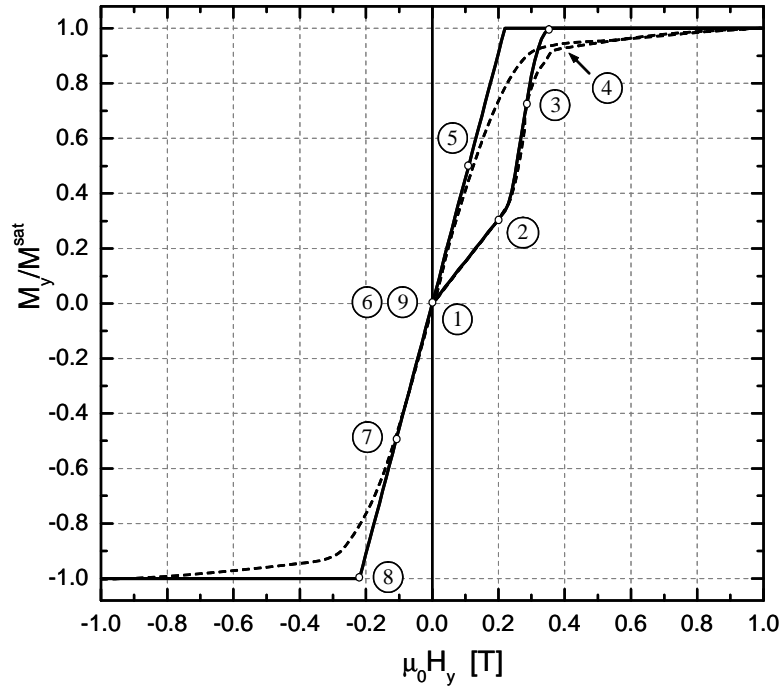

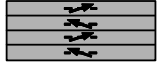



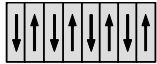
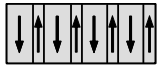
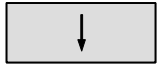
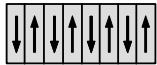


Fig. 24. Prediction of the magnetization response at -0.2 MPa when accounting for partial magnetic domain wall motion. Solid line—model, dashed line—experiment [44].

reaching the critical field of 0.22 T the forward reorientation process is initiated and unfavorable magnetic domains have been assumed to be eliminated instantaneously (see discussion in Chapter II, Section B). Configuration 3 is therefore predicted to consist of a mixed variant arrangement, but only magnetic domain 2.

The critical field value of 0.36 T has been reached in configuration 4, and the forward reorientation process is completed. This results in the depicted single variant, single domain configuration. When the magnetic field is subsequently lowered below the critical value of $\mu_0 H^{\text{crit},\alpha} = 0.22$ T, to 0.11 T in configuration 5 for example, magnetic domain wall motion sets in and the macroscopic magnetization is reduced, even though variant reorientation does not occur. At zero field in configuration 6 the overall magnetization is again zero, but this time because the magnetization

Table V. Configuration schematics and data for the strain hysteresis curve at -0.2MPa with partial magnetic domain wall motion.

#	Schematic	$\mu_0 H_y$	ε_{xx}^r	ξ	θ_1, θ_3	α
1		0.0 T	0.0 %	0.0	$0.0^\circ, 0.0^\circ$	0.5
2		0.2 T	0.0 %	0.0	$-17.9^\circ, 17.9^\circ$	0.5
3		0.284 T	3.1 %	0.5	$—, 25.9^\circ$	1.0
4		0.36 T	6.2 %	1.0	—	1.0
5		0.11 T	6.2 %	1.0	—	0.75
6		0.0 T	6.2 %	1.0	—	0.5
7		-0.11 T	6.2 %	1.0	—	0.25
8		-0.22 T	6.2 %	1.0	—	0.0
9		0.0 T	6.2 %	1.0	—	0.5

vectors in both domains are oriented along the easy axis of variant 2, with opposing orientations. As a negative magnetic field is applied no variant reorientation occurs, since the material already consists entirely of the magnetic field-favored variant 2. The magnetic domain wall motion such as depicted in configuration 7, however, leads to magnetic saturation in configuration 8, at which point the critical value of $-H^{\text{crit},\alpha}$ has been reached. When the magnetic field is removed configuration 9 is obtained, which is identical to configuration 6. Thus the macroscopic magnetization again vanishes, while the field-induced strain remains.

It has thereby been demonstrated that allowing for magnetic domain wall motion significantly improves the accuracy of the magnetization predictions at low stresses.

B. Loading Case 2: Variable Compressive Uniaxial Stress at Different Levels of a Perpendicular Magnetic Field

The second loading case of practical interest is the reorientation of martensitic variants under mechanical loads at constant magnetic field. Such loading occurs, for example, when the compressive stress level is raised to restore the initial single variant 1 configuration between each magnetic cycle of the experiments modeled in the previous section (cf. Fig. 18 on page 78). It is demonstrated in this section that the model, *without* adjustment of the model parameters, is capable of also predicting the reorientation strain and magnetization response caused by the stress-induced reorientation of variants at different magnetic field levels.

Different loading paths for which the response will be predicted are indicated by dashed lines in the variant reorientation diagram shown in Fig. 25. This reorientation diagram is equivalent to the one shown in Fig. 17 on page 74, and is based on the parameters calibrated at -0.2 MPa (cf. Table IV on page 91), instead of -1.0 MPa. This set of parameters was chosen here because it is again important to accurately predict the residual strain at low stress levels. The model predictions in this case are based on parameters which were determined from magnetic field-induced strain curves under constant magnetic field. No experimental data from the response under mechanical loading at constant magnetic field was used in the calibration of the model. This emphasizes the fact that this modeling approach is not merely a curve-fitting exercise.

As depicted in the variant reorientation diagram, the sequence of loading is such

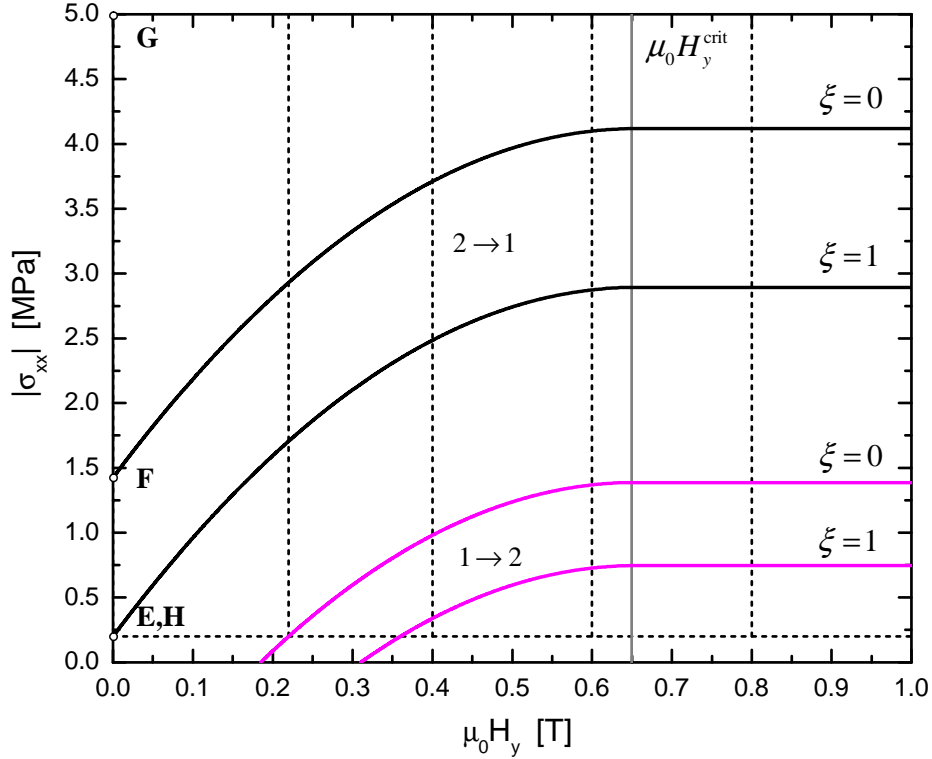


Fig. 25. Loading paths in the $\mu_0 H_y$ - $|\sigma_{xx}|$ variant reorientation diagram. Exemplary loading path E \rightarrow H.

that initially the magnetic field is raised as before to 1 T under the constant stress of -0.2 MPa and then lowered to the magnetic field H_y^{exp} , which in the different cases takes the values of 0.0, 0.2, 0.4, 0.6 or 0.8 T. This initial magnetic field loop at constant stress serves the purpose of establishing a well defined starting configuration for the mechanical loading sequence. At the respective field levels the compressive stress is increased to -5.0 MPa, and then lowered back to -0.2 MPa. Finally the magnetic field is removed under constant stress. A typical loading path at $\mu_0 H_y^{\text{exp}} = 0$ T has been labeled with the letters E \rightarrow H to clarify the sequence of loading.

Since the same components of the stress and magnetic field as in loading case 1 are

applied here, even though the stress is now variable and the magnetic field constant, the same set of reduced model equations apply. Partial magnetic domain wall motion will again be taken into account at magnetic fields below $H^{\text{crit},\alpha}$. The magnetic field- and stress-induced MSMA response is thus described by Eqs. (5.8), (5.11) and (5.12), with the reorientation conditions given by Eq. (4.20). Special attention must be paid to the response to mechanical loading at magnetic field levels below $H^{\text{crit},\alpha}$ because magnetic domain wall motion does occur at these field levels. At $\mu_0 H_y = 0$ T, the magnetic domain volume fraction α takes the value of 0.5 according to Eq. (5.22). The driving force for reorientation π^ξ , however, as specified by Eqs. (4.10a), (4.10b) and (4.17), is independent of α at $\mu_0 H_y = 0$ T, such that

$$\pi^\xi = \sigma_{xx} \varepsilon^{\text{r,max}} - \frac{\partial f^\xi}{\partial \xi}. \quad (5.26)$$

The stress-induced evolution of ξ at 0 T can thus still be described by Eq. (5.11), which was derived for $\alpha = 1$.

The predicted stress-induced reorientation strain response at different magnetic field levels is shown in Fig. 26 along with the initial magnetic field cycle at -0.2 MPa (dashed line), which has previously been shown in Fig. 23. The labels A→E refer to the initial magnetic loading paths at the constant stress level of -0.2 MPa for which the response was previously shown in Figs. 23 and 24. The labels E→H refer to the subsequent stress loading cycle at the exemplary constant magnetic field level of 0 T. In Figs. 22 and 25 both parts of this three-dimensional loading paths were also indicated in the reorientation diagram. It is always very instructional to draw the connection between the loading paths in the reorientation diagram and the predicted response. An interesting feature of this three-dimensional plot is that it contains some of the types of plots shown earlier. For instance, the projection of all curves onto the back wall, plane $\sigma_{xx} = 0$, produces a two-dimensional strain-magnetic field plot such as

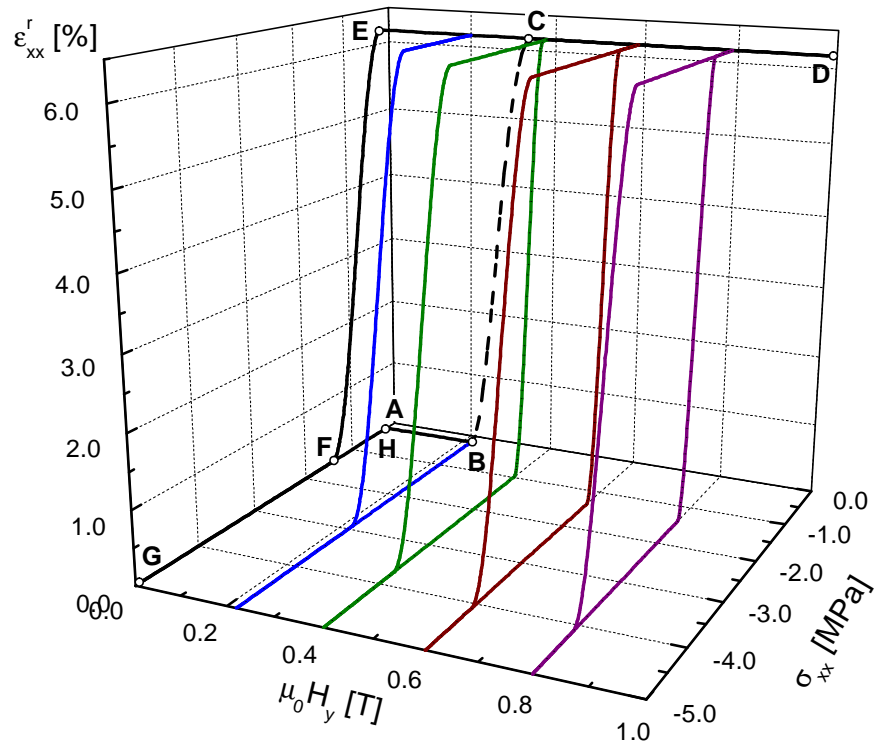


Fig. 26. Stress-induced reorientation strain vs. stress and magnetic field. Initial constant stress loop at -0.2 MPa.

the one depicted in Fig. 18, with the addition of vertical lines for the stress-induced hysteresis loops. If one projects the start and finish points for the reorientation process onto the bottom plane $\varepsilon_{xx}^r = 0$ and connects them with lines, one obtains the variant reorientation diagram of Fig. 25. The projection of the strain curves onto the side wall, plane $\mu_0 H_y = 0$, produces a two-dimensional strain-stress plot, in which the response curves are parameterized by the value of the constant field $\mu_0 H_y$. The result of such a projection is shown in Fig. 27, where for convenience, however, the induced reorientation strain has been plotted as a function of the absolute value of the stress.

Two aspects of the predicted response deserve to be emphasized. First, it is observed that the reorientation process is always completed under mechanical loading,

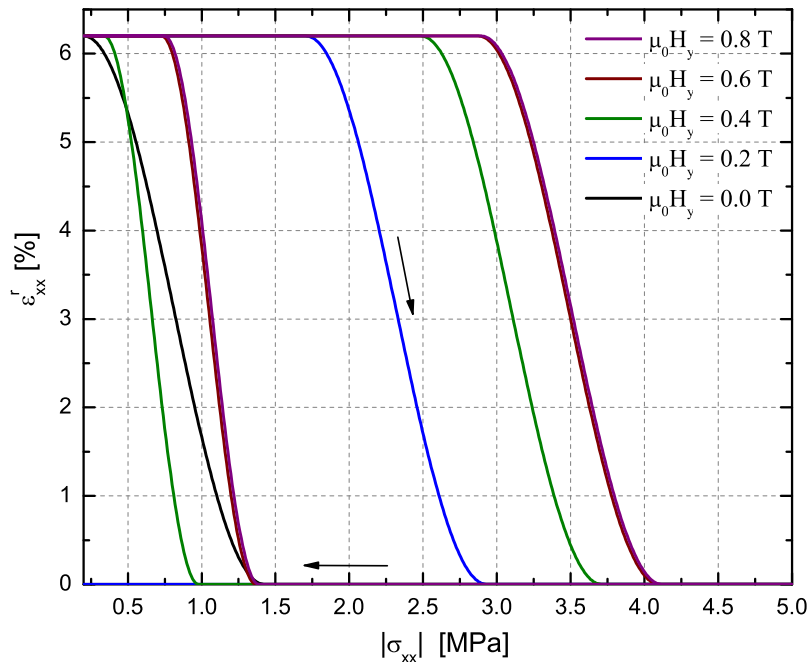


Fig. 27. Stress-induced reorientation strain vs. stress at different levels of $\mu_0 H_y$.

which results in the full recovery of the inelastic strain by stress increase at all magnetic field levels. This is explained by the fact that the magnetic part of the driving force for reorientation in Eq. (5.5) vanishes at full alignment of the magnetization with the applied field, the mechanical part of the driving force does not. This aspect will be explained in more detail shortly.

Secondly, these cases illustrate the loading history dependence of the constitutive response which the model is able to capture by accounting for the evolution of the microstructure through internal state variables. The sequence of loading significantly influence the response and determines the value of the residual strain. At 0.22 T, for example, the reorientation strain is fully recovered under stress application and no residual strain is observed after unloading. If, however, the stress is raised at the magnetic field level of 0.4 T, a residual strain of 6.2 % associated with the magnetic

field-favored variant remains after unloading, although the reorientation strain was temporarily recovered. The material response therefore depends not only on the current values of the independent state variables stress and magnetic field, but also on the loading history, which is reflected in the values of the internal state variables.

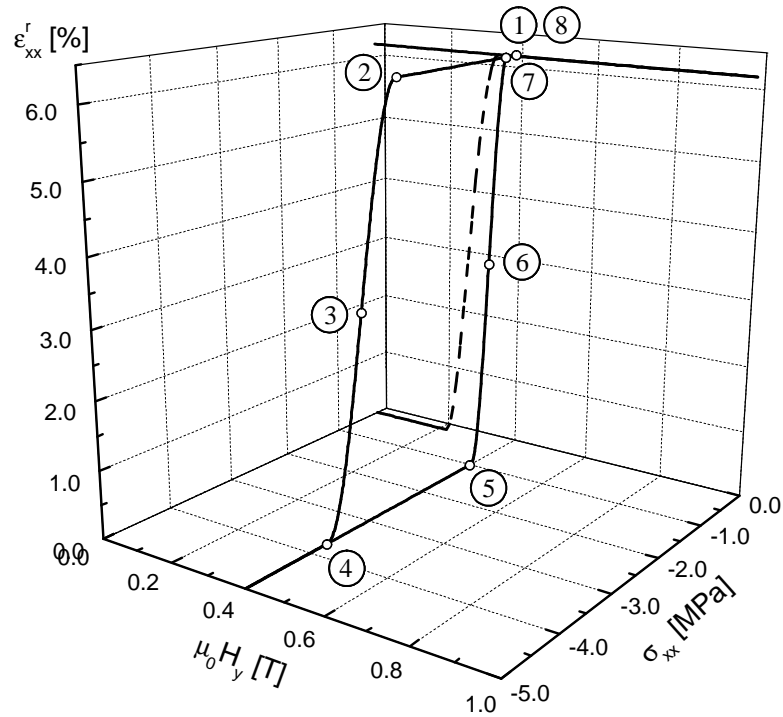




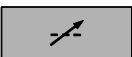





Fig. 28. Detail: Stress-induced reorientation strain hysteresis loop at 0.4 T.

Fig. 28 takes a closer look at the stress-induced reorientation strain response at the exemplary magnetic field level of 0.4 T. The configurational schematics of Table VI again illustrate the connection between the evolution of the internal state variables and the observed macroscopic response. Due to the prior magnetic loading, the material in configuration 1 consists entirely of the second magnetic field-favored variant. Raising the compressive stress level initiates the reverse variant reorientation process at the stress corresponding to configuration 2. At -3.1 MPa in configuration

3 half of variant 1 has been recovered. The process is completed in configuration 4. At the elevated magnetic field level of 0.4 T, however, this stress-induced variant can not be sustained, and the forward reorientation process is again initiated and completed in configurations 5–7, as the stress is subsequently lowered. Configuration 8 at the end of the mechanical loading cycle is identical to configuration 1. Similar explanations of the response apply to all other loading paths.

Table VI. Configuration schematics and data for the strain hysteresis curve under variable σ_{xx} and $\mu_0 H_y = 0.4$ T.

#	Schematic	σ_{xx}	ε_{xx}^r	ξ	θ_3
1		−0.20 MPa	6.2 %	1.0	—
2		−2.49 MPa	6.2 %	1.0	—
3		−3.10 MPa	3.1 %	0.5	38°
4		−3.71 MPa	0.0 %	0.0	38°
5		−0.98 MPa	0.0 %	0.0	38°
6		−0.66 MPa	3.1 %	0.5	38°
7		−0.34 MPa	6.2 %	1.0	—
8		−0.20 MPa	6.2 %	1.0	—

The corresponding stress-induced magnetization curves are shown in Fig. 29. Again, to promote an easier interpretation, the projection of these curves onto the plane $H_y = 0$ is plotted in Fig. 30. These curves have been computed from relations

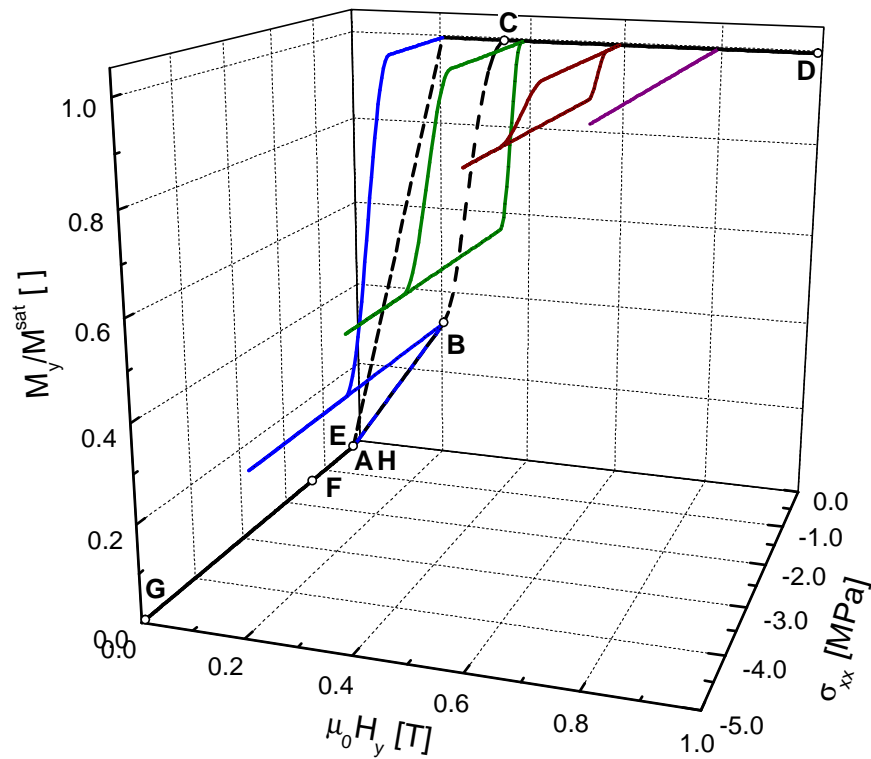


Fig. 29. Normalized magnetization vs. stress and magnetic field. Initial constant stress loop at -0.2 MPa.

(5.8), (5.22) and (5.25). The response to the initial magnetic field cycle at -0.2 MPa, which has previously been shown in Fig. 24, is again depicted as a dashed line. A careful comparison of the results reveals that these magnetic field-induced magnetization hysteresis curves exhibit a different behavior than that predicted in Fig. 21 for loading case 1. The explanation is given by the fact that since the stress is applied at constant magnetic field, the mechanism of magnetization rotation is not activated. As depicted in Schematics 3–6 of Table VI, the magnetization vector in variant 1 remains constant at the rotation angle appropriate for the magnetic field level and the magnetization vector of variant 2 is fixed to its magnetic easy axis.

At magnetic field levels above $\mu_0 H^{\text{crit},\alpha} = 0.22$ T, where magnetic domain wall

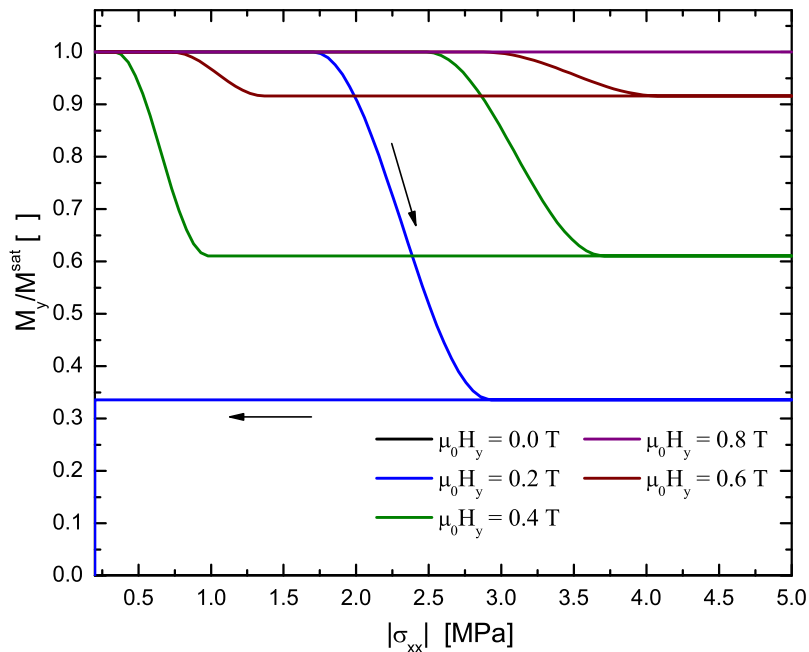


Fig. 30. Normalized magnetization vs. stress at different levels of $\mu_0 H_y$.

motion can be neglected, the only mechanism that leads to changes in the magnetization under mechanical loading at constant magnetic field, is the stress-induced reorientation of variants. In loading case 1 the mechanism of magnetization rotation was also active during variant reorientation. For case 1 it was predicted, in agreement with experimental observations, that the reorientation strain is only partially induced in some cases, and that the magnetization changes from zero to the saturation value M^{sat} at all stress levels. In loading case 2 just the opposite effect is observed. Under mechanical loading the maximum reorientation strain is induced at all magnetic levels, whereas only partial changes of the magnetization occur. The macroscopic magnetization does not reduce to zero at the magnetic field levels of 0.22 T, 0.4 T, 0.6 T and 0.8 T, even if the material at elevated compressive stresses entirely consist of variant 1, because the magnetization vector of this variant remains at a constant rotation angle and thus always has a non-zero y-component. At 0.8 T, which is above

H^{crit} , the magnetization in both variants is fully aligned with the constant applied field and no change in the magnetization is observed, even though it is clear from the strain response shown in Fig. 26 that variant reorientation occurs. Likewise, no change in the magnetization is observed at 0 T, but the reason in this case is that in the absence of an external field the arrangement of magnetic domains again is such that the overall magnetization is zero.

The constitutive model has therefore successfully been employed to capture the response of MSMA as caused by the stress-induced reorientation of martensitic variants. In the following loading case, it will be demonstrated that a magnetic field collinear with the applied stress can also be used to recover the residual reorientation strain, but that during this process one more internal mechanism for magnetization change is activated which further raises the complexity of the predicted response.

C. Loading Case 3: Variable Magnetic Field Collinear to a Constant Compressive Uniaxial Stress at Different Levels of a Perpendicular Magnetic Field

Since variant 1 is not only favored by the compressive stress σ_{xx} , but also by a magnetic field in that same direction, due to the fact that it corresponds to the easy axis of variant 1, such a field can similarly be used to recover the residual reorientation strain at the end of a magnetic loading cycle. The MSMA response under such loading is modeled in this section.

This leads to the simplifying assumptions that $\sigma_{xx} = \text{const.} \leq 0$ is the only non-zero component of the stress and H_x and H_y are the non-zero components of the magnetic field, where H_x is variable and H_y is constant. Since the effect of magnetic domain wall motion under two components of the magnetic field is extremely difficult to analyze, such loading will in this section only be considered at magnetic field

levels for which it is save to assume that unfavorable domains have been eliminated such that $\alpha = 1$. The purpose of this analysis is to show that modeling the MSMA response to the additional application of a magnetic field which is collinear to the applied stress significantly increases the complexity of the governing equations and leads to a magnetomechanical response that is different in nature than the response observed in loading cases 1 and 2. This analysis shall not be further complicated by accounting for the evolution of magnetic domains, which is only of interest at low fields.

The reduced form of the driving force for variant rearrangement is then derived, under the specified assumptions, from the definition (4.17) by using Eqs. (4.10a) and (4.10b), which yields

$$\begin{aligned} \pi^\xi &:= \sigma_{xx} \varepsilon^{r,\max} - \rho \frac{\partial \hat{g}}{\partial \xi} \\ &= \sigma_{xx} \varepsilon^{r,\max} + \mu_0 M^{\text{sat}} \left[- [\cos(\theta_3) + \sin(\theta_4)] H_x - [\sin(\theta_3) - \cos(\theta_4)] H_y \right] \\ &\quad + \rho K_1 [\sin^2(\theta_3) - \sin^2(\theta_4)] - \frac{\partial f^\xi}{\partial \xi}. \end{aligned} \quad (5.27)$$

The following additional constraints are derived from Eqs. (4.11c), (4.11d) and (4.13b)

$$\pi^{\theta_3} := -\rho \frac{\partial \hat{g}}{\partial \theta_3} = 0 \quad \Rightarrow \quad \mu_0 M^{\text{sat}} [H_y - H_x \tan(\theta_3)] - 2\rho K_1 \sin(\theta_3) = 0, \quad (5.28)$$

for $0 \leq \xi < 1$, $0 \leq \theta_3 < \frac{\pi}{2}$ and

$$\pi^{\theta_4} := -\rho \frac{\partial \hat{g}}{\partial \theta_4} = 0 \quad \Rightarrow \quad \mu_0 M^{\text{sat}} [H_x + H_y \tan(\theta_4)] + 2\rho K_1 \sin(\theta_4) = 0, \quad (5.29)$$

for $0 < \xi \leq 1$, $0 \leq \theta_4 < \frac{\pi}{2}$. An explicit closed-form solution of the transcendental equations Eqs. (5.28) and (5.29) for the rotation angles θ_3 and θ_4 can not be found, except for the special case of $H_y = 0$, so that numerical solutions have to be obtained.

Following the same procedure used in Sections A and B of this chapter for the

loading cases 1 and 2, the evolution of the variant volume fraction for the forward reorientation process (V1 \rightarrow V2) is derived from Eq. (5.27) and the reorientation conditions (4.20), using Eq. (4.24), as

$$\Phi^\xi \dot{\xi} = 0 \quad \Rightarrow \quad \Phi^\xi = 0 \quad \Rightarrow \quad \pi^\xi = Y^{\xi,c} .$$

$$\begin{aligned} \xi^{(1,2)} = \frac{1}{2} \cos \left(\frac{1}{A^c} \left[\sigma_{xx} \varepsilon^{r,\max} + \mu_0 M^{\text{sat}} \left(- [\cos(\theta_3) + \sin(\theta_4)] H_x - [\sin(\theta_3) - \cos(\theta_4)] H_y \right) \right. \right. \\ \left. \left. + \rho K_1 \sin^2(\theta_3) - \rho K_1 \sin^2(\theta_4) - B_1^c - B_2^c - Y^{\xi,c} \right] + \pi \right) + \frac{1}{2} . \end{aligned} \quad (5.30)$$

And for the reverse reorientation process (V2 \rightarrow V1)

$$\Phi^\xi \dot{\xi} = 0 \quad \Rightarrow \quad \Phi^\xi = 0 \quad \Rightarrow \quad \pi^\xi = -Y^{\xi,c} .$$

$$\begin{aligned} \xi^{(2,1)} = \frac{1}{2} \cos \left(\frac{1}{C^c} \left[\sigma_{xx} \varepsilon^{r,\max} + \mu_0 M^{\text{sat}} \left(- [\cos(\theta_3) + \sin(\theta_4)] H_x - [\sin(\theta_3) - \cos(\theta_4)] H_y \right) \right. \right. \\ \left. \left. + \rho K_1 \sin^2(\theta_3) - \rho K_1 \sin^2(\theta_4) - B_1^c + B_2^c + Y^{\xi,c} \right] + \pi \right) + \frac{1}{2} . \end{aligned} \quad (5.31)$$

The reorientation strain is still of the form Eq. (5.12). The components of the magnetization, using Eqs. (4.4) and (4.9c), are in this case give by

$$\begin{aligned} M_x &= (1 - \xi) M^{\text{sat}} \cos(\theta_3) - \xi M^{\text{sat}} \sin(\theta_4) ; \\ M_y &= (1 - \xi) M^{\text{sat}} \sin(\theta_3) + \xi M^{\text{sat}} \cos(\theta_4) ; \\ M_z &= 0 . \end{aligned} \quad (5.32)$$

The evolution of ξ in the above equations is governed by Eqs. (5.30) and (5.31) and is subject to the reorientation conditions Eq. (4.20). In this case the magnetization rotation angles can not be eliminated in closed-form. In the example presented below

a point wise numerical solution was obtained by enforcing the constraints (5.28) and (5.29), respectively, while solving for ξ and then evaluating ε^r and \mathbf{M} .

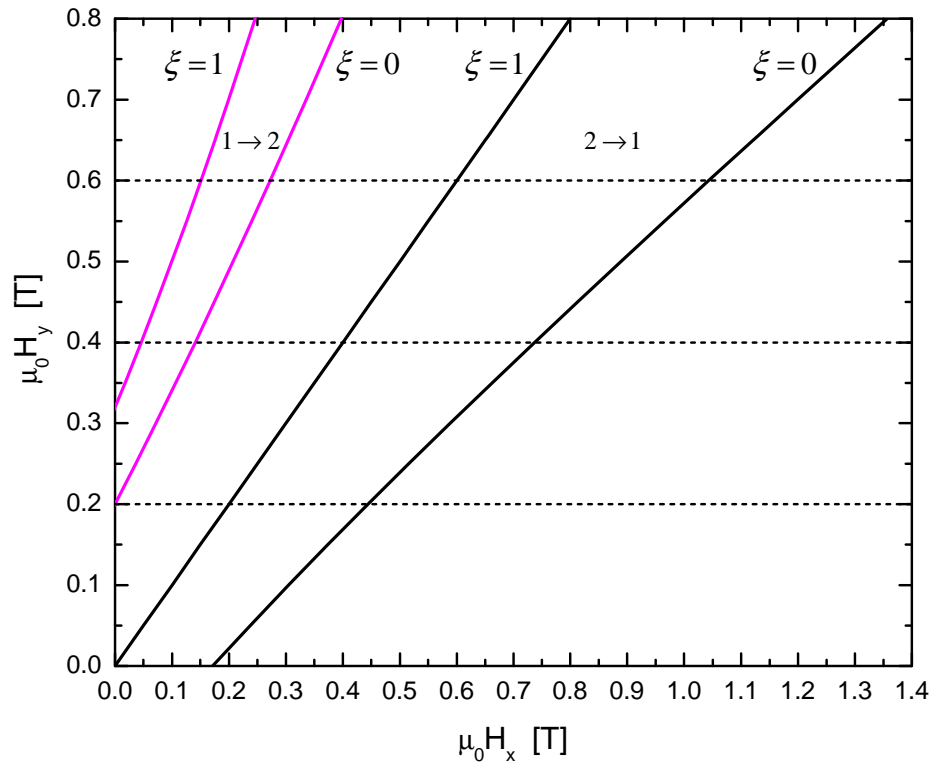


Fig. 31. Loading paths in the $\mu_0 H_x$ - $\mu_0 H_y$ variant reorientation diagram at -0.2 MPa.

The reorientation diagram in $\mu_0 H_x$ - $\mu_0 H_y$ space, shown in Fig. 31, was plotted based on these equations. This particular diagram represents a different cross-section of the same multi-dimensional reorientation diagram for which a cross-section at $H_x = 0$ in $\mu_0 H_x$ - $|\sigma_{xx}|$ -space was previously presented in Figs. 17 and 25. Dashed line indicate the loading at constant values of $\mu_0 H_y$. The diagram is again based on the same set of material parameters of Table IV on page 91 that were obtained from a MFIS hysteresis loop at -0.2 MPa. Alternatively, the model parameters could have been calibrated from the reduced set of equations presented in this section. Ideally this would result in the same set of parameters. Similarly the parameters in con-

ventional SMAs found in an isobaric test should be the same as those found in an equivalent isothermal test [72], but they are usually slightly different.

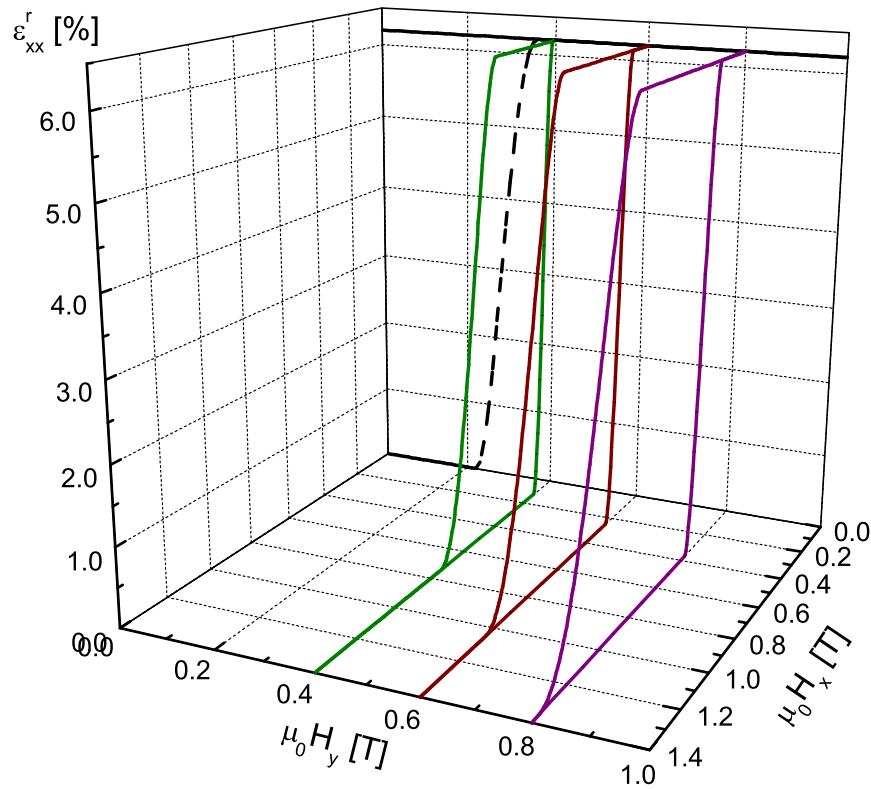


Fig. 32. Magnetic field-induced reorientation strain vs. two components of the magnetic field at a constant stress of -0.2 MPa.

The sequence of loading in this case is similar to that of loading case 1. Initially the magnetic field component H_y is applied at constant stress and $H_x = 0$, raised to 1 T and then lowered to 0.4 T, 0.6 T or 0.8 T, respectively. This again establishes a well-defined initial configuration for subsequent loading. Instead of raising the stress level the magnetic field component H_x is applied in this case, while the stress and the components H_y are kept constant. Fig. 32 depicts the predicted reorientation strain response. The projection of these curves is shown in Fig. 33.

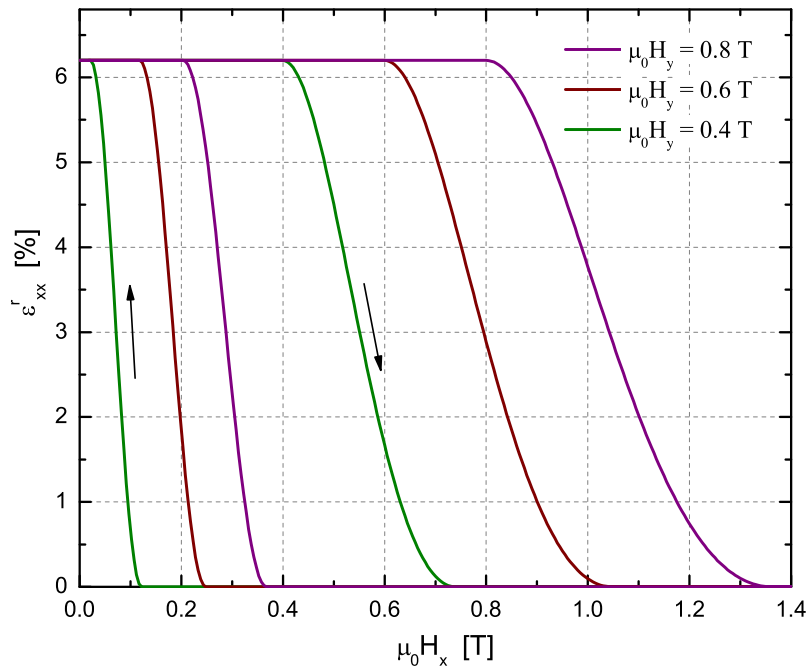


Fig. 33. Magnetic field-induced reorientation strain vs. the x-component of the magnetic field at different levels of $\mu_0 H_y$ and $\sigma_{xx} = -0.2$ MPa.

A close inspection of these curves reveals that the nature of the reorientation strain evolution is different than that of the response previously observed. This is due to the fact that an additional mechanism is activated, namely the rotation of the magnetization vector in variant 2. In the prior loading cases 1 and 2 such a rotation did not occur, since the magnetic field was applied along the easy axis of variant 2. Fig. 34 is analogous to Fig. 28 and takes a closer look at the collinear magnetic field-induced reorientation strain evolution at $H_y = 0.4$ T. Table VII contains the corresponding schematics that have again been created for a few interesting configurations along the loading path. It also lists the internal state variable data.

Configuration 1 in Table VII is identical to that of Table VI on page 102. The application of the H_x field results in a rotation of the magnetization vector in variant

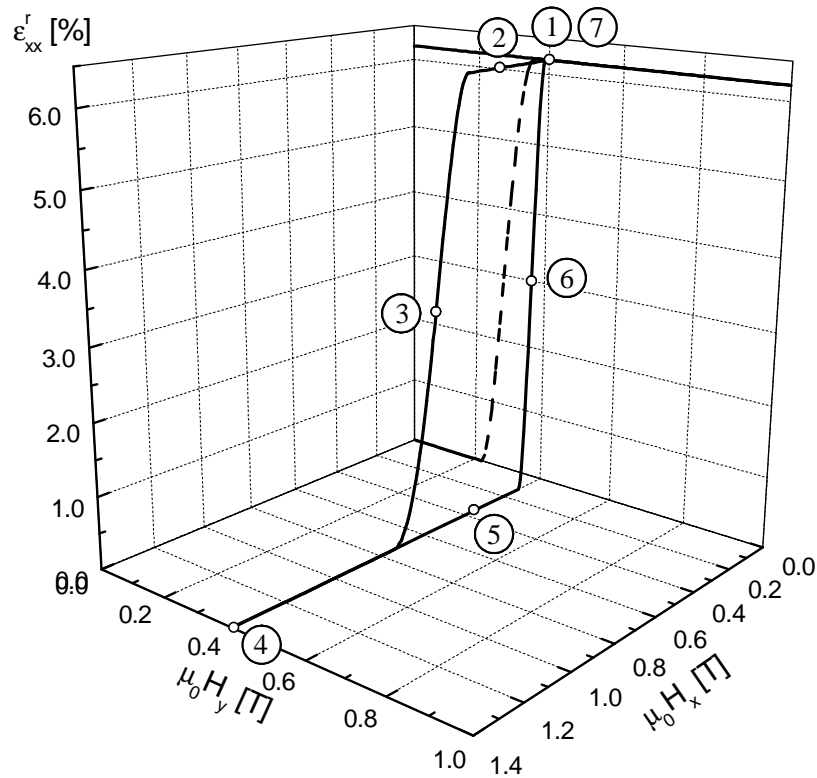

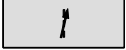




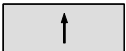


Fig. 34. Detail: H_x -induced reorientation strain hysteresis loop under 0.4 T.

1, which was not observed in the other two loading cases, because there the magnetic field was always applied along the easy axis of that variant. After the reverse variant reorientation process has been activated at $\mu_0 H_x = 0.40$ T and the field has been raised further configuration 3 is obtained, in which 50 % of the first variant have been recovered. One observes that the magnetization vectors in both variant are now rotates away from their preferred axes. The reorientation process is completed at $\mu_0 H_x = 0.74$ T. However, as the magnetic field H_x is again lowered via configuration 5, the variant 1 configuration is not sustained, cf. configurations 5, since the constant field level of $\mu_0 H_y = 0.4$ T creates a strong enough bias for the material to again reorient to the single variant 2 configuration 7.

Table VII. Configuration schematics and data for the strain hysteresis curve under variable H_x at $\mu_0 H_y = 0.4$ T and $\sigma_{xx} = -0.2$ MPa.

#	Schematic	$\mu_0 H_x$	ε_{xx}^r	ξ	θ_3	θ_4
1		0.00 T	6.2 %	1.0	—	0.0°
2		0.25 T	6.2 %	1.0	—	-13.6°
3		0.55 T	3.1 %	0.5	19.0°	-29.6°
4		1.40 T	0.0 %	0.0	11.1°	—
5		0.35 T	0.0 %	0.0	22.9°	—
6		0.07 T	3.1 %	0.5	33.0°	-3.9°
7		0.00 T	6.2 %	1.0	—	0.0°

The fact that the rotation of the magnetization in both variants has a significant impact on the constitutive behavior is evident from Eqs. (5.27), (5.28) and (5.29), and it is clearly observable in the associated magnetization response shown in Fig. 35. For an easier comparison of the magnetic response curves at different levels of H_y , Fig. 36 depicts the projection of the curves shown in Fig. 35 onto the plane $H_y = 0$. It is observed that unlike the magnetization response predicted for loading cases 1 and 2, cf. Fig. 21 on page 85 and Fig. 29 on page 103, every section of these curves exhibits a nonlinear behavior. Furthermore, it is predicted that M_y is non-zero after the reverse reorientation process is completed and variant 1 has been fully recovered as depicted in Schematic 4 of Table VII, and that it approaches zero asymptotically for large H_x . This is due to the fact that the constant component H_y counteracts the

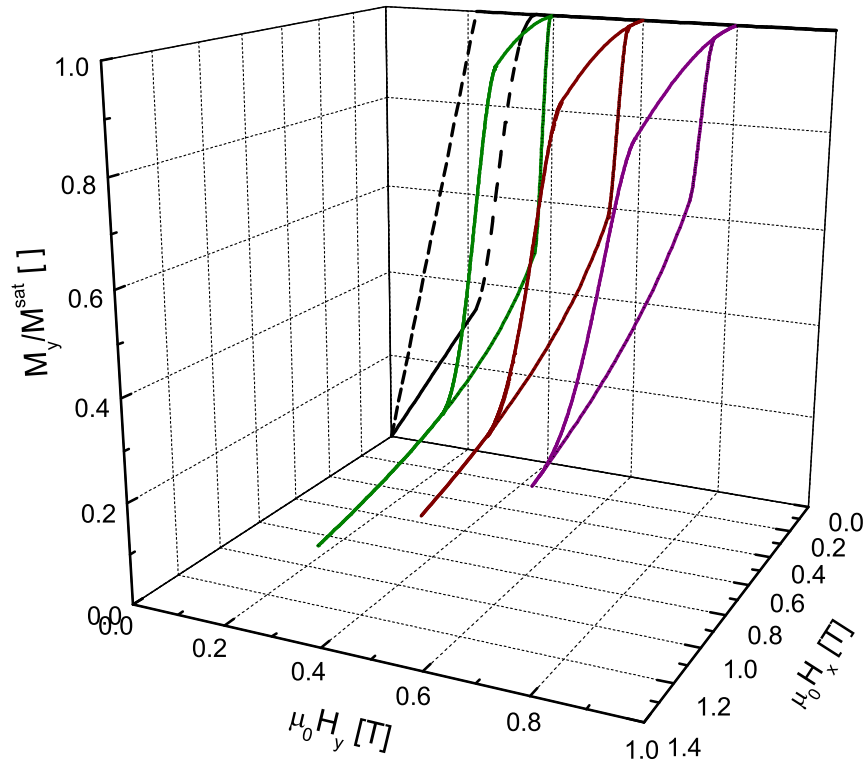


Fig. 35. Normalized magnetization vs. the magnetic field components at -0.2 MPa.

increasing rotation of the magnetization in variant 1 and thus its alignment with the field in the x-direction. This statement is consistent with the observation that M_y approaches zero faster the lower the value of H_y at H_x is applied.

In summary, the model predicts a macroscopic reorientation strain and magnetization behavior that is fundamentally different in nature for the three loading cases, stemming from the fact that different micro-scale mechanisms are activated in each case. In loading case 1 (variable stress σ_{xx} under constant H_y and $H_x = 0$), only the mechanism of martensitic variant reorientation is activated. In loading case 2 (variable H_y under constant stress σ_{xx} and $H_x = 0$), the magnetization in variant 1 rotates in addition to the variant reorientation. In loading case 3 (variable H_x under

constant σ_{xx} and H_y), the rotation of the magnetization vectors

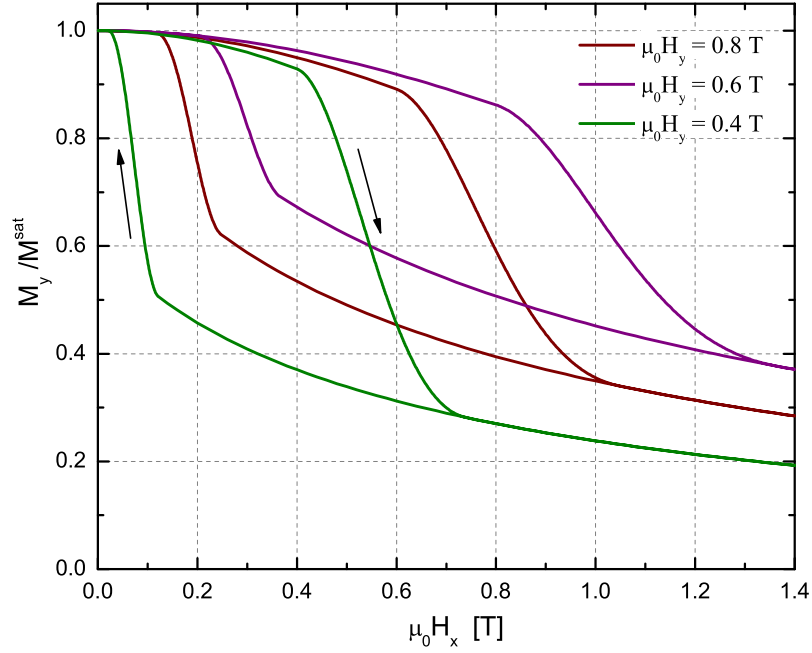


Fig. 36. Normalized magnetization vs. the x-component of the magnetic field at different levels of $\mu_0 H_y$ and $\sigma_{xx} = -0.2$ MPa.

in both variants is activated. Furthermore, the evolution of magnetic domains influences the response at low magnetic field levels. The magnetic domain wall motion has been accurately modeled for special cases in which the variant reorientation does not occur simultaneously.

CHAPTER VI

MAGNETOMECHANICAL BOUNDARY VALUE PROBLEMS FOR MSMAS

This chapter is concerned with the numerical analysis of nonlinear magnetostatic boundary value problems involving MSMA components. These problems are solved using the finite element method, where the nonlinear magnetic properties of the material are provided by the introduced constitutive model for MSMAs. This analysis is important for several reasons:

1. It is needed to properly interpret experimental data. Due to the so-called *demagnetization effect* the magnetic field inside a magnetized MSMA sample is substantially lower than the applied field that magnetized it. In order to accurately calibrate a constitutive model, one needs to know the strain and magnetization response of the material as a function of the internal magnetic field, i.e. the field that the material actually experiences inside the sample. However, one can only measure the strain as a function of the externally applied field. The relation between internal and applied field is not known a priori and depends on the sample geometry. Furthermore, the interpretation of experiments is complicated by the fact that unless ellipsoidal specimen are used, the magnetic field inside a specimen is always nonuniform, even if a uniform field is externally applied. The magnetostatic analysis computes the distribution of the internal magnetic field as a function of the applied field such that these problems can be addressed;
2. The magnetostatic analysis can also be used as a tool to design MSMA experiments and applications. For example, one can determine the optimal placement of the Hall probe used for the measuring of the applied field, if the distribution

of the magnetic field between the pole pieces of the electromagnet and around the MSMA sample in the experiment previously shown in Fig. 4(b) on page 17 is known.

3. This analysis can be considered a first important step toward implementing the fully-coupled magnetomechanical problem for MSMA defined in Chapter III. For the computations presented in this Chapter the influence of magnetic body forces and magnetic body couples, as specified by Eqs. (3.21a) and (3.21b), is considered negligible. The change in the computational domain due to the deformation of the sample during magnetic loading is considered small enough to also be neglected. The coupling of the mechanical and magnetostatic problem in this analysis is thus solely due to the stress level dependence of the magnetic properties of the MSMA.

A. Review of the Magnetostatic Problem

The Gauss-Faraday law and Ampère's law for the magnetostatic approximation were specified in Chapter III, Section A. For convenience, the magnetostatic problem is usually reformulated by introducing either the scalar magnetic potential Φ^m , if free currents are negligible, such that

$$\mathbf{H} = -\nabla\Phi^m, \quad (6.1)$$

or otherwise the vector-valued potential Φ^m , with

$$\mathbf{B} = \text{curl}\Phi^m. \quad (6.2)$$

Eq. (6.1) identically satisfies Ampère's law Eq. (3.7b), whereas Eq. (6.2) satisfies the Gauss-Faraday law Eq. (3.7a). The magnetostatic problem defined by Eqs. (3.7) can

then be reformulated to yield the following two alternative versions of the *Poisson equation of magnetostatics* [152] (see derivation in Appendix B, Section B1).

$$\Delta\Phi^m = \operatorname{div}\mathbf{M} ; \quad (6.3a)$$

$$\text{or } \Delta\Phi^m = -\mu_0 \operatorname{curl}\mathbf{M} . \quad (6.3b)$$

These equations are defined everywhere in \mathbb{R}^3 , the space occupied by the magnetized body and the infinite surrounding free space. Additionally, on all interfaces the field variables \mathbf{B} and \mathbf{H} are subject to jump conditions, which, using Eqs. (3.2b) and (6.1), can also be written in terms of the magnetic potentials, to yield [17]

$$\llbracket\mathbf{B}\rrbracket \cdot \mathbf{n} = \mu_0 \llbracket\mathbf{M} - \nabla\Phi^m\rrbracket \cdot \mathbf{n} = 0 ; \quad \llbracket\mathbf{H}\rrbracket \times \mathbf{n} = -\llbracket\nabla\Phi^m\rrbracket \times \mathbf{n} = \mathbf{0} . \quad (6.4)$$

Surface currents have again been considered negligible. The jump of a generic field A is defined as $\llbracket A \rrbracket = A^+ - A^-$. The plus sign superscript refers to the side of the interface on which the unit normal \mathbf{n} points outward. As a consequence of these conditions, the normal component of the magnetic flux density and the tangential component of the magnetic field strength are continuous over any interface. Similarly, for the vector-valued potential the following interface conditions hold

$$\llbracket\mathbf{B}\rrbracket \cdot \mathbf{n} = \llbracket\operatorname{curl}\Phi^m\rrbracket \cdot \mathbf{n} = 0 ; \quad \llbracket\mathbf{H}\rrbracket \times \mathbf{n} = \llbracket\mu_0^{-1}\operatorname{curl}\Phi^m - \mathbf{M}\rrbracket \times \mathbf{n} = \mathbf{0} , \quad (6.5)$$

where Eqs. (3.2b) and (6.2) were used.

B. The Demagnetization Effect

For illustration purposes a typical magnetic field distribution around a rectangular permanent magnet is depicted in Fig. 37. It is observed that the magnetic field stream lines emanate from the right edge of the specimen and end at the left edge. The

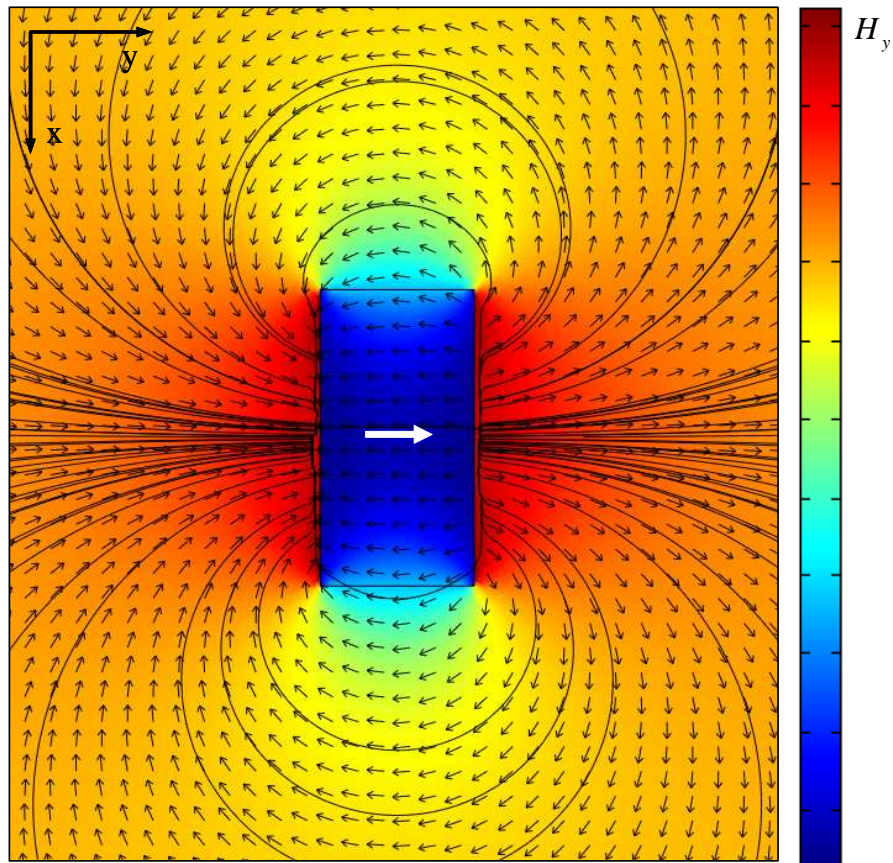


Fig. 37. Magnetic field of a rectangular permanent magnet. The white arrow indicates the direction of the magnetization. Contour plot: $|H_y|$; arrows and streamlines: direction of \mathbf{H} .

”source” of the magnetic field lines is called the *north pole* of the permanent magnet, the ”sink” the *south pole* [16, 17]. It is evident that the depicted stream line pattern satisfies the interface conditions (6.4) or (6.5). While the tangential component of \mathbf{H} is continuous on all interfaces, its normal component can be discontinuous if there exist a discontinuity in the magnetization. Since the normal component of \mathbf{B} is continuous and therefore $[\mathbf{B}] \cdot \mathbf{n} = \mu_0 [\mathbf{H} + \mathbf{M}] \cdot \mathbf{n} = 0$, it is clear that the normal component of \mathbf{H} has to balance the jump in \mathbf{M} that occurs at the interface between the magnetized medium and free space. Inside the specimen the magnetic field opposes the direction

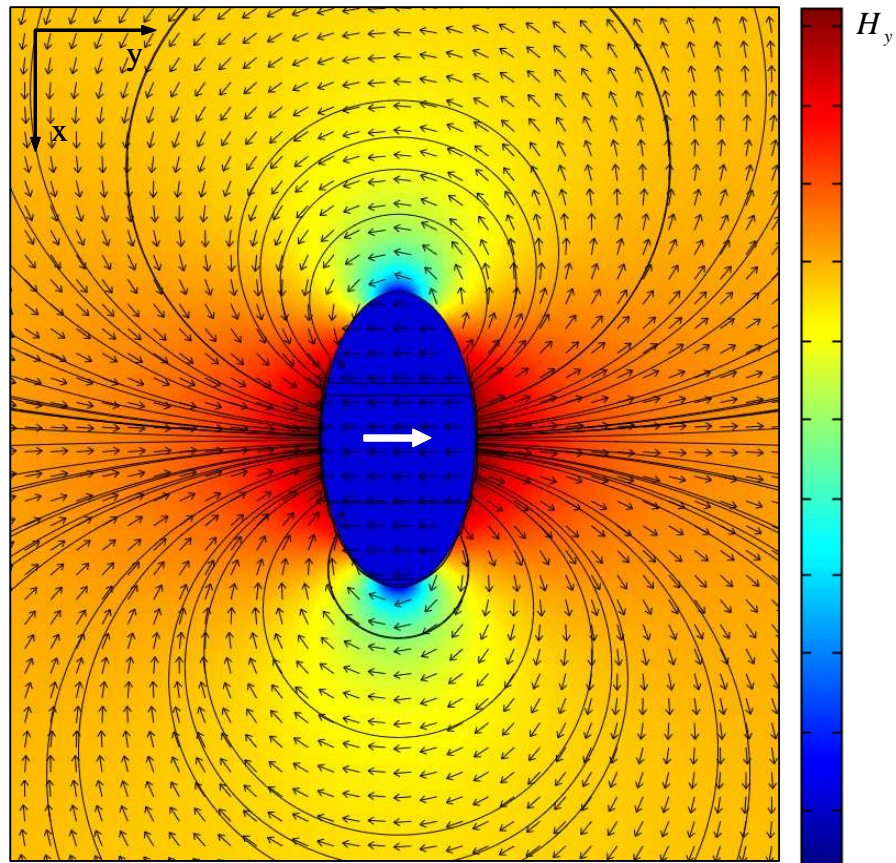


Fig. 38. Magnetic field of an ellipsoidal permanent magnet. The white arrow indicates the direction of the magnetization. Contour plot: $|H_y|$; arrows and streamlines: direction of \mathbf{H} .

of magnetization. The magnetostatic field caused by the body's own magnetization is therefore called the *demagnetizing field* \mathbf{H}^d [16]. Note that the demagnetization field is nonuniform inside the rectangular specimen, even though the magnetization that causes it is uniform. As shown in Fig. 38 the demagnetization field in a uniformly magnetized ellipsoidal sample is always uniform. Furthermore, if the magnetization is caused by an applied field it is uniform inside the ellipsoidal body, while it is nonuniform in a rectangular body.

Permanent magnets exhibit substantial remnant macroscopic magnetization at

zero applied fields and, within certain limits, the magnetization of the magnetic sample does not depend on the applied magnetic field [16]. For magnetostatic problems involving only permanent magnets the Poisson equations (6.9) are linear and the principle of superposition holds. Thus, if additionally an external magnetic field \mathbf{H}^a is applied, the total magnetic field is then given by

$$\mathbf{H} = \mathbf{H}^a + \mathbf{H}^d . \quad (6.6)$$

Generic integral representations of the solution of the magnetostatic problem defined by Eqs. (3.7) or Eqs. (6.3) exist [152, 153]. For uniformly magnetized bodies the magnetization vector can be taken outside the integral expressions for the magnetic field strength [153, 154], such that

$$\mathbf{H}^d(\mathbf{r}) = - \underbrace{\left[\frac{1}{4\pi} \iint_{\partial\Omega^m} \frac{\mathbf{r} - \mathbf{r}'}{|\mathbf{r} - \mathbf{r}'|^3} \otimes \mathbf{n}' dA' \right]}_{=: \mathbf{D}} \mathbf{M} = -\mathbf{D}\mathbf{M} . \quad (6.7)$$

Therein \mathbf{r} is the position at which \mathbf{H} is evaluated in \mathbb{R}^3 and \mathbf{r}' the location of a point on the surface $\partial\Omega^m$, with unit outward normal \mathbf{n}' , of the region Ω^m occupied by the magnetized body. By applying the divergence theorem an equivalent volume integral representation of Eq. (6.7) can be obtained. \mathbf{D} is the demagnetization tensor, which only depends on the geometry of the body and can be computed by evaluating the bracketed integral expression in Eq. (6.7). For a spatially uniformly magnetized body the demagnetization field can thus be computed by simply multiplying the magnetization with an appropriate demagnetization factor. Such factors have been tabularized for ellipsoids of many different aspect ratios [16, 17, 143]. This procedure is analogous to using Eshelby tensors in elasticity theory to determine the strain field inside ellipsoidal inclusions [155, 156]. The demagnetization tensor has the following

properties: i) it is independent of position inside an ellipsoidal body; ii) it is diagonal if its eigenvectors are aligned with the symmetry axes of the body; iii) its trace is 1, if evaluated inside the body. The demagnetization factor for a sphere is therefore $1/3$ in any direction. For a prismatic cylinder with square or cylindrical cross-section the axial and transverse demagnetization factors are related by $D^t = 1/2(1 - D^a)$ [157].

The magnetic field inside a uniformly magnetized sample of non-ellipsoidal shape is always nonuniform. The demagnetization tensor in this case depends on the position inside the sample. It is customary to define average demagnetization tensors for samples of arbitrary shape, sometimes referred to as *magnetometric demagnetization tensors* [157, 158], in the following manner

$$\langle \mathbf{D} \rangle := \frac{1}{\Omega^m} \int_{\Omega^m} \mathbf{D}(\mathbf{r}) \, dV . \quad (6.8)$$

The average demagnetization field can then be written as

$$\langle \mathbf{H}^d \rangle = -\langle \mathbf{D} \rangle \mathbf{M} . \quad (6.9)$$

Numerical solution schemes have been developed to compute the demagnetization factors for uniformly magnetized bodies of arbitrary shape. For many standard geometries, such as prismatic bars with different types of cross-sections, these have also been tabularized [154, 157, 158].

By definition the demagnetization factor loses its meaning for bodies with nonuniform magnetization. Thus, the exact demagnetization field inside a non-ellipsoidal body, whose magnetization is induced by an external magnetic field and therefore not uniform unless complete saturation is reached at high fields, can not be computed with the help of demagnetization factors. Furthermore, if the magnetization is a function of the applied field the magnetostatic problem as described by Eqs. (6.3)

becomes nonlinear and superposition no longer holds. In this case, which is always encountered in experiments unless ellipsoidal specimen are used, an explicit numerical solution of the magnetostatic boundary value problem has to be obtained. For MSMA's the problem is complicated by the fact that the magnetic properties are nonlinear, hysteretic and stress level dependent. Furthermore, the shape of the sample changes due to the magnetic field-induced strain. This effect, however, is expected to have negligible significance.

A general discussion of the influence of the demagnetization effect on the measuring of magnetization curves in ferromagnetic materials can be found in [17]. Shield [27] addressed the problem for experiments on MSMA's by approximating his samples as uniformly magnetized rectangular bars, in which case a constant demagnetization factor according to Eq. (6.9) can be utilized. Shield acknowledges [27] that the demagnetization factor method can only lead to approximations of the demagnetization effect for the prismatic samples typically used in MSMA testing. Nonetheless, this method is often used due to its simplicity or lack of alternatives. However, it is not clear a priori what kind of error one might expect from making this approximation. One aspect of the numerical analysis presented in the following section is aimed at estimating this error.

C. Finite Element Analysis of the Magnetostatic Problem

Based on the numerical analysis of specific magnetostatic boundary value problems, which are defined by the vector-valued Poisson equation (6.3b), the interface jump conditions (6.3b) and constitutive relations of the form $\mathbf{M}(\boldsymbol{\sigma}, \mathbf{H}, \boldsymbol{\zeta})$, the influence of the demagnetization effect on the interpretability of MSMA experiments is investigated in this section. This analysis has also been discussed in [59, 60].

As explained in Chapters II and V, a typical experiment consists of subjecting a martensitic MSMA sample to a constant mechanical load and subsequently to a perpendicular magnetic field. Such an experiment was previously described in Fig. 4. This particular setup has motivated using the computational domain depicted in Fig. 39 to solve a relevant magnetostatic problem using the finite element method. All magnetostatic analysis was performed using the COMSOL Multiphysics (formerly Femlab) finite element software package in which the constitutive model was used to provide the magnetic properties of the MSMA sample.

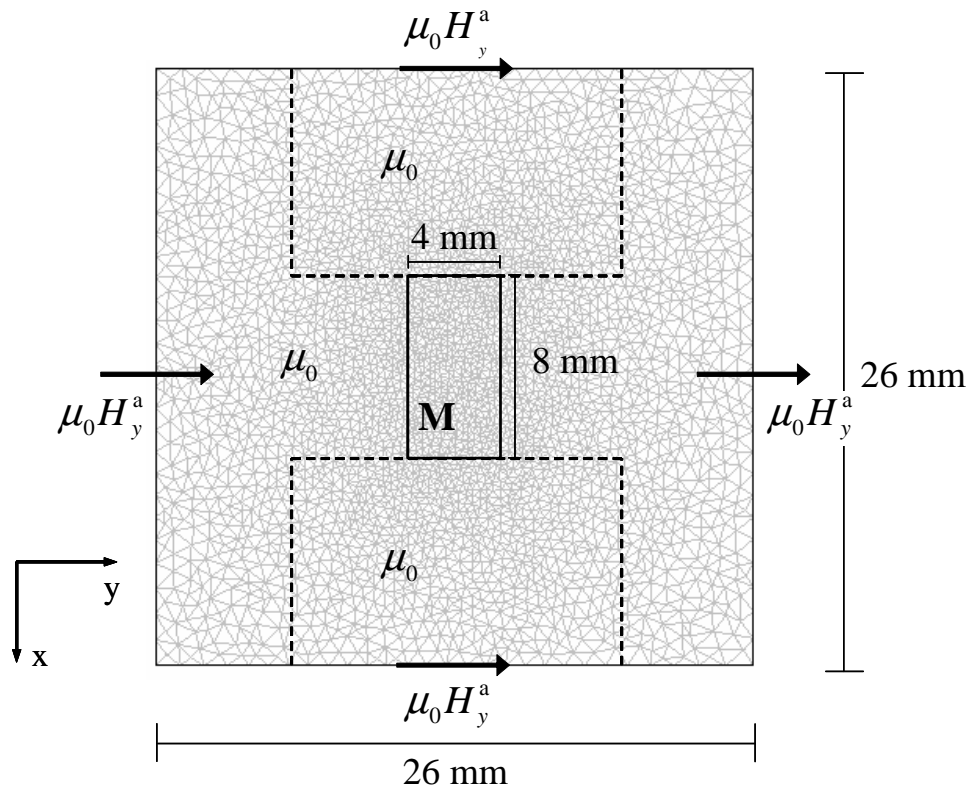


Fig. 39. Domain geometry, mesh and boundary conditions for the magnetostatic problem. Dashed lines indicate the location of the nonmagnetic grips of the load frame.

According to the electromagnet's specifications, a uniform magnetic field can be assumed in the empty gap between the pole pieces of dimensions $26 \text{ mm} \times 26 \text{ mm} \times 26 \text{ mm}$. Fig. 39 also indicates the location of the specimen, and the nonmagnetic grips (dashed lines). Typical specimen dimensions are $8 \text{ mm} \times 4 \text{ mm} \times 4 \text{ mm}$, or aspect ratios of 2:1:1, where the long axis is the x -direction.

A spatially constant magnetic flux is applied on all sides of the boundary, or, more precisely, the potential

$$\Phi_x^m = \Phi_y^m = 0 ; \quad \Phi_z^m = -\mu_0 H_y^a x , \quad (6.10)$$

is applied, such that with Eq. (6.2) it follows

$$\begin{aligned} \mu_0 H_x = B_x &= \frac{\partial \Phi_z^m}{\partial y} - \frac{\partial \Phi_y^m}{\partial z} = 0 ; & \mu_0 H_y = B_y &= \frac{\partial \Phi_x^m}{\partial z} - \frac{\partial \Phi_z^m}{\partial x} = \mu_0 H_y^a ; \\ \mu_0 H_z = B_z &= \frac{\partial \Phi_y^m}{\partial x} - \frac{\partial \Phi_x^m}{\partial y} = 0 . \end{aligned} \quad (6.11)$$

This results in the desired homogeneous magnetic field in the computational domain if no specimen is included. The presence the MSMA sample in the gap of course perturbs the homogeneity of the computed field.

Since only a few experimental setups exist in which the magnetic field-induced magnetization response can be measured [27, 44], this data is usually not available, such that the magnetic properties of the MSMA sample in the magnetostatic analysis have to be provided by the constitutive model. The reduced model equations for the considered loading case were derived in Chapter V, Section A. The same section also introduced the model parameters calibration scheme which was used here to determine the parameters listed in Table VIII. The experiments from which these data were obtained are discussed in [58]. The magnetocrystalline anisotropy coefficient was not available and had to be estimated such that simulation of the predicted magnetic

field-induced strain reflected approximately the same blocking stress as observed in the experiment.

Table VIII. Material parameters for the $\text{Ni}_{51.1}\text{Mn}_{24.0}\text{Ga}_{24.9}$ composition [58], and the resulting hardening and hysteresis parameters calibrated at -2 MPa.

Material Parameters						Model Parameters		
Quantity	Value	Unit	Quantity	Value	Unit	Quantity	Value	Unit
ρK_1	700.0	kJm^{-3}	$\mu_0 H_y^{s(1,2)}$	0.9	T	A^c	-60.807	kPa
M^{sat}	742.4	kAm^{-1}	$\mu_0 H_y^{f(1,2)}$	1.85	T	B_1^c	75.411	kPa
$\varepsilon^{\text{r,max}}$	5.65	%	$\mu_0 H_y^{s(2,1)}$	0.75	T	B_2^c	96.736	kPa
σ^*	-2.0	MPa	$\mu_0 H_y^{f(2,1)}$	-0.17	T	C^c	-183.975	kPa
ξ^{crit}	1.0					$Y^{\varepsilon,c}$	223.572	kPa

For the calibration stress level of -2 MPa the magnetic field-induced strain hysteresis loop depicted in Fig. 40 results from the model parameters of Table VIII. The corresponding magnetization behavior predicted by the model is shown in Fig. 41.

The following assumptions are made for using the magnetization data in the magnetostatic analysis

1. The stress is assumed to be uniaxial, at a constant level and spatially homogeneous, since magnetic body forces and magnetic body couples are neglected. The only coupling between the mechanical and the magnetostatic problem at this point is given by the stress level dependence of the magnetic properties. Thus for each stress level the magnetostatic analysis has to be performed in a separate computation.

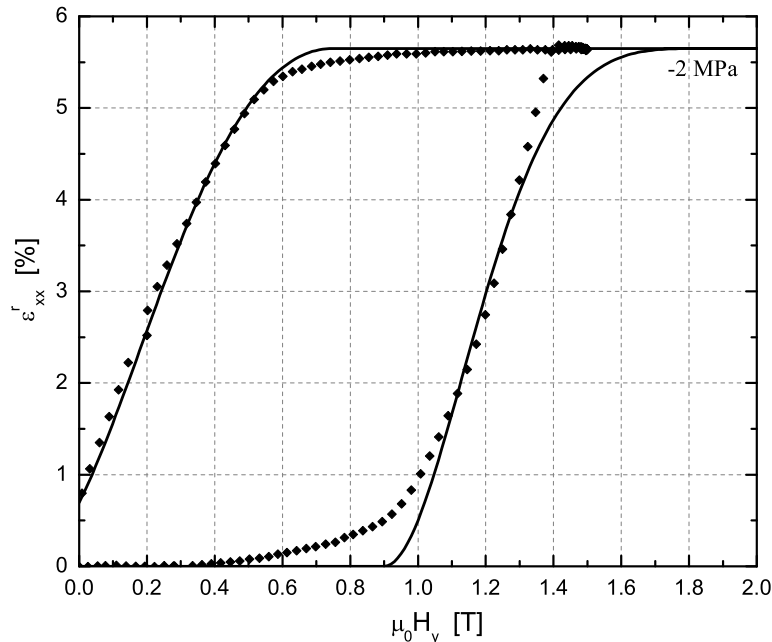


Fig. 40. Model Calibration. Experimental data (diamonds) and model simulation (solid line). Data (taken from [58]) for a $\text{Ni}_{51.1}\text{Mn}_{24.0}\text{Ga}_{24.9}$ alloy tested at -95°C under the compressive stress of 2 MPa.

2. The magnetic field, and thus the magnetization, on the other hand vary spatially inside the prismatic specimen. The magnetic properties predicted by constitutive behavior are evaluated separately at every integration point in the finite element mesh. Since the magnetization depends on the applied field in a nonlinear fashion the magnetostatic problem described by Eq. (6.3b) is highly nonlinear¹. COMSOL Multiphysics provides an appropriate iterative nonlinear solver. The parametric version of this solver was used such that the magnetic field distribution could be computed, while scaling the applied magnetic field from 0 T to 2 T.

¹Even if the relation between field and magnetization were linear the magnetostatic problem would be nonlinear, though numerically most likely easier to handle.

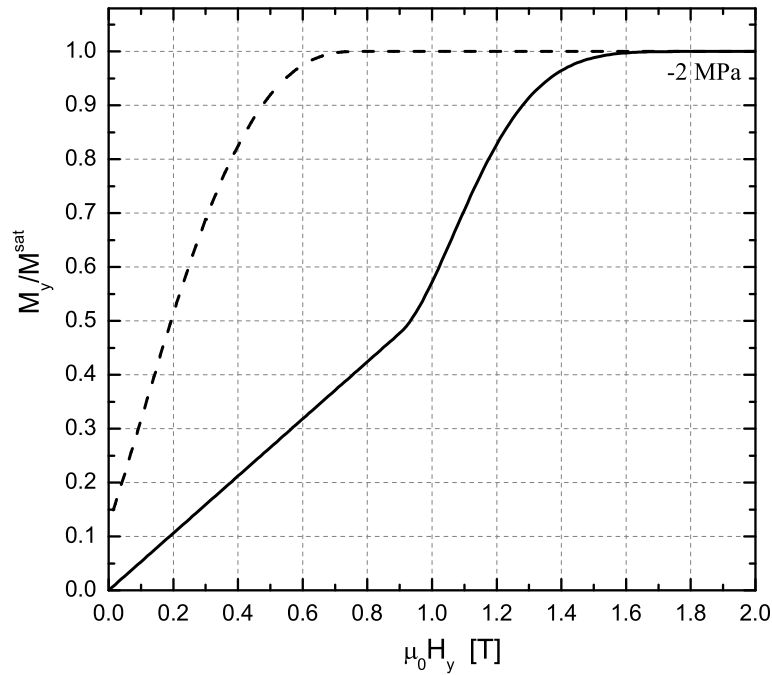


Fig. 41. Predicted y -component of the magnetization at the compressive stress of 2 MPa. Only the solid portion of the curve is used in the magnetostatic analysis.

3. From the discussion in Chapter V, Section A the component M_x is predicted to be zero at low fields, due to the magnetic domain structure, then to suddenly increase as the variant reorientation process sets in and to again decrease to zero as the material is saturated in the y -direction. It is always smaller than M^{sat} . The component $M_y = M_y(H_y)$ is therefore determined to be dominating the component $M_x = M_x(H_y)$, which is neglected in the following analysis. Furthermore, even though the x -component of the applied magnetic field is zero, the same does not hold for the internal field, due to the magnetization of the body and the shape of the specimen (corner effects). However, the dependence $\mathbf{M}(H_x)$, and $\mathbf{M}(H_z)$ in a three dimensional analysis, is assumed to be small and thus neglected;

4. The hysteretic nature of the constitutive response is not addressed in the magnetostatic analysis at this point. To be precise, the hysteresis is not neglected, but the analysis is only carried out from 0 T to 2 T, for which the solid line part of the magnetic hysteresis in Fig. 41 applies, not for the removal of the magnetic field (dashed line).

The nonlinear magnetostatic problem is mathematically described by Eq. (6.3b), the interface conditions (6.5) and the boundary conditions (6.10). The geometry of the computational domain was introduced in Fig. (41). The constitutive relations are reflected in the magnetization curve of Fig. (41). A number of simplifying assumptions have been specified. The problem has thus been fully defined.

Numerical results of the finite element analysis are plotted in Fig. 42 in terms of the distribution of the y -component of the magnetic field for the exemplary applied magnetic flux level of 2 T.

It is observed that indeed, due to the non-ellipsoidal shape of the specimen, the magnetic field and thus the magnetization are nonuniform inside the specimen although a constant magnetic flux is applied at the boundary of the computational domain. The presence of the magnetized specimen clearly perturbs the magnetic field in the free space surrounding the sample. From this distribution one can for example obtain information on how much a Hall probe reading, which is used to measure the applied field as shown in Fig. 4(a) on page 17, can be expected to be influenced by the samples magnetic field. The distribution at 2.0 T, at which essentially all of the material has been magnetized to saturation along the y -axis, is symmetric with respect to both axes of the coordinate system.

It again must be emphasized that in the magnetostatic problem the magnetization is allowed to change locally and its value is determined by evaluating the

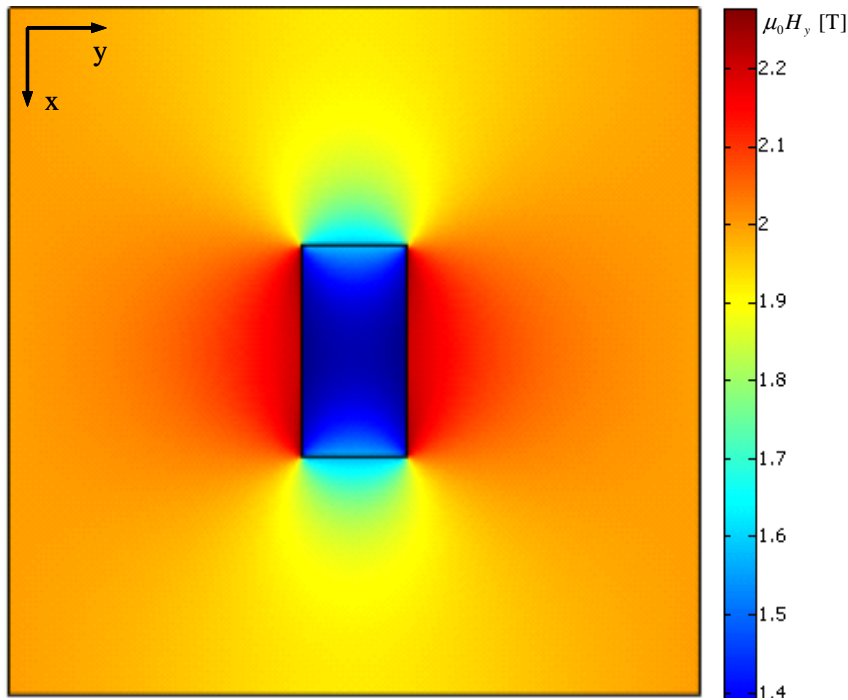


Fig. 42. Distribution of H_y in the computational domain at the applied magnetic field of $\mu_0 H_y^a = 2.0$ T.

magnetization curve for the magnetic field acting at the particular point. The internal mechanism which leads to the macroscopic magnetization response, namely the evolution of the martensitic variants, the magnetic domains and the magnetization rotation angles as predicted by the constitutive model have been discussed in Chapter V. For this loading case, this evolution was also schematically depicted in Table V. As discussed, this assumes that there exists a separation of scales such that at each point in the continuum, the MSMA sample, there exist a smaller length scale at which a sufficient number of martensitic twins and magnetic domains coexist such that average quantities such as the magnetization can be defined for each point. The contributions of the variant and magnetic domains are then taken into account in a phenomenological sense and are no longer "visible" on the continuum scale. It is still a matter of discussion whether this approach is fully justified for single crystals.

To further visualize the local behavior, the variation of the magnetic field within the MSMA sample is plotted in Fig. 43 for two different applied field levels.

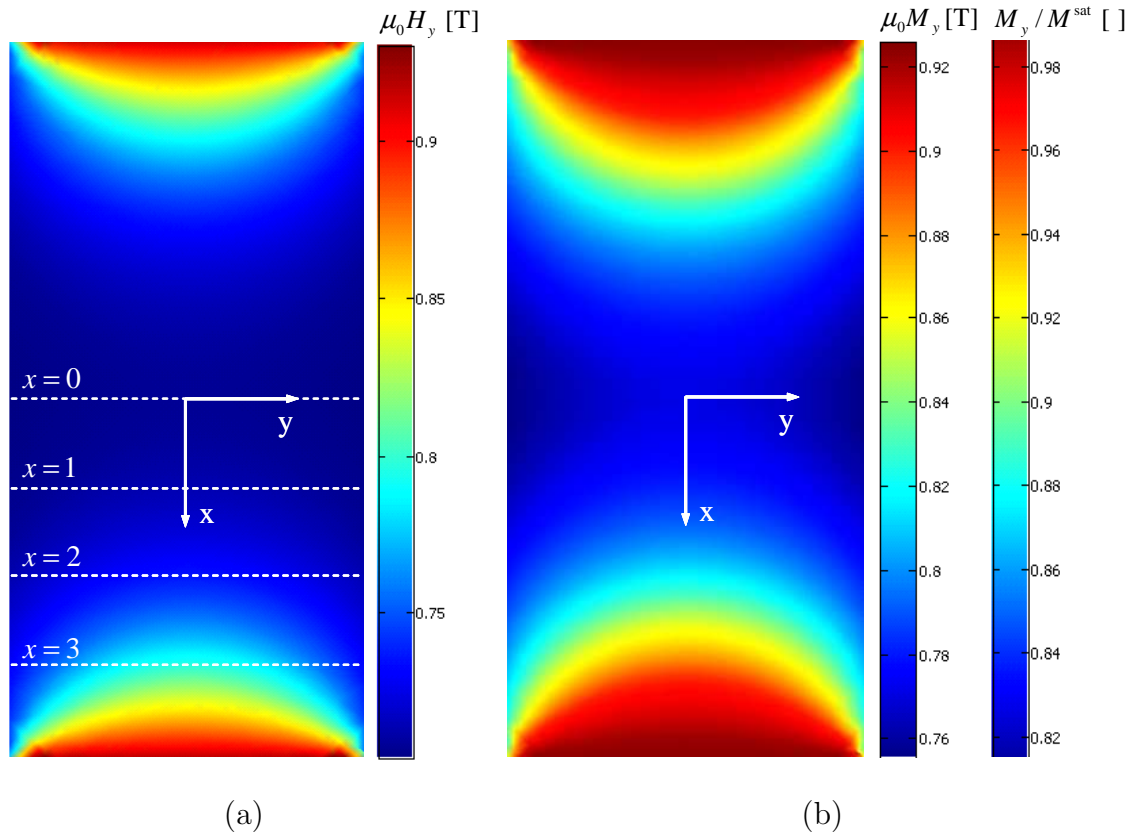


Fig. 43. Distribution of the magnetic field and magnetization within the specimen at the applied magnetic field of $\mu_0 H_y^a = 1.3$ T.

In Fig. 44 the variation of the magnetic field and the magnetization across the specimen are plotted for different locations. Note that at the left ($y = -2$) and right ($y = 2$) sides of the specimen the jump in the magnetic field is balanced by the jump in the magnetization in going from free space into the magnetized material. According to relation (3.2b) the magnetic flux component $B_y = \mu_0(H_y + M_y)$, which is the normal component of the magnetic flux on these interfaces, thus stays constant, so that the first jump condition specified in Eqs. (6.5) is satisfied.

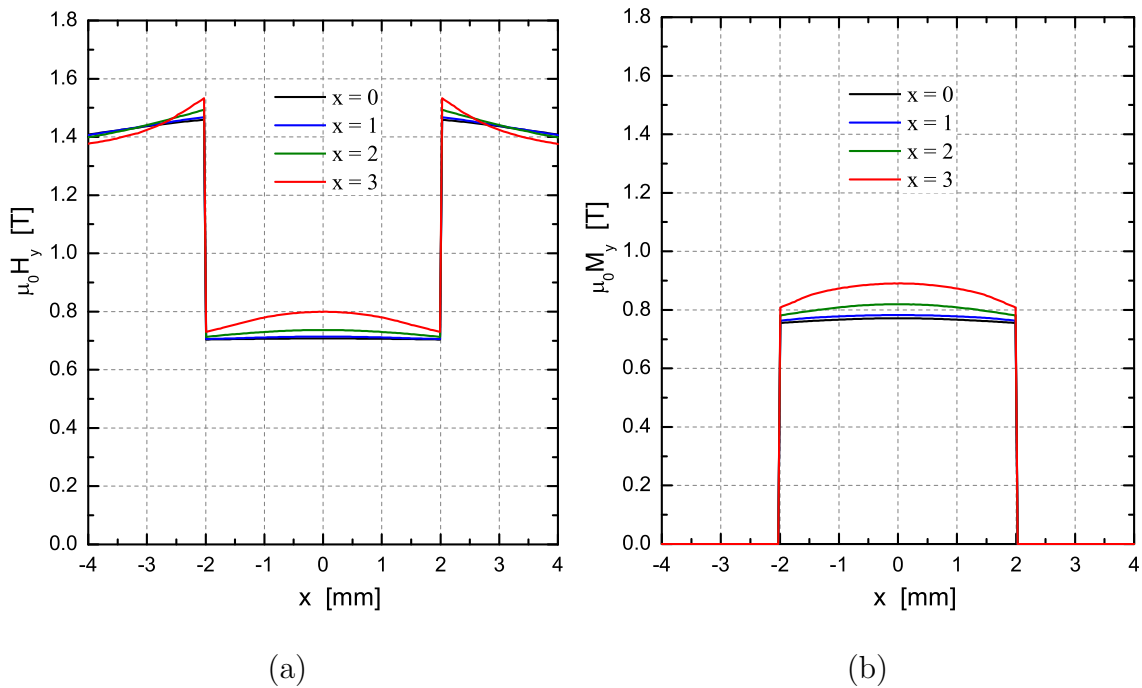


Fig. 44. Distribution of the y -components of the magnetic field and the magnetization across the specimen and its immediate vicinity at different levels of x , as indicated in Fig. 43, for the exemplary applied flux level of 1.3 T.

D. Interpretation of Experimental Data through Magnetostatic Analysis

With the numerical solution of the magnetostatic problem the relation between the internal magnetic field and the applied field is known. However, in this analysis the magnetic properties, which are initially only known in terms of the applied field, were used as if they were the true constitutive response of the material. Thus the relation between the internal and applied field computed in one run of the analysis can only serve as a first correction of the experimental data according to

$$\text{Known: } \langle M_y \rangle(H_y^a), H_y^a \Leftrightarrow \langle H_y^{\text{iter}1} \rangle.$$

$$\text{To be computed: } \langle M_y \rangle(H_y^a) \Rightarrow \langle M_y \rangle(\langle H_y^{\text{iter}1} \rangle). \quad (6.12)$$

Then the analysis is repeated with the magnetic properties given by $\langle M_y \rangle(\langle H_y^{\text{iter}1} \rangle)$ and with the result one can again correct the magnetization curve

$$\text{Known: } \langle M_y \rangle(H_y^a), H_y^a \Leftrightarrow \langle H_y^{\text{iter}2} \rangle.$$

$$\text{To be computed: } \langle M_y \rangle(H_y^a) \Longrightarrow \langle M_y \rangle(\langle H_y^{\text{iter}2} \rangle). \quad (6.13)$$

By following this procedure, the relation between the applied field and the internal field is computed more accurately in each iteration step. This can be considered an *inverse problem*. One aims to determine the actual magnetic properties of the sample such that solving the magnetostatic problem for a sample of this geometry gives back the relation $\langle M_y \rangle(H_y^a)$ that is plotted in Fig. 41. The original and corrected magnetization curves resulting from this iterative procedure are depicted in Fig. 45 for the considered specimen with 2:1 length to width ratio.

As described above, the corrected curves were plotted by using the same data for the vertical magnetization axes, while rescaling the magnetic field axis by means of the relation between the average internal and applied field at each iteration. One observes the relatively fast convergence of the solution. After six iterations the difference to the solution of the previous iteration is small enough to conclude that the solution has converged. The magnetization of curve of iteration six can thus be considered the "true" magnetization response, which is independent of the specimen geometry. The original data is the magnetization behavior that would be measured in an experiment using a prismatic sample of this aspect ratio. In an experiment that uses a sample of the same material, but different aspect ratio a different curve would be measured.

A parametric study has been performed to investigate the sample shape dependence of the demagnetization effect for the prismatic specimen with nonlinear magnetic properties. In Fig. 46 the corrected magnetization data has been plotted

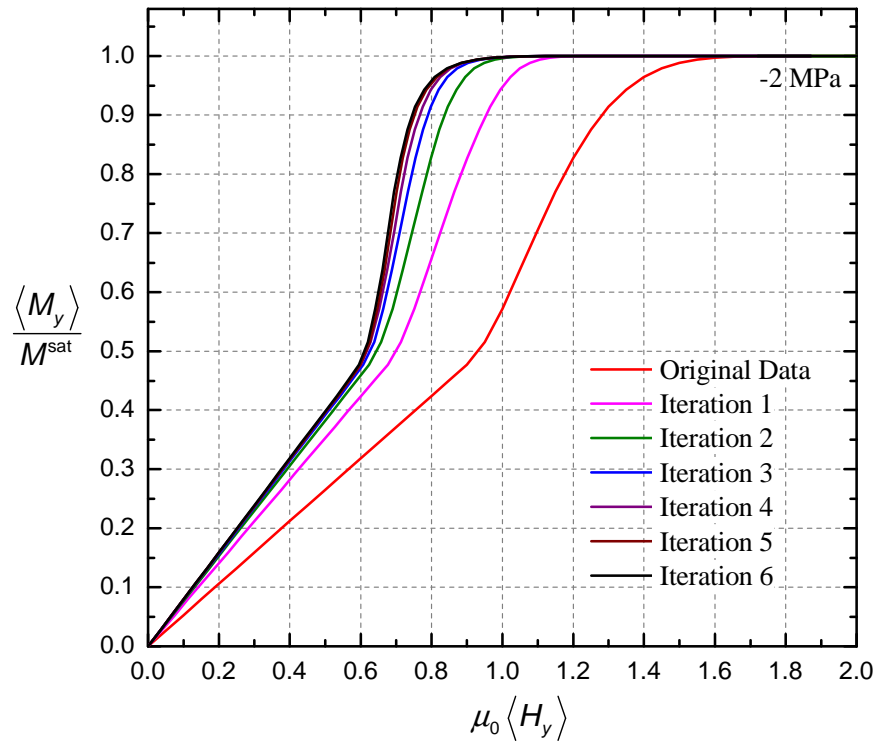


Fig. 45. Magnetization data corrected for demagnetization. Specimen aspect ratio 2:1.

for four different aspect ratios of the prismatic specimen with square cross-section. The corresponding corrections of the magnetic field-induced strain data have been plotted in Fig. 47. It is clearly observed that the influence of the specimen aspect ratio on the difference between the apparent material behavior and the true constitutive response is very significant and must therefore be addressed when using data for model calibration. Once the MFIS data has been corrected for demagnetization, the model parameters can be recalibrated.²

One of the stated goals of this analysis was to investigate the error one can expect when using the demagnetization factor method instead of the finite element analysis

²The specific results presented here are based on solutions of 2-D boundary value problems and can thus only be used qualitatively. The procedure is the same for 3-D problems, which however are computationally much more involved.

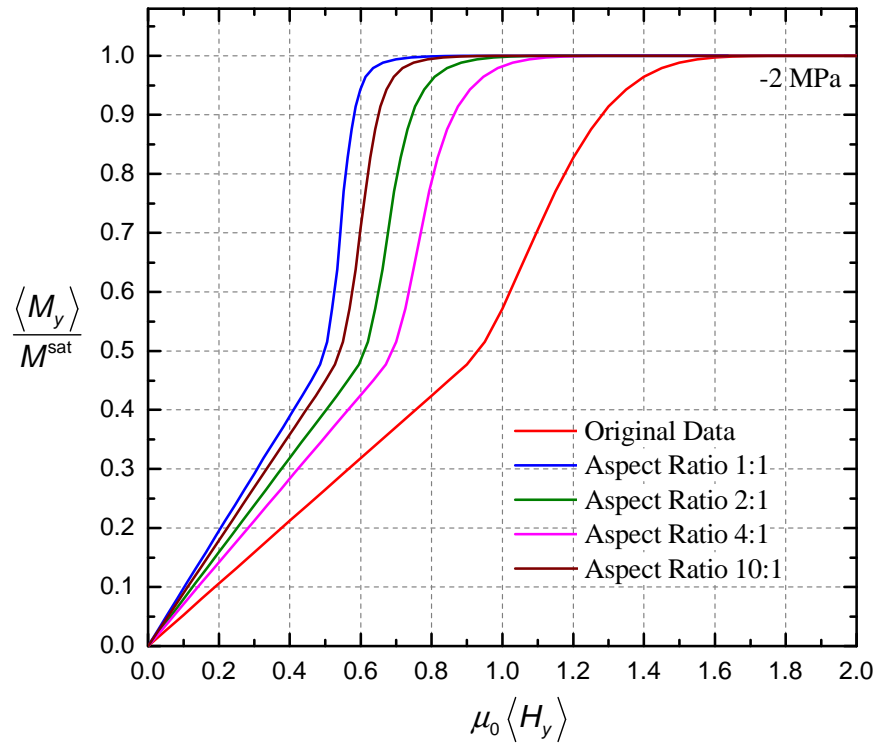


Fig. 46. Influence of specimen aspect ratios on the correction of the magnetization data.

of the nonlinear magnetostatic problem. The average demagnetization factor was defined in Eq. (6.8). Using Eqs. (6.6) and 6.9 one can compute the average internal magnetic field by

$$\langle H_y \rangle = H_y^a + \langle H_y^d \rangle = H_y^a - \langle D_{yy} \rangle \langle M_{yy} \rangle. \quad (6.14)$$

This relation is often applied in the literature [27, 97] to correct magnetization data. As discussed in Section A of this chapter, this procedure of course assumes that the magnetization in the sample is uniform and that superposition holds.

The demagnetization factor for the specimen of the 2:1 aspect ratio is $D_{yy} = 0.651$. Since a literature value was not available for this particular geometry, the factor was computed using finite elements for a sample of constant and spatially

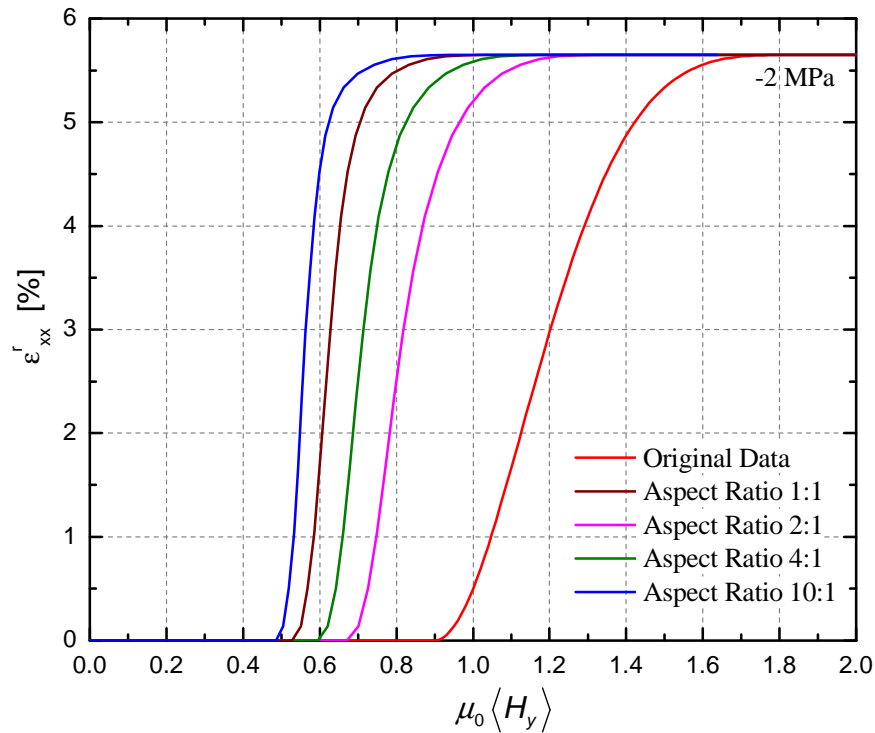


Fig. 47. Influence of specimen aspect ratios on the correction of the magnetic field-induced strain data.

uniform magnetization placed in free space. This method has proven to yield very accurate demagnetization factors for other geometries for which literature data could be referred to [157].

If the magnetization response curve of the MSMA can not be measured and is also not predicted by a constitutive model Eq. (6.14) is sometimes used with a constant M_y , for example $M_y = M^{\text{sat}}$. This is expected to lead to a very crude approximation of the demagnetization effect. If the magnetization response is known or predicted as in Fig. 41 a much better approximation is obtained. The different correction methods are compared in Fig. 48.

These observations suggest that using the demagnetization factor method, which is based on the assumption of uniform magnetization in the specimen, one obtains

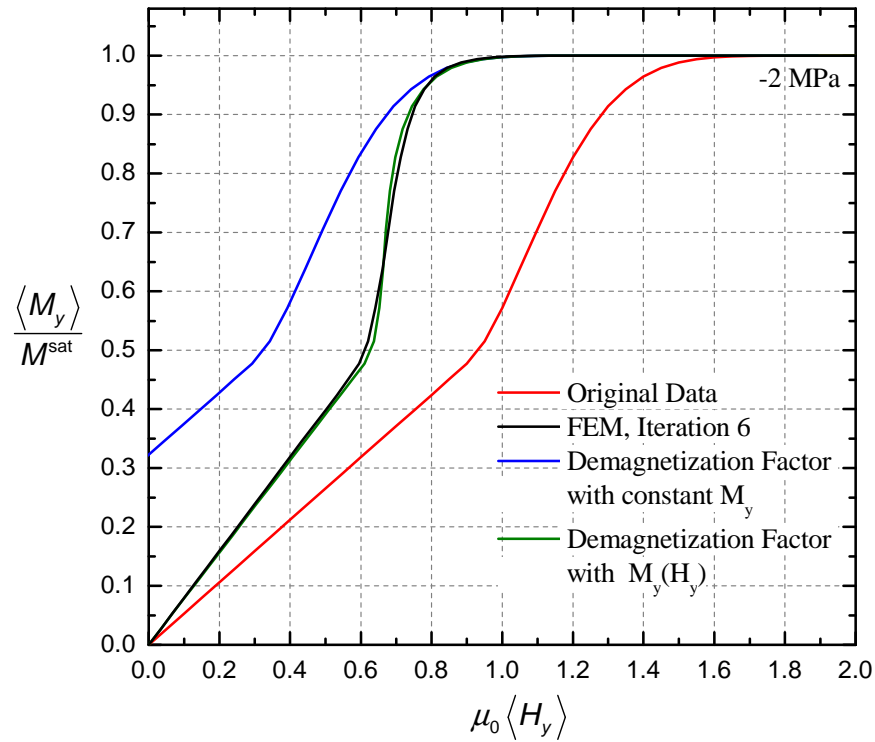


Fig. 48. Comparison of the corrections through demagnetization factors and FEM analysis. Specimen aspect ratio 2:1.

essentially the same result as performing the FEM analysis of the nonlinear magnetostatic problem with nonuniform magnetization, if average field quantities are considered. This conclusion can be misleading, however, because it only holds for average quantities. As evident from Fig. 43 and Fig. 44, there exist a significant variation in the local magnetization.

To further quantify this variation, Fig. 49 displays local values of the magnetic field at several points in the specimen as a function of the applied field.

For problems in which the knowledge of local magnetic field and magnetization is important, one can not avoid solving the magnetostatic problem explicitly, as done here. Such cases are certainly encountered if one is interested in solving magnetome-

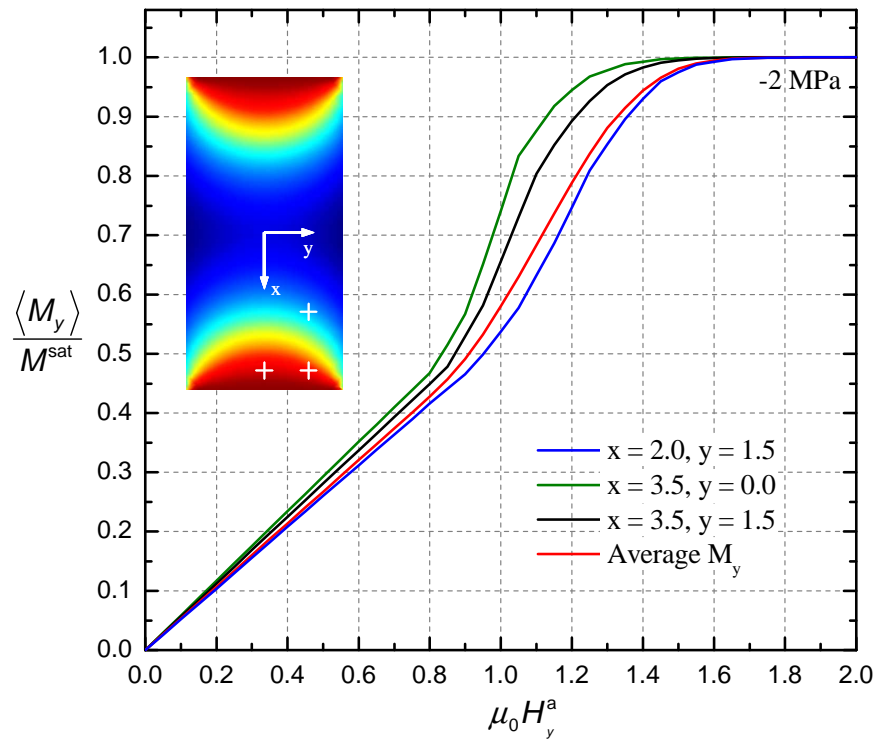


Fig. 49. Position dependence of the magnetization response within the rectangular specimen.

chanical MSMA boundary value problems not just involving simple specimen shapes, but, for example, more complicated geometries of MSMA components in actuators and other applications.

CHAPTER VII

SUMMARY AND CONCLUSIONS

A thermodynamics-based phenomenological constitutive model has been developed to predict the nonlinear, hysteretic and stress-level-dependent strain and magnetization response of magnetic shape memory alloys. The model is formulated in terms of a continuum level free energy function which contains elastic energy, magnetic energy and coupling terms. The independent variable state space of the Gibbs free energy function, usually containing the temperature and stress tensor, was expanded to contain the magnetic field strength vector. The influence of the evolving microstructure on the macroscopic response has been captured through internal state variables. Constitutive equations were derived from the free energy in a thermodynamically-consistent manner. A novel reorientation diagram was proposed to visualize the activation surfaces for the martensitic variant reorientation process, which are mathematically described by a reorientation function and Kuhn-Tucker type reorientation conditions. By linking partial reorientation at higher stress levels to the full rotation of the magnetization vector in the stress-favored variant, the developed model is capable of predicting the stress level dependence of the magnetic field-induced strain.

The MSMA response to several types of loading was modeled: i) the magnetic field-induced variant reorientation under constant levels of stress; ii) the stress-induced variant reorientation under constant levels of the magnetic field; iii) the simultaneous application of two magnetic field components, one constant, one variable, and constant stress. The modeling results were compared to experimental data, where available, and showed good agreement.

Finally, nonlinear magnetostatic boundary value problems for MSMA were analyzed using the finite element method. Partial coupling of the magnetostatic and

the mechanical problem was taken into account through the stress level dependence of the magnetic properties of the MSMA, which were provided by the constitutive model. In the analysis, performed with the COMSOL Multiphysics (Femlab) software package, the magnetic field distribution as a function of the applied field was determined inside a typical sample geometry. This relation was then used to obtain a more accurate interpretation of experimental data.

There are several aspects in which this work can be extended. For example, for the model predictions presented in this dissertation it was assumed that the MSMA single crystal samples were oriented such that the loading and the deformation occurred along certain known crystallographic directions. The reorientation tensor in this case takes a simple form. This is not necessarily too restricting of an assumption, since experiments are typically conducted in this manner. However, if one is interested in analyzing MSMA components which are subjected to multi-dimensional loading in real applications, the model needs to be generalized. Recently there have been some efforts to capture the kinematics of MSMA single crystal deformation more accurately [28, 93]. A general theory of the kinematics of twinning can be found in [2, 159, 160]. If a general reorientation tensor for arbitrary stress and magnetic field loading conditions can be formulated this would also result in a multi-dimensional formulation of the reorientation function.

Furthermore, the evolution of magnetic domains has only been considered for low stress levels and low magnetic fields, at which the variant reorientation does not occur. In principle the model is equipped to handle the simultaneous evolution of all internal state variables. However, a linear hardening function for the domain evolution, as assumed in the presented example, has not yielded satisfactory results in the reorientation regions. This is mainly due to the fact that not enough experimental evidence is available, especially in terms of the magnetization response, to understand

what the response ought to be. This effort to capture the interaction of twin boundary and magnetic domain wall motion for different magnetomechanical loading conditions may also be supported by modeling on other length scales. Jin [161], for example, recently presented some preliminary work aimed at combining phase field method approaches that have successfully been applied to predict the formation and twinning of martensite [162] and the development of magnetic domains in ferromagnetic polytwinned microstructures [163].

In terms of the analyzing relevant boundary value problems for MSMA it is desirable to implement the fully-coupled magnetomechanical problem described in Chapter III. The magnetostatic and the mechanical equilibrium equations then have to be solved simultaneously. The full coupling is given through i) the magnetic body force and body couple, which appear in the equilibrium equations; ii) the constitutive response in terms of the stress-dependent magnetization properties and the magnetic field-dependent stress-strain relation; iii) the magnetic field-induced deformation of the computational domain.

REFERENCES

- [1] V. Birman, Review of mechanics of shape memory alloy structures, *Applied Mechanics Reviews* 50 (11, part I) (1997) 629–645.
- [2] K. Otsuka, C. M. Wayman (Eds.), *Shape Memory Materials*, Cambridge University Press, Cambridge, UK, 1998.
- [3] I. Chopra, Review of state of art of smart structures and integrated systems, *AIAA Journal* 40 (11) (2002) 2145–2187.
- [4] S. J. Murray, M. Marioni, S. M. Allen, R. C. O’Handley, 6% magnetic-field-induced strain by twin-boundary motion in ferromagnetic Ni-Mn-Ga, *Applied Physics Letters* 77 (6) (2000) 886–888.
- [5] L. E. Faidley, M. J. Dapino, G. N. Washington, T. A. Lograsso, Reversible strain in Ni-MnGa with collinear field and stress, in: *Proceedings of SPIE, Smart Structures and Materials: Active Materials: Behavior and Mechanics*, San Diego, CA, 6–10 March 2005. Vol. 5761 (2005) 501–512.
- [6] L. Hirsinger, N. Creton, C. Lexcellent, Stress-induced phase transformation in Ni-Mn-Ga alloys: Experiments and modelling, *Material Science & Engineering A* 378 (2004) 365–369.
- [7] V. A. Chernenko, V. V. Kokorin, O. M. Babii, I. K. Zasimchuk, Phase diagrams in the Ni-Mn-Ga system under compression, *Intermetallics* 6 (1) (1998) 29–34.
- [8] J. Pons, V. A. Chernenko, E. Cesari, V. A. L’vov, Stress-strain-temperature behaviour for martensitic transformation in Ni-Mn-Ga single crystals compressed

- along $\langle 001 \rangle$ and $\langle 110 \rangle$ axes, *Journal de Physique IV France* 112 (2003) 939–942.
- [9] V. V. Martynov, V. V. Kokorin, The crystal structure of thermally- and stress-induced martensites in Ni_2MnGa single crystals, *Journal de Physique III France* 2 (1992) 739–749.
- [10] H. E. Karaca, I. Karaman, D. C. Lagoudas, H. J. Maier, Y. I. Chumlyakov, Recoverable stress-induced martensitic transformation in a ferromagnetic CoNiAl alloy, *Scripta Materialia* 49 (2003) 831–836.
- [11] R. C. O’Handley, S. M. Allen, D. I. Paul, C. P. Henry, M. Marioni, D. Bono, C. Jenkins, A. Banful, R. Wager, Keynote address: Magnetic field-induced strain in single crystal Ni-Mn-Ga , in: *Proceedings of SPIE, Symposium on Smart Structures and Materials* 5053 (2003) 200–206.
- [12] K. Ullakko, J. K. Huang, C. Kantner, R. C. O’Handley, V. V. Kokorin, Large magnetic-field-induced strains in Ni_2MnGa single crystals, *Applied Physics Letters* 69 (13) (1996) 1966–1968.
- [13] R. A. Kellogg, A. B. Flatau, A. E. Clark, M. Wun-Fogle, T. A. Lograsso, Temperature and stress dependencies of the magnetic and magnetostrictive properties of $\text{Fe}_{0.81}\text{Ga}_{0.19}$, *Journal of Applied Physics* 91 (10) (2002) 7821–7823.
- [14] J. Tellinen, I. Suorsa, I. Jääskeläinen, Aaltio, K. Ullakko, Basic properties of magnetic shape memory actuators, in: *Proceedings of the 8th International Conference ACTUATOR 2002, Bremen, Germany, 10-12 June 2002* (2002) 566–569.

- [15] A. Bhattacharyya, D. C. Lagoudas, Y. Wang, V. K. Kinra, On the role of thermoelectric heat transfer in the design of SMA actuators: Theoretical modeling and experiment, *Smart Materials and Structures* 4 (1995) 252–263.
- [16] B. D. Cullity, *Introduction to Magnetic Materials*, Addison-Wesley, Reading, MA, 1972.
- [17] R. C. O’Handley, *Modern Magnetic Materials*, John Wiley & Sons, New York, 2000.
- [18] C. Kittel, *Introduction to Solid State Physics*, 7th Edition, John Wiley & Sons, New York, 1996.
- [19] M. Pasquale, Mechanical sensors and actuators, *Sensors and Actuators A* 106 (2003) 142–148.
- [20] I. Suorsa, J. Tellinen, K. Ullakko, E. Pagounis, Voltage generation induced by mechanical straining in magnetic shape memory materials, *Journal of Applied Physics* 95 (12) (2004) 8054–8058.
- [21] P. Müllner, V. A. Chernenko, M. Wollgarten, Kostorz, Large cyclic deformations of a Ni-Mn-Ga shape memory alloy induced by magnetic fields, *Journal of Applied Physics* 92 (11) (2002) 6708–6713.
- [22] P. J. Webster, K. R. A. Ziebeck, S. L. Town, M. S. Peak, Magnetic order and phase transformation in Ni₂MnGa, *Philosophical Magazine B* 49 (3) (1984) 295–310.
- [23] I. K. Zasimchuk, V. V. Kokorin, V. V. Martynov, A. V. Tkachenko, V. A. Chernenko, Crystal structure of martensite in Heusler alloy Ni₂MnGa, *Physics of Metals and Metallography* 69 (6) (1990) 104–108.

- [24] A. Sozinov, A. A. Likhachev, N. Lanska, O. Söderberg, K. Ullakko, V. K. Lindroos, Effect of crystal structure on magnetic-field-induced strain in Ni-Mn-Ga, in: Proceedings of SPIE, Symposium on Smart Structures and Materials 5053 (2003) 586–594.
- [25] J. Cui, T. W. Shield, R. D. James, Phase transformation and magnetic anisotropy of an iron-palladium ferromagnetic shape-memory alloy, *Acta Materialia* 52 (2004) 35–47.
- [26] R. D. James, M. Wuttig, Magnetostriction of martensite, *Philosophical Magazine A* 77 (5) (1998) 1273–1299.
- [27] T. W. Shield, Magnetomechanical testing machine for ferromagnetic shape-memory alloys, *Review of Scientific Instruments* 74 (9) (2003) 4077–4088.
- [28] T. Yamamoto, M. Taya, Y. Sutou, Y. Liang, T. Wada, L. Sorensen, Magnetic field-induced reversible variant rearrangement in Fe-Pd single crystals, *Acta Materialia* 52 (17) (2004) 5083–5091.
- [29] S. J. Murray, R. Hayashi, M. Marioni, S. M. Allen, R. C. O’Handley, Magnetic and mechanical properties of FeNiCoTi and NiMnGa magnetic shape memory alloys, *Proceedings of SPIE* 3675 (1999) 204–211.
- [30] A. Fujita, K. Fukamichi, F. Gejima, R. Kainuma, K. Ishida, Magnetic properties and large magnetic-field-induced strains in off-stoichiometric Ni-Mn-Al heusler alloys, *Applied Physics Letters* 77 (19) (2000) 3054–3056.
- [31] T. Kakeshita, T. Takeuchi, T. Fukuda, M. Tsujiguchi, T. Saburi, R. Oshima, S. Muto, Giant magnetostriction in an ordered Fe₃Pt single crystal exhibiting a martensitic transformation, *Applied Physics Letters* 77 (10) (2000) 1502–1504.

- [32] M. Wuttig, L. Liu, K. Tsuchiya, R. D. James, Occurrence of ferromagnetic shape memory alloys (invited), *Journal of Applied Physics* 87 (9) (2000) 4707–4711.
- [33] M. Wuttig, J. Li, C. Craciunescu, A new ferromagnetic shape memory alloys system, *Scripta Materialia* 44 (2001) 2393–2397.
- [34] H. Morito, A. Fujita, R. Kainuma, K. Ishida, K. Oikawa, Magnetocrystalline anisotropy in single-crystal Co-Ni-Al ferromagnetic shape-memory alloy, *Applied Physics Letters* 81 (9) (2002) 1657–1659.
- [35] T. Sakamoto, T. Fukuda, T. Kakeshita, T. Takeuchi, K. Kishio, Magnetic field-induced strain in iron-based ferromagnetic shape memory alloys, *Journal of Applied Physics* 93 (10) (2003) 8647–8649.
- [36] A. A. Cherechukin, I. E. Dikshtein, D. I. Ermakov, A. V. Glebov, V. V. Koldov, D. A. Kosolapov, V. G. Shavrov, A. A. Tulaikova, E. P. Krasnoperov, T. Takagi, Shape memory effect due to magnetic field-induced thermoelastic martensitic transformation in polycrystalline Ni-Mn-Fe-Ga alloy, *Physics Letters A* 291 (2001) 175–183.
- [37] S. Jeong, K. Inoue, S. Inoue, K. Koterazawa, M. Taya, K. Inoue, Effect of magnetic field on martensite transformation in a polycrystalline Ni₂MnGa, *Material Science & Engineering A* 359 (2003) 253–260.
- [38] S. J. Murray, M. Farinelli, C. Kantner, J. K. Huang, A. M. Allen, R. C. O’Handley, Field-induced strain under load in Ni-Mn-Ga magnetic shape memory materials, *Journal of Applied Physics* 83 (11) (1998) 7297–7299.
- [39] K. Ullakko, Y. Ezer, A. Sozinov, G. Kimmel, P. Yakovenko, V. K. Lindroos,

- Magnetic-field-induced strains in polycrystalline Ni-Mn-Ga at room temperature, *Scripta Materialia* 44 (2001) 475–480.
- [40] T. Wada, Y. Liang, H. Kato, T. Tagawa, M. Taya, T. Mori, Structural change and straining in Fe-Pd polycrystals by magnetic field, *Material Science & Engineering A* 361 (2003) 75–82.
- [41] M. A. Marioni, R. C. O’Handley, S. A. Allen, Analytical model for field-induced strain in ferromagnetic shape-memory alloy polycrystals, *Journal of Applied Physics* 91 (10) (2002) 7807–7809.
- [42] T. Kakeshita, T. Takeuchi, T. Fukuda, T. Saburi, R. Oshima, S. Muto, K. Kishio, Magnetic field-induced martensitic transformation and giant magnetostriction in Fe-Ni-Co-Ti and ordered Fe₃Pt shape memory alloys, *Materials Transactions, JIM* 41 (8) (2000) 882–887.
- [43] I. Karaman, H. E. Karaca, B. Basaran, D. C. Lagoudas, Y. I. Chumlyakov, H. J. Maier, Stress-assisted reversible magnetic field-induced phase transformation in Ni₂MnGa magnetic shape memory alloys, *Scripta Materialia* 55 (4) (2006) 403–406.
- [44] O. Heczko, L. Straka, K. Ullakko, Relation between structure, magnetization process and magnetic shape memory effect of various martensites occurring in Ni-Mn-Ga alloys, *Journal de Physique IV France* 112 (2003) 959–962.
- [45] A. A. Likhachev, A. Sozinov, K. Ullakko, Different modeling concepts of magnetic shape memory and their comparison with some experimental results obtained in Ni-Mn-Ga, *Material Science & Engineering A* 378 (2004) 513–518.

- [46] A. DeSimone, R. D. James, A theory of magnetostriction oriented towards applications, *Journal of Applied Physics* 81 (8) (1997) 5706–5708.
- [47] A. DeSimone, R. James, A constrained theory of magnetoelasticity, *Journal of the Mechanics and Physics of Solids* 50 (2002) 283–320.
- [48] A. DeSimone, R. D. James, Energetics of magnetoelastic domains in ferromagnetic shape memory alloys, *Journal de Physique* 112 (2003) 969–972.
- [49] R. C. O’Handley, Model for strain and magnetization in magnetic shape-memory alloys, *Journal of Applied Physics* 83 (6) (1998) 3263–3270.
- [50] S. J. Murray, R. C. O’Handley, S. M. Allen, Model for discontinuous actuation of ferromagnetic shape memory alloy under stress, *Journal of Applied Physics* 89 (2) (2001) 1295–1301.
- [51] A. A. Likhachev, K. Ullakko, Magnetic-field-controlled twin boundaries motion and giant magneto-mechanical effects in Ni-Mn-Ga shape memory alloy, *Physics Letters A* 275 (2000) 142–151.
- [52] L. Hirsinger, C. Lexcellent, Modelling detwinning of martensite platelets under magnetic and (or) stress actions on NiMnGa alloys, *Journal of Magnetism and Magnetic Materials* 254–255 (2003) 275–277.
- [53] L. Hirsinger, C. Lexcellent, Internal variable model for magneto-mechanical behaviour of ferromagnetic shape memory alloys Ni-Mn-Ga, *Journal de Physique IV France* 112 (2003) 977–980.
- [54] B. Kiefer, D. C. Lagoudas, Phenomenological modeling of ferromagnetic shape memory alloys, in: *Proceedings of SPIE, Smart Structures and Materials: Ac-*

- tive Materials: Behavior and Mechanics, San Diego, CA, 14–18 March 2004 5387 (2004) 164–176.
- [55] B. Kiefer, D. C. Lagoudas, Magnetic field-induced martensitic variant reorientation in magnetic shape memory alloys, *Philosophical Magazine Special Issue: Recent Advances in Theoretical Mechanics, in Honor of SES 2003 A.C. Eringen Medalist G.A. Maugin* 85 (33-35) (2005) 4289–4329.
- [56] B. Kiefer, D. C. Lagoudas, Modeling of the magnetic field-induced martensitic variant reorientation and the associated magnetic shape memory effect in MSMA, in: *Proceedings of SPIE, Smart Structures and Materials: Active Materials: Behavior and Mechanics, San Diego, CA, 6–10 March 2005* 5761 (2005) 454–465.
- [57] B. Kiefer, D. C. Lagoudas, Modeling of the hysteretic strain and magnetization response in magnetic shape memory alloys, in: *Proceedings of AIAA 2006* paper 1766 (2006) 1–15.
- [58] B. Kiefer, H. E. Karaca, D. C. Lagoudas, I. Karaman, Characterization and modeling of the magnetic field-induced strain and work output in Ni_2MnGa shape memory alloys, *Journal of Magnetism and Magnetic Materials*, in print X (2006) xxx.
- [59] B. Kiefer, D. Lagoudas, Application of a magnetic sma constitutive model in the analysis of magnetomechanical boundary value problems, in: *Proceedings of SPIE, Smart Structures and Materials: Active Materials: Behavior and Mechanics, San Diego, CA, 26 February–2 March 2006* 6170 (2006) 330–341.
- [60] D. C. Lagoudas, B. Kiefer, A. J. Broedersdorf, Accurate interpretation of magnetic shape memory alloy experiments utilizing coupled magnetostatic analysis,

- in: Proceedings of ASME, International Mechanical Engineering Congress and Exposition, Chicago, IL, 5–10 November 2006 IMECE2006-15296 (2006) 1–11.
- [61] H. Tan, M. H. Elahinia, On the modeling of ferromagnetic shape memory alloy actuators, Submitted to Elsevier May 2006 .
- [62] N. I. Glavatska, A. A. Rudenko, I. N. Glavatskiy, V. A. L’vov, Statistical model of magnetostrain effect in martensite, *Journal of Magnetism and Magnetic Materials* 265 (2) (2003) 142–151.
- [63] V. A. Chernenko, V. A. L’vov, P. Müllner, G. Kostorz, T. Takagi, Magnetic-field-induced superelasticity of ferromagnetic thermoelastic martensites: Experiments and modeling, *Physical Review B* 69 (2004) 134410–(1–8).
- [64] P. Müllner, V. A. Chernenko, G. Kostorz, A microscopic approach to the magnetic-field-induced deformation of martensite (magnetoplasticity), *Journal of Magnetism and Magnetic Materials* 267 (2003) 325–334.
- [65] V. D. Buchelnikov, S. I. Bosko, The kinetics of phase transformations in ferromagnetic shape memory alloys Ni-Mn-Ga, *Journal of Magnetism and Magnetic Materials* 258–259 (2003) 497–499.
- [66] S. Govindjee, G. J. Hall, A computational model for shape memory alloys, *International Journal of Solids and Structures* 37 (5) (2000) 735–760.
- [67] R. C. Smith, S. Seelecke, M. Dapino, Z. Ounaies, A unified framework for modeling hysteresis in ferroic materials, *Journal of the Mechanics and Physics of Solids* 54 (2006) 46–85.
- [68] J. Kiang, L. Tong, Modelling of magneto-mechanical behavior of Ni-Mn-Ga

- single crystals, *Journal of Magnetism and Magnetic Materials* 292 (2005) 394–412.
- [69] K. Tanaka, A thermomechanical sketch of shape memory effect: One-dimensional tensile behavior, *Res Mechanica* 18 (1986) 251–263.
- [70] C. Liang, C. A. Rogers, One-dimensional thermomechanical constitutive relations for shape memory materials, *Journal of Intelligent Material Systems and Structures* 1 (1990) 207–234.
- [71] J. G. Boyd, D. C. Lagoudas, A thermodynamical constitutive model for shape memory materials. Part I. The monolithic shape memory alloy, *International Journal of Plasticity* 12 (6) (1996) 805–842.
- [72] D. C. Lagoudas, Z. Bo, M. A. Qidwai, A unified thermodynamic constitutive model for SMA and finite element analysis of active metal matrix composites, *Mechanics of Composite Materials and Structures* 3 (1996) 153–179.
- [73] J. Lubliner, F. Auricchio, Generalized plasticity and shape memory alloys, *International Journal of Solids and Structures* 33 (7) (1996) 991–1003.
- [74] L. C. Brinson, M. S. Huang, Simplifications and comparisons of shape memory alloy constitutive models, *Journal of Intelligent Material Systems and Structures* 7 (1996) 108–114.
- [75] A. Bekker, L. C. Brinson, Temperature-induced phase transformation in a shape memory alloy: Phase diagram based kinetics approach, *Journal of the Mechanics and Physics of Solids* 45 (6) (1997) 949–988.
- [76] Z. Bo, D. C. Lagoudas, Thermomechanical modeling of polycrystalline SMAs

- under cyclic loading, Part I: Theoretical derivations, *International Journal of Engineering Science* 37 (1999) 1089–1140.
- [77] D. C. Lagoudas, Z. Bo, Thermomechanical modeling of polycrystalline SMAs under cyclic loading, Part II: Material characterization and experimental results for a stable transformation cycle, *International Journal of Engineering Science* 37 (1999) 1141–1173.
- [78] E. Patoor, D. C. Lagoudas, P. B. Entchev, L. C. Brinson, X. Gao, Shape memory alloys , Part I: General properties and modeling of single crystals, *Mechanics of Materials* 38 (5–6) (2006) 391–429.
- [79] D. C. Lagoudas, P. B. Entchev, P. Popov, E. Patoor, L. C. Brinson, X. Gao, Shape memory alloys, Part II: Modeling of polycrystals, *Mechanics of Materials* 38 (5–6) (2006) 430–462.
- [80] B. D. Coleman, M. E. Gurtin, Thermodynamics with internal state variables, *The Journal of Chemical Physics* 47 (2) (1967) 597–613.
- [81] B. D. Coleman, W. Noll, The thermodynamics of elastic materials with heat conduction and viscosity, *Archive for Rational Mechanics and Analysis* 13 (1963) 167–178.
- [82] M. A. Qidwai, D. C. Lagoudas, Numerical impementation of a shape memory alloy thermomechanical constitutive model using return mapping algorithms, *International Journal for Numerical Methods in Engineering* 47 (2000) 1123–1168.
- [83] S. Leclercq, C. Lexcellent, A general macroscopic description of the thermo-

- mechanical behavior of shape memory alloys, *Journal of the Mechanics and Physics of Solids* 44 (6) (1996) 953–980.
- [84] S. G. Shu, D. C. Lagoudas, D. Hughes, J. T. Wen, Modeling of a flexible beam actuated by shape memory alloy wires, *Smart Materials and Structures* 6 (1997) 265–277.
- [85] P. Popov, D. C. Lagoudas, A 3-d constitutive model for shape memory alloys incorporating pseudoelasticity and detwinning of self-accommodated martensite, *International Journal of Plasticity*, in print X (2006) xxx.
- [86] P. A. Popov, Constitutive modelling of shape memory alloys and upscaling of deformable porous media, Ph.D. dissertation, Texas A&M University, Department of Aerospace Engineering, College Station, TX (May 2005).
- [87] A. N. Vasil'ev, A. D. Bozhko, V. V. Khovailo, I. E. Dikshtein, V. G. Shavrov, V. D. Buchelnikov, M. Matsumoto, S. Suzuki, T. Takagi, J. Tani, Structural and magnetic phase transitions in shape-memory alloys $\text{Ni}_{2+x}\text{Mn}_{1-x}\text{Ga}$, *Physical Review B* 59 (2) (1999) 1113–1119.
- [88] F. Albertini, L. Pareti, A. Paoluzi, L. Morellon, P. A. Algarabel, M. R. Ibarra, L. Righi, Composition and temperature dependence of the magnetocrystalline anisotropy in $\text{Ni}_{2+x}\text{Mn}_{1+y}\text{Ga}_{1+z}$ ($x+y+z=0$) Heusler alloys, *Applied Physics Letters* 81 (21) (2002) 4032–4034.
- [89] F. Albertini, F. Canepa, S. Cirafici, E. A. Franceschi, M. Napoletano, A. Paoluzi, L. Pareti, M. Solzi, Composition dependence of magnetic and magnetothermal properties of Ni-Mn-Ga shape memory alloys, *Journal of Magnetism and Magnetic Materials* 272–276 (Part 3) (2004) 2111–2112.

- [90] O. Heczko, L. Straka, Compositional dependence of structure, magnetization and magnetic anisotropy in Ni-Mn-Ga magnetic shape memory alloys, *Journal of Magnetism and Magnetic Materials* 272–276 (Part 3) (2004) 2045–2046.
- [91] S. J. Murray, M. Marioni, A. M. Kukla, J. Robinson, R. C. O’Handley, S. M. Allen, Large field induced strain in single crystalline Ni-Mn-Ga ferromagnetic shape memory alloy, *Journal of Applied Physics* 87 (9) (2000) 5774–5776.
- [92] S. J. Murray, Magneto-mechanical properties and applications of Ni-MnGa ferromagnetic shape memory alloy, Ph.D. dissertation, Massachusetts Institute of Technology, Cambridge, MA (February 2000).
- [93] L. Hirsinger, N. Creton, C. Lexcellent, From crystallographic properties to macroscopic detwinning strain and magnetisation of Ni-Mn-Ga magnetic shape memory alloys, *Journal de Physique IV France* 115 (2004) 111–120.
- [94] O. Heczko, N. Lanska, O. Soderberg, K. Ullakko, Temperature variation of structure and magnetic properties of Ni-Mn-Ga magnetic shape memory alloys, *Journal of Magnetism and Magnetic Materials* 242–245 (2002) 1446–1449.
- [95] A. A. Likhachev, K. Ullakko, Quantitative model of large magnetostrain effect in ferromagnetic shape memory alloys, *The European Physical Journal B* 14 (2) (2000) 263–267.
- [96] R. Tickle, R. D. James, Magnetic and magnetomechanical properties of Ni_2MnGa , *Journal of Magnetism and Magnetic Materials* 195 (3) (1999) 627–638.
- [97] R. Tickle, Ferromagnetic shape memory materials, Ph.D. dissertation, University of Minnesota, Minneapolis, MN (May 2000).

- [98] H. E. Karaca, I. Karaman, B. Basaran, Y. I. Chumlyakov, H. J. Maier, Magnetic field and stress induced martensite reorientation in NiMnGa ferromagnetic shape memory alloy single crystals, *Acta Materialia* 54 (1) (2006) 233–245.
- [99] N. A. Spaldin, *Magnetic Materials: Fundamentals and Device Applications*, Cambridge University Press, Cambridge, UK, 2003.
- [100] C. Kittel, Physical theory of ferromagnetic domains, *Reviews of Modern Physics* 21 (4) (1949) 541–583.
- [101] A. Hubert, R. Schäfer, *Magnetic Domains*, Springer-Verlag, New York, 2001.
- [102] O. Heczko, Determination of ordinary magnetostriction in Ni-Mn-Ga magnetic shape memory alloy, *Journal of Magnetism and Magnetic Materials* 290–291 (2005) 846–849.
- [103] O. Heczko, Magnetic shape memory effect and magnetization reversal, *Journal of Magnetism and Magnetic Materials* 290–291 (2) (2005) 787–794.
- [104] A. A. Likhachev, A. Sozinov, K. Ullakko, Optimizing work output in Ni-Mn-Ga and other ferromagnetic shape memory alloys other ferromagnetic shape-memory alloys, in: *Proceedings of SPIE, Symposium on Smart Structures and Materials* 4699 (2002) 553–563.
- [105] Y. Ge, O. Heczko, O. Söderberg, V. K. Lindroos, Various magnetic domain structures in Ni-Mn-Ga martensite exhibiting magnetic shape memory effect, *Journal of Applied Physics* 96 (4) (2004) 2159–2163.
- [106] M. R. Sullivan, H. D. Chopra, Temperature- and field-dependent evolution of micromagnetic structure in ferromagnetic shape-memory-alloys, *Physical Review B* 70 (2004) 094427–(1–8).

- [107] M. R. Sullivan, A. A. Shah, H. D. Chopra, Pathways of structural and magnetic transition in ferromagnetic shape-memory alloys, *Physical Review B* 70 (2004) 094428–(1–8).
- [108] G. A. Maugin, *Continuum Mechanics of Electromagnetic Solids*, Vol. 33 of North-Holland Series in Applied Mathematics and Mechanics, Elsevier Science Publishers, Amsterdam, 1988.
- [109] E. A. Guggenheim, On magnetic and electrostatic energy, *Proceedings of the Royal Society of London. Series A, Mathematical and Physical Sciences* 155 (884) (1936) 49–70.
- [110] E. A. Guggenheim, The thermodynamics of magnetization, *Proceedings of the Royal Society of London. Series A, Mathematical and Physical Sciences* 155 (884) (1936) 70–101.
- [111] L. D. Landau, E. M. Lifshitz, L. P. Pitaevskii, *Electrodynamics of Continuous Media*, 2nd Edition, Pergamon Press, New York, 1984.
- [112] H. F. Tiersten, Coupled magnetomechanical equations for magnetically saturated insulators, *Journal of Mathematical Physics* 5 (9) (1964) 1298–1318.
- [113] W. F. Brown, Jr., *Magnetoelastic Interactions*, Vol. 9 of *Tracts in Natural Philosophy*, Springer-Verlag, New York, 1966.
- [114] P. Penfield Jr., H. A. Haus, *Electrodynamics of Moving Media*, Vol. 40 of *Research Monographs*, MIT Press, Cambridge, MA, 1967.
- [115] B. D. Coleman, E. H. Dill, Thermodynamic restrictions on the constitutive equations of electromagnetic theory, *Zeitschrift für Angewandte Mathematik und Physik* 22 (1971) 691–702.

- [116] B. D. Coleman, E. H. Dill, On the thermodynamics of electromagnetic fields in materials with memory, *Archive for Rational Mechanics and Analysis* 41 (1971) 132–162.
- [117] C. Truesdell, W. Noll, *The Non-Linear Field Theories of Mechanics*, 3rd Edition, Springer-Verlag, Berlin, 2004.
- [118] C. Truesdell, R. Toupin, *Principles of Classical Mechanics and Field Theory*, Vol. III/1 of *Encyclopedia of Physics*, Springer-Verlag, Berlin, 1960, Ch. The Classical Field Theories, pp. 226–795.
- [119] A. C. Eringen, G. A. Maugin, *Electrodynamics of Continua I — Foundations and Solid Media*, Springer-Verlag, New York, 1990.
- [120] A. C. Eringen, G. A. Maugin, *Electrodynamics of Continua II — Fluids and Complex Media*, Springer-Verlag, New York, 1990.
- [121] Y. H. Pao, K. Hutter, Electrodynamic for moving elastic solids and viscous fluids, *Proceedings of the IEEE* 63 (7) (1975) 1011–1021.
- [122] K. Hutter, A. A. F. van de Ven, *Field Matter Interactions in Thermoelastic Solids*, Vol. 88 of *Lecture Notes in Physics*, Springer-Verlag, New York, 1978.
- [123] K. Hutter, Y.-H. Pao, A dynamic theory for magnetizable elastic solids with thermal and electrical conduction, *Journal of Elasticity* 4 (3) (1974) 89–114.
- [124] H. H. Woodson, J. R. Melcher, *Electromechanical Dynamics, Part I: Discrete Systems*, Reprint of 1968 Edition, Krieger Publishing Company, Malabar, FL, 1990.

- [125] H. H. Woodson, J. R. Melcher, *Electromechanical Dynamics, Part II: Fields, Forces and Motion*, Reprint of 1968 Edition, Krieger Publishing Company, Malabar, FL, 1990.
- [126] G. A. Holzapfel, *Nonlinear Solid Mechanics: A Continuum Approach For Engineering*, Reprint with Corrections Edition, John Wiley & Sons, Chichester, UK, 2000.
- [127] M. E. Gurtin, *An Introduction to Continuum Mechanics*, Vol. 158 of *Mathematics in Science and Engineering*, Academic Press, San Diego, 1981.
- [128] H. E. Knoepfel, *Magnetic Fields: A Comprehensive Theoretical Treatise for Practical Use*, John Wiley & Sons, New York, 2000.
- [129] A. G. Maugin, *The Thermodynamics of Nonlinear Irreversible Behaviors*, Vol. 27 of *Nonlinear Science, Series A*, World Scientific, Singapore, 1999.
- [130] L. E. Malvern, *Introduction to the Mechanics of a Continuous Medium*, Series in Engineering of the Physical Sciences, Prentice Hall, Upper Saddle River, NJ, 1969.
- [131] C. Mueller, *Thermodynamic modeling of polycrystalline shape memory alloys at finite strains*, Ph.D. dissertation, Ruhr-Universität Bochum, Bochum, Germany (August 2003).
- [132] W. S. Slaughter, *The Linearized Theory of Elasticity*, Birkhäuser, Boston, 2002.
- [133] J. Lubliner, *Plasticity Theory*, Macmillan Publishing Company, New York, 1990.

- [134] L. Anand, M. E. Gurtin, Thermal effects in the superelasticity of crystalline shape-memory materials, *Journal of the Mechanics and Physics of Solids* 51 (2003) 1015–1058.
- [135] P. B. Entchev, Micromechanical modeling of porous shape memory alloys, Ph.D. dissertation, Texas A&M University, Department of Aerospace Engineering, College Station, Tx (May 2002).
- [136] M. A. Qidwai, D. C. Lagoudas, On the thermodynamics and transformation surfaces of polycrystalline NiTi shape memory alloy material, *International Journal of Plasticity* 16 (2000) 1309–1343.
- [137] F. Auricchio, R. L. Taylor, Shape-memory alloys: Modelling and numerical simulation of the finite-strain superelastic behavior., *Computer Methods in Applied Mechanics and Engineering* 143 (1–2) (1997) 175–194.
- [138] W. M. Lai, D. Rubin, E. Krempl, *Introduction to Continuum Mechanics*, 3rd Edition, Butterworth-Heinemann, Woburn, MA, 1993.
- [139] F. P. Incropera, D. P. DeWitt, *Fundamentals of Heat and Mass Transfer*, 4th Edition, John Wiley & Sons, New York, 1981.
- [140] H. F. Tiersten, *Linear Piezoelectric Plate Vibrations*, Plenum Press, New York, 1969.
- [141] M. Kamlah, Z. Wang, A microscopically motivated constitutive model for piezoceramics under general electromechanical loading, in: *Proceedings of SPIE, Smart Structures and Materials: Active Materials: Behavior and Mechanics*, San Diego, CA, 14–18 March 2004 Vol. 5387 (2004) 390–401.

- [142] C. Kittel, J. K. Galt, Ferromagnetic domain theory, *Solid State Physics* 3 (1956) 437–564.
- [143] R. M. Bozorth, *Ferromagnetism*, reissue of 1951 Edition, IEEE Press, 1993.
- [144] P. B. Entchev, D. C. Lagoudas, Modeling porous shape memory alloys using micromechanical averaging techniques, *Mechanics of Materials* 34 (1) (2002) 1–24.
- [145] A. N. Bogdanov, A. DeSimone, S. Müller, U. K. Rössler, Phenomenological theory of magnetic-field-induced strains in ferromagnetic shape-memory materials, *Journal of Magnetism and Magnetic Materials* 261 (2003) 204–209.
- [146] V. A. Chernenko, V. A. L’vov, Thermodynamics of martensitic transformations affected by hydrostatic pressure, *Philosophical Magazine A* 73 (4) (1996) 999–1008.
- [147] J. C. Simo, T. J. R. Hughes, *Computational Inelasticity*, Vol. 7 of *Interdisciplinary Applied Mathematics*, Springer-Verlag, New York, 1998.
- [148] Y. Sato, K. Tanaka, Estimation of energy dissipation in alloys due to stress-induced martensitic transformation, *Res Mechanica* 23 (1988) 381–392.
- [149] A. S. Khan, S. Huang, *Continuum Theory of Plasticity*, John Wiley & Sons, New York, 1995.
- [150] A. Bekker, L. C. Brinson, Phase diagram based description of the hysteresis behavior of shape memory alloys, *Acta Materialia* 46 (10) (1998) 3649–3665.
- [151] R. Tickle, R. D. James, T. Shield, P. Schumacher, M. Wuttig, V. V. Kokorin, Ferromagnetic shape memory in the NiMnGa system, *IEEE Transactions on Magnetics* 35 (5) (1999) 4301–4310.

- [152] J. D. Jackson, *Classical Electrodynamics*, 2nd Edition, John Wiley & Sons, New York, 1975.
- [153] H. N. Bertram, *Theory of Magnetic Recording*, Cambridge University Press, Cambridge, UK, 1994.
- [154] E. Schlömann, A sum rule concerning the inhomogeneous demagnetizing field in nonellipsoidal samples, *Journal of Applied Physics* 33 (9) (1962) 2825–2826.
- [155] J. D. Eshelby, The determination of the elastic field of an ellipsoidal inclusion, and related problems, *Proceedings of the Royal Society of London. Series A, Mathematical and Physical Sciences* 241 (1226) (1957) 376–396.
- [156] T. Mura, *Micromechanics of Defects in Solids*, 2nd Edition, Mechanics of Elastic and Inelastic Solids, Kluwer Academic Publisher, Dordrecht, The Netherlands, 1987.
- [157] R. Moskowitz, E. Della Torre, Theoretical aspects of demagnetization tensors, *IEEE Transactions on Magnetics* 2 (4) (1966) 739–744.
- [158] H. Fukushima, Y. Nakatani, N. Hayashi, Volume average demagnetizing tensor of rectangular prisms, *IEEE Transactions on Magnetics* 34 (1) (1998) 193–198.
- [159] R. W. Cahn, Plastic deformation of alpha-uranium; Twinning and slip, *Acta Metallurgica* 1 (1) (1953) 49–70.
- [160] B. A. Bilby, A. G. Crocker, The theory of the crystallography of deformation twinning, *Proceedings of the Royal Society of London. Series A, Mathematical and Physical Sciences* 288 (1413) (1965) 240–255.

- [161] Y. M. Jin, Y. U. Wang, A. Kazaryan, Y. Wang, D. E. Laughlin, A. G. Khachaturyan, Magnetic structure and hysteresis in hard magnetic nanocrystalline film: Computer simulation, *Journal of Applied Physics* 92 (10) (2002) 6172–6181.
- [162] Y. M. Jin, A. Artemev, A. G. Khachaturyan, Three-dimensional phase field model of low-symmetry martensitic transformation in polycrystal: Simulation of ζ'_2 martensite in AuCd alloys, *Acta Materialia* 49 (2001) 2309–2320.
- [163] A. Kazaryan, Y. Wang, Y. M. Jin, Y. U. Wang, A. G. Khachaturyan, L. Wang, D. E. Laughlin, Development of magnetic domains in hard ferromagnetic thin films of polytwinned microstructure, *Journal of Applied Physics* 92 (12) (2002) 7408–7414.
- [164] E. Cesari, V. A. Chernenko, J. Font, J. Muntasell, AC technique applied to c_p measurements in Ni-Mn-Ga alloys, *Thermochemica Acta* 433 (1–2) (2005) 153–156.
- [165] I. Gersten, J. F. W. Smith, *The Physics and Chemistry of Materials*, John Wiley & Sons, New York, 2001.

APPENDIX A

CONCEPTS OF CONTINUUM MECHANICS:
DEFINITIONS AND DERIVATIONS

A1. Mathematical Preliminaries

Divergence theorem [127]: If \mathcal{R} is a closed bounded region with piecewise smooth boundary $\partial\mathcal{R}$ (regular region) and unit outward normal \mathbf{n} , and $\mathbf{f} : \mathcal{R} \rightarrow \mathcal{V}$ is a smooth vector field, where \mathcal{V} is the Euclidean vector space associated with the Euclidean point space \mathcal{E} , then

$$\int_{\mathcal{R}} \operatorname{div} \mathbf{f} \, dV = \oint_{\partial\mathcal{R}} \mathbf{f} \cdot \mathbf{n} \, dA . \quad (\text{A.1})$$

Stokes theorem [132]: Let \mathcal{S} be a regular surface in space, with the unit outward normal \mathbf{n} , that is bounded by a simple closed curve $\partial\mathcal{S}$. For the smooth vector field $\mathbf{f} : \mathcal{S} \rightarrow \mathcal{V}$ the identity

$$\int_{\mathcal{S}} \operatorname{curl} \mathbf{f} \cdot \mathbf{n} \, dA = \oint_{\partial\mathcal{S}} \mathbf{f} \cdot d\mathbf{x} , \quad (\text{A.2})$$

holds, where $d\mathbf{x}$ is an increment along $\partial\mathcal{S}$.

A2. Kinematics

In continuum mechanics one defines a *material body* as the collection of particles which in the *reference configuration* occupy the (possibly unbounded) regular region \mathcal{B} of \mathcal{E} (cf. [127]); bounded regular subregions of \mathcal{B} are called *parts* \mathcal{P} . The material body is subjected to the motion $\hat{x} : \mathcal{B} \times \mathbb{R} \rightarrow \mathcal{E}$, such that at time t the body \mathcal{B} and

part \mathcal{P} are mapped (one-to-one) into $\mathcal{B}_t = \hat{x}(\mathcal{B}, t)$ and $\mathcal{P}_t = \hat{x}(\mathcal{P}, t)$, respectively. The material point \mathbf{X} , defined in the reference configuration \mathcal{B} , is thus mapped into the point \mathbf{x} , which is defined in the *deformed (current) configuration* at the time t . The *trajectory* of a particle is defined as [127]

$$\mathcal{T} = \{(\mathbf{x}, t) | \mathbf{x} \in \mathcal{B}_t, t \in \mathbb{R}\} . \quad (\text{A.3})$$

A *material field* is a function of the material point and time with domain $\mathcal{B} \times \mathbb{R}$; a spatial field is a function with domain \mathcal{T} [127]. The material field

$$\mathbf{F} := \text{Grad} \hat{x} , \quad (\text{A.4})$$

is called the *deformation gradient* and has the property $J := \det \mathbf{F} > 0$. The operator $\text{Grad}(\cdot)$, is the gradient taken with respect to the coordinates in the reference configuration.

The *material time derivative* of the smooth spatial fields $\phi(\mathbf{x}, t)$ and $\mathbf{u}(\mathbf{x}, t)$ is defined as [127]

$$\dot{\phi} = \frac{\partial \phi}{\partial t} + \mathbf{v} \cdot (\text{grad} \phi) ; \quad (\text{A.5a})$$

$$\dot{\mathbf{u}} = \frac{\partial \mathbf{u}}{\partial t} + (\text{grad} \mathbf{u}) \mathbf{v} . \quad (\text{A.5b})$$

All lower case differential operators, such as $\text{grad}(\cdot)$, $\text{div}(\cdot)$ and $\text{curl}(\cdot)$, are defined as derivatives with respect to the coordinates of the deformed configuration.

Reynold's transport theorem [127]: For a smooth scalar or vector valued spatial field $\Phi(\mathbf{x}, t)$ the following relation holds

$$\frac{d}{dt} \int_{\mathcal{P}_t} \Phi \, dV = \int_{\mathcal{P}_t} (\dot{\Phi} + \Phi \, \text{div} \mathbf{v}) \, dV = \int_{\mathcal{P}_t} \frac{\partial \Phi}{\partial t} \, dV + \oint_{\partial \mathcal{P}_t} \Phi \, \mathbf{v} \cdot \mathbf{n} \, dA . \quad (\text{A.6})$$

Similarly, for the rate of change of the flux of the vector field \mathbf{A} through the material surface \mathcal{S}_t the following transport theorem holds [121]

$$\frac{d}{dt} \int_{\mathcal{S}_t} \mathbf{A} \cdot \mathbf{n} \, dA = \int_{\mathcal{S}_t} \left[\frac{\partial \mathbf{A}}{\partial t} + \mathbf{v} \operatorname{div} \mathbf{A} - \operatorname{curl}(\mathbf{v} \times \mathbf{A}) \right] \cdot \mathbf{n} \, dA . \quad (\text{A.7})$$

A3. Derivation of the Local Forms of the Balance Laws

The derivation of the local forms of the conservation of mass and linear momentum are fairly straightforward and a standard procedure of continuum mechanics [126, 127, 130, 132, 138]. The steps were outlined in Section B of Chapter III and they differ from the usual derivation only by the electromagnetic body force term, which can be treated just as the usual body force term. The respective derivation for the **conservation of angular momentum**, however, is more involved since both body forces and body couples of magnetic nature will be accounted for and therefore this derivation is presented in detail. A similar derivation of the conservation of angular momentum that accounts for body couples and even surface couples and intrinsic angular momentum can be found in Malvern [130]. For simplicity and without loss of generality, the following proof will be conducted in index notation for cartesian coordinates. In this case the balance Eq. (3.16) takes the form

$$\frac{d}{dt} \int_{\mathcal{P}_t} \rho \epsilon_{ijk} x_i v_j \, dV = \oint_{\partial \mathcal{P}_t} \epsilon_{ijk} x_i t_j \, dA + \int_{\mathcal{P}_t} \rho [\epsilon_{ijk} x_i (f_j + f_j^m) + l_k^m] \, dV , \quad (\text{A.8})$$

where ϵ_{ijk} is the Levi-Civita permutation symbol. Using Cauchy's formula $t_i = \sigma_{ij} n_j$ and the conservation of mass in the form of Eq. (3.13), Eq. (A.8) can be rewritten as

$$\int_{\mathcal{P}_t} \frac{d}{dt} (\epsilon_{ijk} x_i v_j) \rho \, dV = \oint_{\partial \mathcal{P}_t} [\epsilon_{ijk} x_i \sigma_{jl} n_l] \, dA + \int_{\mathcal{P}_t} \rho [\epsilon_{ijk} x_i (f_j + f_j^m) + l_k^m] \, dV . \quad (\text{A.9})$$

By using the divergence theorem (A.1) and the chain rule one derives from Eq. (A.9)

$$\int_{\mathcal{P}_t} \epsilon_{ijk} [x_i \dot{v}_j + \dot{x}_i v_j] \rho dV = \int_{\mathcal{P}_t} \rho \left[\epsilon_{ijk} [x_{i,l} \sigma_{jl} + x_i \sigma_{j,l} + \rho x_i (f_j + f_j^m)] + l_k^m \right] dV . \quad (\text{A.10})$$

Invoking the conservation of linear momentum Eq. (3.15) yields

$$\int_{\mathcal{P}_t} [(\rho \dot{x}_i v_j - \sigma_{ji}) \epsilon_{ijk} - \rho l_k^m] dV = - \int_{\mathcal{P}_t} [\sigma_{ji} \epsilon_{ijk} + \rho l_k^m] dV = 0 . \quad (\text{A.11})$$

The last equality holds since the term $\dot{x}_i v_j \epsilon_{ijk} = v_i v_j \epsilon_{ijk}$ vanishes due to the fact that $v_i v_j$ is symmetric in the indices i and j while ϵ_{ijk} is antisymmetric. Since Eq. (A.11) has to hold for any volume \mathcal{P}_t , the local form of the conservation of angular momentum is given by

$$\sigma_{ji} \epsilon_{ijk} = -\rho l_k^m . \quad (\text{A.12})$$

For convenience this equation can be rewritten by defining \mathbf{L}^m as the dual of the vector \mathbf{l}^m , such that $\mathbf{L}^m \mathbf{a} = \mathbf{l}^m \times \mathbf{a}$ for any vector \mathbf{a} [121]¹. In index notation this relation is expressed as $L_{ij}^m = \frac{1}{2} \epsilon_{ijk} l_k^m$. By multiplying Eq. (A.12) with $-\frac{1}{2} \epsilon_{mnk}$ on both sides and using the identity $\epsilon_{ijk} \epsilon_{pqk} = \delta_{ip} \delta_{jq} - \delta_{iq} \delta_{jp}$ [132], it then follows

$$\begin{aligned} -\frac{1}{2} \epsilon_{mnk} \epsilon_{ijk} \sigma_{ji} &= \frac{1}{2} \rho \epsilon_{mnk} l_k^m \\ \text{or} \quad -\frac{1}{2} (\delta_{mi} \delta_{nj} - \delta_{mj} \delta_{ni}) \sigma_{ji} &= -\frac{1}{2} [\sigma_{nm} - \sigma_{mn}] = \rho L_{mn}^m \end{aligned} \quad (\text{A.13})$$

By defining the skew-symmetric part of the stress tensor as $\text{skw } \boldsymbol{\sigma} = \frac{1}{2} (\boldsymbol{\sigma} - \boldsymbol{\sigma}^T)$, the local form of the conservation of angular momentum accounting for magnetic body

¹This operation is similar to defining the axial vector \mathbf{w} for a skew-symmetric tensor \mathbf{W} such that $\mathbf{W} \mathbf{a} = \mathbf{w} \times \mathbf{a}$, $\forall \mathbf{a}$ [127, 132]. Unfortunately the nomenclature is not always consistent because many authors use the term *axial* and *dual* vector interchangeably [126, 138] for what is termed axial vector here.

couples in direct notation finally follows from Eq. (A.13) as

$$\text{skw } \boldsymbol{\sigma} = \rho \mathbf{L}^m ,$$

which is Eq. (3.17).

In generic terms the **conservation of energy** is expressed as [130]

$$\dot{E}^{\text{tot}} = \dot{K} + \dot{U} = P^{\text{inp}} + Q^{\text{inp}} , \quad (\text{A.14})$$

where E^{tot} is the total energy of the part, K is the kinetic energy, U is the internal energy, P^{inp} the total electro-magneto-mechanical power input and Q^{inp} the heat input. The left hand side of the conservation equation is then given by

$$\dot{E}^{\text{tot}}(\mathcal{P}_t) = \frac{d}{dt} \int_{\mathcal{P}_t} \left[\frac{1}{2} \rho \mathbf{v} \cdot \mathbf{v} + \rho u \right] dV = \frac{d}{dt} \int_{\mathcal{P}_t} \frac{1}{2} \rho \mathbf{v} \cdot \mathbf{v} dV + \int_{\mathcal{P}_t} \rho \dot{u} dV , \quad (\text{A.15})$$

where the conservation of mass Eq. (3.13) has been utilized. To determine the power input expression, a generalized **theorem of power expended** [127] is formulated

$$P^{\text{inp}} = \oint_{\partial \mathcal{P}_t} \mathbf{t}(\mathbf{n}) \cdot \mathbf{v} dA + \int_{\mathcal{P}_t} \rho [(\mathbf{f} + \mathbf{f}^m) \cdot \mathbf{v} + \mathbf{l}^m \cdot \mathbf{w} + \tilde{r}^m] dV . \quad (\text{A.16})$$

The first term on the right hand side of Eq. (A.16) can be rewritten using the divergence theorem Eq. (A.1) and applying the product rule $\text{div}(\mathbf{A}^T \mathbf{b}) = \mathbf{A} : (\text{grad } \mathbf{b}) + \mathbf{b} \cdot \text{div } \mathbf{A}$ [127], such that

$$\oint_{\partial \mathcal{P}_t} \mathbf{t}(\mathbf{n}) \cdot \mathbf{v} dA = \int_{\mathcal{P}_t} \text{div}(\boldsymbol{\sigma}^T \mathbf{v}) dV = \int_{\mathcal{P}_t} [\boldsymbol{\sigma} : (\text{grad } \mathbf{v}) + \mathbf{v} \cdot \text{div } \boldsymbol{\sigma}] dV . \quad (\text{A.17})$$

Using Eq. (A.17) in Eq. (A.16) yields

$$P^{\text{inp}} = \int_{\mathcal{P}_t} \left[[\text{div } \boldsymbol{\sigma} + \rho(\mathbf{f} + \mathbf{f}^m)] \cdot \mathbf{v} + \boldsymbol{\sigma} : (\text{grad } \mathbf{v}) + \rho r^m \right] dV . \quad (\text{A.18})$$

The term ρr^m now also contains the work done by the body couple $\rho \mathbf{l}^m$ [121]. The first term in the integrand of the above equation can be modified by using the conservation of linear momentum Eq. (3.15), the product rule of differentiation and the conservation of mass Eq. (3.13), so that

$$\begin{aligned} \int_{\mathcal{P}_t} [\operatorname{div} \boldsymbol{\sigma} + \rho(\mathbf{f} + \mathbf{f}^m)] \cdot \mathbf{v} \, dV &= \int_{\mathcal{P}_t} \rho \dot{\mathbf{v}} \cdot \mathbf{v} \, dV = \int_{\mathcal{P}_t} \frac{d}{dt} \left[\frac{1}{2} \mathbf{v} \cdot \mathbf{v} \right] \rho \, dV \\ &= \frac{d}{dt} \int_{\mathcal{P}_t} \frac{1}{2} \rho \mathbf{v} \cdot \mathbf{v} \, dV . \end{aligned} \quad (\text{A.19})$$

Using Eq. (A.19) in Eq. (A.18) one obtains the generalized theorem of power expended

$$P^{\text{inp}} = \frac{d}{dt} \int_{\mathcal{P}_t} \frac{1}{2} \rho \mathbf{v} \cdot \mathbf{v} \, dV + \int_{\mathcal{P}_t} [\boldsymbol{\sigma} : (\operatorname{grad} \mathbf{v}) + \rho r^m] \, dV . \quad (\text{A.20})$$

The heat input is given by the usual expression

$$Q^{\text{inp}} = \int_{\mathcal{P}_t} \rho r^h \, dV - \oint_{\partial \mathcal{P}_t} \mathbf{q} \cdot \mathbf{n} \, dA = \int_{\mathcal{P}_t} [\rho r^h - \operatorname{div} \mathbf{q}] \, dV , \quad (\text{A.21})$$

where \mathbf{q} is the heat flux through the boundary, ρr^h is an energy source term and the divergence theorem Eq. (A.1) has again been used. Substituting the expressions Eq. (A.15), Eq. (A.20) and Eq. (A.21) into Eq. (A.14) one finds

$$\frac{d}{dt} \int_{\mathcal{P}_t} \frac{1}{2} \rho \mathbf{v} \cdot \mathbf{v} \, dV + \int_{\mathcal{P}_t} \rho \dot{u} \, dV = \frac{d}{dt} \int_{\mathcal{P}_t} \frac{1}{2} \rho \mathbf{v} \cdot \mathbf{v} \, dV \quad (\text{A.22})$$

$$+ \int_{\mathcal{P}_t} [\boldsymbol{\sigma} : (\operatorname{grad} \mathbf{v}) + \rho r^m + \rho r^h - \operatorname{div} \mathbf{q}] \, dV . \quad (\text{A.23})$$

Canceling terms, rearranging and considering the fact that the equality has to hold for any part \mathcal{P}_t , one finally arrives at the local form the conservation of energy

$$\rho \dot{u} = \boldsymbol{\sigma} : (\operatorname{grad} \mathbf{v}) + \rho r^m + \rho r^h - \operatorname{div} \mathbf{q} , \quad (\text{A.24})$$

which is Eq. (3.20).

A4. Stress Power for a Small Strain Approximation

According to Eq. (3.20) the local form of the conservation of energy is given by

$$\rho \dot{u} = \boldsymbol{\sigma} : (\text{grad } \mathbf{v}) + \rho r^m + \rho r^h - \text{div } \mathbf{q} . \quad (\text{A.25})$$

The impact of a small strain approximation on the energy term $\boldsymbol{\sigma} : (\text{grad } \mathbf{v})$, often referred to as the *stress power* [126, 127], shall be investigated.

Every tensor, can be expressed uniquely as the sum of a symmetric and an a skew-symmetric tensor [127]. For the *velocity gradient tensor* $\mathbf{L} := \text{grad } \mathbf{v}$ it follows

$$\mathbf{L} = \mathbf{D} + \mathbf{W} , \quad (\text{A.26})$$

with

$$\mathbf{D} := \text{sym } \mathbf{L} = \frac{1}{2} (\text{grad } \mathbf{v} + (\text{grad } \mathbf{v})^T) ; \quad (\text{A.27})$$

$$\mathbf{W} := \text{skw } \mathbf{L} = \frac{1}{2} (\text{grad } \mathbf{v} - (\text{grad } \mathbf{v})^T) . \quad (\text{A.28})$$

\mathbf{D} is known as the *rate of deformation tensor* and \mathbf{W} as the *spin tensor* [126, 127, 138].

The stress power can then be rewritten as

$$\boldsymbol{\sigma} : \text{grad } \mathbf{v} = (\text{sym } \boldsymbol{\sigma} + \text{skw } \boldsymbol{\sigma}) : (\mathbf{D} + \mathbf{W}) = \text{sym } \boldsymbol{\sigma} : \mathbf{D} + \text{skw } \boldsymbol{\sigma} : \mathbf{W} , \quad (\text{A.29})$$

where the property that the inner product (contraction) of a symmetric and a skew-symmetric tensor is zero has been used [127]. The first term in the result of Eq. (A.29) is the work done by the stress in stretching the body, while the second term represents the work done in spinning the body [118, 130]. If the stress tensor is symmetric, i. e. if body couples are negligible, cf. Eq. (3.17), the second term vanishes.

In order to derive the reduction of the stress power associated with \mathbf{D} for a small strain approximation, it is easier to consider the equivalent term

$$\frac{1}{\rho} \boldsymbol{\sigma} : \mathbf{D} = \frac{1}{\rho_0} \mathbf{S} : \dot{\mathbf{E}}, \quad (\text{A.30})$$

where \mathbf{S} is the *second Piola-Kirchhoff stress tensor* and \mathbf{E} is the *Green-Lagrange strain tensor* [126, 127, 132]. The following proof of this relation can also be found in [130, 132]. The tensors $\boldsymbol{\sigma}$ and \mathbf{D} are defined in the *deformed configuration*, whereas \mathbf{S} and \mathbf{E} are defined in the *reference configuration*. The following relations hold [126]

$$\mathbf{S} = J \mathbf{F}^{-1} \boldsymbol{\sigma} \mathbf{F}^{-\text{T}}; \quad (\text{A.31a})$$

$$\dot{\mathbf{E}} = \mathbf{F}^{\text{T}} \mathbf{D} \mathbf{F}. \quad (\text{A.31b})$$

Using Eqs. (A.31), it can be shown that Eq. (A.30) must indeed hold

$$\begin{aligned} \frac{\rho_0}{\rho} \boldsymbol{\sigma} : \mathbf{D} &= J \boldsymbol{\sigma} : \mathbf{D} = J \boldsymbol{\sigma} : (\mathbf{F}^{-\text{T}} \dot{\mathbf{E}} \mathbf{F}^{-1}) = J (\mathbf{F}^{-1} \boldsymbol{\sigma}) : (\dot{\mathbf{E}} \mathbf{F}^{-1}) \\ &= J (\mathbf{F}^{-1} \boldsymbol{\sigma} \mathbf{F}^{-\text{T}}) : \dot{\mathbf{E}} = \mathbf{S} : \dot{\mathbf{E}}. \end{aligned} \quad (\text{A.32})$$

The Green-Lagrange strain tensor can be expressed in terms of the displacement gradient tensor $\text{Grad } \mathbf{u}$ [126, 132]

$$\mathbf{E} := \frac{1}{2} (\mathbf{F}^{\text{T}} \mathbf{F} - \mathbf{I}) = \frac{1}{2} \left(\text{Grad } \mathbf{u} + (\text{Grad } \mathbf{u})^{\text{T}} + (\text{Grad } \mathbf{u})^{\text{T}} \text{Grad } \mathbf{u} \right), \quad (\text{A.33})$$

where the relation [127]

$$\mathbf{F} = \text{Grad } \mathbf{u} + \mathbf{I}, \quad (\text{A.34})$$

has been used, and \mathbf{I} is the second order identity tensor. In the infinitesimal strain approximation it is assumed that the norm of the deformation gradient is small, i. e. $\|\text{Grad } \mathbf{u}\| = \sqrt{(\text{Grad } \mathbf{u}) : (\text{Grad } \mathbf{u})} \ll 1$, and $\text{Grad } \mathbf{u} \approx \text{grad } \mathbf{u} = \nabla \mathbf{u}$, such that

from Eq. (A.33) it follows

$$\mathbf{E} \approx \frac{1}{2} \left(\nabla \mathbf{u} + (\nabla \mathbf{u})^T \right) = \boldsymbol{\varepsilon} . \quad (\text{A.35})$$

Similarly, it follows $J = \rho_0/\rho \approx 1$ and $\mathbf{S} \approx \boldsymbol{\sigma}$ (for details refer to [132]). Thus, for small strains the part of the stress power associated with the rate of deformation can finally be approximated as

$$\frac{1}{\rho} \boldsymbol{\sigma} : \mathbf{D} = \frac{1}{\rho_0} \mathbf{S} : \dot{\mathbf{E}} \approx \frac{1}{\rho} \boldsymbol{\sigma} : \dot{\boldsymbol{\varepsilon}} . \quad (\text{A.36})$$

A5. Derivation of Thermodynamic Restrictions on Constitutive Equations

Combining the first and the second law of thermodynamics in the form of Eqs. (3.25) and (3.27), and considering the dissipation through heat conduction separately, leads to the *Clausius-Planck inequality* [126]

$$\rho(T\dot{s} - \dot{u}) + \boldsymbol{\sigma} : \dot{\boldsymbol{\varepsilon}} + \mu_0 \mathbf{H} \cdot \dot{\mathbf{M}} \geq 0 . \quad (\text{A.37})$$

Taking the material time derivative of the Legendre transformation Eq. (3.23) and reorganizing yields

$$\rho\dot{u} = \rho\dot{g} + \rho(\dot{s}T + s\dot{T}) + \dot{\boldsymbol{\sigma}} : \boldsymbol{\varepsilon} + \boldsymbol{\sigma} : \dot{\boldsymbol{\varepsilon}} + \mu_0 \dot{\mathbf{H}} \cdot \mathbf{M} + \mu_0 \mathbf{H} \cdot \dot{\mathbf{M}} . \quad (\text{A.38})$$

Using Eq. (A.38) in Eq. (A.37) results in

$$-\rho\dot{g} - \rho s\dot{T} - \dot{\boldsymbol{\sigma}} : \boldsymbol{\varepsilon} - \mu_0 \dot{\mathbf{H}} \cdot \mathbf{M} \geq 0 . \quad (\text{A.39})$$

If \hat{g} is sufficiently smooth in all arguments its total differential leads to the expression

$$\dot{g} = \frac{\partial \hat{g}}{\partial T} \dot{T} + \frac{\partial \hat{g}}{\partial \boldsymbol{\sigma}} : \dot{\boldsymbol{\sigma}} + \frac{\partial \hat{g}}{\partial \mathbf{H}} \cdot \dot{\mathbf{H}} + \frac{\partial \hat{g}}{\partial \boldsymbol{\zeta}} \cdot \dot{\boldsymbol{\zeta}} . \quad (\text{A.40})$$

Combining Eqs. (A.39) and (A.40) yields

$$-\rho \left(\frac{\partial \hat{g}}{\partial T} + s \right) \dot{T} - \left(\rho \frac{\partial \hat{g}}{\partial \boldsymbol{\sigma}} + \boldsymbol{\varepsilon} \right) : \dot{\boldsymbol{\sigma}} - \left(\rho \frac{\partial \hat{g}}{\partial \mathbf{H}} + \mu_0 \mathbf{M} \right) \cdot \dot{\mathbf{H}} - \rho \frac{\partial \hat{g}}{\partial \boldsymbol{\zeta}} : \dot{\boldsymbol{\zeta}} \geq 0,$$

which is Eq. (3.28). From this inequality and the arguments given in Chapter III, Section C the constitutive relations of Eqs.(3.29) and the reduced form of the Clausius-Planck inequality Eq.(3.30) follow.

APPENDIX B

DERIVATIONS RELATED TO ELECTROMAGNETISM

B1. Magnetostatic Poisson Equations

By introducing the scalar magnetic potential Φ^m , such that $\mathbf{H} = -\nabla\Phi^m$, Ampère's law Eq. (3.7b) is identically satisfied if free currents are negligible, since $\text{curl}(\nabla\alpha) = \mathbf{0}$, $\forall\alpha$. Using Eq. (3.2b) and Eq. (3.7a) it then follows

$$\text{div}\mathbf{B} = \mu_0(\text{div}\mathbf{H} + \text{div}\mathbf{M}) = \mu_0(\text{div} - \nabla\Phi^m + \text{div}\mathbf{M}) = 0, \quad (\text{B.1})$$

such that with the definition of the Laplacian operator $\Delta\alpha := \text{div}(\nabla\alpha)$ one obtains

$$\Delta\Phi^m = \text{div}\mathbf{M}, \quad (\text{B.2})$$

which is Eq. (6.3a).

Alternatively, by introducing the vector valued potential Φ^m , such that $\mathbf{B} = \text{curl}\Phi^m$, the Gauss-Faraday law Eq. (3.7a) is identically satisfied. Combining Eq. (3.2b), Eq. (3.7b) and the identity $\text{curl}(\text{curl}\mathbf{A}) = \nabla(\text{div}\mathbf{A}) - \Delta\mathbf{A}$, where $\Delta\mathbf{A} := \text{div}(\nabla\mathbf{A})$ is the vector-valued Laplace operator, yields

$$\begin{aligned} \text{curl}\mathbf{H} &= \text{curl}\left(\frac{\mathbf{B}}{\mu_0} - \mathbf{M}\right) = \text{curl}\left(\frac{\text{curl}\Phi^m}{\mu_0} - \mathbf{M}\right) \\ &= \frac{1}{\mu_0}\left(\nabla(\text{div}\Phi^m) - \Delta\Phi^m\right) - \text{curl}\mathbf{M} = \mathbf{0}. \end{aligned} \quad (\text{B.3})$$

Since the relation $\mathbf{B} = \text{curl}\Phi^m$ determines the magnetic potential only up to a constant, one is free to choose this constant such that $\text{div}\Phi^m = 0$. This is usually referred

to as *setting the Coulomb gauge* [152]. Rearranging then leads to

$$\Delta\Phi^m = -\mu_0 \operatorname{curl}\mathbf{M} , \quad (\text{B.4})$$

which is Eq. (6.3b).

B2. Field Transformations

The following derivation has been compiled from material presented in [114, 122, 124]. The different formulations of Maxwell's equations for moving matter distinguish themselves by the relations between electromagnetic fields measured by an observer in a stationary (laboratory) frame and an observer moving with a material point (rest frame). For the Minkowski these relations are found by imposing the invariance of Maxwell's equations under Galilean transformations for the non-relativistic approximation. A Galilean transformation between two frames, or *change in observer*, is defined by

$$t = t' ; \quad (\text{B.5a})$$

$$\mathbf{x} = \mathbf{x}' + \mathbf{v}t , \quad (\text{B.5b})$$

where additionally a rigid body rotation could be superimposed [127]. The classical equations of motion (the local form of the conservation of linear momentum) in continuum mechanics, for example, are known to be invariant under Galilean changes in observer [127], i. e. the equations are of the same form in both frames. In the following paragraphs field transformation relations for the Minkowski formulation are derived under the requirement of invariance of Maxwell's equations under Galilean changes in observer.

From Eqs. (B.5) the following relations between derivatives in the two frames

hold [114, 122, 124]

$$\nabla'(\cdot) = \nabla(\cdot) ; \quad (\text{B.6a})$$

$$\text{div}'(\cdot) = \text{div}(\cdot) ; \quad (\text{B.6b})$$

$$\text{curl}'(\cdot) = \text{curl}(\cdot) . \quad (\text{B.6c})$$

Similarly the convective derivative of a vector is defined as

$$(\cdot)^* := \frac{\partial(\cdot)}{\partial t'} = \frac{\partial(\cdot)}{\partial t} + [\nabla(\cdot)]\mathbf{v} = \frac{\partial(\cdot)}{\partial t} + \mathbf{v} \text{div}(\cdot) - \text{curl}(\mathbf{v} \times (\cdot)) , \quad (\text{B.7})$$

where the identity $\text{curl}(\mathbf{a} \times \mathbf{b}) = \mathbf{a} \text{div} \mathbf{b} - \mathbf{b} \text{div} \mathbf{a} + (\nabla \mathbf{a})\mathbf{b} - (\nabla \mathbf{b})\mathbf{a}$ was used in addition to the fact that the velocity field \mathbf{v} is spatially constant.

The local form of Maxwell's equations in the laboratory frame were given in Eqs. (3.4). In order to establish invariance of these equations, the local form of Maxwell's equations in the co-moving rest frame must be of the form [124]

$$\text{Gauss's law:} \quad \text{div}' \mathbf{D}' = \rho'_f ; \quad (\text{B.8a})$$

$$\text{Gauss-Faraday law:} \quad \text{div}' \mathbf{B}' = 0 ; \quad (\text{B.8b})$$

$$\text{Ampère's law:} \quad \text{curl}' \mathbf{H}' = \mathbf{J}'_f + \frac{\partial \mathbf{D}'}{\partial t'} ; \quad (\text{B.8c})$$

$$\text{Faraday's law:} \quad \text{curl}' \mathbf{E}' = -\frac{\partial \mathbf{B}'}{\partial t'} . \quad (\text{B.8d})$$

Using the relations (B.6), Eqs. (B.8) can be rewritten in the form

$$\text{Gauss's law:} \quad \text{div} \mathbf{D}' = \rho'_f ; \quad (\text{B.9a})$$

$$\text{Gauss-Faraday law:} \quad \text{div} \mathbf{B}' = 0 ; \quad (\text{B.9b})$$

$$\text{Ampère's law:} \quad \text{curl} \mathbf{H}' = \mathbf{J}'_f + \frac{\partial \mathbf{D}'}{\partial t} + \rho'_f \mathbf{v} - \text{curl}(\mathbf{v} \times \mathbf{D}'); \quad (\text{B.9c})$$

$$\text{Faraday's law:} \quad \text{curl} \mathbf{E}' = -\frac{\partial \mathbf{B}'}{\partial t} + \text{curl}(\mathbf{v} \times \mathbf{B}'). \quad (\text{B.9d})$$

By rearrangement and comparison of the terms in Eqs. (B.9) and Eqs. (3.4) the transformation relations (3.10) are deduced.

APPENDIX C

DISCUSSION OF THE GIBBS FREE ENERGY

C1. Interpretation of the Gibbs Free Energy for a Hyperelastic Material

The Gibbs free energy in this case is of the general form

$$g = \hat{g}(T, \boldsymbol{\sigma}) . \quad (\text{C.1})$$

Neglecting magnetic terms, using the Legendre transformation Eq. (3.23), and considering the heat conduction problem separately, the first and second law of thermodynamics as specified in Eqs. (3.20) and Eq. (3.27), respectively, can be combined to yield

$$\rho T \dot{s} - \rho r^h + \text{div } \mathbf{q} = -\rho \dot{g} - \dot{\boldsymbol{\sigma}} : \boldsymbol{\varepsilon} - \rho s \dot{T} \geq 0 . \quad (\text{C.2})$$

From Eq. (C.1) one can find \dot{g} using the total differential of g , which substituted into Eq. (C.1) leads to

$$-\rho \left(\left. \frac{\partial \hat{g}}{\partial T} \right|_{\boldsymbol{\sigma}} + s \right) \dot{T} - \left(\rho \left. \frac{\partial \hat{g}}{\partial \boldsymbol{\sigma}} \right|_T + \boldsymbol{\varepsilon} \right) : \dot{\boldsymbol{\sigma}} \geq 0 , \quad (\text{C.3})$$

which is the equivalent of Eq. (3.28) for the elastic case. In this expression it has been emphasized that the partial derivatives imply that the other independent variables are kept constant when taking the derivative. With the same arguments as given in Section C of Chapter III, for the inequality to hold for arbitrary processes, the

following constitutive relations must hold

$$s = - \left. \frac{\partial \hat{g}}{\partial T} \right|_{\boldsymbol{\sigma}} ; \quad (\text{C.4a})$$

$$\boldsymbol{\varepsilon} = \boldsymbol{\varepsilon}^e = - \rho \left. \frac{\partial \hat{g}}{\partial \boldsymbol{\sigma}} \right|_T . \quad (\text{C.4b})$$

The *complementary strain energy* of a *hyperelastic* material is defined such that the integral

$$\mathcal{U}^c(\boldsymbol{\sigma}) := \int_0^{\boldsymbol{\sigma}} \boldsymbol{\varepsilon} : d\bar{\boldsymbol{\sigma}} , \quad (\text{C.5})$$

is independent of the integration path in stress space, with the conditions $\mathcal{U}^c(\boldsymbol{\sigma}) \geq 0$ and $\mathcal{U}^c(\boldsymbol{\sigma}) = 0$, if and only if $\boldsymbol{\sigma} = \mathbf{0}$ [132]. This definition implies

$$\boldsymbol{\varepsilon} = \frac{\partial \mathcal{U}^c}{\partial \boldsymbol{\sigma}} . \quad (\text{C.6})$$

Thus by comparing Eqs. (C.4b) and (C.6) the following relation must hold for a hyperelastic material

$$\frac{\partial \mathcal{U}^c}{\partial \boldsymbol{\sigma}} = - \rho \left. \frac{\partial \hat{g}}{\partial \boldsymbol{\sigma}} \right|_T . \quad (\text{C.7})$$

For isothermal conditions and negligible changes in the density, Eq. (C.7) can be integrated to yield

$$\mathcal{U}^c = - \rho g . \quad (\text{C.8})$$

Thus *for a hyperelastic material under isothermal conditions the Gibbs free energy can be interpreted as the complementary strain energy potential* (with a factor of $-\rho$).

C2. Discussion of an Alternative Gibbs Free Energy Expression for MSMA

The Gibbs free energy for the MSMA constitutive model was proposed in the form of Eq. (4.8) in Chapter IV. Alternatively the more common approach of using a

Taylor series expansion of the free energy about a reference point can be employed. At first the discussion shall be restricted to a comparison of the two approaches for general non-dissipative magnetoelastic materials. In series expansion approach the free energy is then given by²

$$g = \hat{g}(\sigma_{ij}, H_i) = -\frac{1}{2\rho} S_{ijkl} \sigma_{ij} \sigma_{kl} - \frac{1}{2\rho} \chi_{ij}^{\text{sc}} H_i H_j - \frac{1}{2\rho} \chi_{ijkl}^{\text{ms}} \sigma_{ij} H_i H_j + g_0, \quad (\text{C.9})$$

where S_{ijkl} , χ_{ij}^{sc} and χ_{ijkl}^{ms} are the components of the compliance tensor, the susceptibility tensor and the magnetostrictive coefficient tensor. The effect of temperature is not explicitly considered since the focus is on isothermal processes. Other coupling terms, such as a piezomagnetic coupling for example, have been omitted. It is straightforward to include these terms, but in the context of MSMA modeling they are deemed negligible.

Then from the thermodynamic restrictions (3.29b) and (3.29c) the following constitutive equation are derived

$$\varepsilon_{ij} = \varepsilon_{ij}^e = -\rho \frac{\partial \hat{g}}{\partial \sigma_{ij}} = S_{ijkl} \sigma_{ij} + \frac{1}{2} \chi_{ijkl}^{\text{ms}} H_k H_l; \quad (\text{C.10a})$$

$$\mu_0 M_i = -\rho \frac{\partial \hat{g}}{\partial H_i} = \chi_{ij}^{\text{sc}} H_j + \chi_{jkl}^{\text{ms}} \sigma_{jk} H_l. \quad (\text{C.10b})$$

One can consider the constrained MSMA single crystal discussed in Chapter II, Section B as such a magnetoelastic material. The constitutive response for the magnetization of this material along the easy axis (x-axis) and the hard axis (y-axis),

²Index notation is used here instead of direct notation wherever it is deemed more convenient.

cf. Figs.8-10, follow from Eq. (C.10b), neglecting magnetostriction, as

$$M_x^{\text{easy}} = \chi_{xx}^{\text{sc}} H_x ; \quad (\text{C.11a})$$

$$M_y^{\text{hard}} = \chi_{yy}^{\text{sc}} H_y . \quad (\text{C.11b})$$

These equations represent a linear approximation of the magnetization response curves of Fig. 10 on page 24 for fields up to the magnetic saturation limit. The coefficients χ_{xx}^{sc} and χ_{yy}^{sc} can be determined from these curves.

This result shall be compared to the magnetization response of the constrained single crystal as predicted by the proposed model. Since $\xi = 0$, due to the compressive stress bias along the x-axis, Eqns. (4.9c), (4.10c), (4.11a) and (4.11c) take on the following reduced form

$$\begin{aligned} \mathbf{M} &= (1 - \alpha)\mathbf{M}^1 + \alpha\mathbf{M}^3 \\ &= - (1 - \alpha)M^{\text{sat}} (\cos(\theta_1) \mathbf{e}_x + \sin(\theta_1) \mathbf{e}_y) \\ &\quad + \alpha M^{\text{sat}} (\cos(\theta_3) \mathbf{e}_x + \sin(\theta_3) \mathbf{e}_y) ; \end{aligned} \quad (\text{C.12})$$

$$\begin{aligned} \pi^\alpha &= -\rho \left[-\frac{\mu_0}{\rho} (\mathbf{M}^3 - \mathbf{M}^1) \cdot \mathbf{H} + g^{\text{an},3}(\theta_3) - g^{\text{an},1}(\theta_1) \right] - \frac{\partial f^\alpha}{\partial \alpha} \\ &= \mu_0 M^{\text{sat}} \left[\cos(\theta_3) \mathbf{e}_x + \sin(\theta_3) \mathbf{e}_y + \cos(\theta_1) \mathbf{e}_x + \sin(\theta_1) \mathbf{e}_y \right] \cdot \mathbf{H} \\ &\quad - \rho K_1 \sin^2(\theta_3) + \rho K_1 \sin^2(\theta_1) - \frac{\partial f^\alpha}{\partial \alpha} . \end{aligned} \quad (\text{C.13})$$

$$\begin{aligned} \pi^{\theta_1} = & -\rho(1-\alpha) \left[\frac{\mu_0 M^{\text{sat}}}{\rho} \left[-\sin(\theta_1)H_x + \cos(\theta_1)H_y \right] \right. \\ & \left. + 2K_1 \sin(\theta_1) \cos(\theta_1) \right]; \end{aligned} \quad (\text{C.14})$$

$$\pi^{\theta_3} = -\rho\alpha \left[-\frac{\mu_0 M^{\text{sat}}}{\rho} \left[-\sin(\theta_3)H_x + \cos(\theta_3)H_y \right] + 2K_1 \sin(\theta_3) \cos(\theta_3) \right]. \quad (\text{C.15})$$

For the magnetization along the **easy axis**, i. e. $H_x \neq 0$ and $H_y = 0$, the constraint (4.13b) on the rotation angle θ_1 , with Eq. (C.14), leads to

$$(1-\alpha) \sin(\theta_1) \left[\mu_0 M^{\text{sat}} H_x - 2\rho K_1 \cos(\theta_1) \right] = 0. \quad (\text{C.16})$$

This equation is satisfied for all values of H_x if $\theta_1 = 0$ and $0 \leq \alpha < 1$. Similarly, it follows from Eq. (C.15) and (4.13b)

$$\alpha \sin(\theta_3) \left[\mu_0 M^{\text{sat}} H_x + 2\rho K_1 \cos(\theta_3) \right] = 0, \quad (\text{C.17})$$

which is satisfied for all values of H_x if $\theta_3 = 0$ and $0 < \alpha \leq 1$. Thus, if the field is applied the direction of the easy axis, the model predicts the expected result that the magnetization vectors do not rotate away from their preferred directions.

in this case the constraint (4.13a) on the driving force for the evolution of the domain volume fraction as described by Eq. (C.13) reduces to

$$\pi^\alpha = 2\mu_0 \mathbf{M}^{\text{sat}} H_x - \frac{\partial f^\alpha}{\partial \alpha} = 0. \quad (\text{C.18})$$

If one assumes a linear hardening behavior of the type $\frac{\partial f^\alpha}{\partial \alpha} = a\alpha + b$ solving Eq. (C.18)

for α leads to

$$\alpha = \frac{1}{a} \left[2\mu_0 M^{\text{sat}} H_x - b \right]. \quad (\text{C.19})$$

With the conditions $\alpha(H_x = 0) = 1/2$ and $\alpha(H_x = H^{\text{crit},\alpha}) = 1$ the evolution equation for the magnetic domain volume fraction is finally derived to be

$$\alpha = \frac{H_x + H^{\text{crit},\alpha}}{2H^{\text{crit},\alpha}}. \quad (\text{C.20})$$

$H^{\text{crit},\alpha}$ is the critical field at which magnetic saturation is achieved through domain wall motion and its value can be determined from an easy axis magnetization curve of the type shown in Fig. 10 on page 24. Substituting Eq. (C.20) as well as $\theta_1 = \theta_3 = 0$ into Eq. (C.12) and considering the x -component yields

$$M_x^{\text{easy}} = (2\alpha - 1)M^{\text{sat}} = \left(\frac{H_x + H^{\text{crit},\alpha}}{H^{\text{crit},\alpha}} - 1 \right) M^{\text{sat}} = \frac{M^{\text{sat}}}{H^{\text{crit},\alpha}} H_x. \quad (\text{C.21})$$

For the magnetization along the **hard axis**, i.e. $H_x = 0$ and $H_y \neq 0$, the constraint (4.13b) on the rotation angle θ_1 , with Eq. (C.14) and $0 < \alpha \leq 1$ leads to

$$\cos(\theta_1) \left[\mu_0 M^{\text{sat}} H_y + 2\rho K_1 \sin(\theta_1) \right] = 0. \quad (\text{C.22})$$

For $0 \leq \theta_1 < \frac{\pi}{2}$ one obtains the relation

$$\sin(\theta_1) = -\frac{\mu_0 M^{\text{sat}}}{2\rho K_1} H_y. \quad (\text{C.23})$$

The equivalent expression for $\theta_3(H_y)$ was derived as Eq. (5.3). Note that $\sin(\theta_3) =$

$-\sin(\theta_1)$. With these relations the hard axis magnetization is derived to be

$$\begin{aligned}
 M_y^{\text{hard}} &= -(1 - \alpha)M^{\text{sat}} \sin(\theta_1) + \alpha M^{\text{sat}} \sin(\theta_3) \\
 &= -(1 - \alpha)M^{\text{sat}} \sin(\theta_1) - \alpha M^{\text{sat}} \sin(\theta_1) = -M^{\text{sat}} \sin(\theta_1) \\
 &= \frac{\mu_0 (M^{\text{sat}})^2}{2\rho K_1} H_y .
 \end{aligned} \tag{C.24}$$

A comparison of Eqs. (C.11) with Eqs. (C.21) and (C.24) reveals that if one sets

$$\chi_{xx}^{\text{sc}} = \frac{M^{\text{sat}}}{H^{\text{crit},\alpha}} \quad \text{and} \quad \chi_{yy}^{\text{sc}} = \frac{\mu_0 (M^{\text{sat}})^2}{2\rho K_1} , \tag{C.25}$$

the same magnetization response is predicted for the constrained MSMA by the current constitutive model and the model based on the alternative form of the Gibbs free energy (C.9). In fact by substituting Eq. (C.10b) into Eq. (C.9) and neglecting ordinary magnetostriction the term

$$-\frac{1}{2\rho} \chi_{ij}^{\text{sc}} H_i H_j = -\frac{\mu_0}{2\rho} \mathbf{H} \cdot \mathbf{M}(\mathbf{H}) , \tag{C.26}$$

can be interpreted as the equivalent of the Zeeman energy term in Eq. (4.2). The difference between the two energy terms is that in Eq. (C.26) the magnetization vector \mathbf{M} is a linear function of \mathbf{H} , which also explains the factor of 1/2 in Eq. (C.25), whereas in Eq. (4.2) it is a function of the internal state variables α and θ_i and a function of \mathbf{H} only after the evaluation of the additional constraints (4.13). However, as was demonstrated, both energy expressions predict the same magnetization response for the MSMA with suppressed variant reorientation. The magnetocrystalline anisotropy energy does not explicitly appear in Eq. (C.9), but according to Eqs. (C.25) it is captured in the component χ_{yy}^{sc} . The anisotropic nature of the magnetization response is further evident from the fact that $\chi_{xx}^{\text{sc}} \neq \chi_{yy}^{\text{sc}}$.

One of the reasons the Gibbs free energy was chosen to be of the form specified in Eq. (4.8) is the fact that the change in the magnetization due to variant reorientation can easily be incorporated. Instead of having a Zeeman energy term of the form $-\frac{\mu_0}{\rho}\mathbf{M}(\alpha, \theta_i)\cdot\mathbf{H}$ as was assumed for the constrained MSMA, the term now becomes $-\frac{\mu_0}{\rho}\mathbf{M}(\xi, \alpha, \theta_i)\cdot\mathbf{H}$. In the series expansion approach of Eq. (C.9), however, it is not straightforward to incorporate the contribution of the evolving variant volume fraction to the magnetization change. The inelastic reorientation strain was accounted for by assuming an additive decomposition of the total strain in Eq. (4.1) and then postulating the corresponding evolution equation (4.15). A similar decomposition of the magnetization in this case is difficult to justify because the magnetic domain wall motion is typically reversible in MSMA (cf. Fig. 8) such that the macroscopic magnetization always vanishes as the applied field is reduced to zero. This situation is different from the magnetic hysteresis observed in permanent magnets in which *irreversible* magnetic domain wall motion leads to remnant magnetization and hysteresis [16, 17] such that the magnetization can actually be decomposed into a reversible and an irreversible part [129].

A second reason for not choosing the series expansion approach is the fact that the internal state variables ξ , α and θ_i and their evolution are directly connected to the physical processes that cause the unique magnetomechanical response of MSMA. By being able to keep track of these variables and schematically visualizing the martensitic variant and magnetic domain volume fractions as well as the orientation of the magnetization vectors, as for example shown in Tables III–VII in Chapter V, one can analyze the model predictions in much greater detail and compare them with physical intuition. The susceptibility tensor χ^{sc} on the other hand captures the macroscopic effect of the magnetic domain wall motion, the magnetization vector rotation and the resulting anisotropy through the values of its coefficients. Information about the

current values of the rotation angles and the domain volume fractions as functions of the magnetic field is not available in this case.

C3. Accounting for Temperature Changes During Variant Reorientation

The expanded expression of the free energy is then given by

$$g = g^{\text{Eq. (4.8)}} + c_p \left[(T - T_0) - T \ln \left(\frac{T}{T_0} \right) \right], \quad (\text{C.27})$$

where c_p is the effective heat capacity defined as $c_p = c_p^{\text{V1}} + \xi(c_p^{\text{V2}} - c_p^{\text{V1}})$, and T_0 is the reference temperature. Furthermore, the free energy reference state value in Eq. (4.8) is interpreted as $g_0(T) = u_0 - s_0 T$, where u_0 and s_0 are the internal energy and entropy at the reference state. Within reasonable limits, and far below the Curie and the austenitic transformation temperatures, the magnetic properties such as the saturation magnetization and the magnetocrystalline anisotropy are assumed to be constant with respect to temperature. Thermal expansion has been neglected, since only small temperature changes are considered.

From Eq. (C.27) the following constitutive equation for the entropy is derived, which is an extension of Eq. (4.9a)

$$s = -\frac{\partial \hat{g}}{\partial T} = c_p \ln \left(\frac{T}{T_0} \right) + s_0. \quad (\text{C.28})$$

All other constitutive equations remain the same. Using Eq. (A.40), the conservation of energy Eq. (3.26) can be rewritten as

$$\begin{aligned} & \rho \left[\frac{\partial \hat{g}}{\partial T} \dot{T} + \frac{\partial \hat{g}}{\partial \boldsymbol{\sigma}} : \dot{\boldsymbol{\sigma}} + \frac{\partial \hat{g}}{\partial \mathbf{H}} \cdot \dot{\mathbf{H}} + \frac{\partial \hat{g}}{\partial \boldsymbol{\zeta}} \cdot \dot{\boldsymbol{\zeta}} \right] + \rho(\dot{s}T + s\dot{T}) + \dot{\boldsymbol{\sigma}} : \boldsymbol{\varepsilon} \\ & + \mu_0 \dot{\mathbf{H}} \cdot \mathbf{M} + \rho r^{\text{h}} - \text{div } \mathbf{q} = 0. \end{aligned} \quad (\text{C.29})$$

Using the constitutive relations (4.9), canceling terms and rearranging then leads to

$$\rho \frac{\partial \hat{g}}{\partial \zeta} \cdot \dot{\zeta} + \rho \dot{s} T - \rho r^h + \operatorname{div} \mathbf{q} = 0 . \quad (\text{C.30})$$

With the definitions of the thermodynamic driving forces in Eqs. (4.10), (4.11) and (4.17), the first term can, in agreement with Eq. (4.12), be written as

$$\begin{aligned} \rho \frac{\partial \hat{g}}{\partial \zeta} \cdot \dot{\zeta} &= - \left[\boldsymbol{\pi}^r : \dot{\boldsymbol{\varepsilon}}^r + \tilde{\pi}^\xi \dot{\xi} + \pi^\alpha \dot{\alpha} + \sum_{i=1}^4 \pi^{\theta_i} \dot{\theta}_i \right] \\ &= - \left[\pi^\xi \dot{\xi} + \pi^\alpha \dot{\alpha} + \sum_{i=1}^4 \pi^{\theta_i} \dot{\theta}_i \right] = -\pi^\xi \dot{\xi} . \end{aligned} \quad (\text{C.31})$$

For the last equality the constraints (4.13) have been imposed. Substituting Eq. (C.31) into Eq. (C.30) yields

$$\pi^\xi \dot{\xi} - \rho \dot{s} T + \rho r^h - \operatorname{div} \mathbf{q} = 0 . \quad (\text{C.32})$$

From Eq. (C.28) it follows $\dot{s} = \frac{c_p}{T} \dot{T}$, where the reference state entropy has been assumed to be identical in both martensitic variants, i. e. $\Delta s_0 = 0$. The conservation of energy can then finally be expressed as

$$\rho c_p \dot{T} - \pi^\xi \dot{\xi} = \rho r^h - \operatorname{div} \mathbf{q} . \quad (\text{C.33})$$

This expression can be used to calculate the temperature increase during a magnetic cycle due to the dissipated heat associated with the reorientation of martensitic variants. If one assumes adiabatic conditions to find an upper bound for the temperature change in a complete cycle, using the reorientation function Eq. (4.19) and the Kuhn-Tucker conditions (4.20), it follows

$$\begin{aligned}
\Delta T &= \frac{1}{\rho c_p} \left[\int_0^1 \pi^{(1,2)} d\xi + \int_1^0 \pi^{(2,1)} d\xi \right] \\
&= \frac{1}{\rho c_p} \left[\int_0^1 Y^\xi d\xi + \int_1^0 -Y^\xi d\xi \right] = \frac{2Y^\xi}{\rho c_p} .
\end{aligned} \tag{C.34}$$

For a typical Ni-Mn-Ga composition which has the properties $\rho = 8300.0 \text{ kgm}^{-3}$, $c_p = 480.0 \text{ Jkg}^{-1}\text{K}^{-1}$ [164] and 223.6 kPa (see Table VIII), one calculates a temperature change of $\Delta T = 0.11 \text{ K}$ per magnetic cycle. This value is at least one order of magnitude lower than the temperature change induced by the austenite-martensite phase transformation in an adiabatic *pseudoelastic* cycle of NiTi, but seems reasonable, nonetheless, since the variant reorientation process is not a first order phase transition [165]. In fact for the stress-induced phase transformation in SMAs the energy balance Eq. C.33 contains an extra term $\rho \Delta s_0 T$ [71, 76], which reflects the entropy difference between the austenite and martensite phases.

APPENDIX D

SELECTED MAPLE FILES

D1. Determination of Model Parameters

```
> restart:
> with(plots):
> xis:=0:
> xif:=0.96: (in case of partial reorientation, xif<1)
```

Evaluation of the reorientation surfaces at xis and xif

```
> eqn1:={sigp*emax+mu0*Msat*Hs12-(mu0*Msat)^2/(4*rhoK1)*Hs12^2
        -(-A*(Pi-arccos(2*xis-1))+B1+B2)-Yk=0, sigp*emax+mu0*Msat*Hf12
        -(mu0*Msat)^2/(4*rhoK1)*Hf12^2-(-A*(Pi-arccos(2*xif-1))+B1+B2)-Yk=0,
        sigp*emax+mu0*Msat*Hs21-(mu0*Msat)^2/(4*rhoK1)*Hs21^2
        -(-C*(Pi-arccos(2*xif-1))+B1-B2)+Yk=0,
        sigp*emax+mu0*Msat*Hf21-(mu0*Msat)^2/(4*rhoK1)*Hf21^2
        -(-C*(Pi-arccos(2*xis-1))+B1-B2)+Yk=0}:

> xi12:=1/2*cos(-1/A*(-sigma*emax-mu0*Msat*H+(mu0*Msat)^2/(4*rhoK1)*H^2
        +B1+B2+Yk)+Pi)+1/2:
> xi21:=1/2*cos(-1/C*(-sigma*emax-mu0*Msat*H+(mu0*Msat)^2/(4*rhoK1)*H^2
        +B1-B2-Yk)+Pi)+1/2:
> sol1:=solve(eqn1,{A,C,B1,Yk}):
> assign(sol1):
```

Evaluation of hardening function at ksi=1

```
> intgr1:=-A*(Pi-arccos(2*xi-1)):
> term1:=simplify(int(intgr1,xi=0..1)):
> f12:=term1+B1+B2:
> intgr2:=-C*(Pi-arccos(2*xi-1)):
> term2:=simplify(int(intgr2,xi=0..1)):
> f21:=term2+B1-B2:
> sol2:=solve(f12=f21,B2):
> B2:=simplify(sol2):
```

Material parameters

```
> mu0:=4*Pi*1E-7:
> Msat:=514.0E3:
> rhoK1:=1.67E5:
> sigp:=-1.0E6:
> emax:=0.062:
> Hcrit:=evalf(2*rhoK1/(mu0*Msat)):
```

```
> Hcrit_bar:=evalf(Hcrit*mu0):
```

```
Hcrit_bar := .6498054475
```

```
Conversion from kG to A/m.
```

```
> Hs12:=0.39/mu0:
```

```
> Hf12:=Hcrit:
```

```
> Hs21:=0.35/mu0:
```

```
> Hf21:=-0.15/mu0:
```

D2. Numerical Evaluation of the Constitutive Response

```
> with(plots):
> with(plottools):
> plotsetup(default):
> unassign('sigma'):
> Digits:=32:
```

```
Evolution of the variant volume fraction. (with magnetization
rotation and cosine hardening function)
```

```
> Pi_s12:=sigma*emax+mu0*Msat*H-mu0^2*Msat^2/(4*rhoK1)*H^2-B1-B2-Yk:
```

```
> Pi_f12:=sigma*emax+mu0*Msat*H-mu0^2*Msat^2/(4*rhoK1)*H^2+A*Pi-B1-B2-Yk:
```

```
> Pi_s21:=sigma*emax+mu0*Msat*H-mu0^2*Msat^2/(4*rhoK1)*H^2+C*Pi-B1+B2+Yk:
```

```
> Pi_f21:=sigma*emax+mu0*Msat*H-mu0^2*Msat^2/(4*rhoK1)*H^2-B1+B2+Yk:
```

```
> Pi_s12neg:=sigma*emax-mu0*Msat*H-mu0^2*Msat^2/(4*rhoK1)*H^2-B1-B2-Yk:
```

```
> Pi_f12neg:=sigma*emax-mu0*Msat*H-mu0^2*Msat^2/(4*rhoK1)*H^2+A*Pi-B1-B2-Yk:
```

```
> Pi_s21neg:=sigma*emax-mu0*Msat*H-mu0^2*Msat^2/(4*rhoK1)*H^2+C*Pi-B1+B2+Yk:
```

```
> Pi_f21neg:=sigma*emax-mu0*Msat*H-mu0^2*Msat^2/(4*rhoK1)*H^2-B1+B2+Yk:
```

```
> xi12pos:=1/2*cos(-1/A*(-sigma*emax-mu0*Msat*H+mu0^2*Msat^2/(4*rhoK1)*H^2
+B1+B2+Yk)+Pi)+1/2:
```

```
> xi21pos:=1/2*cos(-1/C*(-sigma*emax-mu0*Msat*H+mu0^2*Msat^2/(4*rhoK1)*H^2
+B1-B2-Yk)+Pi)+1/2:
```

```
> xi12neg:=1/2*cos(-1/A*(-sigma*emax+mu0*Msat*H+mu0^2*Msat^2/(4*rhoK1)*H^2
+B1+B2+Yk)+Pi)+1/2:
```

```
> xi21neg:=1/2*cos(-1/C*(-sigma*emax+mu0*Msat*H+mu0^2*Msat^2/(4*rhoK1)*H^2
+B1-B2-Yk)+Pi)+1/2:
```

```
Material parameters
```

```
> eoff:=0:
```

```
> sigmax:=0E6:
```

```
> sigmin:=-6E6:
```

```
> Hmax_bar:=1.0:
```

```
Derived material constants
```

```
> evalf(A);
```

```
> evalf(B1);
```

```
> evalf(C);
```

```

> evalf(B2);
> evalf(Yk);
-9747.0632020485761666980459447134
-34847.411377245508982035928143712
-79393.749892589101796407185628742
54700.379820347183593573556532629
58451.026167676768502234826700902

```

Critical magnetic fields for onset and termination of reorientation

```

> sol1:=solve(Pi_s12,H):
> sol2:=solve(Pi_f12,H):
> sol3:=solve(Pi_s21,H):
> sol4:=solve(Pi_f21,H):
> sol5:=solve(Pi_s12neg,H):
> sol6:=solve(Pi_f12neg,H):
> sol7:=solve(Pi_s21neg,H):
> sol8:=solve(Pi_f21neg,H):

```

Value for full magnetization rotation ($\theta_3=90$)

```

> xicrit:=evalf(subs(sigma=-1E6,H=Hcrit,xi12pos));

```

```

xicrit := .95999999999885874972759125659926

```

Blocking stress

```

> sigb:=solve(sol1[SNP]*mu0=0.99999*Hcrit_bar,sigma);

```

```

sigb := -.14305807318148662400708181499898 107

```

```

> SN1:=evalf(mu0*subs(sigma=sigp,sol1[1]));
> SN2:=evalf(mu0*subs(sigma=sigp,sol1[2]));
> if (SN1 > SN2) then SNP:=2; SNN:=1 else SNP:=1;SNN:=2 end if;

```

Stress level 1

```

> sigma:=-1.0E6:

```

Note conversion from kG to A/m. In the calculation all the quantities are in SI units, but for convenience the magnetic field in the plots is measured in kG.

Critical magnetic fields for considered stress level

```

> sol1_bar:=evalf(sol1[SNP]*mu0);
> sol2_bar:=evalf(sol2[SNP]*mu0);
> sol3_bar:=evalf(sol3[SNP]*mu0);
> sol4_bar:=evalf(sol4[SNP]*mu0);
> sol5_bar:=evalf(sol5[SNN]*mu0);
> sol6_bar:=evalf(sol6[SNN]*mu0);
> sol7_bar:=evalf(sol7[SNN]*mu0);
> sol8_bar:=evalf(sol8[SNN]*mu0);
sol1_bar:=.39000000000000000000000000000001
sol2_bar:=.64980544747081712062256809338521

```

```

-.099623400159566407042786338670848 I
sol3_bar:=.55471790525222673927592588307912
sol4_bar:=-.15000000000000000000000000000001
sol5_bar:=-.39000000000000000000000000000001
sol6_bar:=-.64980544747081712062256809338521
+.099623400159566407042786338670848 I
sol7_bar:=-.55471790525222673927592588307912
sol8_bar:=.15000000000000000000000000000001

```

Critical values in case of partial reorientation

```

> xicrit:=evalf(subs(H=Hcrit,xi12pos));
> xicritH0:=evalf(subs(H=0,xi21pos));

      xicrit := .95999999999885874972759125659926
      xicritH0 := .26574541432721612330354739487652

> Pi_21:=sigma*emax+mu0*Msat*H-mu0^2*Msat^2/(4*rhoK1)*H^2
      +C*(Pi-arccos(2*xi-1))-B1+B2+Yk:
> Pi_12neg:=sigma*emax-mu0*Msat*H-mu0^2*Msat^2/(4*rhoK1)*H^2
      +A*(Pi-arccos(2*xi-1))-B1-B2-Yk:
> sol3_crit_bar:=evalf(mu0*solve(subs(xi=xicrit,Pi_21),H)[1]);
> sol1neg_crit_bar:=evalf(mu0*solve(subs(xi=xicritH0,Pi_12neg),H)[2]);

      sol3_crit_bar := .34999999999999999999999999999965
      sol1neg_crit_bar := -.44780580528774753855737534904424

> xicrit*emax*100;
> xicritH0*emax*100;

      5.9519999999929242483110657909154
      1.6476215688287399644819938482344

```

Plot the MFIS curves

```

> eps01:=eoff:
> eps12:=xi12pos*emax+eoff:
> eps23:=xicrit*emax+eoff:
> eps34:=xi21pos*emax+eoff:
> eps45:=xicritH0*emax+eoff:
> eps56:=xi12neg*emax+eoff:
> eps67:=emax*xicrit+eoff:
> eps78:=xi21neg*emax+eoff:

> pl1:=plot(subs(H=1/mu0*Hbar,eps01)*100,Hbar=0.0..sol1_bar,y=-0.8..6):
> pl2:=plot(subs(H=1/mu0*Hbar,eps12)*100,Hbar=sol1_bar..Hcrit_bar):
> pl3:=plot(subs(H=1/mu0*Hbar,eps23)*100,Hbar=sol3_crit_bar..Hmax_bar):
> pl4:=plot(subs(H=1/mu0*Hbar,eps34)*100,Hbar=0..sol3_crit_bar):
> pl5:=plot(subs(H=1/mu0*Hbar,eps45)*100,Hbar=0..sol1neg_crit_bar):
> pl6:=plot(subs(H=1/mu0*Hbar,eps56)*100,Hbar=-Hcrit_bar..sol1neg_crit_bar):
> pl7:=plot(subs(H=1/mu0*Hbar,eps67)*100,Hbar=-Hmax_bar..-sol3_crit_bar):
> pl8:=plot(subs(H=1/mu0*Hbar,eps78)*100,Hbar=-sol3_crit_bar..0):
> dplstrain:=display(pl1,pl2,pl3,pl4,pl5,pl6,pl7,pl8):

```

Plot the Magnetization Curves (M_y at $\theta_4=0$)

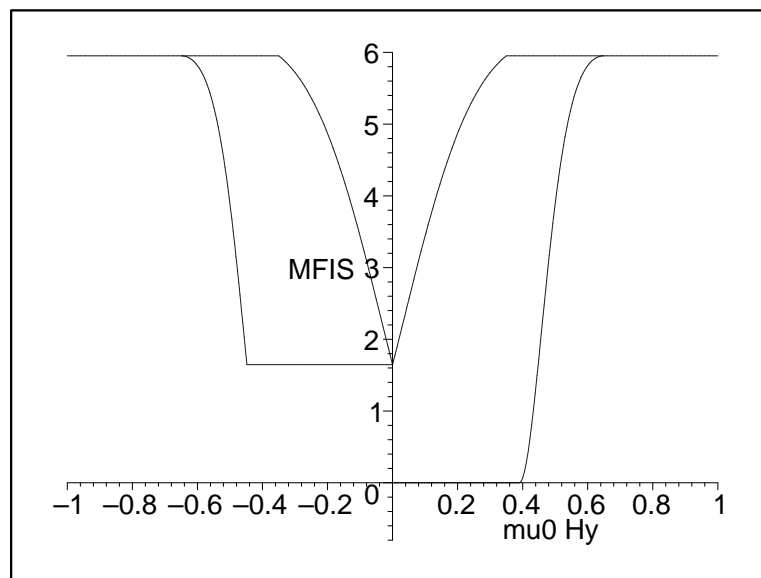
```

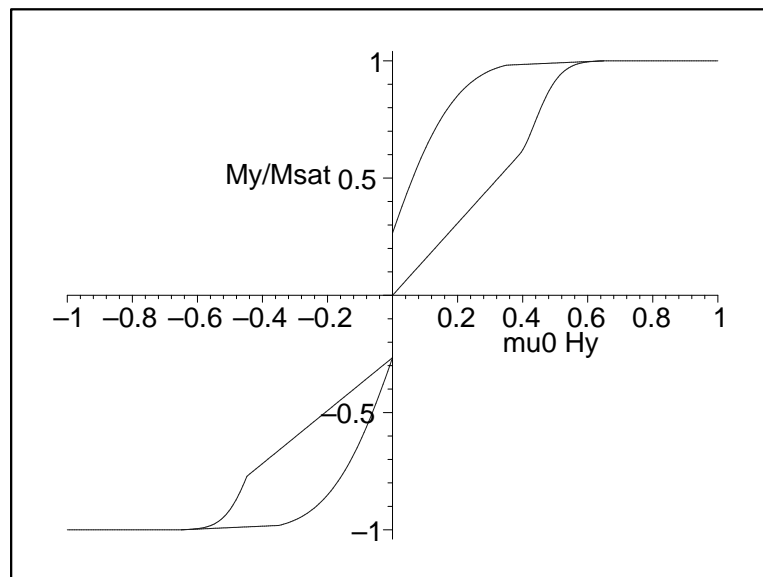
> My01:=mu0*Msat^2/(2*rhoK1)*H:
> My12:=(1-xi12pos)*mu0*Msat^2/(2*rhoK1)*H+Msat*xi12pos:
> My22b:=Msat:
> My2b3:=(1-xicrit)*mu0*Msat^2/(2*rhoK1)*H+Msat*xicrit:
> My34:=(1-xi21pos)*mu0*Msat^2/(2*rhoK1)*H+Msat*xi21pos:
> My45:=(1-xicritH0)*mu0*Msat^2/(2*rhoK1)*H-Msat*xicritH0:
> My56:=(1-xi12neg)*mu0*Msat^2/(2*rhoK1)*H-Msat*xi12neg:
> My66b:=-Msat:
> My6b7:=(1-xicrit)*mu0*Msat^2/(2*rhoK1)*H-xicrit*Msat:
> My78:=(1-xi21neg)*mu0*Msat^2/(2*rhoK1)*H-xi21neg*Msat:

> pl01my:=plot(subs(H=1/mu0*Hbar,My01)/Msat,Hbar=0.0..sol1_bar):
> pl12my:=plot(subs(H=1/mu0*Hbar,My12)/Msat,Hbar=sol1_bar..Hcrit_bar):
> pl22bmy:=plot(subs(H=1/mu0*Hbar,My22b)/Msat,Hbar=Hcrit_bar..Hmax_bar):
> pl2b3my:=plot(subs(H=1/mu0*Hbar,My2b3)/Msat,Hbar=sol3_crit_bar..Hcrit_bar):
> pl34my:=plot(subs(H=1/mu0*Hbar,My34)/Msat,Hbar=0..sol3_crit_bar):
> pl45my:=plot(subs(H=1/mu0*Hbar,My45)/Msat,Hbar=0..sol1neg_crit_bar):
> pl56my:=plot(subs(H=1/mu0*Hbar,My56)/Msat,Hbar=sol1neg_crit_bar..-Hcrit_bar):
> pl66bmy:=plot(subs(H=1/mu0*Hbar,My66b)/Msat,Hbar=-Hcrit_bar..-Hmax_bar):
> pl6b7my:=plot(subs(H=1/mu0*Hbar,My6b7)/Msat,Hbar=-Hcrit_bar..-sol3_crit_bar):
> pl78my:=plot(subs(H=1/mu0*Hbar,My78)/Msat,Hbar=-sol3_crit_bar..0):
> dplmagn:=display(pl01my,pl12my,pl22bmy,pl2b3my,pl34my,pl45my,pl56my,pl66bmy
    ,pl6b7my,pl78my):

> display(dplstrain,labels=["mu0 Hy","MFIS"]);
> display(dplmagn,labels=["mu0 Hy","My/Msat"]);

```





VITA

Bjoern Kiefer is married and has two daughters. He received his Diplom degree (M.S. equivalent) in mechanical engineering specializing in applied mechanics from the Ruhr-Universität Bochum, Germany, in September of 2001. He then enrolled in the graduate program in aerospace engineering at Texas A&M University in the spring of 2002, where he has worked under the guidance of Dr. Dimitris C. Lagoudas. His research interests include the constitutive modeling of active and multifunctional materials, nonlinear continuum mechanics and multi-field coupling phenomena. An extended resume as well as list of his publications and conference presentations can be found at <http://smart.tamu.edu>.

Mr. Kiefer can be reached at his permanent address: Gräfrather Str. 133, 42329 Wuppertal, Germany. His email address is bjoernkiefer@hotmail.com